

CNO nucleosynthesis products in mass-transfer binary stars

Kolbas, Vladimir

Doctoral thesis / Disertacija

2014

Degree Grantor / Ustanova koja je dodijelila akademski / stručni stupanj: **University of Zagreb, Faculty of Science / Sveučilište u Zagrebu, Prirodoslovno-matematički fakultet**

Permanent link / Trajna poveznica: <https://um.nsk.hr/um:nbn:hr:217:489862>

Rights / Prava: [In copyright](#)/[Zaštićeno autorskim pravom.](#)

Download date / Datum preuzimanja: **2025-03-29**



Repository / Repozitorij:

[Repository of the Faculty of Science - University of Zagreb](#)





University of Zagreb

University of Zagreb
Faculty of Science
Physics Department

Vladimir Kolbas

CNO NUCLEOSYNTHESIS PRODUCTS IN MASS-TRANSFER BINARY STARS

DOCTORAL THESIS

Supervisor:
prof. dr. sc. Krešimir Pavlovski

Zagreb, 2014.



Sveučilište u Zagrebu

Prirodoslovno-matematički Fakultet
Sveučilište u Zagrebu
Fizički odsjek

Vladimir Kolbas

**PRODUKTI CNO NUKLEOSINTEZE U
DVOJNIM ZVIJEZDAMA S
PRIJENOSOM TVARI**

DOKTORSKI RAD

Mentor:
prof. dr. sc. Krešimir Pavlovski

Zagreb, 2014.

Summary

Close binary stars of Algol type consist of a main sequence star accompanied with a cool sub-giant or giant, where former is now a more massive component. Apparently, this violates principles of the stellar evolution, and episodic mass transfer between the components has been postulated to explain this evolutionary paradox. In this short-lived process the initially more massive component has been converted into a low-mass giant, and layers which were originally deep within the star and have been altered by thermonuclear fusion during the stars's main sequence evolution are now exposed. The surface chemical composition of both stars are precious diagnostic of the nucleosynthesis processes that occur deep within stars. Theoretical evolutionary models predict changes in abundances of the elements involved in CNO nucleosynthesis.

Principal goal of present observational study was the determination of the abundance pattern in mass transferring binary stars. The two representative systems, archetype of a whole class, Algol itself, and its more massive counterpart, υ Her, have been selected for detailed examination. High-resolution and high S/N time-series of spectra were secured with fibre-fed échelle spectrographs at the NOT, La Palma, Spain, BOAO, South Korea, and CAHA, Spain. These spectra were disentangled into individual component spectra of the components which eventually make possible detail atmospheric diagnostics including determination of the elemental composition. A number of auxiliary codes have been developed to facilitate analysis and estimate uncertainties of measured quantities.

Algol is a hierarchical triple system in which the inner pair is partially eclipsing. This makes study of this binary quite challenging. For the first time the individual spectra of its components have been separated which eventually yield their complete characterisation. Their orbits and masses are revised which making possible determination of appropriate evolutionary models. The ratio of carbon and nitrogen is a very sensitive indicator of hydrogen-core CNO nucleosynthesis and a different mixing processes occurring before and after episode of mass-transfer. In present work constraints on C/N have been found for the case of low and high mass Algol-type binary system.

Sažetak

Bliski dvojni zvjezdani sustavi Algolova tipa sastoje se od zvijezde na glavnom nizu sa pratiocem u evolucijskoj fazi poddivova ili divova, pri čemu je prva masivnija. Ovakva situacija je paradoksalna uzevši u obzir evoluciju zvijezda te je postuliran period u kojem je došlo do procesa prijenosa tvari kako bi se objasnila paradoksalna situacija. Taj je kratkotrajan proces inicijalno masivniju zvijezdu pretvorio u diva manje mase, a slojevi koji su bili duboko u zvjezdanoj unutrašnjosti gdje su bili pod utjecajem nuklearnih reakcija su sada izloženi. Kemijska zastupljenost na površini obje zvijezde je dragocjen dijagnostički alat za procese nukleosinteze koji se odvijaju u dubokim slojevima zvijezda. Teorijski modeli evolucije predviđaju promjenu zastupljenosti elemenata koji sudjeluju u CNO nukleosintezi.

Glavni je cilj proučavanja određivanje zastupljenosti kemijskih elemenata u dvojnim zvjezdanim sustavim sa prijenosom tvari. Dva reprezentativna sustava izabrana za proučavanje su Algol, po kojem je nazvana cijela klasa sustava te njegova verzija veće ukupne mase u Her. Spektri visoke rezolucije i odnosa signal-šum su osigurani na échelle spektrografima NOT, La Palma, BOES, J. Koreja te CAHA, Španjolska. Ti su spektri raspjetljani u individualne spektre komponenata što omogućava detaljnu analizu uvjeta u zvjezdanoj atmosferi kao i određivanje kemijske zastupljenosti. Velik broj pomoćnih kompjuterskih kodova je razvijen za ostvarivanje tog cilja.

Algol je hijerarhijski trostruki sustav u kojem unutrašnji par zvijezda pokazuje djelomične pomrčine. To, us postojanje treće komponente, znatno otežava analizu. Prvi su put raspjetljani spektri sve tri komponente iz kojih je izvršena karakterizacija zvijezda. Orbite i mase su revidirane omogućivši određivanje evolucijskog modela. Omjer zastupljenosti dušika i ugljika je vrlo osjetljiv indikator CNO nukleosinteze u sredici te različitih procesa miješanja koji se događaju prije i nakon faze prijenosa tvari. U trenutnom radu, omjer C/N je određen za dvojne sustave Algolovog tipa male i velike mase.

Key words: stars, fundamental parameters, binaries, eclipsing, spectroscopic, elemental abundances, CNO, Algol, u Her, codes, genetic algorithms, spectra, reduction, echelle, disentangling, evolutionary models, mass transfer, stellar atmospheres

Ključne riječi: zvijezde, fundamentalni parametri, zvjezdane atmosfere, dvojne zvijezde, pomrčinske zvijezde, zastupljenost elemenata, CNO, Algol, u Her, kod, genetski algoritam, spektar, redukcija, echelle, raspetljavanje, evolucijski modeli, prijenos tvari

Acknowledgements

I wish to thank my menthor, prof. dr. sc. Krešimir Pavlovski for his continuous support and mentorship. His infinite pool of ideas that needed implementation motivated me to become better programmer and scientist.

I also wish to thank my colleagues, dr. John Southworth for obtaining Algol spectra at FIES and dr. Chung-Uk Lee and Dong Joo Lee for obtaining Algol spectra at BOES and dr. Ahmet Dervişoğlu. Without their help, this work wouldn't have been possible. Furthermore, I wish to thank dr. Saša Ilijčić. His program FDBINARY has been an invaluable tool.

It would be inconsiderate of me not to mention my current and ex roommates and colleagues Vernesa, Mario, Željko, Ivica, Mladen, and Marko for all the fun and distracions :)

Finally, I wish to thank my parents for making this all possible and my wife Kristina for her endless support. Also, our seven cats for never messing up my computer in all these years.

Contents

1	Introduction	7
1.1	Algols and the evolution paradox	7
1.2	CNO nucleosynthesis and chemical evolution	8
1.3	Motivation and goals	10
2	Theoretical background	12
2.1	Binary and multiple stellar systems	12
2.1.1	Why are binary stars important	12
2.2	Orbital elements	13
2.3	The Roche model for binary stars	15
2.4	Semidetached binaries	16
2.5	Mass-loss mechanism	17
2.5.1	Conservative mass loss	18
2.5.2	Non-conservative mass loss	18
2.5.3	Observational tracing of mass loss	19
2.5.4	Mixing in the mass gainer	19
2.5.5	Expected chemical profiles during core H burning	20
3	Previous observational research	21
3.1	Determinations of underabundance of carbon	21
4	Échelle spectrographs	30
4.1	Échelle spectrographs	30
4.2	Échelle spectrographs used in this work	33
4.2.1	FIES	33
4.2.2	BOES	35
4.2.3	FOCES	35
5	Tools	36
5.1	Échelle spectra reduction	36
5.1.1	Reduction introduction	36
5.1.2	Securing spectra with échelle spectrographs	36

5.1.3	Bias, Flat and Normflat	37
5.1.4	Extraction of spectral orders	37
5.1.5	Scattered light	37
5.1.6	Wavelength Calibration	38
5.1.7	Normalisation	38
5.1.8	Order merging	42
5.2	MULTIPEEGLA - Blaze Correction Software	42
5.3	Genetic algorithms	44
5.4	WDGEN	52
5.5	Genetic Disentangling	53
5.5.1	Tests	57
5.6	Bootstrap error estimates in SPD	59
5.7	Parallel	61
5.7.1	Tests	62
5.8	STARFIT	67
5.8.1	Errors using Monte Carlo Markow Chain (MCMC)	69
6	Tracing CNO exposed layers in the Algol-type binary system u Her	71
6.1	Introduction	71
6.2	Spectroscopy	73
6.3	Spectroscopic orbit through spectral disentangling	75
6.4	Light curve modelling	76
6.5	Spectral analysis of both components	80
6.5.1	The effective temperatures	80
6.5.2	Abundances	81
6.6	Evolutionary analyses	85
7	Spectroscopically resolving the Algol triple system	94
7.1	Introduction	94
7.2	Algol in a nutshell	95
7.3	High-resolution spectroscopy	97
7.4	Orbits and masses through spectral disentangling	97
7.5	Atmospheric diagnostics	102
7.5.1	Renormalisation of disentangled spectra	102
7.5.2	Effective temperatures for the components	106
7.5.3	The elemental composition and metallicity	106
7.6	Discussion	111
7.6.1	Fundamental properties of the components of Algol	111
7.6.2	Chemical composition and evolution of the components	112

8	Discussion and conclusions	114
8.1	Development of new tools	115
8.2	Abundance pattern for mass-transfer systems	116
8.3	Future plans	119
9	Prošireni sažetak	121
9.1	Motivacija i ciljevi	121
9.2	Dvostruki i višestruki zvjezdani sustavi	122
9.2.1	Zašto su dvojne zvijezde važne	122
9.3	Orbitalni elementi	122
9.4	Poluodvojene dvojne zvijezde	124
9.5	Échelle spektrografi	125
9.5.1	Korišteni échelle spektrografi	127
9.6	Genetički algoritmi	127
9.7	STARFIT	132
9.7.1	Procjena pogreške - Monte Carlo Markow Chain (MCMC)	134
9.8	Analiza CNO područja u dvostrukom sustavu Algolova tipa u Her	135
9.8.1	Analiza spektara obje komponente	135
9.8.2	Evolucijski modeli	138
9.9	Algol	141
9.9.1	Spektroskopija visoke rezolucije	141
9.9.2	Fundamentalne veličine za komponente sustava	141
9.9.3	Kemijski sastav i evolucija komponenata	143

Chapter 1

Introduction

Stars are the main building blocks of galaxies and the central engines in their evolution. Understanding the principles of their structure and evolution were a big success of the 20th century astrophysics. However, theory of stellar structure and evolution is not a closed story, and a number of open questions are awaiting a proper explanation (c.f., Langer 2012).

In order to understand stellar structure, nuclear sources and evolution, highly accurate and precise observations of many different kinds are needed. Only this would allow us to constrain and test various physical ingredients in the theoretical models, and calibration of a number of free parameters. Eclipsing binary stars are invaluable source of fundamental stellar properties (mass and radius) to a precision of $\leq 1\%$. Therefore, they serve as stringent tests of the predictions of evolutionary models. Both components must be spectroscopically detectable for direct determination of these quantities. For a useful comparison with theoretical evolutionary models further observables are needed: effective temperature (T_{eff}), and metallicity ($[M/H]$). We can then perform detailed abundance analyses of the observed systems.

1.1 Algols and the evolution paradox

Algols are close binary stars, named after the archetype stellar system of Algol (β Per). In Algol, which is a triple system, inner system is composed of a close binary system in which cool giant component is less massive than its hot main sequence companion. Evolutionary paradox that less massive component is apparently in an evolutionary more advanced stage than its more massive companion has been resolved postulating a mass-transfer episode between the components in their recent past (Crawford 1955, Kopal 1955, Hoyle 1955).

Unlike the evolution of single stars, the evolution of binaries is highly affected by their companion. Therefore, only a limited amount of space is allowed due to its gravitational potential, the Roche lobe. As the stellar evolution speed is mostly determined by the star's mass, the more massive star will evolve quicker and fill its available Roche Lobe, reaching the critical limiting radius. This can occur at various evolutionary stages: during the main sequence evolution (case A), during transition to the red giant phase (case B) or during the post-red giant or supergiant

phase (case C). At this point a rapid mass transfer occurs. Most of the initially more massive component is accreted by its companion, with some mass loss to the system, and the Algol-type binary is formed as the result. The previously more massive star is now a low mass subgiant filling its Roche lobe, while its companion is now the hotter and more massive component. This mass-transfer scenario is the well established solution to the "Algol paradox" (Hilditch 2001). This evolutionary process causes many effects - changes in the orbital period, distances between the components, effects due to surrounding dust, but one of the consequences is particularly important. Up to 80% of the mass of the originally more massive star can be lost, either to its companion or into or out of the system.

Due to the mass transfer process the layers which were originally deep within the nuclear fusion region of a star, completely unavailable to inspection have been deposited onto the surface of its companion. The surface chemical composition of both stars are a precious diagnostic tool of the nucleosynthetic processes that occur deep within the stars. By determining chemical abundances, we can both test the nucleosynthesis processes that are ongoing deep within the star, and probe stellar evolution in order to constrain the models of binary evolution. The initial characteristics of these systems vary, but can be determined by fine spectroscopic abundance analysis so we can discriminate between different evolutionary paths and mass and angular momentum loss mechanisms.

The spectra of close binary stars are complex due to their composite nature and moreover, continuously varying Doppler shifts of spectral lines. This makes the measurement of radial velocities (RVs) difficult, in particular in the cases of severe line blending, whilst in the same time prevent any reliable distinction of the underlying individual spectra of the component.

The method of spectral disentangling (herewith SPD) enables isolation of the individual component spectra simultaneously with the determination of the optimal set of the orbital elements. It is a way out of the previously mentioned obstacles and opens quantitatively new opportunities in the study of binary stars and their components. In particular, previously almost unexplored territory of chemical composition and chemical evolution of binary stars is now open for research.

For that, multiple high resolution and S/N spectra of the system are necessary. They are separated using spectral disentangling technique, which produces component spectra from a series of composite spectra, further enhancing S/N due to co-addition process. Using the disentangled spectra, we can both determine precise chemical abundances and fundamental properties of the binary stellar system with high precision and accuracy.

1.2 CNO nucleosynthesis and chemical evolution

Nuclear fusion occurring in stellar cores is the main source of energy with formation of elements as by-product of the process. These processes occur in the parts of the star that are not available for direct observations. Nucleosynthetic products can normally be detected only if

there is an efficient mixing mechanism within the star transporting newly created elements towards the surface. This has put stellar rotation mechanism, previously considered an secondary effect and neglected in modelling, into the focus of stellar evolution models. It changes all the model outputs substantially, bringing observed properties into much better agreement with the theoretical predictions. To further improve models, the influence of magnetic fields to rotation and mixing is added. The inclusion of stellar rotation has profound effects on stellar evolution models, particularly on high-mass stars (c.f., Meynet & Maeder 2000, Heger & Langer 2000). Centrifugal force changes the stellar shape and structure, causes meridional circulation and induces turbulent mixing. In turn, the effective temperature and luminosity of the rotating star changes, effecting its lifetime on the main sequence. As a consequence abundance pattern changes too, heavily affecting the expected photospheric nitrogen abundance. This makes nitrogen abundance viable as a new observable. However, the observations have shown the situation more complex than predicted from the models. Hunter et al. (2009) have found from the observations of a large sample of the Galactic and Magellanic Clouds B stars that N is enhanced not only for rapidly rotating stars but also for a slow rotators. Also, no any tight correlation of the nitrogen abundance with the strength of the magnetic field was found so far (Morel et al. 2008, Martins 2012).

Energy production in stars on the main sequence is generated by two processes: proton-proton (pp) and CNO cycle. Each of the processes converts hydrogen nuclei to helium nuclei, releasing energy in the process. PP process involves fusion of protons into α particles.

CNO process uses C, N and O as catalyst cores for helium nuclei production leaving catalytic cores intact. However, it is important to notice that although C, N and O are not converted themselves and their total number in the process is conserved, their relative ratios do vary and can be determined. As each process is determined by its slowest component, in this case an overabundance of nitrogen occurs as its fusion to oxygen is the slowest process. Therefore the number of carbon cores decreases due to conversion to nitrogen, as well as number of oxygen nuclei which are in cyclic process converted back to carbon. In the cyclic process, the number of protons (hydrogen nuclei) decreases as it is processed and converted into helium, which abundance increases.

It is important to know when CNO processes are active or dominant to pp processes. CNO process has a higher temperature dependence than PP process. Therefore, it becomes dominant energy source only in stellar cores with sufficiently high temperatures ($\geq 17 \cdot 10^6 \text{K}$). As core temperature is linked to stellar mass, CNO processes only occur in mid and high mass stars ($M > 1.4 M_{\odot}$). Additionally, it is important to recognise that C, N and O nuclei are used as catalysts and it is necessary for them to be present in the stellar core. If the initial chemical composition of a star is deficient in those elements, CNO process can not occur and will be postponed until they are fused by other processes.

The CNO cycle is dominant during the early evolution of more massive stars. It causes an increase of nitrogen abundance at the expense of primarily carbon, and in a lesser extent oxygen.

Typical cosmic abundance ratios are $C/N \approx 0.3$ and $N/O \approx 0.1$ (Przybilla et al. 2010).

In the case of more massive stars, carbon quickly reaches equilibrium abundance by the CN cycle and is turned to N. The maximal expected overabundance of nitrogen is $N/C \approx 3$ (Sarna & De Greve 1996). The oxygen is also slowly destroyed to produce nitrogen. If we take number of C atoms as constant, we can describe this situation as (Maeder et al. 2014)

$$d(N/C) = dN/C \quad (1.1)$$

$$dO = -dN \quad (1.2)$$

giving the ratio of change

$$d\left(\frac{N}{O}\right) = \frac{dN}{O} - \frac{N}{O^2}dO = \frac{dN}{O}\left(1 + \frac{N}{O}\right) \quad (1.3)$$

Now, we can calculate the change in N to C and N to O ratio as

$$\frac{d\frac{N}{C}}{d\frac{N}{O}} = \frac{N/C}{N/O} \frac{1}{\left(1 + \frac{N}{O}\right)} \quad (1.4)$$

enabling us to calculate the ratio and compare it to the measured one.

In the case of intermediate mass stars, we assume that the cycle starts with C to N conversion, leaving O number relatively constant

$$dC = -dN \quad (1.5)$$

$$d(N/O) = dN/O \quad (1.6)$$

thus resulting in

$$\frac{d\frac{N}{C}}{d\frac{N}{O}} = \frac{N/C}{N/O} \left(1 + \frac{N}{C}\right) \quad (1.7)$$

For intermediate mass stars, we get ratio of 3.97 (eq. 1.7, and for more massive stars 1.79 (eq. 1.4).

1.3 Motivation and goals

The motivation of this work is to make use of photospheric CNO and elemental abundances to gain insight into chemical composition of stellar interiors tracing both CNO stellar core nucleosynthesis and mass transfer episodes. By determining precise abundances for stars which

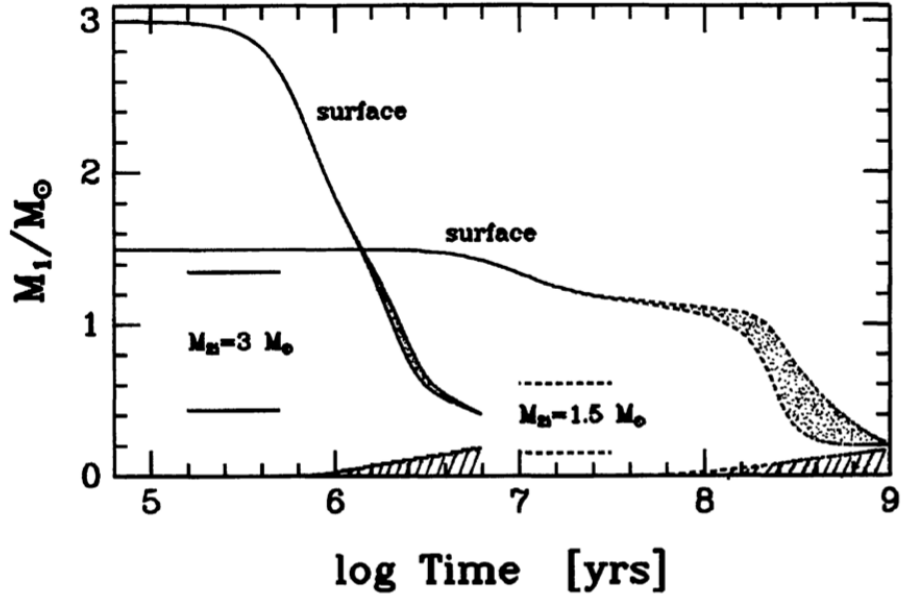


Figure 1.1: Time evolution of CNO influenced stellar volume (dashed) and outer convection zone depth (dotted) for 3 and 1.5 M_{\odot} stars (Sarna & De Greve 1996)

experienced mass transfer processes, we can also derive system's evolutionary path and initial system properties. Also, by determining expected abundance changes, we can both determine scenarios in which the mass transfer occurred (at which of evolutionary points did it occur) and the properties of the stars. The measured abundance determined on the mass-gainer, primary star, depends on thermohaline mixing in the star which gradually returns abundances from N overabundance to standard abundances. On the surface of the mass-donor, now a less massive secondary component, the abundance depends on the development of the upper convective zone which reaches deeper for less massive stars reaching the CNO processed areas making mixing more effective than in the more massive stars where the upper convective zone does not reach CNO changed regions (Fig. 1.1). For this purpose we selected two systems, one with high mass hot components, u Her, and the other Algol, prototype semidetached binary which is a low-mass system. High resolution and high S/N spectra secured in the course of this project would be disentangled and individual spectra of the components examined in details.

Chapter 2

Theoretical background

2.1 Binary and multiple stellar systems

Most of the stars have stellar companions, some directly visible, some invisible. The latter can be detected using spectroscopy (measuring doppler shifts of spectral lines in time series), photometry (measuring change in brightness due to other object's transit) or astrometry (cyclic change in star's position due to gravitational influence of the unseen object). Stars in binary systems do evolve in a similar manner, but the nearby accompanying star can have influence both on the evolution itself and the outcome of certain evolutionary stages. Binary stars are gravitationally bound objects, both orbiting the mutual center of gravity. They are also bound in a mutual gravitational potential, which is naturally, more complex than in a single-star scenario. In this case, the gravitational equipotential lines form an eight-shaped figure in close proximity to the system, and become spherical only far away, where the binarity influence lessens. The equipotential at which stellar matter ends being gravitationally bound to the star is called the *Roche Lobe*, and can be seen in Fig. 2.1.

2.1.1 Why are binary stars important

The importance of binary stars is due to the possibility of determining fundamental stellar parameters with great accuracy, especially compared to parameters we can derive for single stars. That gives us the opportunity to precisely compare and match measured properties to evolutionary model predictions in order to validate and confirm, or further improve them. Gravitational interaction between two stars gives us opportunity to determine their masses. In general case, mass ratio can be determined, and in more opportune situations individual masses themselves. If light curve is available, we can derive orbital inclination, eccentricity, star's relative sizes, mass ratio and the ratio of surface brightnesses. From spectroscopic data we can derive projection of velocities resulting also in orbital separation and mass can be determined. Analysis of spectral lines can give us further insight in stellar rotation, temperature and surface gravitational acceleration, as well as light contribution of each component to the total light of the system.

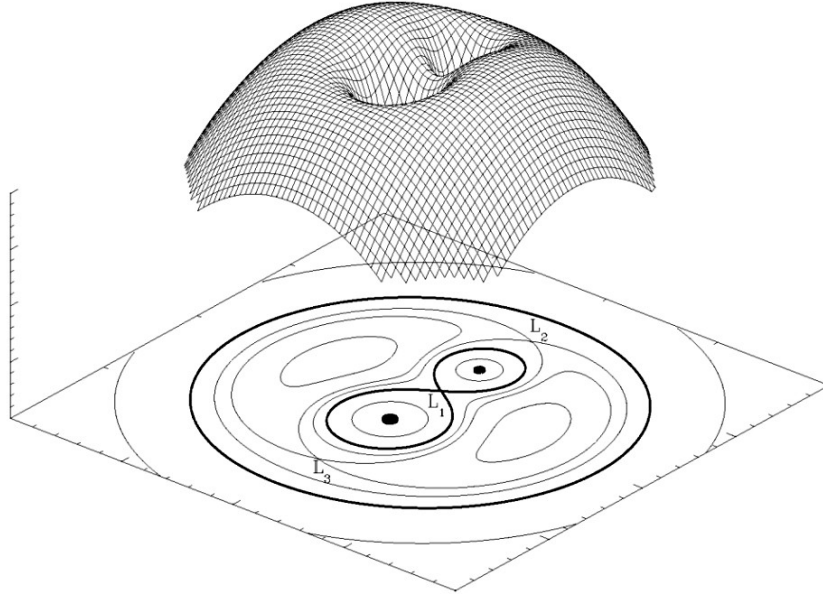


Figure 2.1: 3D gravitational potential and 2D cross section contour plot. On the contour plot is obvious an 8-shaped figure called the Roche Lobe (<http://hemel.waarnemen.com/Informatie/Sterren/hoofdstuk6.html>)

Furthermore, due to possible interactions between the two components, the shapes of stars can deviate from spherical shape of single stars due to tidal interactions, resulting both in change of observable properties and evolutionary processes. Therefore, it is not yet clear if single star evolutionary models accurately describe binaries' evolution.

2.2 Orbital elements

The term orbital elements originated in the study of planetary motions, but can be directly applied to stellar orbits. In order to define it, we need six quantities (see Fig. 2.2).

Period P is linked to the semimajor axis of the orbit by a generalised form of the Kepler's equation

$$\frac{a^3}{P^2} = \frac{G}{4\pi^2}(M_1 + M_2) \quad (2.1)$$

where M_1 and M_2 are the masses of the two stars. A complete dynamical description of the system requires the knowledge of the period, which has come to be regarded as an extra orbital element. From observations of the eclipsing binary system, the quantities P , i , ω , e and T can be determined. However, unless radial velocity (RV) measurements are available, it is impossible to distinguish between the ascending and descending nodes of the orbit, leading to an ambiguity of 180 deg in the longitude of periastron (ω). For the semimajor axis, only the apparent value can be determined from the observations, unless we know the parallax or the distance to the system

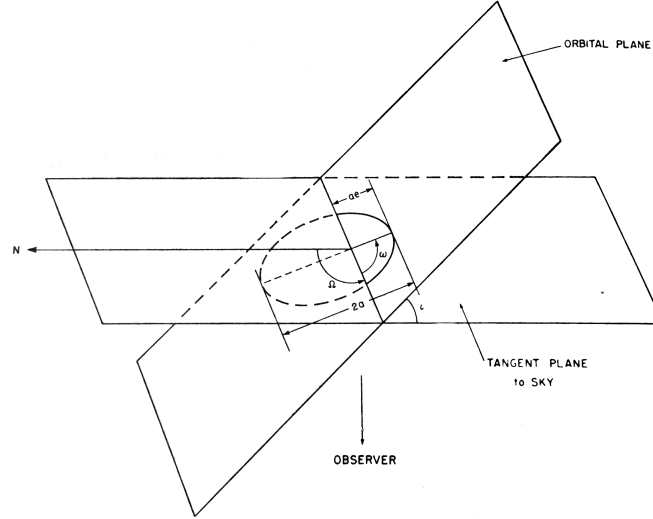


Figure 2.2: Plot of the orbital elements. The orbit is contained in a plane which is projected to another plane, perpendicular to the observer's line of sight. (Batten 1973)

in which case we can determine the true semimajor axis. If both components are seen in the spectrum, mass can be determined from velocity amplitudes. Eccentricity, e , and longitude of periastron, ω are very correlated and are usually treated as a combination of $e \cos(\omega)$ which can be determined using the times of the primary and secondary eclipse and $e \sin(\omega)$ which depends on eclipse duration and are less correlated than e and ω alone. Additionally, two other quantities can be determined:

- V_o - the radial velocity of the center of mass of the system
- K_1 - semi-amplitude of the radial velocity of the primary component
- K_2 - semi-amplitude of the radial velocity of the secondary component

The velocities are measured in km/s, period in days. Given these units, the values of K are related to the orbital elements as

$$a_{1,2} \sin i = 13751 (1 - e^2)^{1/2} K_{1,2} P \text{ [km]} \quad (2.2)$$

$$M_{1,2} \sin i = 1.0385 \cdot 10^{-7} (1 - e^2)^{3/2} (K_1 + K_2)^2 K_{2,1} P \text{ [M}_\odot\text{]} \quad (2.3)$$

where

$$a = a_1 + a_2 \text{ and} \quad (2.4)$$

$$a_2/a_1 = K_2/K_1 = M_1/M_2 \quad (2.5)$$

$K_1 + K_2$ is thus a measure of the major semi-axis projected onto a plane that contains the line of sight. If only one spectrum is recorded, one can determine only the value of $a_1 \sin i$ and the only information on the mass is the so called mass function

$$f(m) = \frac{M_2^3 \sin^3 i}{(M_1 + M_2)^2} = 1.0385 \cdot 10^{-7} (1 - e^2)^{3/2} K_1^3 P [\text{M}_\odot] \quad (2.6)$$

If the secondary star is also the less massive one, it can be shown that the minimum values of $m_{1,2} \sin^3 i$ are given by $4f(m)$. In the case of an eclipsing binary, period can be easily determined and the angle i can be found as it affects both the shape and depth of the light curve. If both eclipses can be observed, $e \cos \omega$ can be determined from the displacement between them, expressed as a fraction of the period. From the light curve, nothing can be determined for semimajor axis. The shape and duration of eclipses in the light curve depend on the component's radii R_i , expressed as the fractions of the separation. If the system is also observed spectroscopically, the radii in the absolute units can be determined.

2.3 The Roche model for binary stars

The gravitational potential for a binary system Φ at the arbitrary point (x, y, z) can be expressed as

$$\Phi = -\frac{Gm_1}{r_1} - \frac{Gm_2}{r_2} - \frac{\omega^2}{2} \left[\left(x - \frac{m_2}{m_1 + m_2} \right)^2 + y^2 \right] \quad (2.7)$$

where the coordinates r_i are $r_1 = \sqrt{(x^2 + y^2 + z^2)}$ and $r_2 = \sqrt{((x-1)^2 + y^2 + z^2)}$. Furthermore, if we define the normalised potential $\Phi_n = -2\Phi/(m_1 + m_2)$ and mass ratio $q = m_2/m_1$, we have the following expression

$$\Phi_n = \frac{2}{(1+q)r_1} + \frac{2q}{(1+q)r_2} + \left(x - \frac{q}{1+q} \right)^2 + y^2 \quad (2.8)$$

which can be evaluated at any point (x, y, z) around the two mass points. One example of the results is plotted in Fig. 2.1. Equipotential surfaces are circular in the resulting plot both near each of the stars and far away from the system, but in between the mass distribution makes the curve more complicated. One can note the point noted as L_1 called the inner Lagrangian point, and two other Lagrangian points L_2 and L_3 located at the far sides of the equipotential curve. The two curves joining at point L_1 are called Roche Limits and define two 3D limiting volumes called the Roche Lobe. It represents the maximal volume a body can occupy whilst having all its mass bound. Any particle that exits the Roche lobe is lost to the host star, either to the other component or the system in general forming a common envelope. The size of limiting lobes is primarily determined by separation of components a , and less so by their mass ratio.

For well detached systems, the ratio of star's size R vs. the separation is $R/a \leq 0.1$, and the component stars are spherical. For a higher ratio, stars become more and more deformed. One

of commonly used parameters is r_L - the effective radius of a Roche Lobe, meaning the radius of a sphere that has the same volume as the non-spherical Roche lobe. It can be expressed in terms of the mass ratio as

$$r_L = \frac{0.49q^{2/3}}{0.69q^{2/3} + \ln(1 + q^{1/3})} \quad (2.9)$$

The actual effective radius for a star at Roche lobe is then $R_L = r_L a$ where a is the semimajor axis of the relative orbit.

2.4 Semidetached binaries

If in a binary system one component fills its Roche lobe, it is very probable that the system has passed through at least one phase of mass transfer between the two components, or mass loss from the system, or both. Therefore, it would be wrong to make comparison between the empirical data on the masses and absolute dimensions of such system and the theoretical stellar evolution models for single stars alone. Evolution codes must be modified to take into account the existence of the upper volume of a star in a binary and to allow for changes in orbital periods and sizes consequent upon the mass-exchange process.

The classical Algol systems are known to have a main-sequence primary of intermediate mass that lies within its Roche lobe, and a Roche-lobe-filling secondary of the substantially lower mass, with typical mass ratio $q \sim 3$. The secondary is classified as a subgiant and seemingly more evolved than its more massive companion, creating a paradox situation considering the stellar evolution. The paradox was resolved following a suggestion by Crawford (1955), and Kopal (1955) when it became clear that the Roche lobe overflow (RLOF) was an important mechanism in binary star evolution which leads to mass ratio reversal in a binary system, such that originally the more massive component would become the secondary, while its initially less massive companion would become the primary. The first models of mass transfer included only conservative mass transfer scenario, in order to limit the range in investigated parameter space. As it became obvious that conservative mass transfer was an unrealistic oversimplification (Popper 1973) it became an imperative to postulate non-conservative mass and angular momentum loss. Many grids for models involving case A, B and C mass-transfer cases (Section 2.5) and for varying amount of mass and angular momentum loss. Specifically for Algol systems, De Greve (1989, 1993), De Greve and de Loore (1992) and de Loore and De Greve (1992) have considered a substantial range of evolution calculations, whilst Sarna (1993) has discussed in detail evolutionary status of Algol itself. The overall conclusion is that the conservative evolution cannot explain the properties of Algol systems and that non-conservative mass exchange in early case B is required. In an attempt to provide more accurate quantitative data for comparison with models, Maxted and Hilditch (1996) collected data on nine Algol systems for which astrophysical parameters had been derived from self-consistent solutions of the light

curves and the radial velocity curves of the two components, including taking account of non-Keplerian corrections. The current primary components appear as normal main sequence stars, whilst the secondaries are all oversized and overluminous relative to the main-sequence star of the same mass, by amount that range up to factors of 10. On the basis of comparison between the data and the models, it would seem that more angular-momentum loss is required and currently employed within the models. Within the limits of quality of obtainable spectra for Algol type secondaries, determined C abundances can act as major constraints on the evolutionary models, provided that the data is sufficiently accurate. With the currently available data, Sarna and De Greve (1996) have shown that the agreement between the observed C deficiencies and the theoretical models is reasonable but not definitive.

2.5 Mass-loss mechanism

Single stars have go through their evolutionary stages unaffected by their surroundings. In case of binary stars, each star has its Roche lobe in which it resides. During the first stage of its evolution, it resides more or less unaffected by its companion inside its Roche lobe. However, as the evolution progresses, it enters stages where its radius increases and starts filling its Roche lobe more and more. It can the fill its limiting Roche surface by several mechanisms - by following its natural evolution and expanding to fill the Roche lobe at phases:

- **Case A** - during the main sequence phase
- **Case B** - during transition to the red giant phase or
- **Case C** - during the post-red giant of supergiant phase

or in between of the cases. On the other hand, the Roche Lobe around a star can shrink itself due to orbital momentum loss.

During the time, a star can loose mass via various routes, resulting in different changes of the orbital period P . P is the best defined quantity in a binary system, therefore good knowledge of its change can give us reliable evidence of the undergoing mass-exchange and its magnitude.

Mass loss can be conservative or non-conservative, described by parameter β denoting the the mass-gaining efficiency of the primary star.

$$\beta = 1 - \frac{\dot{M}}{\dot{M}_2} \quad (2.10)$$

where \dot{M} represents mass lost from the system, and \dot{M}_2 mass lost by the mass losing component. Also, although it is frequently kept constant for the modelling simplicity, β can be varying and is often considered as $\beta(q)$

2.5.1 Conservative mass loss

The simplest case of mass transfer is a *conservative* mass transfer where all the mass lost by one component is acquired by its companion, and parameter $\beta = 1$. Therefore, the total mass of the system is conserved, as well as the orbital momentum J_{orb} . Total mass $M = M_1 + M_2$ remains unchanged, while $dM_1 = -dM_2$. Orbital momentum is

$$J_{orb} = \left[\frac{GM_1^2 M_2^2 a (1 - e^2)}{M} \right]^2 \quad (2.11)$$

and utilising Kepler's third law, we can derive the change in period

$$\frac{P}{P_i} = \left[\frac{M_{1i} M_{2i}}{M_1 M_2} \right]^3 \quad (2.12)$$

where i denotes initial values, and non-subscripted values after mass transfer. This equation can be time differentiated to obtain time-change of the period as

$$\frac{\dot{P}}{P_i} = \frac{3\dot{M}_1(M_1 - M_2)}{M_1 M_2} \quad (2.13)$$

taking into account the mass conservation. If the initially more massive star loses mass, the period decreases as well as the orbital separation up to the point where $M_1 = M_2$. If the mass-losing star continues to lose mass, the orbital period will start increasing along with the separation. As we can measure time very precisely, we are able to register small changes in orbital periods.

2.5.2 Non-conservative mass loss

It is more expected that the mass transfer is the non-conservative mass loss where some of the mass is lost into the common envelope, along with the angular momentum, resulting in $\beta < 1$. Although this scenario can occur when one of the stars has strong stellar winds or goes nova or supernova, for us the most interesting scenario is Roche lobe overflowing. In that case, the mass losing star loses its material via L_1 point, some of which is accreted onto the mass gaining star, while the rest flows freely via L_2 point. That leads to decrease in the orbital period both because of the mass and momentum loss. As the momentum is also not conserved, the time change of P can be expressed as

$$\frac{\dot{P}}{P} = 3 \left[\frac{\dot{J}}{J} + \frac{\dot{M}}{M_1 + M_2} - \frac{\dot{M}_1}{M_1} - \frac{\dot{M}_2}{M_2} \right] \quad (2.14)$$

where $\dot{M} = \dot{M}_1 + \dot{M}_2$. In case of no accretion $\dot{M}_2 = 0$ and $\dot{M} = \dot{M}_1$, we can express angular momentum change as

$$\dot{J} = \frac{\dot{M} d^2 2\pi}{P} \quad (2.15)$$

where d is the separation from the centre of mass to the L_2 point. Therefore, the change in orbital period is

$$\frac{\dot{P}}{P} = 3\dot{M} \left[\frac{M_1 + M_2}{M_1 M_2} \frac{d^2}{a^2} - \frac{M_2}{M_1(M_1 + M_2)} \right] \quad (2.16)$$

and the orbital period for this case necessarily decreases. All those calculations assume circular orbit, as the circularisation and synchronisations were expected to occur.

2.5.3 Observational tracing of mass loss

Mass loss gives us an unique opportunity of directly observing stellar interior and probing evolutionary models. It is separated in two mass-losing stages - rapid following by the slow one. In terms of length of the evolution, rapid stage really is rapid (length ranging $10^4 - 10^5$ years) which makes it difficult to observe because it is a rare opportunity to catch the system in that phase. Also, β during this stage is low meaning that most matter is lost to the system. However, as during that phase mass losing star is depleted of its surface material which is largely unaffected by the nuclear processes, it is not a great scientific loss if that stage is not observed. It is only during the next stage, slow mass transfer that the very core of a star is revealed exposing deep layers where results of nuclear reactions are present. In case of hotter stars with active CNO cycle, stars with $T > 17 \cdot 10^6$ K or $M > 1.4 M_\odot$, layers with remnants of CNO are exposed as well as some of that layer can be even deposited onto the surface of the much brighter, mass gaining companion available for inspection. As the mass gainer in this stage becomes more effective of successfully accreting most of the matter, β has a larger value. Therefore, binary stars in or after slow mass losing phase are perfect candidates for testing our knowledge of CNO cycle, both because we have a direct insight in the affected layers and because, due to the binarity of the system, we have precise and precious information of fundamental stellar properties of the stars involved. For that, we need detailed spectra with as large as possible wavelength range - échelle spectra.

2.5.4 Mixing in the mass gainer

As chemically enriched material is deposited onto the primary's surface, consisting mostly of hydrogen, an inverted gradient of mean molecular weight is developed. This can result in mixing processes as the situation is unstable according to the Ledoux criterion. This mixing tends to smear out the inverted and unstable inverted gradient. After this fast mixing, a smooth transition zone is established, but with possibility of further instabilities. This instability is known as the *thermohaline mixing* (Kippenhahn 1980), a process first introduced in context of hydrodynamic instabilities in salt waters where a layer of salt water is located above a cooler, more dense layer. This situation analogous to the layers of higher molecular density being on top of layers of lower molecular density. The instability starts to resolve itself by propagating fingers

of high molecular density matter propagating downwards and initiating the mixing process. The process of matter transfer is not spherically symmetric, resulting in deposited hot-spots of accreted material over the cooler host material, a perfect candidate for mixing. This mixing tends to keep hydrogen abundance values similar to the original, pre-transfer values and carbon abundance lower than the abundance on the surface of the secondary. Furthermore, if the primary is observed at the end or long after the mass transfer phase, mixing will restore its surface composition to the values close to the original ones, making detection of CNO remnants impossible, especially in case when the remainder of the secondary is very low in luminosity and can not be detected spectroscopically.

2.5.5 Expected chemical profiles during core H burning

From the calculation for the single stars (Iben, 1967) it is well known that the distribution of C, N and O changes during main-sequence evolution of a star in which CNO is the dominant hydrogen burning process. The central ^{12}C abundance decreases from the cosmic value to the equilibrium value of $[\text{C}/\text{H}]_{\text{sec}} = -1.8 - -2$. At the same time, the abundance of the slowest to be processed core - ^{14}N increases. The region in which C is depleted and N abundance increases outwards in time to the larger mass fractions. The underabundance of C stops when approx 15% of core hydrogen is depleted. In the outer region of star, there is still a cosmic abundance, and the regions are separated by a transition layer. This situation persists until the forming of thick convective surface layer that starts mixing and transporting material between the surface and inner layers. As the mass gainer in this stage becomes more effective of successfully accreting most of the matter, β has a larger value. The $[\text{N}/\text{C}]$ ratio starts from initial cosmic ratio of -0.35 to finally up to ~ 3 . However, such thick convective envelope can be formed only in late B case scenario, when the secondary fills its Roche lobe when it is on the giant branch. However, most mass transfer systems are case A or early B, resulting in less abundance inversion.

When measuring abundances on the surface of the primary and secondary, we can expect both similar abundances, depending on the onset of mixing processes. Should the system be observed prior to the thermohaline mixing, similar abundances are expected. As this is only a brief phase, it is more likely that the observed system will have different abundances. Large carbon depletion is expected in secondaries at the end of the mass transfer, provided their initial mass is not too low (not less than $2.5M_{\odot}$), as the lower mass secondaries develop deep convective cores which mix material efficiently, decreasing carbon abundance.

Chapter 3

Previous observational research

A great number of papers exists on Algol itself, and also at Algol-type systems showing both the importance of mass transfer systems, but also the facts that those systems are not easy to understand and solve. The variability of Algol was well known since ancient times, and it's variability resolved only in 1773 by John Goodricke. It's reason for observed paradox evolutionary stage was finally determined by Crawford in 1955, after a long time of dedicated research by many researchers. Algol has been a target for many photometric, spectroscopic and nowadays interferometric studies, confirming it's importance for astrophysics.

3.1 Determinations of underabundance of carbon

Underabundance of C was primarily studied in the UV part of the spectrum (Cugier & Hardorp 1988, De Greve & Cugier 1989, Cugier 1989), visual part (Parthasarathy et al. 1979, 1983, Balachandran et al. 1986, Tomkin et al. 1989, 1993) and even CN molecule (Yoon & Honeycutt 1992) and bigger spectral ranges (Tkachenko et al. 2010).

Parthasarathy et al. (1979) used Reticon spectra from McDonald telescope to determine metals abundance in two Algol type secondaries. They determined normal metal abundance. Unfortunately, they did not search for C underabundance. In the next article of their series, (Parthasarathy et al 1983) they used Digicon spectra of CH and CN molecules in the secondaries of U Cep and U Sge, also from McDonald Observatory. They first compared spectra to broadened spectra of selected standard stars. That comparison strongly suggested the normal metal abundance of observed Algol secondaries and C depletion in excess of the evolutionary changes observed in normal giants. Source of C abundance measurements are numerous CH lines in 4290 - 4328 Å interval. A small C deficiency for the secondaries of U Cep and U Sge is determined relative to comparison stars. For U Cep the underabundance of C is $[C/Fe] = -0.45$ and overabundance of N $[N/Fe] = 0.50$ with uncertainties of 0.2 dex. For U Sge, $[C/Fe] = -0.50$ and $[N/Fe] = 0.55$ with same uncertainties. However, N abundance was determined solely from CN bands which, obviously include C abundance therefore introducing further uncertainty. So, the N abundance estimate lies on the proposed initial C/N ratio of 4, the solar value. They also

Table 3.1: Elemental abundances for β Lyr primary (Balachandran al 1986). Values are relative to hydrogen abundance defined as $\log \epsilon(\text{H}) = 12.0$

Element	Solar Abundance	Measured abundance
He	11.0	11.89 ± 0.21
C I	8.69	< 7.56
C II	8.69	< 7.61
N	7.99	8.90 ± 0.13
O	8.91	7.90

determined mass transfer rate of $10^{-6} - 10^{-7} M_{\odot}/\text{yr}$. Another interesting system observed was β Lyr (Balachandran et al. 1986) in which they determined He, C, N and O abundances of the primary (mass losing star is still the observational primary because mass gaining component is hidden in an opaque disk and is not directly visible). From the weak 4437 and 5047 Å He I lines they determined a definite He enrichment $N(\text{H}) = 0.4$ and $N(\text{He}) = 0.6$. Microturbulent velocity v_{turb} of 10.0 km/s determined from Fe II lines. Determined C and O abundances were much lower than N abundance. β Lyr is currently in a stage of fast mass transfer. As the measured period is increasing, they concluded that the less massive component is still losing mass. As there is no evidence of the secondary in the spectrum, the value of q could not be measured directly. Measured abundances can be seen in Table 3.1.

The measured He enrichment indicates that the primary has overflowed its Roche lobe during the shell hydrogen burning, case B started only 6500 years ago (Ziolkowski 1976). In the fourth article of the series, Tomkin & Lambert (1989) determined abundances from the low-noise Reticon R CMa spectra. The determined masses for both primary and secondary are 1.1 and 0.17 M_{\odot} respectively. The very low secondary mass indicates that it has undergone a significant mass transfer process so the CNO compositions of the both components are of interest. Unfortunately, measurements of secondary's composition were impossible due to its low fractional light contribution, although its spectrum has been detected and used for RV determination. The measured EWs of the primary measured from the composite spectrum renormalised in respect the continuum of the primary component only. The measured abundances are $[\text{C}/\text{H}] = 0.0 \pm 0.2$, $[\text{N}/\text{H}] = 0.4 \pm 0.2$ and $[\text{O}/\text{H}] = 0.3 \pm 0.3$, almost the solar one (taking into account the large uncertainties).

Finally, Tomkin, Lambert and Lemke (1993) disclosed C deficiencies in the primaries of 8 Algol-like systems from low-noise CCD spectra from C II line at 4267 Å. In all systems C II line was measured in primaries only, after renormalising composite spectra to primaries' continuum. Measured EWs were compared to comparison stars of the similar temperature (Fig. 3.1).

The average C abundance of comparison stars is $\log \epsilon(\text{C}) = 8.28 \pm 0.21$, 0.32 dex lower than the solar value, but consistent with other studies of B stars. Results vary from moderate deficiency in the case of RS Vul to large deficiency in U CrB with the average abundance of $[\text{C}/\text{H}] = -0.34 \pm 0.17$. δ Lib was excluded due to the weakness of C line for its temperature, and possible contamination from other lines. All measured abundances are show in Table 3.2.

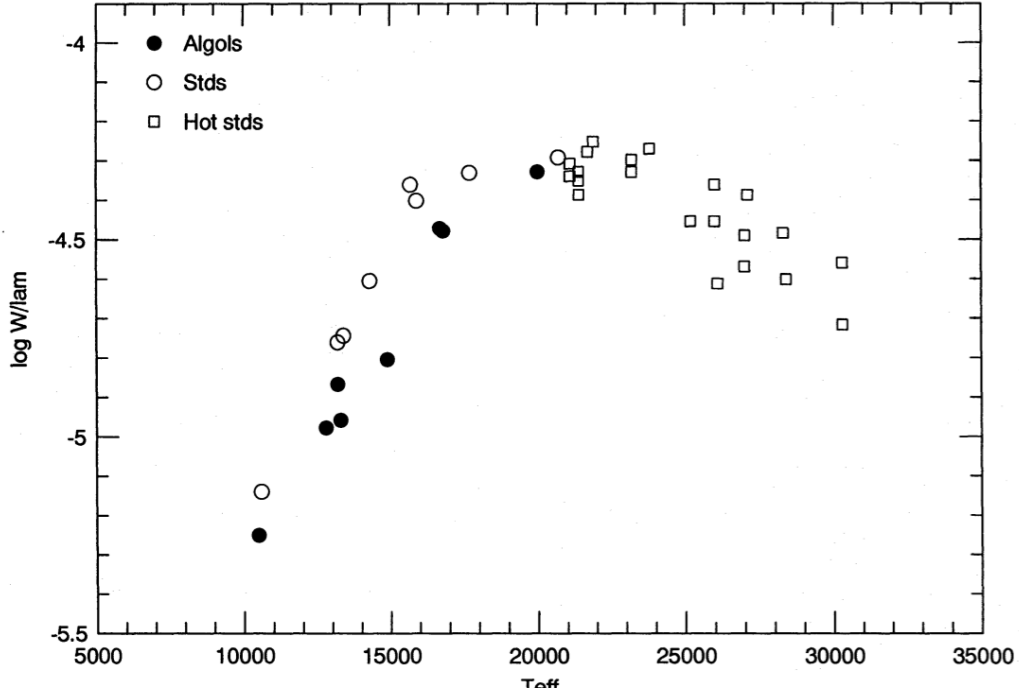


Figure 3.1: The EW of measured C lines compared to the sample stars (Tomkin, Lambert & Lemke 1993)

Cugier & Hardop (1988, 1989) examined β Per, λ Tau and 6 other stellar systems in UV part of the spectrum to determine predicted C underabundance. The expected C depletion is in ranges from -1.1 to 2.0 dex, and is hoped to be confirmed if sufficient mass was lost from the loser in order to expose depleted layers. The analysis was performed using high resolution spectra in the UV region from IUE satellite from the archival data. Their first targets were two short period systems, β Per and λ Tau. For Algol system, the main contribution in the measured UV part is expected to come from primary of component for which they assume ($T_{\text{eff}} = 13000 \pm 1000$ K) as the other components are much cooler than the primary and not expected to have any significant contribution in UV part of the spectrum. The analysed lines were C II multiplets at 1324 and 1335 Å shown in Fig. 3.2. They also confirmed synchronous

Table 3.2: C abundances of 8 measured primaries (Tomkin, Lambert & Lemke 1993)

Star	$\log \epsilon(\text{C})$	[C/H]
U CrB	7.66	-0.62
u Her	7.94	-0.34
δ Lib	≤ 8.52	$\leq +0.24$
β Per	8.06	-0.22
U Sge	8.10	-0.18
λ Tau	7.80	-0.48
TX UMa	7.93	-0.35
RS Vul	8.12	-0.16

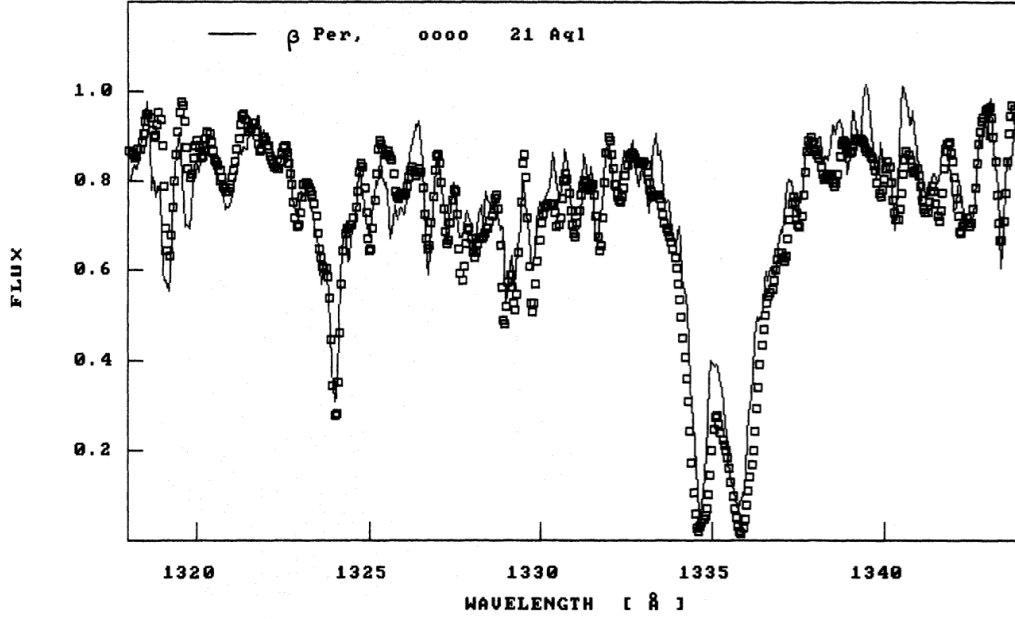


Figure 3.2: Measured C profile in the UV spectrum of β Per (full line) compared to comparison spectrum of 21 Aql (squares) broadened to the same rotational velocity. Image contains measured C lines where a slight underabundance in C multiplet line profile can be seen (Cugier & Hardorp 1998)

Table 3.3: 6 Algol-like systems with C determined abundances (Cugier 1989)

Star	LTE	non-LTE
δ Lib	-3.58 ± 0.15	-3.64 ± 0.20
U Sge	-3.50 ± 0.15	-3.54 ± 0.20
TX Uma	-3.80 ± 0.15	-3.85 ± 0.20
U CrB	-3.95 ± 0.15	-4.00 ± 0.20
RS Vul	-3.48 ± 0.15	-3.55 ± 0.20
u Her	-3.58 ± 0.30	-3.76 ± 0.30

rotation of Algol A ($v \sin i = 53.3 \pm 3 \text{ km s}^{-1}$). As for λ Tau, higher $T_{\text{eff}} = 18000 \pm 600 \text{ K}$ better assures its domination in UV spectrum. A relative difference in measured elemental abundances was performed comparing to reference stars of the same temperature.

C abundance was calculated using atomic data from Naussbaumer & Stornay (1981), and the damping mechanism supposed to be natural. For Algol, abundance for the 1335 Å line was determined $\log N(\text{C}/\text{H}) = -3.98 \pm 0.15$ dex under LTE assumption and $\log N(\text{C}/\text{H}) = -3.87 \pm 0.20$ dex under non-LTE. The accuracy was estimated by taking into account errors in T_{eff} , $\log g$, v_{turb} , Stark broadening and continuum level error. The determined value is relatively similar considering errors, however line profile is not very sensitive to change in C abundance. The increase in abundance by 0.30 dex changes the equivalent width 14%. On the other hand, 5% error in continuum estimation also changes the abundance by 0.30 dex. For λ Tau, determined abundances are $\log N(\text{C}/\text{H}) = -4.09 \pm 0.15$ dex under LTE assumption and $\log N(\text{C}/\text{H}) = -3.92 \pm 0.20$ dex under non-LTE with the same error source considerations. Therefore their conclusion

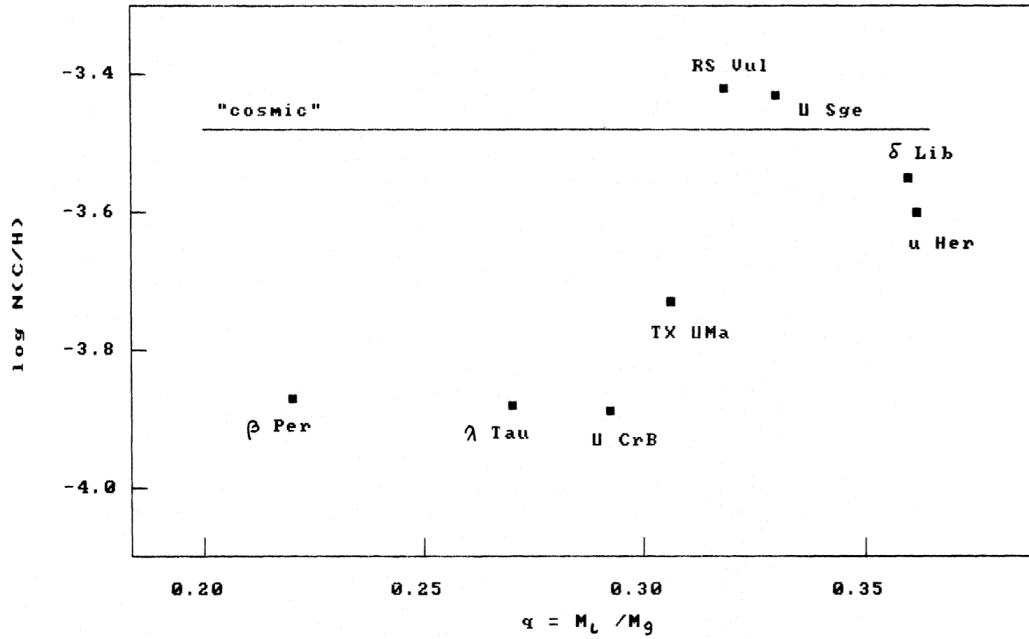


Figure 3.3: The determined C abundance in Algol-type stellar systems as a function of the mass ratio (Cugier 1989)

is the measured C depletion of both stars by -0.40 ± 0.20 dex for the cosmic abundance value of $\log N[C/H] = -3.48$ (Allen 1973).

For the rest of Algol-like systems (Table 3.3), C was also determined (Cugier 1989) with the same assumption of major flux contribution in UV from the hotter, more massive component only. The source of the uncertainties was determined as before. He concluded that only u Her shows similar to cosmic C abundance. Determined C abundance vs mass ratio q for his sample is shown in Fig. 3.3

As can be seen, all mass-accreting stars with $q \leq 0.32$ have a cosmic abundance of C, while ones with lower q show C depletion of about -0.4 dex, which indicates that β Per, λ Tau, TX UMa and U CrB are in the advanced evolutionary stage and have exposed deeper layers of the interior of initially more massive components than the remaining examined systems. In Fig. 3.4 C abundance is plotted against mass fraction (Iben 1965, 1966) showing that expected C underabundance in the photosphere of the gainer is -1.1 to -2.0 dex, much more than observed -0.4 dex. That with addition that all the systems with $q \leq 0.31$ show the same depletion leads to a conclusion that a large-scale mixing mechanism must occur in Algols. Also, there are good reasons to believe that mass exchange between components leads to increase in rotation of mass-accreting stars and therefore additional mixing mechanism by meridional circulations (Tassoul & Tassoul 1984).

Yoon & Honeycut (1992) report abundance analysis in 12 Algol secondaries compared to field stars of the similar type as previous results are only for the primaries. They determine C

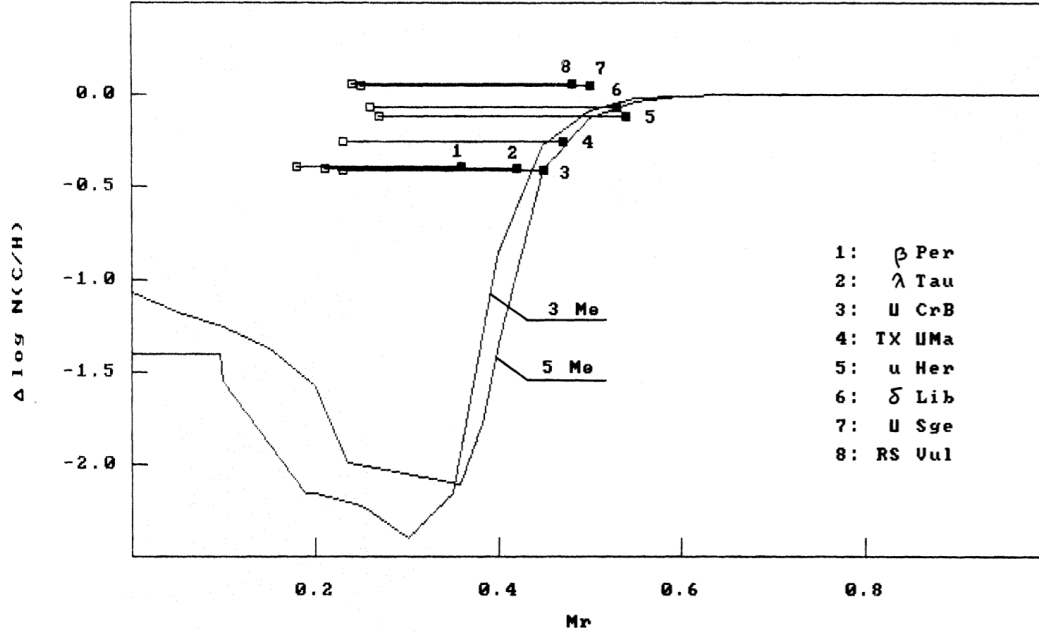


Figure 3.4: C evolution against mass fraction for two mass-donors (Cugier 1989)

abundance by measuring g-band of the CH molecule using 2.5 \AA resolution spectra obtained at Kitt Peak using IIDS spectrometer. Case B mass transfer was assumed for all 12 systems as all the published masses for the systems give $M_1 + M_2 \leq 7M_\odot$. Their results can be seen in Table 3.4.

The observed carbon abundances are much larger than the abundance in interior radius of a single star indicating that any mass loss occurring prior to mixing did not exhaust the unprocessed envelope. They are also smaller than the abundances of field comparison G and K giants. Since mass loss subsequent to mixing will not change the surface abundances, the variety of $\log \epsilon(\text{C})$ may represent varying amounts of mass which has been lost after convective mixing developed.

Tkachenko et al (2010) used high resolution échelle spectra to determine abundances in Algol-like system TW Dra. It has a similar period to Algol, $P = 2.897 \text{ d}$, but lower primary mass $M_1 = 2.01 \pm 0.22 M_\odot$ with similar secondary $M_2 = 0.89 \pm 0.07 M_\odot$. The primary eclipse is a total one. Additionally, δ -Scuti type oscillations were detected in the primary (Kusakin et al. 2001). The change in period of $4.43 \cdot 10^{-6} \text{ d/yr}$ was also measured (Qian & Boonrucksar 2002) that was attributed to a dynamical mass transfer of $6.8 \cdot 10^{-7} M_\odot/\text{yr}$. The star also showed alternating changes in the orbital cycle due to magnetic activity cycle. KOREL code (Hadrava 2004) was used to derive the orbital elements and obtain components spectra. It was used on 396 échelle spectra obtained at TLS 2m telescope in Tautenberg and BOES spectrograph in South Korea. Normalised extracted spectrum of the primary component was used for detailed abundance and orbital parameter analysis on a large wavelength range. Parameters were ob-

Table 3.4: 12 Algol-like systems with determined C abundances for the secondary components. C is given in logarithmic scale where H abundance is 12. Error estimate is 0.15 dex (Yoon & Honeycut 1992)

Star	$M_2(M_\odot)$	Observed	$\log\epsilon(C)$ IRS
TW And	0.4	8.08	6.50
S Cnc	0.2	8.02	6.61
WW Cyg	1.8	8.00	6.62
RR Dra	0.8	8.37	6.63
TW Dra	0.9	7.94	6.62
TZ Eri	1.0	7.29	6.62
GU Her	1.0	8.21	6.62
RW Mon	1.3	7.47	6.58
UX Mon	1.5	7.83	6.62
RV Psc	1.3	7.33	6.44
RW Tau	0.6	7.74	6.62
X Tri	1.3	8.14	6.62

Table 3.5: TW Dra elemental abundances of the primary of TW Dra (Tkachenko et al. 2010)

Element	Abundance	[X/H] Solar abundance
C	-3.56	+0.09
O	-3.56	-0.14
Mg	-4.16	+0.35
Si	-4.66	-0.13
Ca	-5.63	+0.10
Sc	-8.73	+0.26
Ti	-7.07	+0.07
Cr	-6.20	+0.20
Fe	-4.43	+0.16
Ni	-5.61	+0.20
Y	-9.74	+0.09

tained fitting a complete spectral range simultaneously using an iterative procedure. Obtained astrophysical parameters are $T_{\text{eff}} = 8150 \pm 20$ K, $\log g = 3.88 \pm 0.02$, $v \sin i = 47.1 \pm 0.5$ km/s and $v_{\text{turb}} = 2.9 \pm 0.3$ km/s. Determined abundances are shown in Table 3.5.

Ibanođlu et al. (2011) determined C abundances measuring the equivalent widths of C II at $\lambda 4267$ Å of 18 Algol-type binary systems. In the preceding study (Derviřođlu et al. 2010) determined observed rotational velocities of gainers 40% smaller than the critical ones, possibly due to the balance between the spin-up by accretion and spin-down due to stellar wind linked to a magnetic field. Equivalent widths were determined for Algol primaries due to low light dilution contribution of secondaries of only a few percent, which could be only observed during eclipses when the primary is covered by the secondary. Therefore, they decided to take spectrum of the gainers which dominate in the spectra and have high enough temperatures that the lines of ionised carbon and nitrogen can be formed. However, due to high rotational velocities, some

lines are blended. Spectroscopic observations were performed at two spectrographs, at Asiago Observatory (ASI) and Turkish National Observatory (TUG). Both spectrographs are échelle and with R of 50 000 for ASI and even 125 000 for TUG. Wavelengths covered range from 3900 to 7300 Å in the common range. Unfortunately, no spectral disentangling was performed so the composite spectra were analysed. They claim that EWs can be measured only for the stars earlier than A0 spectral type, because in cooler stars EW falls below 10 mÅ which is beyond the measurement limit. Since the C II line is produced only for the T_{eff} above 10 000 K, the standard stars were selected from the main-sequence stars with the temperatures between 10 000 and 30 000 K.

The spectral region around the measured C line is absorption-line free in the selected stars and temperature range. Therefore EWs can be easily measured in the spectra of the stars earlier than the spectral type A0. They founds that EWs in the gainers are systematically smaller than those of the standard stars in the main sequence. The average C abundance was determined for the five comparison stars as $\log\epsilon(\text{C}) = 8.28 \pm 0.10$ dex which is in a good agreement with measurements of Tomkin, Lambert and Lemke (1993) of 8.31 for the same stars. They take $\log\epsilon(\text{C}) = 8.52$ for the solar abundance adopted from Grevesse and Sauval (1998). Compared to solar value, standard stars show 0.24 dex decrease in measured C abundance. The primaries of Algols have lower abundances, except δ Lib and RY Gem. The average C abundance of $\log\epsilon(\text{C}) = 7.75 \pm 0.19$ is obtained for 80 Algol primaries. Measured EWs in relation to T_{eff} is shown in Fig. 3.5.

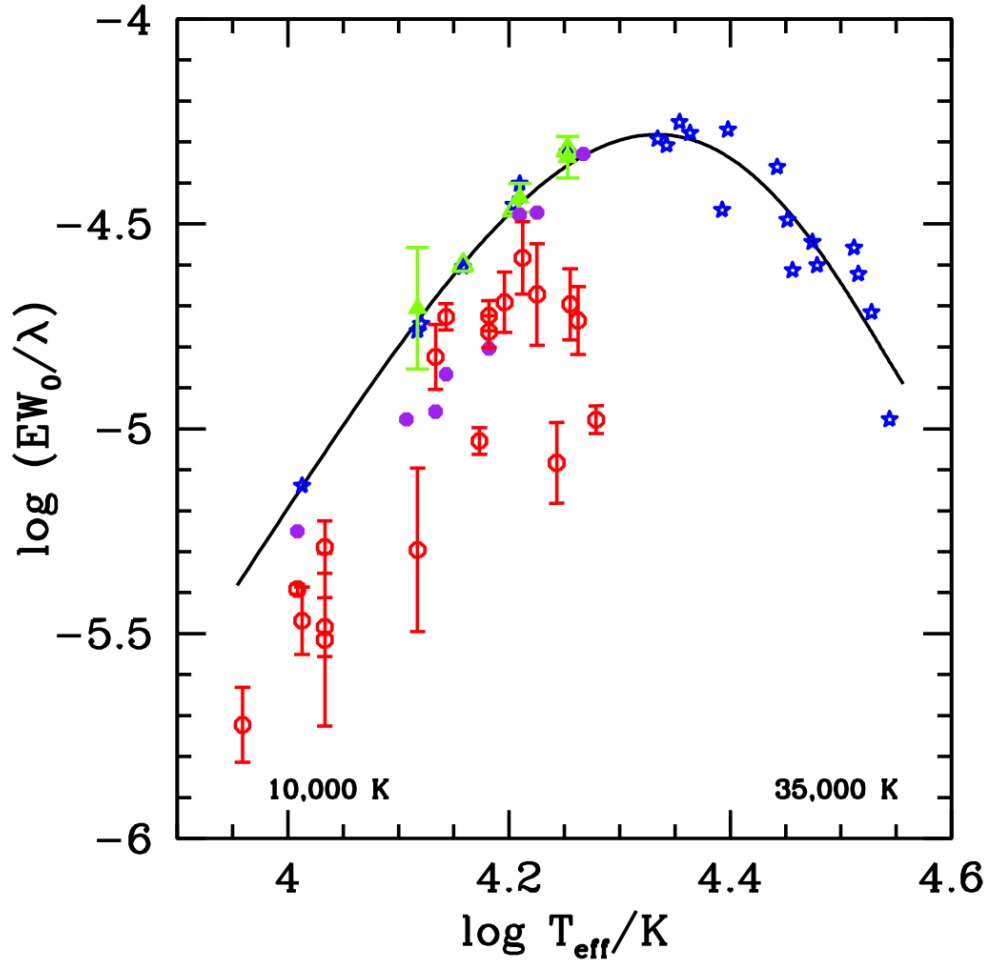


Figure 3.5: Measured EWs for different temperatures. Algol primaries are shown in red, and comparison single stars in blue. A relative smaller EW is evident for all Algol primaries. The error bars refer to the uncertainty of measuring the EW (Ibanoglu 2011)

Chapter 4

Échelle spectrographs

4.1 Échelle spectrographs

Échelle spectrographs are a special version of grating spectrograph, which can take and separate spectral orders in a large wavelength range with very high spectral resolution. They are described by the grating equation

$$m\lambda = d(\sin\alpha \pm \sin\beta) \quad (4.1)$$

where m is the diffraction order, λ wavelength, d separation between dispersive elements and α and β incident and dispersed ray angle measured from the normal to the grating (Fig. 4.1)

One of the quantities describing every spectrograph (grating) is spectral resolution defined as

$$R_0 = \frac{\Delta\lambda}{\lambda} = \frac{mW}{d} = mN \quad (4.2)$$

where R_0 is the resolution, $\Delta\lambda$ the smallest difference in wavelengths that can be resolved at wavelength λ , W grating width and N number of dispersive elements (grooves). Échelle spectrograph is based on a normal grating as a dispersive element, however the incident light is dispersed on a smaller side of the grating (one that is perpendicular to the one show in Fig. 4.1, at a high angle to the grating normal. The result is that reflected orders are close-by and overlapping, which would render it unusable in normal spectrograph. However, as échelle spectrographs use a cross-disperser, an additional element which disperses the reflected orders along a perpendicular plane, the orders are no more overlapped. This setup can be seen in Fig. 4.1, in which both incident and reflected beam is on the same side to the grating normal. In this mode, the resolution is defined as

$$R_0 = \frac{2W\sin\delta}{\lambda} \quad (4.3)$$

where δ is the angle shown in Fig. 4.1. Spectral orders in this high-order setup are overlapping so a free spectral range can be defined as wavelengths uncontaminated in each order by evaluating

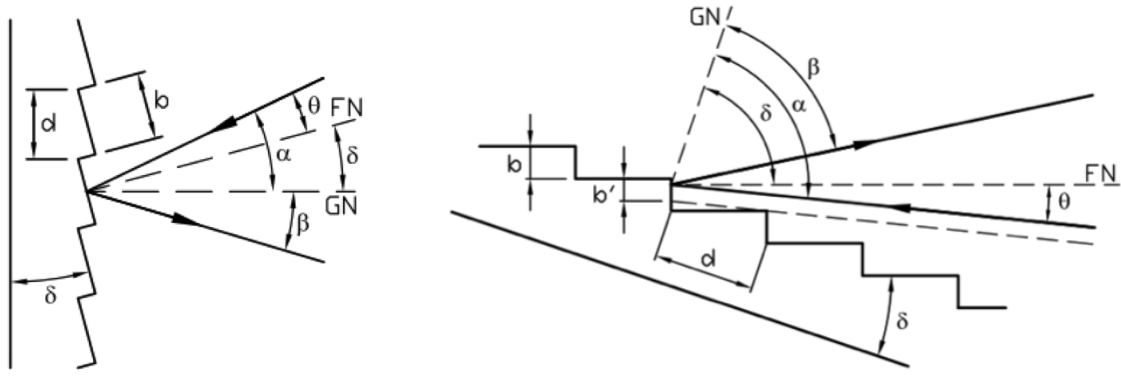


Figure 4.1: Example of diffraction (left) and échelle grating (right)

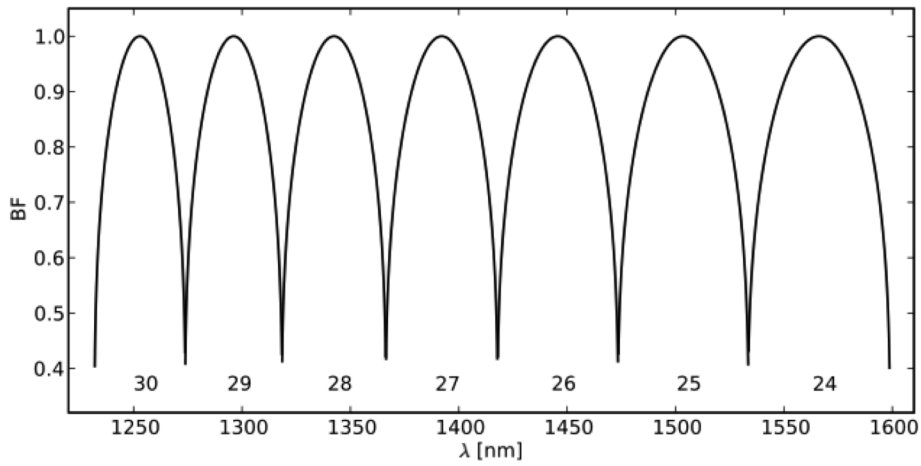


Figure 4.2: Free spectral range of adjacent orders

a condition

$$m\lambda' = (m + 1)\lambda \quad (4.4)$$

where λ' is the central wavelength of the order m , and λ of the order $m + 1$. Central wavelength of $i - th$ order (also called the blaze wavelength) can be calculated as

$$\lambda_i = \frac{2d\sin\delta\cos\theta}{m} \quad (4.5)$$

with δ and θ defined as show in Fig. 4.1. Therefore, free spectral range $\Delta\lambda$ of the order m is

$$\Delta\lambda = \lambda' - \lambda = \frac{\lambda}{m} \quad (4.6)$$

and can be seen in Fig. 4.2. It is obvious that it changes in a monotone manner from order to order.

Finally, the intensity of each order varies as the grating relation describes the direction in

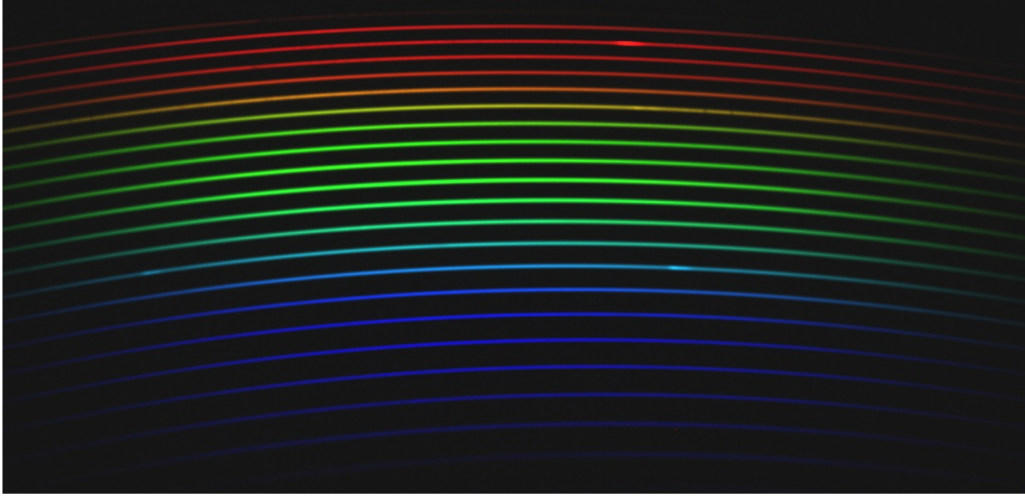


Figure 4.3: Dispersed and cross-dispersed échelle spectrum. Initially, grating separates the spectrum into a set of highly merged orders which are then further separated by cross-dispersing prism into adjacent strips of a single spectrum, here shown in the y-direction

which the light is reflected, but not the quantity of light reflected. It is determined by Eq. 4.7

$$I(\alpha, \beta) = \left(\frac{\sin\left(N\frac{\pi d}{\lambda}(\sin\beta + \sin\alpha)\right)}{N\sin\left(\frac{\pi d}{\lambda}(\sin\beta + \sin\alpha)\right)} \right)^2 \cdot \left(\frac{\sin\left(\frac{\pi b}{\lambda}(\sin\beta + \sin\alpha)\right)}{\frac{\pi b}{\lambda}(\sin\beta + \sin\alpha)} \right)^2 \quad (4.7)$$

where b is the groove width. The blaze function has a maximum when $\alpha = \beta$, in reflection which is not usable. To be used as a dispersion element, the grating should have its blaze peak at some useful higher number of diffraction order, which is accomplished by tilting each groove with respect to the plane of the grating until specular reflection of each groove facet is obtained.

Close-by reflected orders are cross-dispersed by a additional optical element to separate now highly overlapping orders. As high dispersion is not required for this, usually a prism is used. Resulting spectrum is show in Fig. 4.3. The complete setup of an echelle spectrograph is shown in Fig. 4.4.

The spectrograph needs to be very stable, resistant to physical deformations due both to movement and atmospheric influence. In order to achieve permanent and stable position, it is not mounted onto the telescope but is typically located in a nearby facility that is non-movable and heavily damped for all possible oscillations. Additionally, it is always kept at a fixed temperature and humidity in order not to be influenced by thermal distortions that would change optical paths and atmospheric influences. Due to thermal noise in the CCD camera, the setup is located in a cryostat ensuring constant and low temperature. As the spectrograph is dislocated from the telescope, the light from the telescope to the spectrograph is fed by an optical fibre. This setup is called a fibre-fed setup.

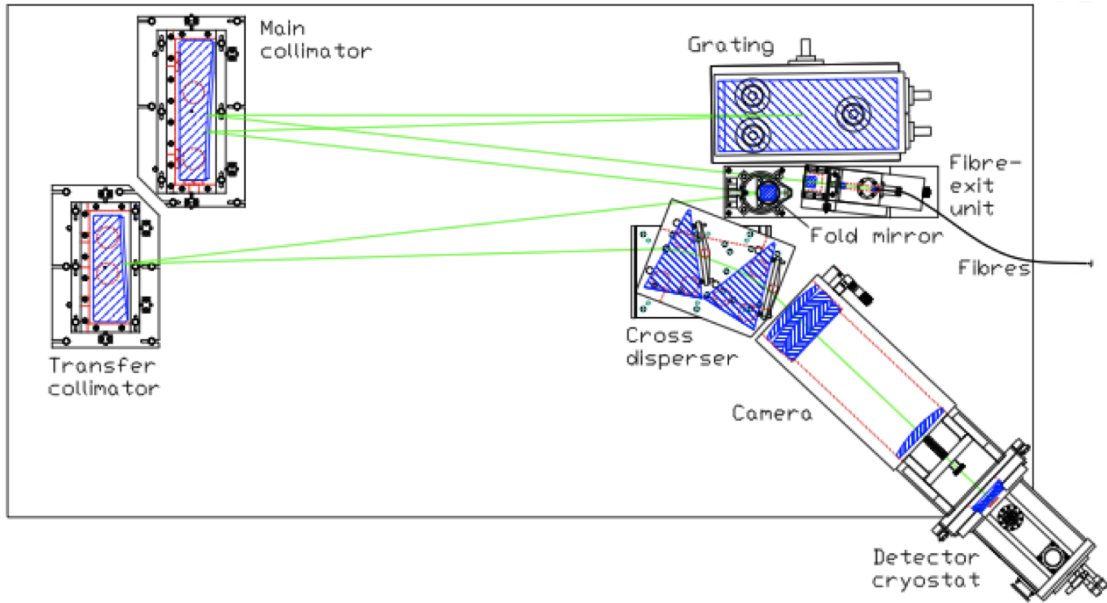


Figure 4.4: Setup of échelle spectrograph dispensing elements

4.2 Échelle spectrographs used in this work

Spectra in this dissertation are obtained from the three spectrographs, FIES mounted on the Nordic Optical Telescope (NOT) on the island of La Palma, BOES mounted at the Bohyunsan Optical Astronomy Observatory (BOAO) in South Korea and FOCES, formerly mounted at Centro Astronomico Hispano-Aleman (CAHA)



Figure 4.5: NOT location (left) and FIES spectrograph (right)

4.2.1 FIES

FIES is the fibre-fed échelle spectrograph from a 2.5m telescope with maximal spectral resolution of $R = 67000$, more than adequate for high resolution spectra. It covers wavelengths ranging from 3700 to 7300 Å without gaps in all orders. It is mounted in a separated, heavy

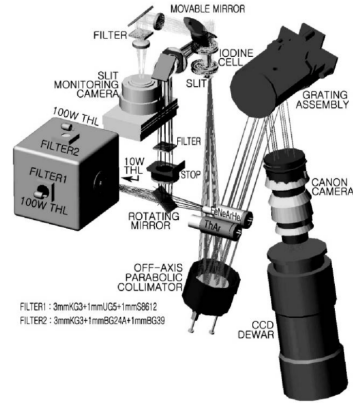


Figure 4.6: Bohyunsan Optical Astronomy Observatory (left) and BOES spectrograph optical layout (right)

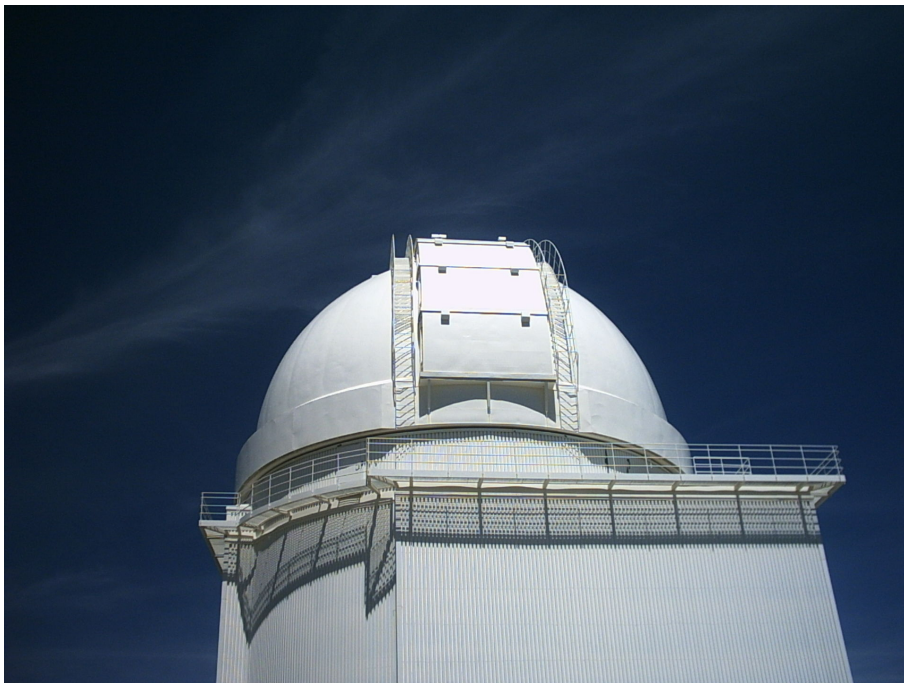


Figure 4.7: Centro Astronomico Hispano-Aleman observatory

insulated building separated but adjacent to the NOT dome to isolate it from sources of thermal and mechanical instability. It uses a Thorium-argon (ThAr) lamp as a source for wavelength calibration. Of all the used spectrographs, FIES is proven to be the most stable with well-defined blaze shapes, a very strong requirement for optimal data reduction, for all the available exposures. It also comes with a well documented ThAr atlas necessary for wavelength calibration.

4.2.2 BOES

BOES is an fibre-fed high resolution échelle spectrograph mounted on the 2m telescope at Bohyunsan Optical Astronomy Observatory, located in South Korea. It has multiple available spectral resolutions up to $R = 80000$ and is covering big wavelength range from 3600 to 10 000 Å. Spectral range is divided into 83 spectral orders without gaps up to ~ 9000 Å. The spectrum is recorded by a $2k \times 4k$ CCD camera. Iodine cell source is used for wavelength calibration.

4.2.3 FOCES

FOCES was installed on the 2.2m telescope at the CAHA observatory. It had maximum spectral resolution of $R = 65000$ which is more than satisfactory. It covered wavelengths ranging from 3800 to 7500 Å in 70 spectral orders, all of them overlapping. Unfortunately, its maintenance was cancelled and the detector CCD chip developed defects making data reduction very difficult, leaving significant percentage of each spectral order unusable. This means that special care needs to be taken when reducing data to obtain best possible results. However, as it was designed to be a very good instrument, the remaining good parts produced excellent and very useful parts of spectrum, but with big caveat for reduction.

Chapter 5

Tools

5.1 Échelle spectra reduction

5.1.1 Reduction introduction

High resolution échelle spectra are essential for high quality astrophysical results. They make possible obtaining of high quality spectra covering both big wavelength ranges and with excellent resolution, which were not so long ago non-complementary qualities. However, observing time competition is a limiting factor in their availability. If they are fibre-fed, they also provide an unprecedented wavelength stability, giving us opportunity for measuring radial velocities with high precision. As a trade-off, échelle spectra are notoriously difficult to reduce, that is convert from raw spectra images to calibrated, non-biased spectra ready to be measured. Therefore it is of great importance to reduce raw spectra as good as possible in order to obtain valid and reliable spectra. In order to do that, we usually rely on *pipeline* reduction which would not be sufficient. That results in high uncertainties in derived spectra that can greatly influence scientific results. Bad reduction can influence spectral features more than the very effects that are subject of the study. Therefore, we use some pre-existing tools for échelle spectra reduction, as well as a number of custom made software we've developed in order to make the reduction of the best possible quality. This semi or fully manual approach of reduction gives us confidence that we're really measuring astrophysical effects, and not reduction artefacts.

5.1.2 Securing spectra with échelle spectrographs

All the spectra used in this thesis were obtained from modern high resolution spectrographs with spectral resolving power of at least $R = 45\,000$, mounted on a 2m class telescopes or better. Spectrographs we used are FIES at NOT, FOCES at CAHA and BOES at Bohyunsian Observatory.

5.1.3 Bias, Flat and Normflat

As with all image reduction, bias subtraction and flat field correction should be done first. Bias files, additive effect due mostly to camera readout and operation voltage, are combined into a master bias file, which is then subtracted from all other frames. Bias files are taken as zero-exposure images with CCD camera detector covered and are subtracted from other obtained frames. After that, obtained flat field images are combined. Flat field correction removes several influences

- primarily pixel-to-pixel sensitivity variations
- distortions in optical path
- possible artefacts due to dust covering lens or other impurities on the optical path

Flat field images are ideally taken with exposures as long as possible, but also not too long to produce CCD saturation. They are usually taken with telescope pointing to an uniformly lit dome wall uniform or part of morning or evening sky. Uniformity of sky is assured by small field of view. Furthermore, master flat field is normalised in areas that contain spectral data on the science frames, in order to have intensity of 1 with variations from unity due to before mentioned causes. Therefore, total mean intensity in spectral region stripes is 1 with some small pixel to pixel variations. Areas between data stripes is ignored. All those steps are performed in standard IRAF¹ échelle package (Tody 1996).

5.1.4 Extraction of spectral orders

In order to locate parts of obtained image containing spectral data, usually slightly curved stripes due to optical setup, one has to roughly mark the general location of those stripes which are used as first guess for precise spectral track tracing (Fig. 5.1). Spectral tracks are then automatically traced using IRAF task `aptrace`. This procedure is performed only once, on a well taken image and position information is saved as template for all the other procedures.

5.1.5 Scattered light

The last important step before spectra extraction is removal of scattered light. As mentioned, all the spectral data is contained in strips, however in reality spectrum is not contained in strips only, but there is cross-order contamination of light from one order to its neighbours introducing additional light or intensity into them. Therefore, intensity information in between orders is used in order to fit the scattered light intensity profile and subtract that modelled scattered light

¹IRAF is distributed by the National Optical Astronomy Observatories, which are operated by the Association of Universities for Research in Astronomy, Inc., under cooperative agreement with the National Science Foundation.

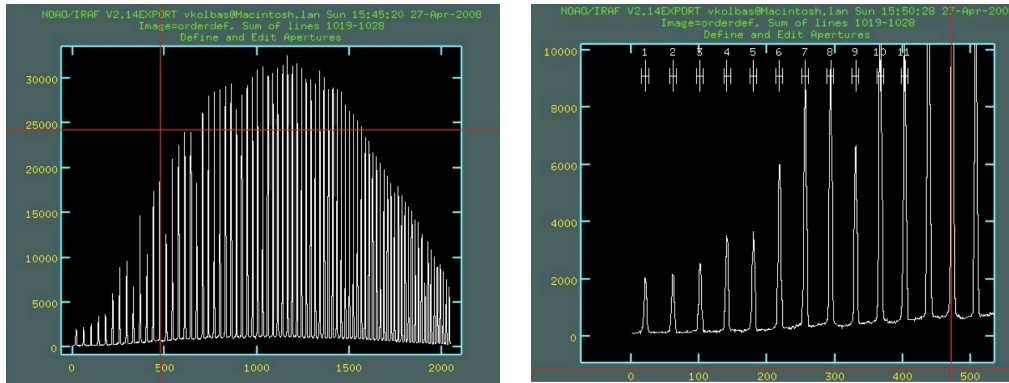


Figure 5.1: Determining location of échelle orders. Full range plot is shown on the left, and detailed range used for order marking is shown in the right.

leaving only spectral information in orders themselves (Fig. 5.2). After that, we can proceed with order extraction - extracting spectral data from strips (orders) from original 2D obtained image. Extraction is performed using the *apall* task with *clean* option set which automatically sets the extraction weights to variance, along with cleaning any detected cosmic rays. The result is a file containing spectral (intensity) data of as many orders as the spectrograph is designed to create (usually 40-80 orders covering wavelengths from 3000 to 10000 Å).

5.1.6 Wavelength Calibration

Extracted orders are now uncalibrated, meaning we have spectral data with axes defined with intensity and pixel position. To convert pixel positions to wavelengths we use another important image obtained from the spectrograph - calibration lamp image. Calibration image is taken with same échelle setup, but imaged is Thorium-argon (ThAr) calibration lamp (or some other well known source rich in spectral lines). The idea is that emission spectrum of known source will have a large number of recognisable spectral lines. By manually identifying as many as possible of those lines, in all extracted orders, we can create a calibration function connecting pixel positions with wavelengths. Using that calibration function, previously pixel-calibrated extracted spectra can be converted to wavelength calibrated spectra.

5.1.7 Normalisation

Once the spectra are wavelength calibrated, calibration quality can be inspected by overplotting neighbouring orders in which spectral features should overlap perfectly. If that is the case, we have only one more, but extremely important step to perform - spectral normalisation. Extracted and calibrated orders come in so called *blaze* shape. Blaze is a bell-shaped curve with low intensities on order edges and highest intensity in order center. It is not due to spectral energy distribution of the source, but due to optical setup and characteristics of échelle spectrograph. Therefore, the spectra must be carefully normalised to unity where there are no spectral features,

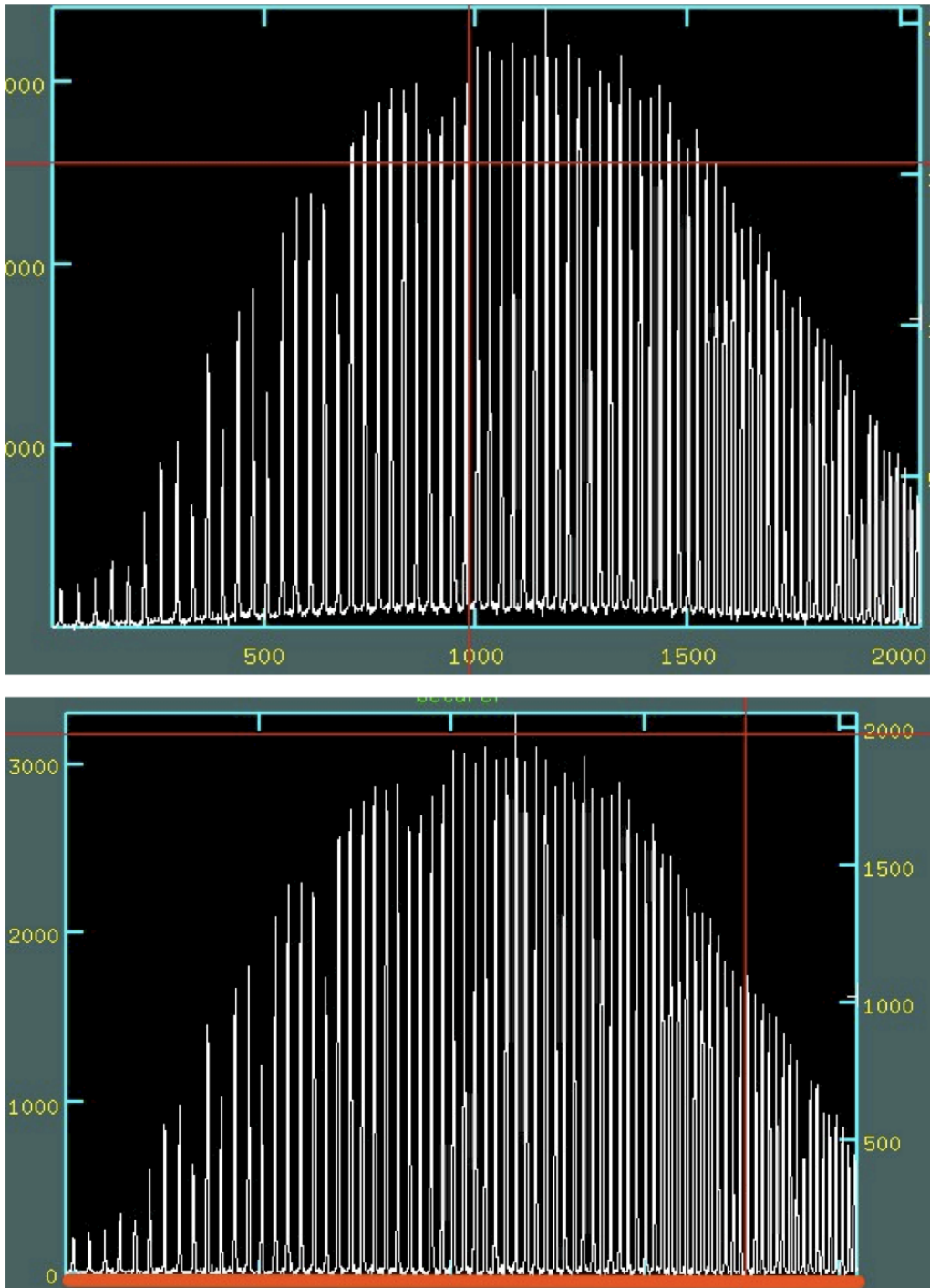


Figure 5.2: Sample of a frame before scattered light correction (upper image) and after (lower image)

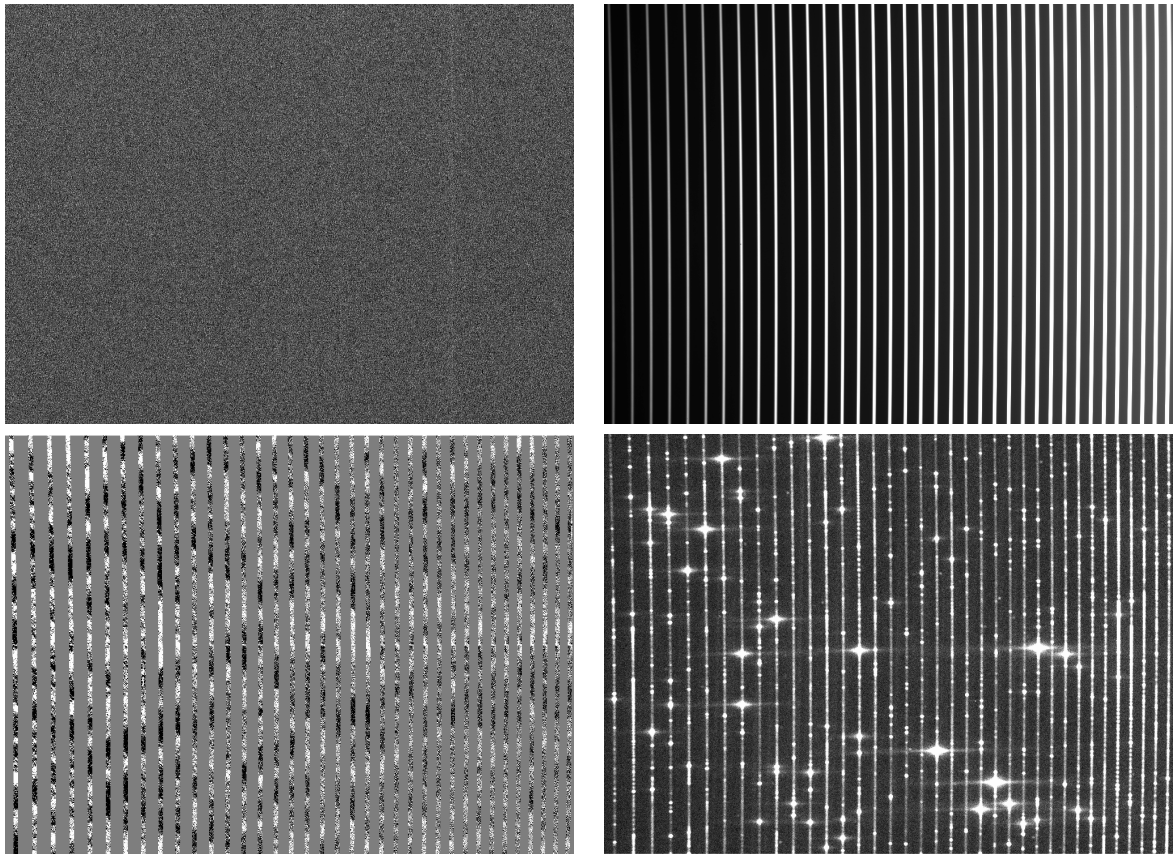


Figure 5.3: Calibration images used for échelle spectra reduction. Bias frame (top left), flat field (top right), normalised flat field (bottom left) and ThAr wavelength calibration lamp (bottom right)

but continuous intensity and to less than unity in spectral lines. This step is usually performed automatically with pipelines, introducing big errors in final spectra. Therefore, we've developed a number of procedures, each applicable to different type of spectrum, in order to make the best possible normalisation.

First and the easiest way of normalising blazed spectra is dividing with fitted flat-field profile giving a non-unity, but locally more or less normalised spectra of each order. This procedure is applicable only if the flat field light source is of compatible characteristic as the obtained spectrum. Final spectrum should be further normalised using some low degree polynomial. However, as mentioned, this method is known to work only occasionally and is to be used only if all the other methods fail as last resort.

Second technique is normalisation of orders using our dedicated fully-interactive code - `MULTIPEGLA` written in `JAVA`. It requires input blazes to be saved as ASCII data which can be loaded. Input single-order blaze is approximated by some polynomial of adequate degree. Points of the blaze function can be positioned interactively using a mouse. Those points can be added, moved or deleted for easy manipulation. Function that is fitted is an ordinary polynomial up to 9th order. In our experience, for most spectrographs if the obtained spectra are well taken and reduction procedure is well performed, 9th order polynomial should give an excellent fit. If it is not sufficient, it is an indication of error in data or reduction, or also an attempt to over-normalize data, meaning the user is trying to normalise to continuum parts of spectrum that is below continuum, e.g. wide wings of Balmer lines for A and late B-type stars that have the widest Balmer lines, that can cover from 3 to even 5 adjacent orders, depending on spectrograph setup. Fitted orders can be zoomed in all axes, and the normalisation result can be examined in additional window containing the order that is currently being normalised, with adjacent orders plotted. All that procedure is updated live. There is also a possibility to interpolate in-between blazes of some orders in order to have a first guess for orders that are difficult to normalise. Furthermore, any template spectrum (synthetic or other object) can be plotted along with normalisation result as a check of normalisation, but with care not to introduce bias in normalised spectrum. Product of this code are as many ASCII normalised files as there were input orders.

Our final code for spectra normalisation is a semi-automatic code, written in `C`. For input it requires spectrum in `FITS` format, normalisation curves also in `FITS` format, as well as ASCII file with order positions. The latter is needed because order spacing on 2D obtained frame varies with position on the frame and is necessary for optimal interpolation. Normalisation curves are fitted parts of spectrum with low number of spectral features, where continuum can be found using `IRAF sfit` task, and the code is used only in orders that have a large number of spectral lines shifting the spectrum below continuum for broad Balmer lines. Those well-fitted orders are now used to interpolate orders with missing continuum position information, which are provided to code using an input file. Result of this code is also a `FITS` file containing `sfit` provided calibration curves as well as computed interpolated curves that were missing. Using

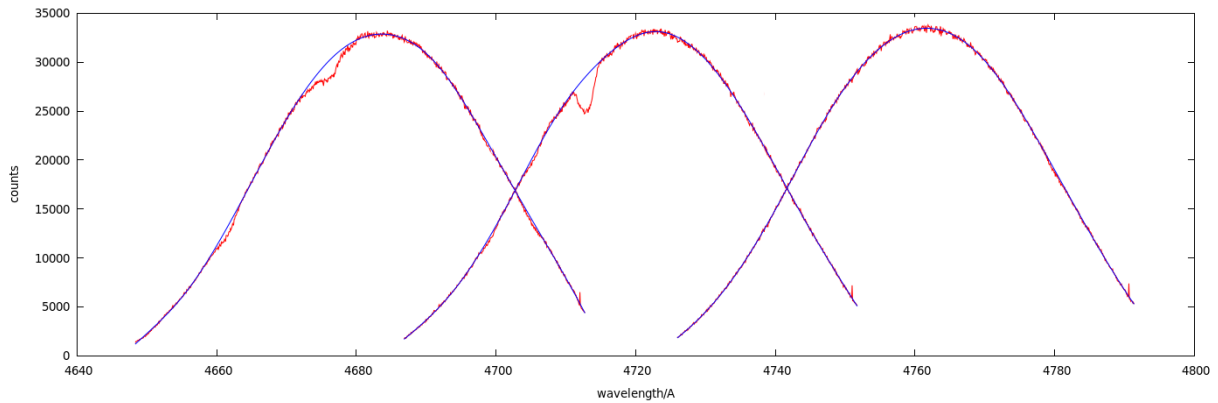


Figure 5.4: Example of three neighbouring, overlapping échelle blazes. Spectra are plotted in red, and fitted blaze functions used for normalisation in blue.

that file, we can return to IRAF to divide blazes with newly created calibration files producing as good as possible normalised spectrum. By overplotting, it can be checked if the procedure was successful, meaning that spectral lines that are available in two neighbouring orders should overlap perfectly (Fig. 5.4).

5.1.8 Order merging

Final step in reduction of spectra is merging of normalised orders into a single spectrum file. It is done using code, SPECTRAJOINER (Fig. 5.5, also written in JAVA. It requires normalised orders in ASCII format as input and plots two by two neighbouring orders in a interactive windows where one can select at which position one want sthem to be merged. One can choose to accept only the spectral data with higher S/N of the two overlapping orders by selecting a single connection point or calculate an average value for each of the point pairs contained in the selected overlapping region. This procedure is repeated for each neighbouring pair of orders, finally producing a single ASCII file with a complete, normalised and connected spectrum (Fig. 5.7).

5.2 MULTIPLEGLA - Blaze Correction Software

As mentioned, careful normalisation of blaze shaped recorded spectral to normalised ones is a crucial for retaining original spectral information in order to correctly determine all the astrophysical quantities. For that purpose, we've developed an graphical tool MULTIPLEGLA in JAVA programming language due to its ease of use with graphical interfaces. Due to the nature of problem at hand, no existing drawing code was sufficient for the task, therefore it was developed from scratch by overriding drawing methods on JPanel and JFrame to create the adequate and responsive user interface for spectra manipulation.

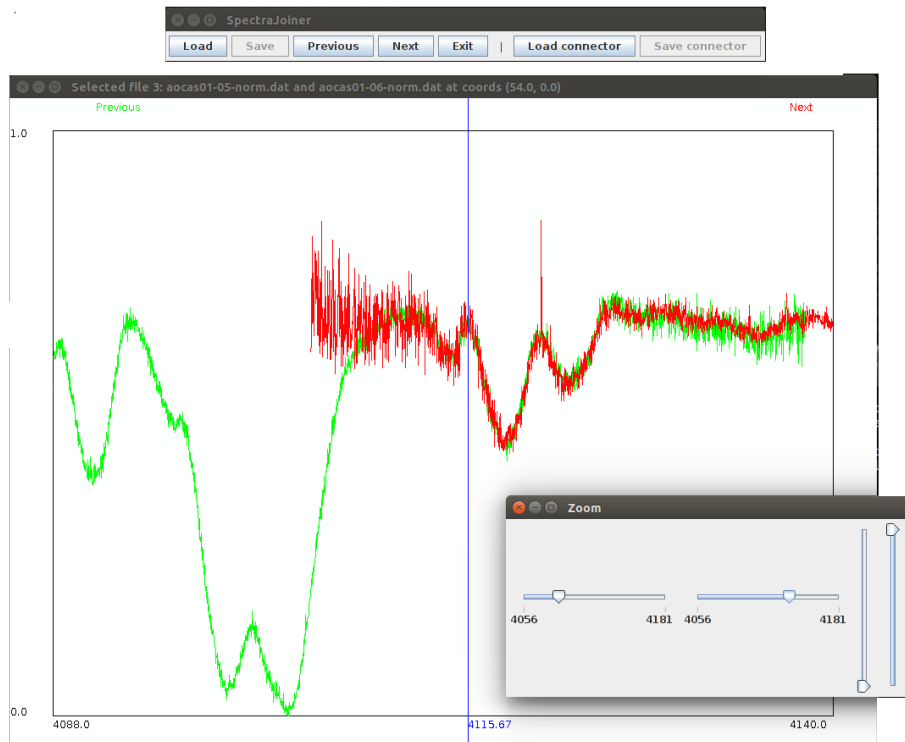


Figure 5.5: SpectraJoiner JAVA code for erging normalised blazes. Two adjacent segments are shown with wavelength range selectors for better clarity. Connection point can be seen as the vertical blue line which can be interactively positioned using mouse. For similar spectra, connection points can be saved and later reused for joining spectra of the object

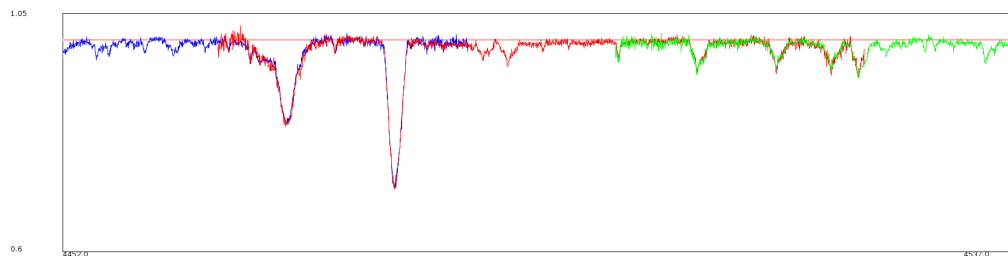


Figure 5.6: Example of careful manual order merging using MULTIPLEGLA software. Only three adjacent orders are shown for clarity

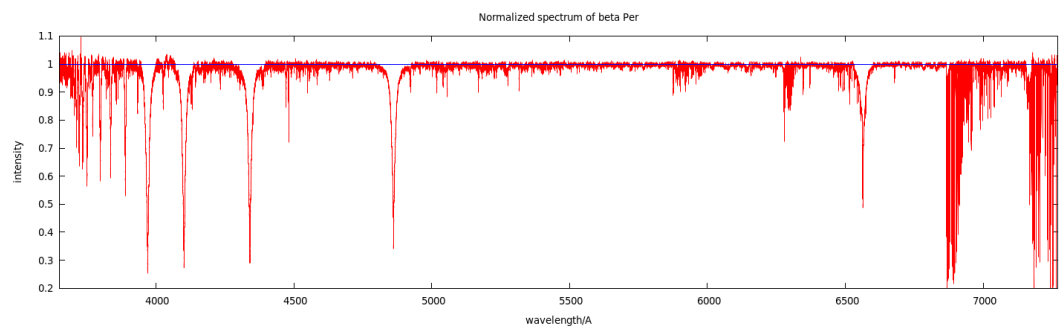


Figure 5.7: Merged spectrum of β Per in full range

The software expects orders to be in separate ASCII files, one for each order. They can be simultaneously loaded. Then, main window of the program is shown, with a few supplementary ones - window with spectral order to be fitted, one with normalisation results and two for determining visible ranges of the orders. In the results window, one can choose to display only the fitted segment with overlapping neighbouring ones that are overlapping in the region or complete three adjacent segments in total. Additionally, one can choose wavelength subrange to be displayed, as well as lower intensity limit for better clarity in normalising smaller spectral features.

In the main window, one spectral order is shown and one can position fitting points interactively using mouse. One can mark as many as desired fitting points onto the spectrum. However, the maximum order of fitted blaze function is 9th order polynomial. It is our experience that all the well formed blazes should be possible to fit using that function, and all the deviations that occur are either the result of reduction or instrument problems or that one is trying to overfit features that are, for example below continuum (regions rich in spectral lines or broad wings of Balmer lines in A and late B-type stars. Already defined points can be either deleted if necessary or moved interactively with instant interactively visible results in fitted function and display window for better precision. For global fitting correction, fitted polynomial can be shifted (by dividing/multiplication) for a desired amount in order to rescale the blaze. Also, one can interpolate blaze function for an order with problematic shape or features based on selected neighbouring ones that are fitted without uncertainties. In the results window, one can load any desired background template spectrum (also in ASCII format) for visual guidance if necessary, which can be additionally Doppler-shifted for better matching. It is important to stay unbiased when fitting using proposed template. Finally, all the clicked points can be saved into a file and then reloaded for use with that same or similar other spectrum at later time. Run-time of the software can be seen in Fig. 5.8.

5.3 Genetic algorithms

Genetic algorithms (GA) are becoming more and more popular method of optimisation, invented by Holland (1975). With increasing CPU power GAs can find solutions to complex problems in shorter and shorter times. Genetic algorithms were introduced in astrophysics by Charbonneau (1995) with routine PIKAIA, used as a rough procedure guide for all of our codes that implement GA.

The principal idea of genetic algorithm is replicating Nature's selection process in order to find and promote best solutions (in real life - fittest entities) for selected problem. GAs are mimicking this natural evolutionary process in a procedural way that can be easily implemented in code. Of course, they have many advantages compared with other optimisation techniques, and also some drawbacks. The main advantage of GA is the ability to search the complete given multiparameter space for solution, e.g. global maximum, without being stuck at local maxima

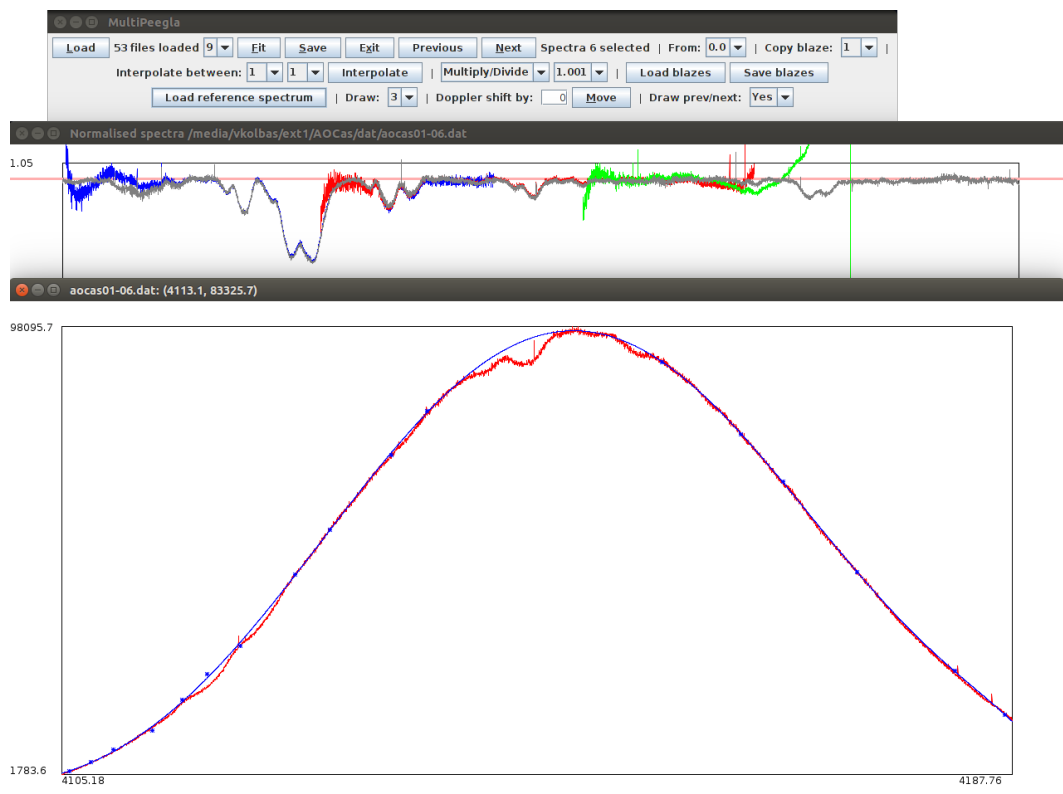


Figure 5.8: MULTIPLEGLA blaze correction code. Bottom window is the order to be corrected. Middle window is normalisation results window with previous order (blue), current order (red) and next order (green). Overplotted in grey is loaded reference spectrum.

like all gradient-based optimisation methods. Because of this ability to move away from local extremes, they are also not heavily influenced by selected starting point for optimisation as many other methods are. As for the downsides, the biggest one is a big requirement on CPU time. Furthermore, it is also possible that GA will never find optimal or the most optimal solution, due to its nature as it is a probability-based optimisation method. This is a very unlikely, but possible outcome which needs to be taken into account.

The basic principle of GA is very simple. Because of GA's motivation by natural selection process, nomenclature used is one of real life evolution and selection process. The main object in GA is an *entity*, in our terms one particular of many possible solutions to our problem. An entity consists of *genes*, characteristics that describe our parameter space. Entities are grouped in *generation* in which each entity is somehow examined for its *fitness* or how well it solves given problem. Entities from one generation are combined to produce a new generation, each generation being examined for fitness. The idea of GA, as mentioned, is very simple in its basic application. Complexity usually comes in programming part, in the way of describing genes and in the problem of evaluating fitness. More precisely, we need to have a objective way of associating a numerical value that uniquely describes how good each entity solves our problem, which can be a very non-trivial problem. A good example can be seen in Fig. 5.9. Plot of function

$$f(x, y) = [x(1 - x)y(1 - y)\sin(n\pi x)\sin(n\pi y)]^2, n = 7 \quad (5.1)$$

as good test benchmark case is shown as a good test example. Below 3D plot is a surface plot of intensity for additional clarity. It is obvious that there is just one global maximum, however there is a number of local maxima that would cause grave problems for gradient methods. GA can, given enough computing time (generations), easily deal with local maxima.

The basic principle of GA is time evolution of entities. An entity is considered to be a complete package of information for solving a problem. It is defined by its parameters - genes. For example, to find global maximum of the function plotted on Fig. 5.9, information is needed for two coordinates to define a position in 2D parameter space. Therefore, an entity describing one possible solution would have two genes which represent x and y coordinates of the proposed solution. For simplicity, genes are encoded to have a numerical value between 0 and $0.\overline{99}$ for simplicity of code. This range can then be expanded to desired range of parameter in parameter space. The first problem in programming GAs is how to represent the genes internally. In C programming language, one can use simple floats, but a better approach would be an array of integers or array of characters. This may seem to be contrainuitive and a bit clumsy, but is quite convenient for GA code implementation. Another decision to make is the precision of genes, how many decimal places do we consider. Second big problem is a way to calculate fitness. In this example, one can simply insert x and y values, after decoding from e.g. char array into float into function in the function $f(x, y)$ and calculating its value. As there is usually no information where the maximum is, the only information we can get out of fitness function

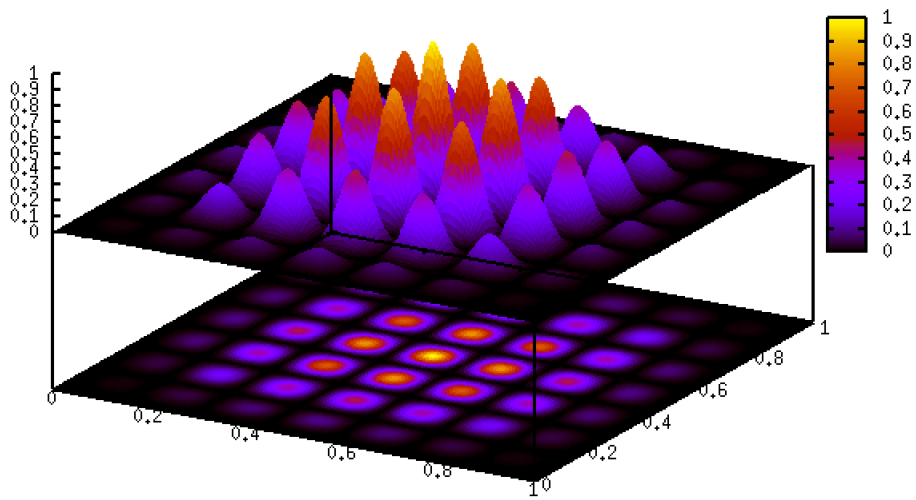


Figure 5.9: Example function for GA optimisation

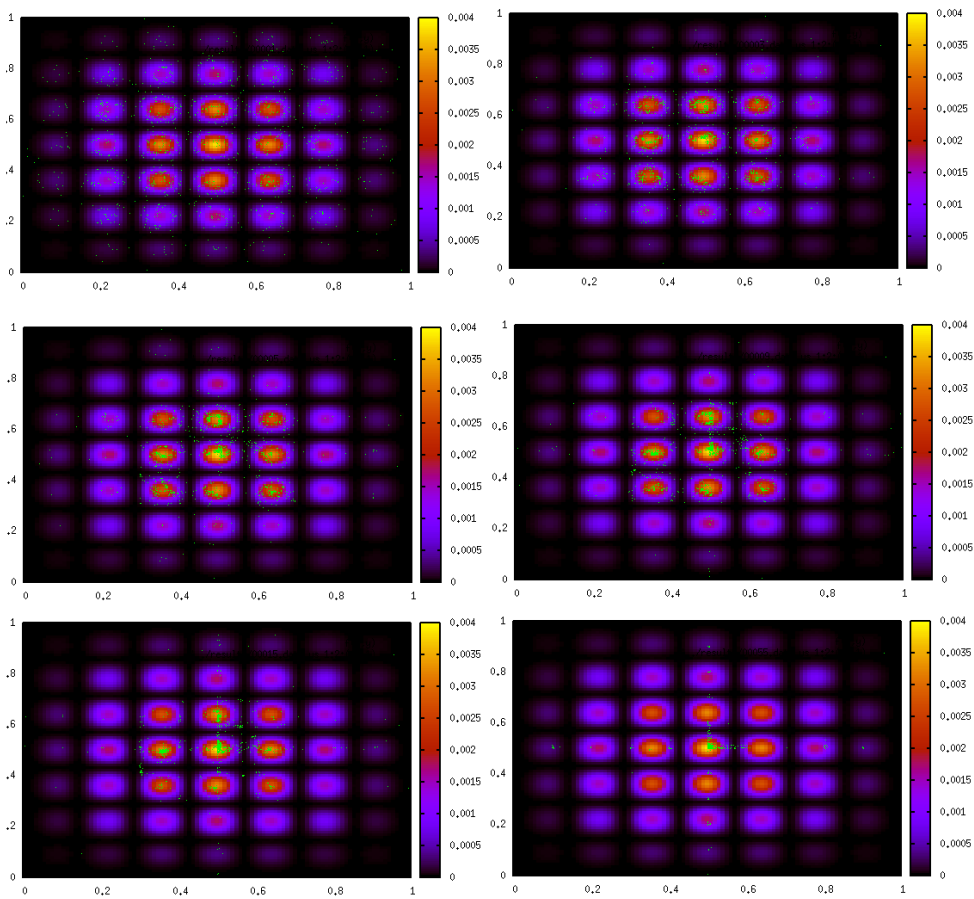


Figure 5.10: Example of GA convergence in time.

is relative fitness of one solution (entity) compared to all others and conclude that a new biggest value means a fitter solution.

As an example of GA itself, we decide on a number of entities for starting generation, lets take 100. Therefore, we create 100 entities and give them two genes with random values between 0.0 and $0.\overline{99}$, one for x , and one for y value. We also decide on desired gene precision. Lets take that we have one of those entities with genes

$$x = 0.234354$$

$$y = 0.594839$$

Next, fitness must be calculated for each of 100 entities. Then the initial population is done. Next step is reproduction - combining entities from previous (now, initial) generation to create a new generation. For that we select 50 pairs of two entities. The selection is not random, but fitter entities have a bigger chance to be selected for reproduction. Depending on our choice, two most popular selection algorithms are ranking and roulette wheel selection.

Ranking is simply sorting entities by their respective fitness. A probability for selection of its entity is given as $1/i$ where i is each entities number in sorting. Therefore, the fittest entity will have selection chance of 1 (which should not be confused with probability of 1, meaning certainty), second of $1/2$, third of $1/3$ and so in. Then all of those selection chances are added up to get their sum $S = \sum_{i=1}^n x/i$ to get a total probability. Next, a random number between 0 and S is selected. As the fittest entity has selection probability of 1, and the least fit of $1/100$, the fittest entity has the biggest chance of being selected. We can see each entities' chances of being selected on image 5.11. In blue is the fittest entity which has the greatest chance of being selected.

Roulette wheel selection is another way of assigning selection probability to each entity, in which we usually use their fitness value. If the fittest entity has fitness of 50. and one of the least fit ones 0.15, we again calculate total sum of fitnesses and select a random number between 0 and S . As we can see on image 5.12, now the fittest entity has a greater chance of selection than other, especially ones in least-fit part of a generation.

The choice of selection algorithm varies from application to application and should be based on user's experience with GAs and understanding of particular problem to be solved. If fitness of a few best entities greatly outweighs others, than roulette wheel selection can run into problem of degeneracy - selecting of only a few entities resulting in depleted gene pool in a few generations only. On the other hand, using ranking algorithm can favour less fit entities and decrease optimisation speed. Specifically, for a GA run that requires up to a few days to find solution using optimal parameters and selection method, any non-optimal choices can significantly increase optimization time.

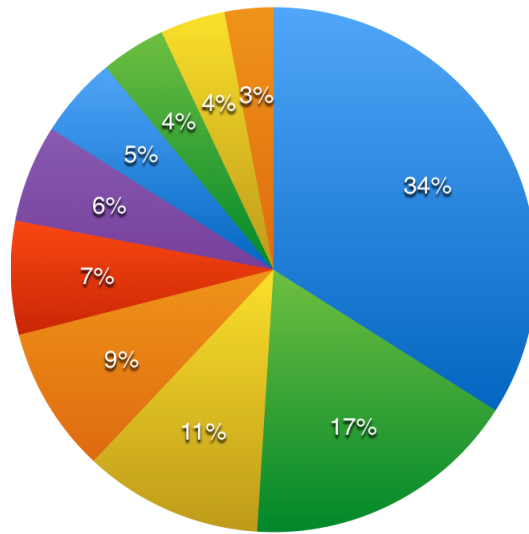


Figure 5.11: Selection chance for ranking selection

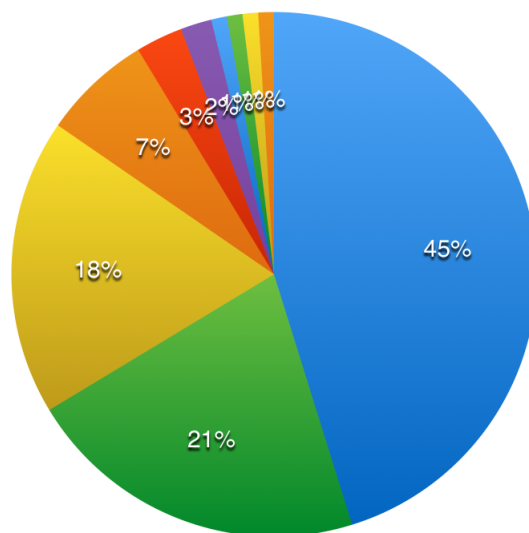


Figure 5.12: Selection chance for roulette wheel selection

Having chosen selection algorithm, one can proceed with reproduction. The idea is to generate a new population with new 100 entities, from previous generation of also 100 entities. For that, we select 50 pairs from original generation, ensuring that each pair consists of different entities - parents. If selection algorithm gives us the same entity for both parents, we repeat selection process as necessary. Having selected two parents, we proceed with generating another random number between 0.0 and 1.0. If the random number is less or equal than a chosen probability of, for example 0.3, we just copy entities to the new generation. If the random number n is in range $0.3 < n \leq 1.0$, we perform gene crossing. For that, we generate a random integer between 0 and chosen numerical precision of gene representation. If we end up with number 3, we temporarily disregard leading 0. and split the rest of parent genes after 3rd number, e.g. for example just for the x gene:

$$\begin{aligned}
 x_1 &= 0.234354 \\
 x_2 &= 0.670383 \\
 &\text{becomes} \\
 x_1 &= 234354 \\
 x_2 &= 670383 \\
 &\text{split after the 3rd number} \\
 x_1 &= 234|354 \\
 x_2 &= 670|383
 \end{aligned}
 \tag{5.2}$$

Then we create two new entities, offsprings, to be inserted into new generation by switching genes from two parents at that randomly chosen position, generating new gene for x value of two entities, after appending the leading 0.:

$$\begin{aligned}
 x_1 &= 0.234383 \\
 x_2 &= 0.670354
 \end{aligned}$$

Depending on the position of split point, newly generated genes can more or less significantly move in the parameter space. Finally, we also introduce mutation as a possibility of changing gene pool. For that, we again pick a random number between 0.0 and 1.0 and preselect a desired mutation probability, which is usually a very small number, e.g. 0.002. We generate a random number for each decimal place in our gene representation and check if we want to mutate it. If it happens that mutation probability for 1st digit in second x gene is satisfied, we select a new integer from 0 to 9 to replace that digit, so we get a new x_2 value

$$x_2 = 0.670354 \Rightarrow x_2 0.270354$$

therefore changing entities position in parameter space significantly. Repeating this process 50 times, we generate new 100 entities with 70% of them having their genes switched at some arbitrary point, and additionally mutated with a low but non-zero probability. To be more precise, we usually generate only 98 new entities if we choose to enforce a rule of *elitism*, which means that we always copy the two best entities from one generation to the next one, ensuring that the best solution is never lost. Elitism can greatly improve convergence speed, or in many complex situations can also mean the difference between converging to a solution of permanently scanning parameter space and never converging.

For more complex GA applications, where one simultaneously needs to fit many parameters, from more than 5 up to hundreds as is the case in genetic spectral disentangling (Sect. 5.5), we should introduce further mechanisms of optimization of GA and parameter choices. For example, in case of fitness testing that is very time consuming, we use a small number of entities in each generation while introducing higher mutation rate. Chosen number of digits gene precision does not vary runtime speed significantly, therefore the usual selected precision is from 6 to 10. In case when one or a few entities have considerably higher breeding selection probability, usually in roulette wheel selection process and in small number of entities, it is possible (and usually happens) that most if not all of entities in a generation have genes with very similar numerical value, meaning that the parameter space search is limited or nonexistent, apart from possible mutation. In that case, we can choose to introduce one generation with significantly increased mutation probability. For example, if we know that degeneracy of entities is a possibility, we can increase mutation probability from e.g.. 0.3% to 30% in every 100th generation to force new numerics to enter our gene pool and resume parameter space search. Another approach is to replace a certain percentage of entities, e.g. 30% of lowest fitness entities with completely new entities with randomly generated genes, just like populating initial generation thus introducing new numerics. The possibilities are endless and are bound only by the programmer's imagination and experience with GA and understanding how it performs, or more precisely how it can get stuck in a particular application to the problem. In cases when one can efficiently deal with many entities in a generation without significant decrease in computing speed, there is also a probability that most of them will be 'junk' entities with very low fitness and will almost never be selected, we also should find a way of dealing with them, just like in the opposite case of low number of entities. Unfortunately, most complex applications of GA require programmer's or user's understanding and experience with underlying process.

Nowdays, there is an relatively easy way to increase speed of GA implementation, by using multi-core or even multi processor computers or clusters of computers. There are some parts of GA that are performed on each entity individually, for example fitness value generation, we can make them parallel using multiple cores simultaneously. In C implementations, posix threads are utilised. Therefore, on a 4 core system we can perform 4 simultaneous fitness tests, resulting

in approx. 3-3.5x runtime speed increase. Furthermore, using different compiler like LLVM², we can also increase runtime speed by additional 30-40%. Finally, if we completely skip entities sorting, especially in cases when we choose a large number of entities in a generation, we can additionally speed up the process. All those can mean the difference between GA run of a few days vs. weeks or longer making the difference between feasible use vs. unjustified computer requirements.

Finally, there is have a fundamental problem of not knowing the final solution, therefore not knowing if the algorithm has found a solution. There are several ways of making an informed decision if a solution has been reached. The solution, of course, must be physically justified. When GA finds a solution which it keeps with possibly small numerical variations in less and less significant digits, one should be able to determine if that solution is meaningful. If additional GA runs end up with the same solution, the solution is either correct or there is a fundamental problem either with our GA configuration or chosen problem to solve. Still, GAs have time and time again proven to be very reliable in finding solutions, even in extreme cases when it really seems that the problem is too complex or difficult.

5.4 WDGGEN

Wilson and Devinney³ (1971) have developed a code for solving light curves of eclipsing binaries, probably not realising the success and longevity of their code which is still in use and absolutely invaluable. Changes to the code were made and new releases published a few times, but basically it is still the only light curve solution package in wide use. In time, many third-party additions and changes were made to the original code by third parties, in order to make the code more user friendly and perform semi-automatic analysis, but the changes were never approved by the authors. The package consists of two programs - LC (light curve), a program for general light-curve calculating and DC (differential correction), program for fine-tuning parameters found by LC. As many parameters of the light curve can be fitted, there is a dangerous possibility of producing relatively good fits with unphysical parameters. Therefore, the authors insisted for long on using the code completely manually, emphasising the importance of understanding all the possible parameters and their consequences on the result.

The only addition to the code the authors recognised is the front-end (GUI), PHOEBE (Prša & Zwitter 2005). It enables user to enter and change input parameters to the LC code interactively in a GUI, making the process user friendly. Additionally, it enables some parameter optimization, as well as plotting the resulting light curve fits for easier inspection. Although very useful, the main purpose of the program is not automation and extensive multiparameter fitting. That is why we decided to make our own code for LC parameter fitting, based on GA.

²llvm.org

³The Wilson-Devinney program is distributed by Robert E. Wilson (University of Florida) and available at <ftp://ftp.astro.ufl.edu/pub/wilson/lcdc2007>

WDGEN is a optimisation code, which uses GA to vary input parameters to the LC code and find optimal solutions (with caveat to unphysical results that may easily occur) to the light curve. The latest version uses LC2003 version of the code. The code then creates input files for LC, runs the code to generate the fitting light-curve and output files. It then parses the output files reading in computed values and corresponding χ^2 needed for GA to work. Output file from the best entity in each generation is saved for later reference. As light-curve fitting can be a time consuming process, the code is multithreading enabled, utilising all available CPUs and CPU cores. Therefore, it is of paramount importance to set population size as a multiple of CPUs/cores.

5.5 Genetic Disentangling

Spectral disentangling is a method for obtaining individual spectra of multiple stellar systems. Spectra are secured only as composite spectrum in which there is a linear influence of all the component spectra combined. The disentangling of composite spectra solves for a self-consistent solution for individual spectra and system parameters. The technique was developed by Simon & Sturm (Simon & Sturm 1994). Hadrava (1995) reformulated the problem in Fourier domain which is more efficient and less demaning on CPU time. Fourier disentangling was further improved in the code FDBINARY (Ilijic 2003, Ilijic et al 2004) The total light coming from a binary or multiple stellar system of K components adds up linearly to an observed spectrum. For component k the Doppler shifted velocity v_{kj} at time t_j where j is one of the J observations (observed composite spectra), the normalised observed spectrum at time point j - $y_j(\ln\lambda)$ is

$$y_j(\ln\lambda) = \sum_{k=1}^K l_{kj} x_k(\ln\lambda - v_{kj}/c) + \text{noise} \quad (5.3)$$

where l_{kj} is the light factor of component k at time j ($\sum_{k=1}^K l_{kj} = 1$) and v_{kj} is the orbital radial velocity in the units of speed of light. Depending on the phases of observed spectra, it is possible that the light factors for each component remain constant. In that case, the solution is not unique and the shape of the reconstructed spectra is correct, but additional information on the light ration between components is needed to reconstruct the intensity of each component.

The disentangling problem can be solved both in matrix form using single value decomposition (SVD) method or using discrete Fourier transforms (DFT), but in any case the problem is overdetermined. There are more equations to be solved than variables, so there is more than one solution. Some of those solutions are physically not meaningful, like the ones with negative intensity for any spectral point. Using DFT is a computationally more efficient method, but with several limitations. Firstly, all component spectra must be sampled on a common grid of points. That means that spectra obtained at different spectrographs must be resampled to a common grid, which itself must be equidistant in $\ln\lambda$ scale, meaning that the separation is $\Delta\lambda = v_g/c$,

where v_g is grid sampling in radial velocity space. The big requirement for disentangling is imposed on choosing segment limits. One can not pick a segment that has an ending in a spectral line, but both ends must be in the continuum at least far from spectral lines as the Doppler shift moves the spectral lines. Therefore, disentangling spectral regions rich in spectral lines can be difficult. Any spectral lines that enter and leave the selected region for disentangling for a certain phase leads to a Gibbs phenomenon, a wavy pattern of deviations from real component spectrum.

Genetic disentangling is yet another way of obtaining separate component spectra of binary or multiple stellar systems. It has some advantages, and of course disadvantages to other disentangling methods. Spectral disentangling technique (SPD) makes possible separation of individual component spectra in binary or multiple system, and determination of orbital elements in self consistent way. One only needs a time series of binary star spectra. There is no need for template spectra as in technique of cross-correlation, which are the main source of bias in measuring RVs of the components, and hence determination of orbital elements (detail discussion is given in review paper by Hensberge & Pavlovski 2007). In spectral disentangling the role of templates are overtaken by the spectra of components themselves. The advantage of SPD is obvious, beside set of orbital elements, individual spectra of the components are calculated with gain in S/N for the individual component spectra. These separated spectra of the components then can be analysed by all means as single star spectra and a variety of important astrophysical informations can be extracted. A number of different techniques have been implemented to separate individual spectra of components from complex binary (or multiple)

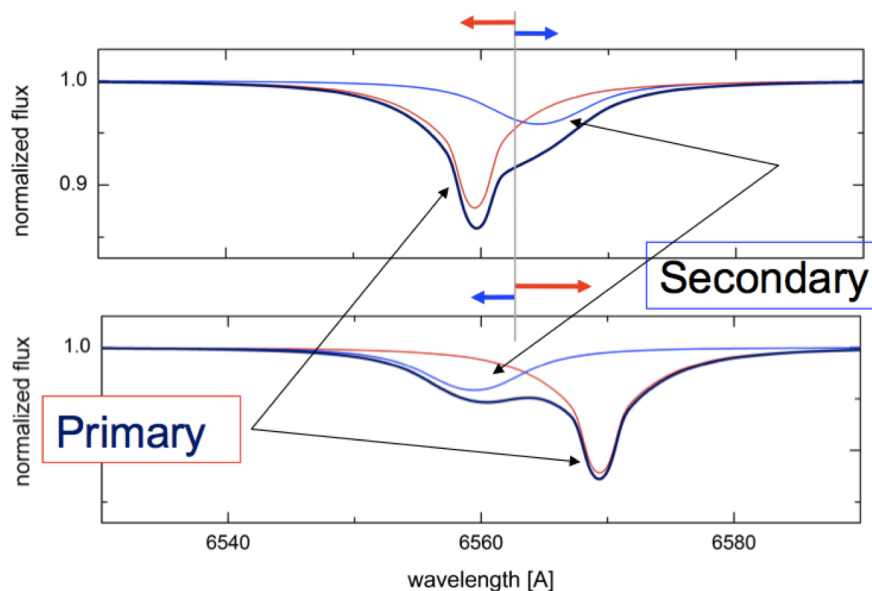


Figure 5.13: Example of a combined spectrum of a binary system (black line) in two different phases, consisting of two individual component spectra (red and blue).

star spectra. They go from simple subtraction technique to very sophisticated numerical methods (see Pavlovski & Hensberge 2010). In Fig. 5.13, we can see an example of model binary system, two component spectra and resulting combined spectrum.

SPD in the formulation of Simon & Sturm (1994) is based on solving the matrix equation $\mathbf{Ax} = \mathbf{y}$, where vector \mathbf{y} contains all observed spectra, and vector \mathbf{x} contains the spectra of the components. Matrix \mathbf{A} has elements (blocks) corresponding to Doppler shifts and light dilution factors. The system is an over-determined system of linear equations (more equations than unknowns) since usually in practice we have more observed spectra than stellar components. Therefore, least squares solution is required in order to minimise the norm of the residuals $r = \|\mathbf{Ax} - \mathbf{y}\|$ (Eq. 5.4). Vector \mathbf{x} are spectra of components a and b and \mathbf{y} the composite spectra and matrix \mathbf{A} is a rectangular matrix the linear transformation which maps \mathbf{x} to \mathbf{y} .

$$\begin{pmatrix} A_{a1} & A_{b1} \\ \vdots & \vdots \\ A_{an} & A_{bn} \end{pmatrix} \times \begin{pmatrix} x_a \\ x_b \end{pmatrix} = \begin{pmatrix} y_a \\ y_b \end{pmatrix} \quad (5.4)$$

On computational side this method is very demanding. Fourier disentangling as invented by Hadrava (1995) overcomes this problem. Method is not limited by a number of input spectra, as well as the length of spectral interval. Only limitation is that both ends of spectral stretch to be disentangled should be exactly in continuum. In GA disentangling, there is no such requirement. Ends of spectra can be selected anywhere, in continuum or deep in a spectral line. Another important advantage is that one can disentangle only a part of spectral line, in case it is too broad, contains blemishes, interstellar bands or nebular emission lines.

The idea of GA disentangling is as follows. We create a generation of entities, each consisting of genes. Each gene represents one intensity point of to-be-separated spectra. For example, if we have a composite spectrum consisting of 1000 points and two components, each entity will have 2000 genes, each representing one point of a component disentangled spectrum. It is obvious that in this particular GA case, number of parameters is extremely large. However, it will be shown that all those points are not completely independent. The procedure starts with generating initial population, choosing random number for each gene of each entity. Then the generation is evaluated as follows. Resulting component spectra should represent real component spectra, with constraint that they should reproduce as good as possible all the input composite spectra for each phase. This means that each primary component spectrum is Doppler shifted for that phase's velocity, as well as secondary component's and then added to produce a composite spectrum. Then χ^2 is calculated compared to real composite spectrum for that phase. Finally, all χ^2 s are summed for all the phases resulting in total χ^2 for an entity. As initial population consists of random points, resulting composite spectrum is also a random distribution, as can be seen on initial, top left picture of Fig. 5.14. Next, entities are procreated from generation

to generation, as described in GA algorithm (Section 5.3). We can see that given time, intensity of each point is slightly varied and slowly converges to reproduce composite spectrum. As expected, due to high number of free parameters, this code runs very slowly. Also, due to this, selected number of entities in a generation is very low in order to have an acceptable calculation time. This results in a very low available gene pool, as well as quick fall into a complete generation degeneracy. Therefore, other ways of enforcing progress are required. First, mutation rate is set to a higher rate. Secondly, every desired number of generations (empirically selected), a significant part of population is replaced with new random entities introducing new genes. All these parameters enable this GA application to reach a solution, and do so in a reasonable time. Reasonable time, for an arbitrary binary star system scenario means runtime from 0.5 to a few days. Introducing higher number of entities would increase this runtime significantly, however it seems that number of generations necessary for reaching a solution remains about the same,

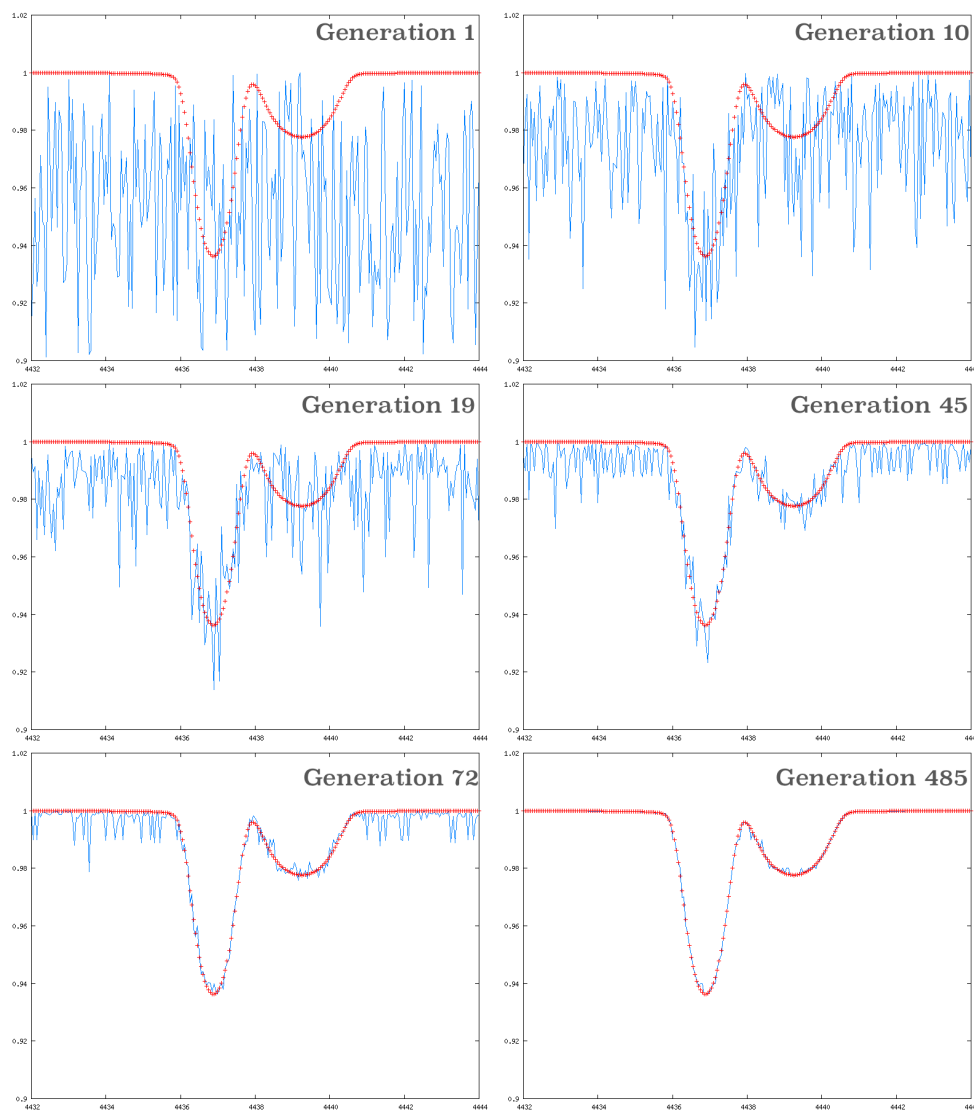


Figure 5.14: Example of GA disentangling process. Time series goes from the upper left picture. In this example, only one composite spectrum (one phase) is shown for clarity.

despite of increased number of entities. One possible explanation is that increase in number of entities from 40 to e.g. 140 does not make a significant difference in number of required generations when we're dealing with 2000 parameters, but does mean a significant difference in computation time. The usual number of generations required, due to quick degeneracy and small gene pool, as well as newly introduced non-optimal random gene values, ranges from hundreds of thousands to millions. However, after that, convergence satisfying composite spectra is actually reached, perhaps contrary to one's intuition and expectations keeping in mind the number of parameters and complexity of problem.

5.5.1 Tests

First test was performed on a synthetic spectrum. Chosen limits were selected well into the part with continuum, the usual requirement for Fourier disentangling. Results can be seen in Fig. 5.15. It is obvious that all the composite spectra are well satisfied, and the initial synthetic spectrum is well-reproduced.

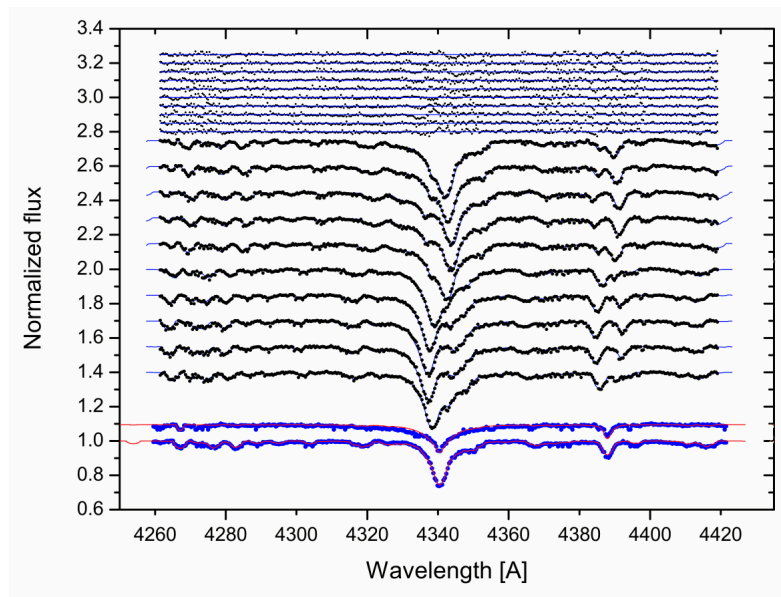


Figure 5.15: Test of GA disentangling on a synthetic spectrum. In the middle part, composite spectra of 10 phases are shown (blue lines) with resulting GA composite spectrum reproductions (black dots). At the bottom, two synthetic spectra to be reproduced are shown with red lines and best GA solution is shown with blue dots. Residuals from composite spectra are shown the upper part.

Further test was performed on a synthetic spectrum, but this time we chose to set disentangling limits deep into spectral line, testing this method's insensitivity for SPD limits selection. Result can be see in Fig. 5.16.

Finally, a test on a real system - V453 Cyg (spectra used were kindly provided by Simon & Sturm 1994) was performed. The advantage of this system is that one spectrum was taken in total eclipse. This makes possible to compare disentangling result with one of the component's

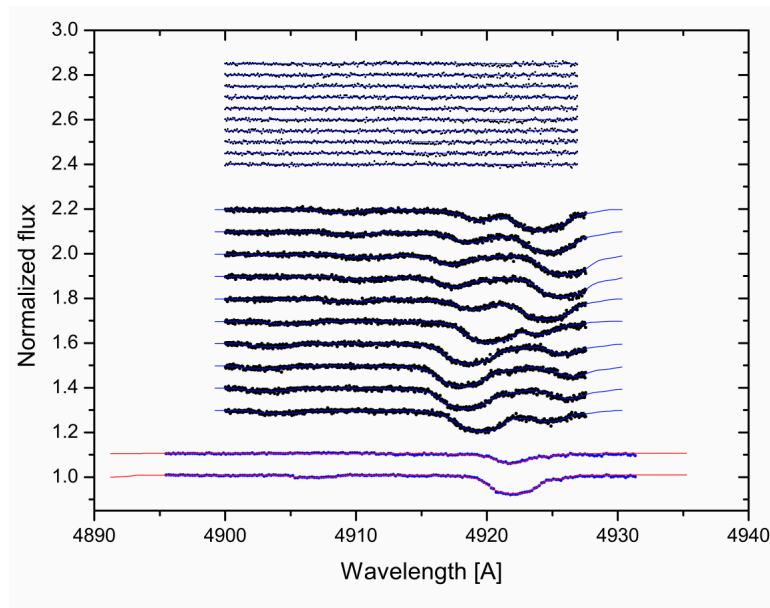


Figure 5.16: Second test of GA disentangling on a synthetic spectrum. This time, limits are chosen to be in a spectral line. Plot is composed as in Fig. 5.15

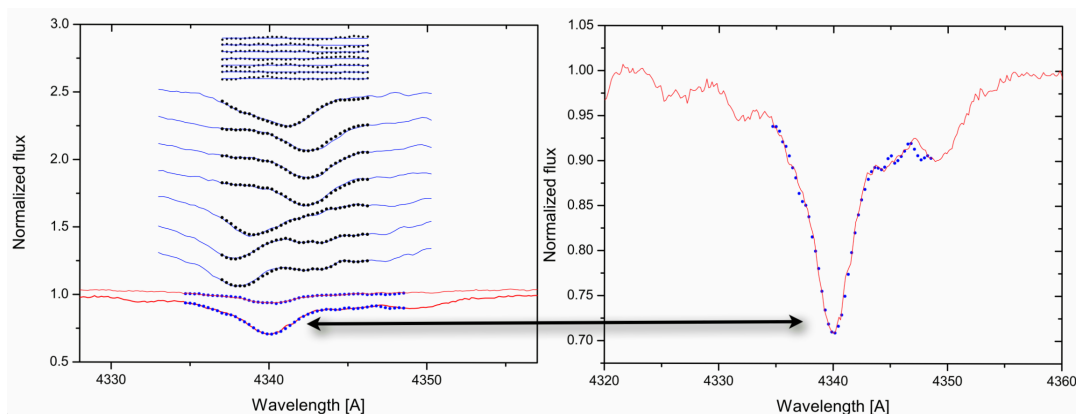


Figure 5.17: Third test was performed on a real system - V453 Cyg, for which one component spectrum can be measured during a total eclipse. In the plot on the left, GA and Fourier SPD results are compared, and in the right plot, GA result is overplotted (blue dots) on top of a real component spectrum (red line) confirming that it reproduces real data.

spectrum. Results can be seen in Fig. 5.17. It is obvious that the disentangling limits are chosen well into spectral line, not affecting the result. Another limit selection can be seen in Fig. 5.18

In conclusion, genetic spectral disentangling is a promising alternative method for SPD, that will be ever more useful with CPU speed increase and can be further improved with parallelization and running on a computer cluster. Currently, code implementation can separate only two components due to CPU power limits, and is planned to be improved in upcoming versions.

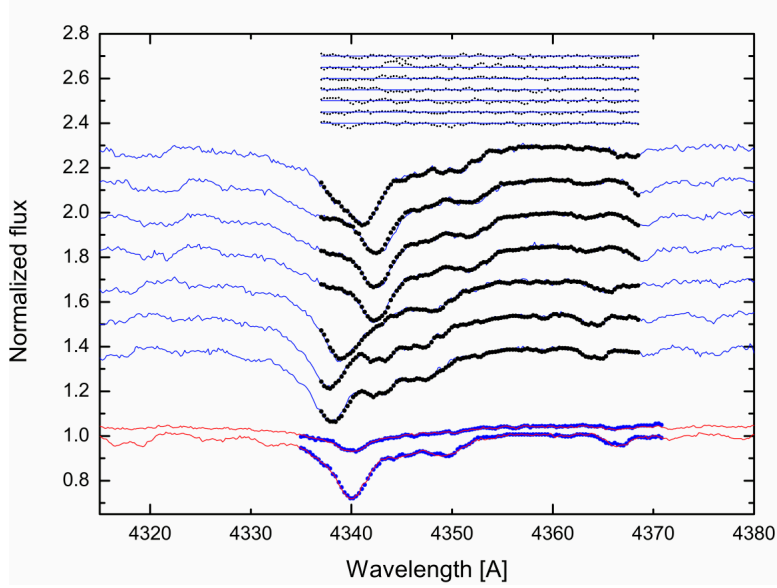


Figure 5.18: Final test on V453 Cyg, with different SPD limits.

5.6 Bootstrap error estimates in SPD

As both FDBINARY and genetic forward disentangling do not provide error estimates, an auxiliary tool is created that implements bootstrapping (Efron 1979) as an error estimate method. The code creates bootstrap samples for the error analysis. It relies on resampling the given data set. For a simple case of N measurements, the mean value is simply

$$\bar{\mu}_0 = \sum_{i=1}^N x_i \quad (5.5)$$

For bootstrap, another sample is selected from the available N samples, selecting them randomly with possibility of omitting some values and repeating other multiple times, therefore we get another mean, for example

$$\begin{aligned} \bar{\mu}_1 &= x_2 + x_1 + x_{10} + x_7 + x_3 + x_4 + x_6 + x_7 + x_5 + x_2 \\ \bar{\mu}_2 &= x_4 + x_3 + \dots \\ &\dots \end{aligned}$$

Then M of those samples are calculated, getting M means μ_i which represents the empirical bootstrap distribution of sample mean. From the empirical distribution, we can derive bootstrap confidence interval.

In case of disentangling, input data set are all available composite spectra of the selected object. Normally, one would prepare input configuration files and spectra to enter disentangling procedure. Bootstrap uses all available spectra to create a bootstrap sample that is provided

to disentangling. However, bootstrap sample does not necessarily use all the available spectra, but selects randomly N spectra from a N items sample. However as they are randomly chosen, some are used more than once and some are therefore omitted. Then disentangling is performed for that particular sample, resulting in disentangled spectra and orbital parameters. For M bootstrap samples chosen in the described manner, we get the same number M different orbital solutions, sets of orbital elements, which are (or should be) all be located in the parameter space in the vicinity to the solution, and the deviations from the solution and their distribution (Gaussian) maps the uncertainty of the statistics of interest and can be used to estimate bias and standard error, as well as other statistics. The number of possible bootstrap samples is not indefinite, it is $N!$, but for any bigger number of spectra, the sample is sufficiently big. If the N is small, the possibility of successful and meaningful disentangling itself is at question.

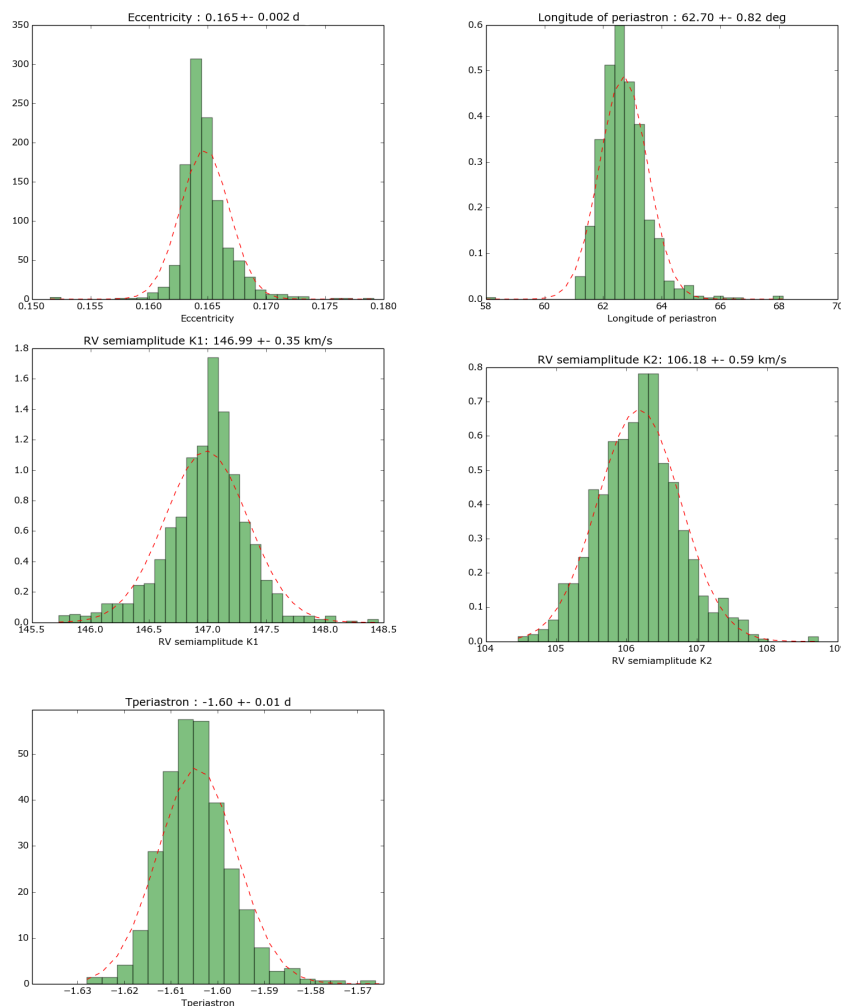


Figure 5.19: Histogram plots of bootstrap parameters for AS Cam

Developed tool was tested on available AS Cam data. The number of calculated samples was 1000, a compromise between sufficient number of data points and computational time. In this case, 1000 samples took 4 days to calculate. Determined results (Pavlovski et al. 2011)

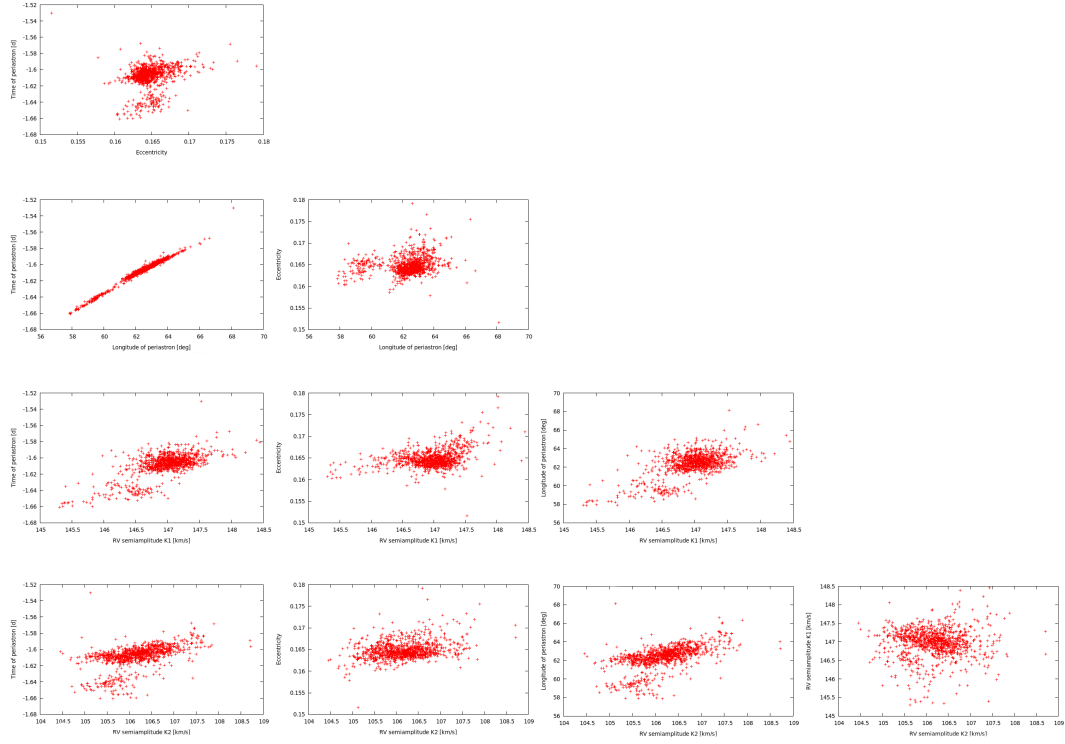


Figure 5.20: Parameter vs. parameter plots of bootstrap parameters for AS Cam

and Bootstrap analysis are listed in Table 5.1. Related histograms are shown in Fig. 5.19 and resulting parameter-parameter plots of bootstrap samples in Fig. 5.20. Given more time to obtain more samples, the resulting histograms would be even better.

5.7 Parallel

Parallel is a GA optimization code for simultaneous spectral disentangling and calculation of astrometric orbit. It utilizes two supplementary codes, FDBINARY⁴ for spectral disentangling

⁴<http://sail.zpf.fer.hr/fdbinary>

Table 5.1: Bootstrap error analysis test on AS Cam. Presented are results (Pavlovski et al. 2011) and determined Bootstrap mean values and errors.

Parameter	Jackknife method	Bootstrap method
P (d)	3.430973 (fixed)	(fixed)
T_p (HJD)	2454399.75 ± 0.06	2454399.83 ± 0.01
e	0.164 ± 0.004	0.165 ± 0.002
ω (deg)	61.5 ± 1.9	62.7 ± 0.8
K_A	106.22 ± 0.75	106.2 ± 0.6
K_B	146.92 ± 0.52	147.0 ± 0.4

(Ilijić et al. 2004) and BINARY⁵ (Gudehus 2001) for astrometry solution from different interferometric measurements.

The complete set of orbital elements of binary and multiple systems can only be determined from complementary observables. The ambiguity in determining of the eccentricity and longitude of periastron for an eccentric binary system from the light curve or RV curves only is a very well known problem. In spectral disentangling the orbital elements are optimised along with simultaneous determination of the individual spectra of components. Therefore, it is very convenient to obtain complementary disentangling and astrometric solution thus removing the degeneracy between some orbital elements.

With the advance in instrumentation more and more binary and multiple systems are spatially and spectroscopically resolved which makes the solution of orbital elements more precise and accurate. A code for simultaneous orbit solution was developed which enables spectral disentangling of time-series of spectra with the constraints from interferometric (astrometric) measurements. It finds the best fitting parameters that simultaneously satisfy spectroscopic and astrometric solution. The code tests input parameters for spectroscopy and astrometry and uses resulting χ^2 's to find the mutual optimal set of orbital parameters.

5.7.1 Tests

Tests were done twofold, on model spectra and on a real system, Θ^2 Tau. Model spectra were synthesised and Doppler shifted using UCLSYN⁶ (Smith 1992, Smalley et al. 2001) code. Corresponding interferometric data was created using EDITBINARY auxiliary code. First test was done with infinite S/N to test the code, and later on, S/N of 200 was simulated. Determined parameters were almost a perfect match, in spite of very wide allowed search space, and could be even improved if genetics was given more entities and generations to work with. Final test was done on real spectroscopic and astrometric data for non-eclipsing binary Θ^2 Tau, member of the Hyades cluster. 117 high precision published spectra were obtained from Elodie spectrograph archive and were carefully renormalized for disentangling, while interferometric 34 data points were obtained by Armstrong et al. (2005). Optimization was performed simultaneously for 5 parameters, of which three are solely interferometric (Ω , i and a) and remaining two are shared between interferometry and spectroscopy (e and ω). A relatively large search space for optimization was allowed which could cause false results due to degeneracy and shallowness in minima space, however results agree very well with published values.

First test was performed on simulated spectra generated by UCLSYN code for parameters given in Table 5.2. RVs and astrometric positions were calculated by EDITBINARY, part of Binary package. RV' s are shown in Fig. 5.21.

Two tests were performed for this simple system. In first, only eccentricity and inclination

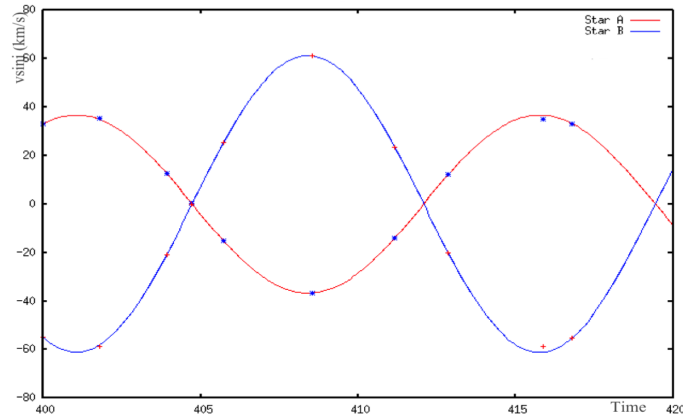
⁵<http://www.astro.gsu.edu/gudehus/binary.html>

⁶<http://www.mmnt.net/db/0/0/ftp.astro.keele.ac.uk/pub/bs/UCLSYN>

Table 5.2: First simulated system properties

Parameter	Units	Star A	Star B
M	M_{\odot}	2.5	1.5
R	R_{\odot}	15	25
T_{eff}	K	11000	6000
$\log g$		4.2	4.0
L	L_{\odot}	40	5
K	kms^{-1}	40	61.6
e		0	
ω	deg	90	

were optimised, eccentricity being common parameter shared by disentangling and interferometry, and inclination optimised only by interferometric solution. Resulting convergence after 60 generations with 160 entities was $e = 0.002$ and $i = 44.8$ deg, which is in excellent agreement with expected values. Phase coverage of synthesised data is shown in Fig. 5.21, convergence of χ^2 can be seen in 5.22 and resulting spectra in Figure 5.23. Final solution was found after 30 generations, and given time it would be even better. Plot of the final orbit can be seen in Fig. 5.24.

**Figure 5.21:** RV curves for primary (red) and secondary (blue) components. Spectra used for disentangling were synthesised for phases marked with dots.

Further test was performed on the same system with all the same data sets, and all the same parameters except for eccentricity which was set to $e = 0.38$ and longitude of periastron which was set to $\omega = 125$ deg. Additionally, an S/N ratio of 100 was added to the input spectra. A series of tests were performed, each time with increasing number of parameters to be determined. Results are show in Table 5.3. This solution is even closer to the expected values as the number of entities in a generation was increased to 200 and 600 generations were calculated. Also, due to a more complex situation, a more dense set (in phase coverage) of input spectra was calculated. Resulting spectra can be seen in Fig. 5.25, and astrometric orbit in Fig. 5.26.

Final test was performed on a real binary system - Θ^2 Tau, for which there are both good

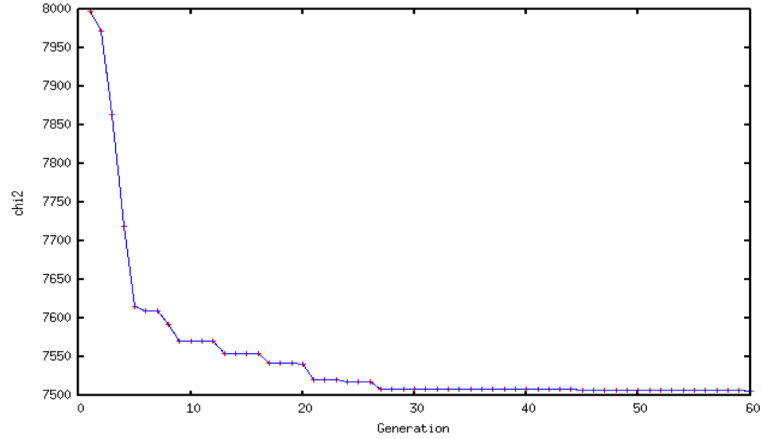


Figure 5.22: Convergence of total χ^2 with the number of generations

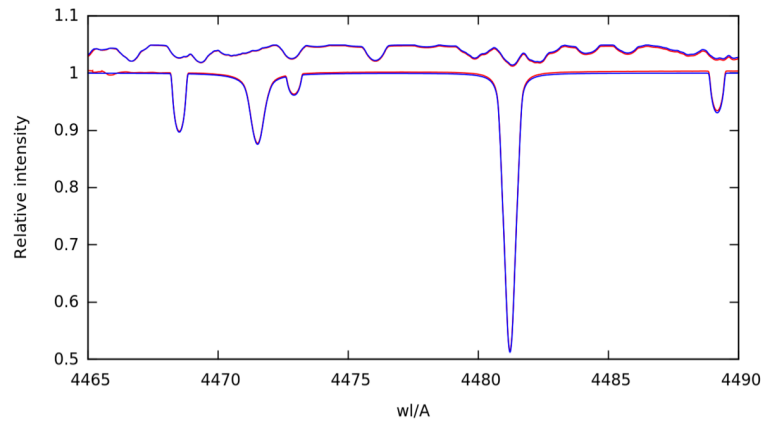


Figure 5.23: Resulting spectra (red line) vs synthetic ones (blue dots). Component A is at relative intensity 1.0, and component B at 1.05 for better clarity

spectroscopic and astrometric measurements for simultaneous orbit optimization. Spectra of Θ^2 Tau were obtained from Elodie spectrograph at OHP, and 34 interferometric measurements were obtained by Armstrong et al. It was done for 5 parameters, three of them solely interferometric (Ω , i and a), and two shared (e and ω). GA was given a relatively large search space for optimization which tests its ability to leave local minima if better solution is found. Final results are given in Table 5.4. Considering all the difficulties of large search space, determined results agree very well with other published values (Torres et al 2011). Final disentangled spectra for those values are shown in Fig. 5.27, and astrometric orbit in Fig. 5.28.

In conclusion, from tests we can conclude that the combination of spectroscopic and astrometric solution is successful and able to give reasonable results for common parameters. However, as the code is based on two independent programs each giving its χ^2 , manual adjustment of both values to at least an order of magnitude difference is required in order to have both contributions with the same weight. This makes use of this program somewhat complicated

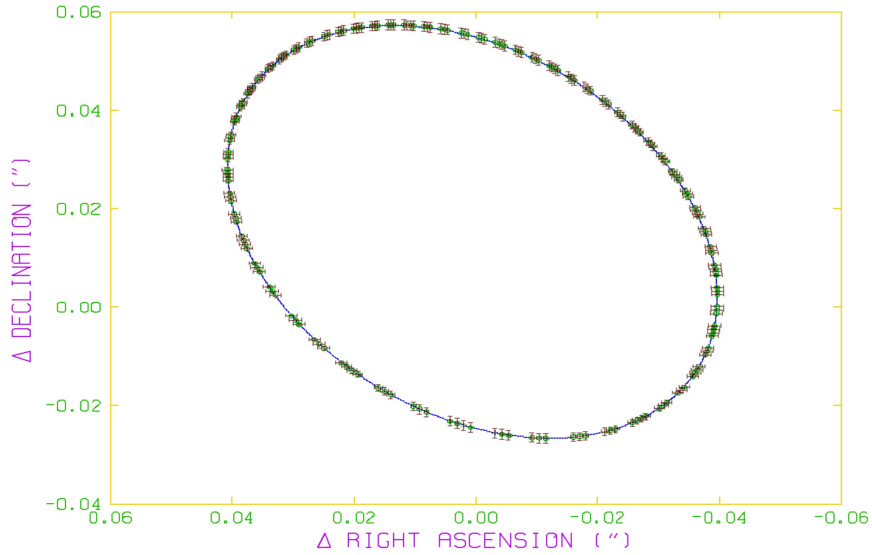


Figure 5.24: Results of interferometric solution for determined parameters. Input data is marked with green circles and calculated solution is plotted as blue line. Error bars are show in red.

Table 5.3: Second simulated system properties with added S/N of 100

Parameter	Units	Expected value	Determined value
e		0.38	0.3799
ω	deg	125	124.99
K_a	km/s	40.0	39.9
Ω	deg	47.4	47.48
i	deg	45	45.10
a	arcsec	0.04949	0.04954

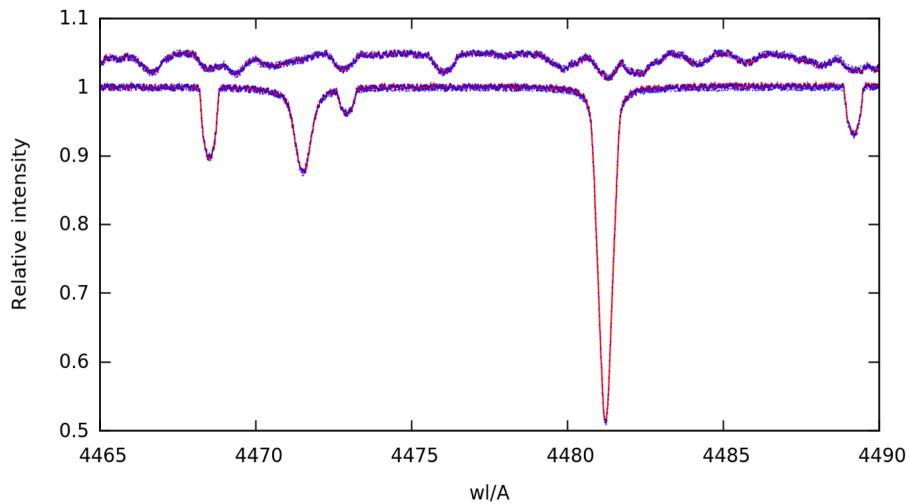


Figure 5.25: Resulting (red) vs synthetic spectra (blue) for both components. Component B is shifted in intensity by 0.05 for better clarity.

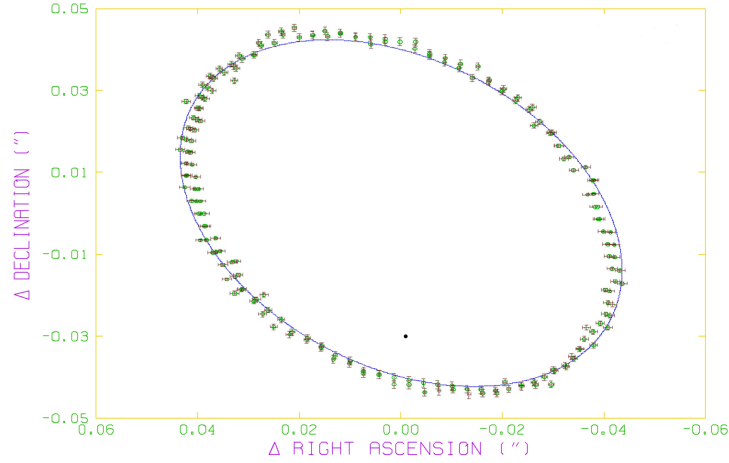


Figure 5.26: Plot of interferometric solution for second system. Interferometric points are shown in green, error bars with red and calculated orbit in blue.

Table 5.4: Results of testing on a real system - Θ^2 Tau

Parameter	Units	Expected value	Search range	GA Result
e		0.737	0.7 - 0.8	0.723
ω	deg	55.40	45 - 60	56.06
Ω	deg	173.73	160 - 180	176.62
i	deg	47.61	30 - 60	47.38
a	arcsec	18.796	16 - 20	18.80

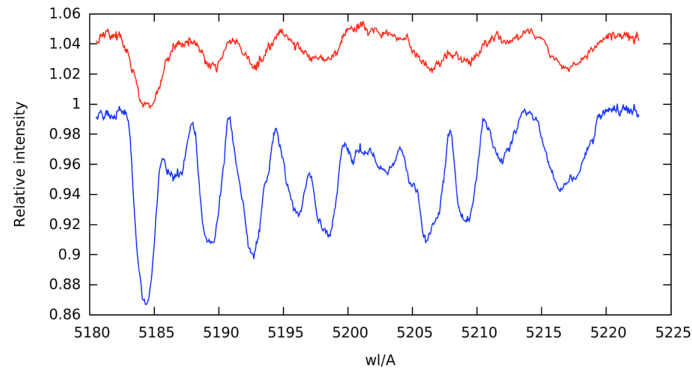


Figure 5.27: Disentangled spectra of Θ^2 Tau. Primary component is plotted in blue, and secondary in red colour. Secondary component is shifted by 0.05 in relative intensity for better clarity.

and requires understanding of the code, GA and system properties. Until we produce the our implementation of code for disentangling and astrometric solution, this combinations proves to be acceptable and reliable.

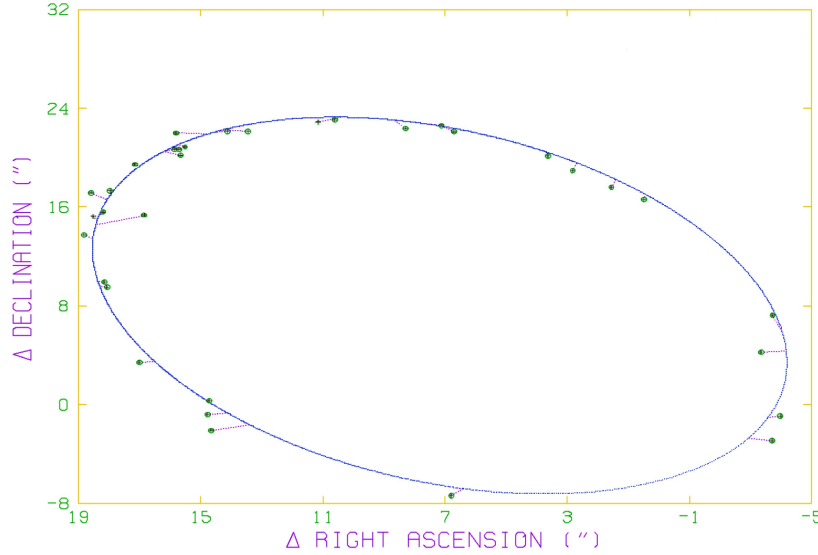


Figure 5.28: Plot of interferometric solution for Θ^2 Tau

5.8 STARFIT

STARFIT is probably the most used program written for this dissertation. It is a GA based optimization program for diagnosing stellar atmosphere parameters. The following astrophysical quantities can be optimized from stellar spectra: effective temperature, T_{eff} , surface gravitational acceleration, $\log g$, light contribution, lf and projected rotational velocity ($v \sin i$). Additionally, two more auxiliary parameters are needed - shift in velocities and continuum adjustment factor. So, in total the six parameters per spectrum can be optimized.

However, perhaps one of its most important features, especially for use in binary star research, is its ability to do simultaneous parameter optimization for two stars. All six parameters for each of the stars can be fitted completely independently or in constrained mode, where combined light contribution of both stars can be fixed to a predetermined total level (being unity for binary system or less if there is an additional component). This constraint introduces a great possibility to determine individual light contribution of a component, i.e. for non-eclipsing binaries. Also, running in non-constrained mode where the two light contributions are independent, results in combined light contributions for e.g. binary system adding up to 1.0 with a high precision. It is another assurance that the spectra are well taken and well reduced and other parameter solutions are valid.

One can also run the code in parallel with completely independent components making possible its use for single stellar systems or simultaneous parameter space search for a single component searching different parts of parameter space where solution could be expected, saving computing time and perhaps even more scarce available research time.

Additional convenience is introduced by so-called patches. One can decide on the general wavelength range to be used, however, it can contain badly reduced or normalised parts

Table 5.5: Currently available grids

No.	T_{eff}/K	$\log g$	wls /Å	Remark
0	15000 - 25000	3.0 - 4.5	968 - 33310278	NLTE
1	25000 - 33000	3.6 - 4.5	968 - 33310278	NLTE
2	5000 - 9750	2.0 - 5.0	3900 - 6000	UCLSyn Z_{sol}
3	27500 - 55000	3.0 - 4.75	3001 - 7490	Hubeny Ostars
4	7000 - 15000	2.5 - 5.0	3900 - 6800	UCLSyn Z_{sol}
5	4000 - 16000	2.5 - 5.0	3900 - 5900	UCLSyn Z_{sol}
6	4000 - 16000	2.5 - 5.0	4200 - 4700	UCLSyn Z_{sol}
7	4000 - 16000	2.5 - 5.0	4700 - 5200	UCLSyn Z_{sol}
8	4000 - 16000	2.5 - 5.0	5200 - 5900	UCLSyn Z_{sol}
9	4000 - 16000	2.5 - 5.0	3900 - 4200	UCLSyn Z_{sol}
10	4000 - 16000	2.5 - 5.0	5900 - 7000	UCLSyn Z_{sol}
11	15000 - 30000	3.0 - 4.75	3201 - 9997	Hubeny Bstars LMC
12	27500 - 40000	3.5 - 4.75	3000 - 7498	Hubeny Ostars LMC
13	15000 - 33000	3.6 - 4.5	968 - 33310278	UCLSyn Z_{sol}
14	11000 - 15000	2.5 - 5.0	3900 - 7000	Gray, H and He only

of spectra, lines that are not present in models or lines that differ in abundance compared to model, all of which introduces errors in optimization. Therefore, one can decide to block some selected spectral stretches, segments that are excluded in optimization for both components independently. Those patch ranges are defined in external ASCII files that are provided to code as input parameters. In output files, ranges excluded for optimization are clearly marked as will be described in section covering resulting files.

As mentioned, input spectrum or the two spectra of a binary system are matched. Database of theoretical spectra are composed from grids of LTE and NLTE synthetic spectra. Additionally, some of the models are further separated into wavelength ranges for faster code startup because of smaller files to be loaded. First the program starts and reads the configuration file to see which models to load and loads the appropriate model. Then, global wavelength range is read in and the models are reinterpolated in that desired range, making sure that they are interpolated in the same wavelength points in which real spectra, the ones to be fitted, are available. Models are loaded for both components. Initial models are loaded for all T_{eff} 's and $\log g$'s for which the model is calculated and are initially not rotationally broadened. Currently available models are listed in Table 5.5.

For each entity in generation and for each component, a model spectrum with desired T_{eff} and $\log g$ is interpolated from initially loaded and reinterpolated model grid. Rotational broadening is then done for that particular interpolated spectrum, as well as lf correction at GA runtime for each entity as the fitness is tested producing each entity's χ^2 .

5.8.1 Errors using Monte Carlo Markow Chain (MCMC)

Monte Carlo Markow Chain (MCMC), described in detail in Gilks et al. (1996), Tegmark (2004) and Collier Cameron et al. (2007) is generally used for multiparameter fitting, especially when the parameter space has high dimensionality. Here it will be used for determining uncertainties. It is used to evaluate a set of parameters s_i for solving our problem, where $i = 1 \dots N$, N is the chosen length of chain. The procedure starts with selecting initial parameters s_1 . For it we calculate a new set, a step, $s_* = s_1 + \Delta p$ where Δs is a chosen step, deviation from initial values, drawn from the jump probability $f(\Delta s)$. s_i is a set of parameters, consisting in example for STARFIT T_{eff} , $\log g$, $v \sin i$ and $l f$. Each of the parameters is varied for the next proposed step as

$$T_i = T_{i-1} + \sigma_T G(O, 1) f \quad (5.6)$$

$$\log g_i = \log g_{i-1} + \sigma_{\log g} G(O, 1) f \quad (5.7)$$

$$v \sin i_i = v \sin i_{i-1} + \sigma_{v \sin i} G(O, 1) f \quad (5.8)$$

$$l f_i = l f_{i-1} + \sigma_{l f} G(O, 1) f \quad (5.9)$$

where $G(0, 1)$ is a random Gaussian deviate with mean of zero and unit standard deviation, the scale factor is adaptive step-size controller and σ is the standard deviation. Initial values of σ are determined otherwise or put as some reasonable value. The problem is then evaluated at newly proposed point p_* . This means that the new step depends only on the previous one:

$$p(\Theta_{i+1} | \{\Theta_i\}) = p(\Theta_{i+1} | \Theta_i) \quad (5.10)$$

where p is the probability, and Θ parameters. Therefore, given the current value, all the past and future values are independent, meaning that MCMC is memoryless. To reach equilibrium, it is also necessary that the transition probability is symmetric

$$p(\Theta_{i+1} | \Theta_i) = p(\Theta_i | \Theta_{i+1}) \quad (5.11)$$

So, if the χ^2 decreases, the step is accepted, and if it increases (meaning we deviate away from the solution), the step is accepted with 20% chance. This enables the procedure to "probe" the parameter space and result in statistics for determining errors. MCMC uses a number of described steps both to find the solution and determine errors. A run consists of starting from a random point and converging from it towards an area in parameter space where the result lies (Burn-in phase) and scanning the solution area afterwards. Multiple runs can and should be performed choosing different starting points to confirm the solution and statistics. We have used this idea and existing STARFIT routines to generate a MCMC package that will generate and evaluate steps and calculate χ^2 for each proposed step, accepted or not. Accepted parameters

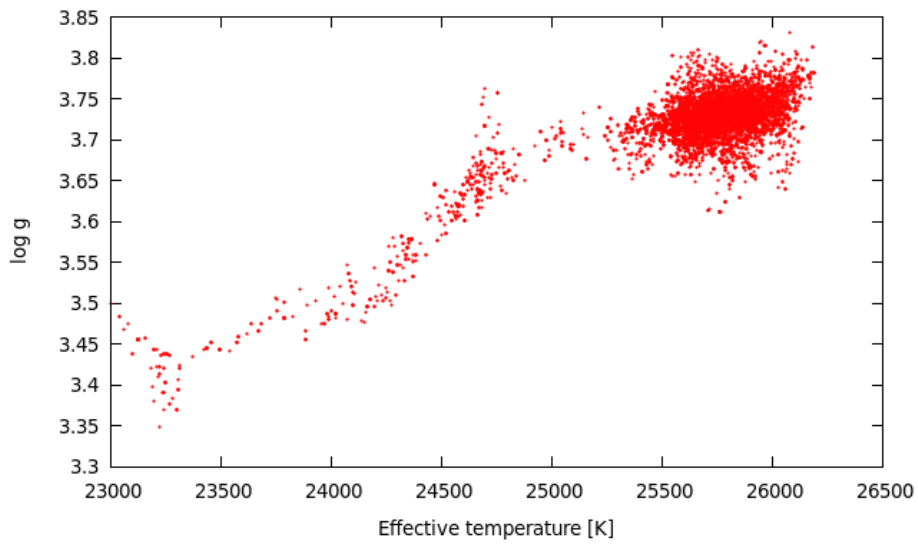


Figure 5.29: MCMC test performed on Spica (α Vir) (Tkatchenko et al. 2014, in prep). In red dots are MCMC test points of Spica for varying T_{eff} and $\log g$. Obvious is the trail representing the search for optimal solution in the parameter space, so called burn-in phase

and χ^2 s are saved for later determination of uncertainties.

Chapter 6

Tracing CNO exposed layers in the Algol-type binary system u Her

6.1 Introduction

The evolution of a star in a binary system is affected by the presence of its companion. Only a limited space is allowed for evolution due to the mutual gravitational pull of the components, and the star which was initially more massive will be the first to reach this limiting radius (i.e. the Roche lobe). At this point a rapid phase of mass transfer happens. Most of the more massive component is accreted by its companion, and an Algol-type binary system is formed. The previously more massive star is now a low-mass subgiant filling its Roche lobe, and its companion is now the hotter and more massive component with the characteristics of a main sequence star. The mass-transfer scenario, first hypothesised by Crawford (1955), is a well-established solution to the Algol paradox (c.f. Hilditch 2001).

This evolutionary process causes many observable effects (changes in orbital period, erratic light variability, distorted radial velocity curves, etc.), but one is particularly important. Up to 80% of the mass of the initially more massive star can be lost, exposing layers which were originally deep within the star and have been altered by thermonuclear fusion during the star's main sequence evolution. Some of the material transferred to the companion is similarly altered. The surface chemical compositions of both stars are therefore a precious diagnostic of the nucleosynthesis processes that occur deep within stars. The abundance pattern in Algol-type binaries could reveal their past, and would be strong evidence for postulated mass transfer between the components (c.f. Sarna & De Greve 1996).

In pioneering studies a general trend has been revealed with an underabundance of carbon and an overabundance of nitrogen relative to solar values (Parthasarathy et al. 1983, Cugier & Hardrop 1988, Cugier 1989, Tomkin et al. 1993). This is in line with expectations for the CNO cycle, which is dominant during the early evolution of a high-mass star (Przybilla et al. 2010). However, for Algol systems, this picture may be altered depending on the initial conditions,

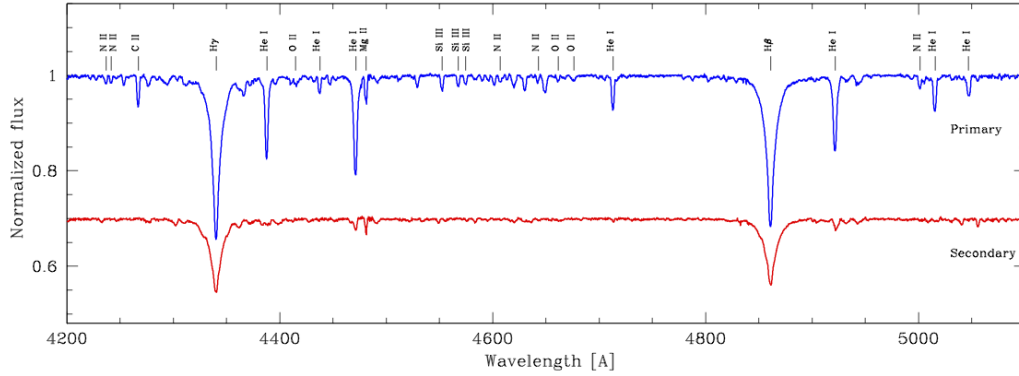


Figure 6.1: The portion of disentangled spectra of both components of the binary system u Her in the region of the Balmer lines $H\gamma$ and $H\beta$. The spectrum of the secondary component was shifted down by 0.3 for clarity. The lines of hydrogen, helium and some metals used in the analysis of the primary component are labelled.

component masses and the mass ratio (Sarna 1992). If a deep convective layer has developed, a standard cosmic abundance pattern is expected instead (Sarna & de Greve 1994).

Early observational studies were hampered by line blending and/or the relative faintness of the secondary star. Therefore a very limited line list was studied. The methods of spectral disentangling (SPD; Simon & Sturm 1994, Hadrava 1995) and Doppler tomography (Bagnuolo & Gies 1991), in conjunction with big advances in high-resolution spectrographs, now make possible separation of the individual spectra of the components. These disentangled spectra in turn make feasible a precise determination of the components' effective temperatures (T_{eff}) and photospheric chemical abundances, as elaborated by Hensberge, Pavlovski & Verschueren (2000) and Pavlovski & Hensberge (2005).

As already stated, the photospheric abundance pattern in mass-transfer binary systems preserves information on their past history. The initial characteristics of these systems vary, and a fine spectroscopic analysis of the abundance patterns can provide additional evidence for proper discrimination between different evolutionary paths and mass loss mechanisms (e.g. what fraction of mass loss is by stellar wind, are mass loss and angular momentum changes conservative or non-conservative, etc). With this aim in mind we initiated an observational project of high-resolution échelle spectroscopy of bright Algol-type (semi-detached) binary systems.

The binary system u Her (68 Her, HD 156633) belongs to a small group of early-type semidetached systems first recognised by Eaton (1978). It differs from normal Algols in several aspects: (i) the total mass is larger; (ii) the components are more similar in T_{eff} ; and (iii) the mass ratio is larger (Hilditch 1984). Their evolutionary paths might also differ from those of normal Algols, which are the product of case B mass transfer: it is supposed that in 'hot Algols' case A mass transfer is involved (Webbink 1976). This was supported by the theoretical calculations of Nelson & Eggleton (2001).

u Her is an eclipsing and double-lined spectroscopic binary with a rich observational history

thanks to its brightness ($V = 4.80$ mag at maximum light). The most recent studies of u Her are those of Hilditch (2005) and Saad & Nouh (2011). Both studies contributed with new spectroscopic observations, but their measured stellar masses differ. Whilst the masses for the components in Saad & Nouh (2011) are similar to earlier determinations (c.f. Kovachev & Seggewiss 1975, Hilditch 1984), Hilditch's (2005) revised values are considerably greater, by $2.0 \pm 0.7 M_{\odot}$ and $0.6 \pm 0.3 M_{\odot}$ for the primary (mass-gaining) and secondary (mass-losing) components, respectively.

The carbon abundance for the primary star has been estimated in two studies, which disagree. First, Cugier (1989) analysed UV spectra obtained with the International Ultraviolet Explorer (IUE) satellite for a group of Algols, and concluded that u Her shows an essentially cosmic abundance of carbon. Contrarily, an analysis of optical spectra by Tomkin, Lambert & Lemke (1993) revealed a carbon deficiency in the primary star with respect to the average carbon abundance of single B-type standard stars.

The primary goal of our study is the determination of the photospheric chemical composition for the primary component in u Her. We have secured a new series of the high-resolution échelle spectra and used SPD to isolate the spectra of the two components. This enables us to determine the atmospheric parameters and the elemental abundances from the entire optical spectral range. As a by-product the two masses were also derived and compared to the previous solutions. In Sect. 6.6 an overview of the evolutionary calculations is presented, and a possible evolutionary path for the components is discussed. The observed [N/C] abundance ratio strengthens our conclusions from the model calculations.

6.2 Spectroscopy

We obtained 43 spectra of u Her in the course of two observing runs (May and August 2008) at the Centro Astronómico Hispano Alemán (CAHA) at Calar Alto, Spain. We used the 2.2 m telescope, FOCES échelle spectrograph (Pfeiffer et al. 1998), and a Loral #11i CCD binned 2×2 to decrease the readout time. Using $150 \mu\text{m}$ slit we obtained a spectral coverage of roughly $3700\text{--}9200 \text{ \AA}$ in each exposure, at a resolving power of $R \approx 40\,000$. Wavelength calibration was performed using thorium-argon exposures, and flat-fields were obtained using a tungsten lamp. The observing conditions were generally good but several exposures suffered from the presence of thin clouds.

The échelle spectra were bias-subtracted, flat-fielded and extracted with the IRAF échelle package routines. Normalisation and merging of the orders was performed with great care, using custom programs, to ensure that these steps did not cause any systematic errors in the resulting spectra.

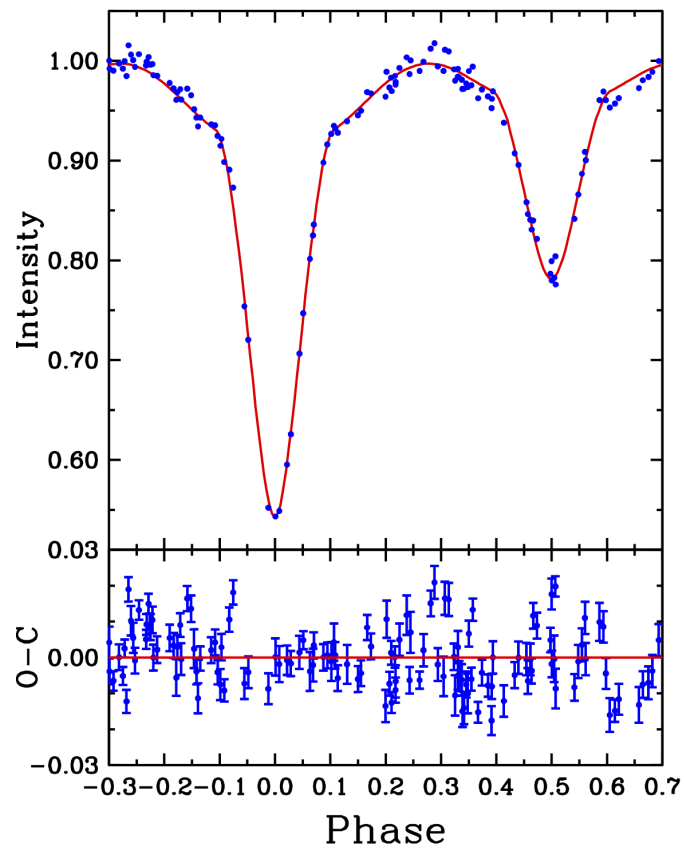


Figure 6.2: Observed phased Hipparcos H_p -band light-curves of u Her with the best-fitting PHOEBE model light curves. The error bars are of similar size to the data points. In the lower panel the residuals have been plotted to show the goodness of the fit.

6.3 Spectroscopic orbit through spectral disentangling

In SPD the individual component spectra are isolated simultaneously with the determination of the optimal set of orbital elements. The reliability of the separated spectra and orbital elements depends on the spectral characteristics of the components and their contribution to the total light of the system.

According to previous photometric solutions for u Her (c.f. Hilditch 2005), the primary star is about 3.3 times brighter than the secondary. Also, their T_{eff} s are quite different. For the primary star ($T_{\text{eff}} \sim 22\,000$ K) the He I lines are expected to be at maximum strength. For the secondary star ($T_{\text{eff}} \sim 12\,500$ K) the He I lines should be quite weak but the Balmer lines stronger than for the primary. Metal lines, quite prominent in the primary, are much weaker in the secondary, both intrinsically and due to the component's relative faintness. Therefore, we concentrate on the Balmer and helium lines, putting more emphasis on the latter.

The Fourier method (Hadrava 1995), is the best choice for disentangling spectra covering an extensive spectral range with high spectral resolution. The code FDBINARY (Ilijć et al. 2004) was used to perform SPD in spectral regions centred on the prominent helium and Balmer lines, covering 50–150 Å in each region (Fig. 6.1). The orbital solution obtained by SPD yields velocity amplitudes of $K_1 = 94.6 \pm 2.3$ km s⁻¹ and $K_2 = 267.4 \pm 3.3$ km s⁻¹, and thus a mass ratio of $q = 0.354 \pm 0.010$, under the assumption of a circular orbit.

In both recent studies of u Her a spectroscopic orbit was determined, but the results are in astonishingly poor agreement for such a bright object. Our values for the two velocity amplitudes are much closer to those found by Saad & Nouh (2011) and in clear disagreement with those from Hilditch (2005). Saad & Nouh (2011) based their solution on red-optical spectra covering H α and the He I 6678 Å line, finding $K_1 = 98$ km s⁻¹ and $K_2 = 265$ km s⁻¹ (no errors are quoted). Hilditch (2005) used grating spectra covering 450 Å of the blue-optical spectral region, finding $K_1 = 102.4 \pm 2.4$ km s⁻¹ and $K_2 = 274.8 \pm 0.9$ km s⁻¹. In particular K_2 is considerably higher than earlier measurements. We suspect that the disagreement between the orbital solutions stems primarily from the different spectral resolution employed; Hilditch's grating spectra have a resolution of 0.46 Å/px, while our échelle spectra have a much higher resolution of 0.02 Å/px. However, the study by Kovachev & Seggewiss (1975) yielded $K_1 = 95.6 \pm 1.4$ km s⁻¹ and $K_2 = 263 \pm 3$ km s⁻¹, from photographic spectra of a similar resolution to Hilditch's digital spectra, and RV measurements by the classical oscilloscopic method.

Discrepancies in the masses calculated from the above spectroscopic solutions are more pronounced for the primary, $M_1 = 7.9$ to $8.8 M_{\odot}$, than for the secondary, $M_2 = 2.8$ to $3.3 M_{\odot}$. In his final solution Hilditch (2005) corrected the two velocity amplitudes for the distorted shape of the stars and their mutual irradiation, resulting in masses of $M_1 = 9.61 \pm 0.14 M_{\odot}$ and $M_2 = 3.48 \pm 0.13 M_{\odot}$. These are, as noted by Hilditch, considerably higher than in earlier solutions for u Her.

6.4 Light curve modelling

Since u Her is a bright object it has a long history of photometric measurements. All published ground-based light curves show night-to-night variations and a scatter of about 0.04 mag (Söderhjelm 1978, Rovithis & Rovithis-Livaniou 1980, van der Veen 1984). In contrast, the *Hipparcos* satellite photometry (H_p passband) covers about 1160 days between 1989 and 1993, and is of good quality (Fig. 6.2). Hilditch (2005) discussed possible explanations for the erratic night-to-night variations and concluded that they are intrinsic to the system. Since no periodicity could be determined he flagged it as a semi-regular variable. He asserted that the time coverage of the *Hipparcos* photometry corresponds to a quiescent period of the system. Therefore, we decided to reanalyse only the H_p photometry.

In a period analysis of ten semi-detached Algol-type binaries, İbanoğlu et al. (2012) found u Her to be the system with the smallest period changes. We used their ephemeris¹ during our analysis; $T_{\text{prim.min.}}(\text{HJD}) = 2447611.5007(15) + 2.05102685(68) \times E$ where the standard deviations in the last significant digits are given in brackets.

Initially we set the primary's T_{eff} to 20 000 K, as derived by Hilditch (2005) using *uvby* photometry and the $[u - b] - T_{\text{eff}}$ calibration from Tomkin et al. (1993) and Napiwotzki et al. (1993). In a second iteration we fixed it at our revised value of $T_{\text{eff}} = 21\,600 \pm 220$ K (Sect. 6.5.1). Our value for the primary T_{eff} agrees within 1σ with Hilditch's, who also noted that there is no significant effect on the light curve solutions when values between 19 000 and 21 500 K are used.

In order to analyse the light curve we deployed the Wilson-Devinney (WD) code implemented into the PHOEBE package by Prša & Zwitter (2005). Our initial unconstrained system parameters immediately converged to a semi-detached configuration. Thus, we used the MODE=5 option for subsequent solutions. Since WD uses Roche geometry, the solutions are sensitive to the mass ratio, which we fixed at the value derived from our orbital solution above, $q = 0.354 \pm 0.010$. Other fixed parameters in our light curve calculations are listed in Table 6.1.

The orbital inclination, secondary-star T_{eff} , primary-star surface potential, phase shift, and fractional primary-star luminosity were put as adjustable parameters. We kept the other parameters as fixed. Iterations were carried out until convergence was achieved. The formal parameter uncertainties calculated by WD's differential correction solver (DC) are not trustworthy, so we implemented a more robust approach to error estimation. We simulated a range of solution sets around our fixed parameter values and calculated the χ^2 value of each. Then we accepted each parameter's 2σ confidence level as our error range, assuming that the χ^2 values follow a Gaussian distribution. In Table 1 we show the final parameter set and their corresponding error estimations. The computed light curve and residuals from observations is shown in Fig. 6.2.

¹In Table 6 of İbanoğlu et al. (2012) there is a typo, confusing u Her with U Her, a common mistake in the literature, see Hilditch (2005).

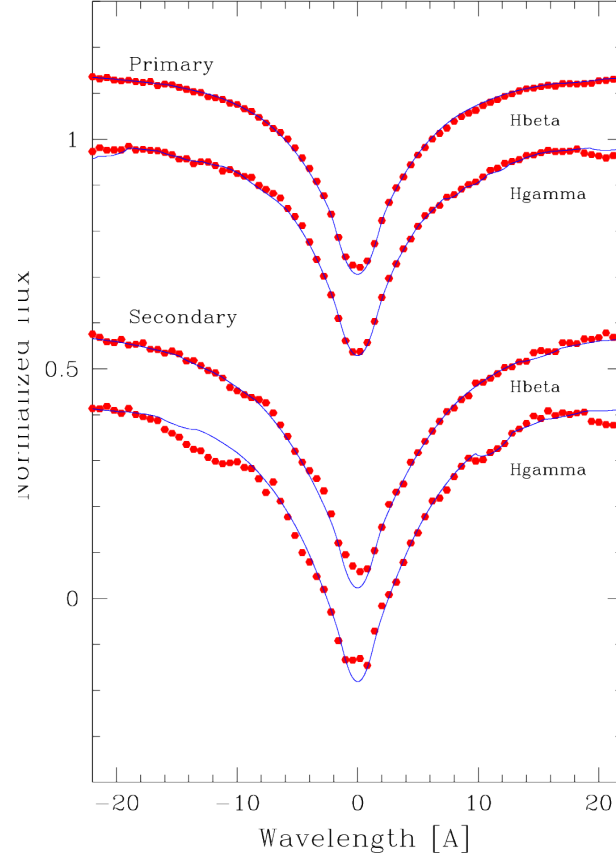


Figure 6.3: The best-fitting synthetic spectra (lines) compared to the renormalised disentangled spectra (filled circles) of the two stars. For both components H β (upper) and H γ (lower) profiles are shown.

Table 6.1: Results from the solution of H_p band light-curves of u Her.

Parameter	Unit	Value
<i>Fixed parameters:</i>		
Orbital period P	d	2.05102685
Primary eclipse time HJD	d	2 447 611.5007
Mass ratio q		0.354
T_{eff} of star A	K	21 600
Primary LD coefficients		0.434, 0.252
Secondary LD coefficient		0.568, 0.318
Gravity darkening		1.0, 1.0
Bolometric albedo		1.0, 1.0
Third light		0.0
<i>Fitted parameters:</i>		
Star A potential		3.437 ± 0.250
Orbital inclination	deg	78.9 ± 0.4
T_{eff} of star B	K	$12\,700 \pm 140$
<i>Derived parameters:</i>		
$L_1/(L_1 + L_2)$		0.739 ± 0.026
Fractional radius of star A		0.330 ± 0.009
Fractional radius of star B		0.285 (fixed)

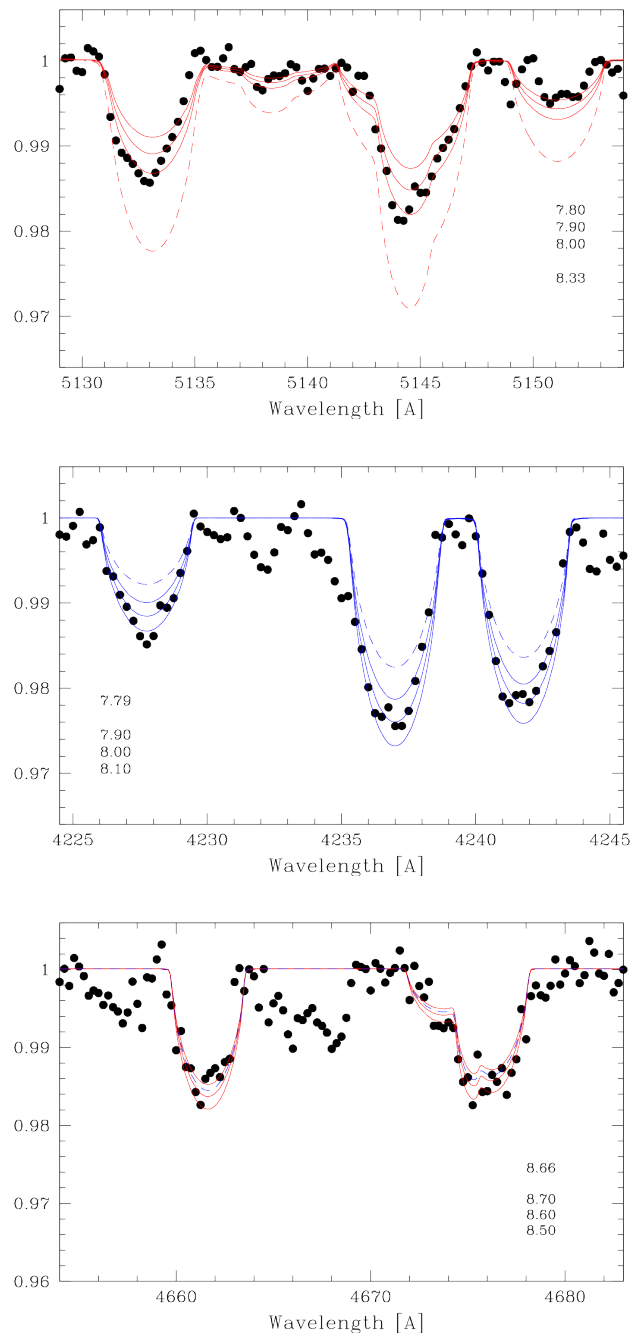


Figure 6.4: Comparison between the renormalised disentangled spectrum of the primary component in u Her (filled circles) and a grid of theoretical spectra computed assuming different abundances. From top to bottom, the panels show selected lines for carbon, nitrogen, and oxygen, respectively. The abundances used for the theoretical spectra are indicated in the labels. Spectra calculated for the ‘present-day cosmic abundances’ for the Galactic OB stars (Nieva & Przybilla 2012) are indicated by dashed lines.

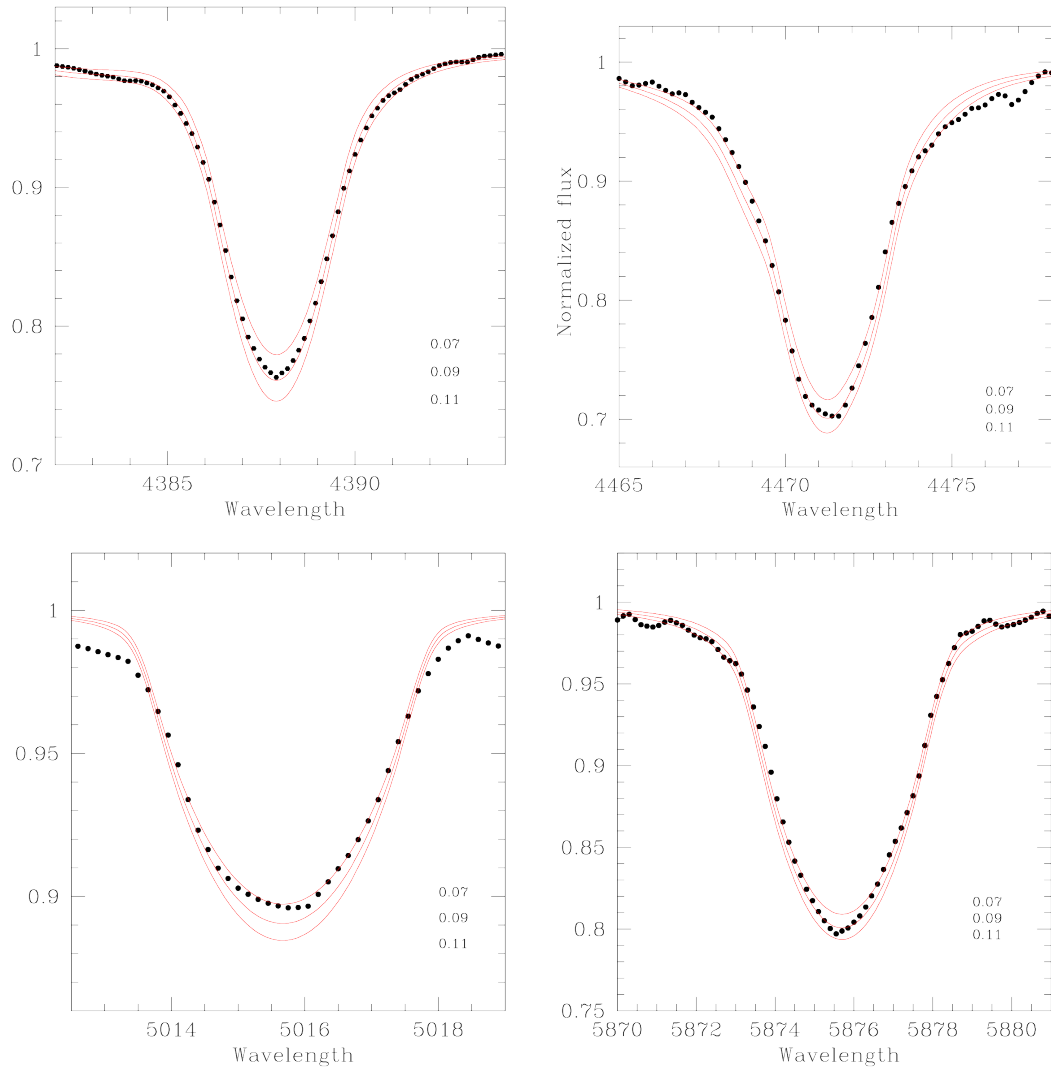


Figure 6.5: The quality of the fits for selected He I lines at 4387.9, 4471.5, 5015.7 and 5876.7 Å to the theoretical spectra (lines). Theoretical spectra were calculated for the stellar parameters listed in Table 2; the assumed helium abundances are indicated in the bottom-right corner of each panel, and are expressed by a fraction of the helium atoms to the total number of atoms in the stellar atmosphere. The renormalised disentangled spectra are represented by filled circles.

6.5 Spectral analysis of both components

6.5.1 The effective temperatures

To construct model atmospheres for the individual components of binary system, we first need to set their T_{eff} s and surface gravities ($\log g$ s). When stars are in binary systems for which accurate masses and radii can be derived from radial velocity and light curves, the resulting $\log g$ measurements have a much higher precision than those determinable from spectroscopic analysis alone. In the case of u Her, and even though our observational data give only a modest accuracy in the masses and radii (about 3–4% and 2–3% respectively) we measured $\log g$ values to about 0.013 dex for the primary and 0.018 dex for the secondary.

The availability of these $\log g$ measurements lifts the degeneracy between T_{eff} and $\log g$ as determined from Balmer line profiles. However, the trade-off is that the disentangled spectra of the components must be renormalised to their intrinsic continuum flux. Pure SPD returns the components' spectra relative to a common continuum level, and the individual spectra of the components are diluted by the factor proportional to their fractional contribution to the total light of the system. If no input spectra were obtained during eclipse (i.e. the component light ratio is the same for all spectra), the zeroth-order mode in the Fourier disentangling is singular, and an ambiguity in the proper renormalisation of the disentangled spectra to their own continuum appears (Pavlovski & Hensberge 2005). Hence, external information on the light ratio is needed (see Pavlovski & Hensberge 2010 and Pavlovski & Southworth 2012). In the case of u Her we can use the light ratio as determined by the light curve solution (Sect. 6.4), $l_1/l_2 = 0.300 \pm 0.003$, where l_1 and l_2 are the fractional contributions of the components to the total light of the system. As H_p is a wide passband centered on 4900 Å, light ratio calculated from light curve solution can both be applied to $H\beta$ and $H\gamma$. $H\alpha$ was not used. Also, calculations for light ratio at $H\gamma$ show that the light ratio does not change.

The optimal fitting of the Balmer lines in the renormalised component spectra to the grid of synthetic spectra was performed with our STARFIT code. This optimisation routine uses a genetic algorithm inspired by the PIKAIA subroutine of Charbonneau (1995). The following parameters for each component can be either optimised or fixed: T_{eff} , $\log g$, light factor, projected rotational velocity ($v \sin i$), velocity shift, and continuum level adjustment. The velocity shift is needed because in SPD there is no absolute wavelength scale, and disentangled spectra are returned on a wavelength scale with an arbitrary zero point. The reason for the continuum level adjustment is the fact that disentangled spectra are shifted according to the line blocking of the individual components, and an additive constant is needed to rectify disentangled spectra to a continuum of unity (Pavlovski & Hensberge 2005). This is the main improvement over our previous code GENFIT (Tamajo et al. 2011). STARFIT can be run in constrained mode (simultaneous fit for both components with the condition that $l_1 + l_2 = 1.0$) or unconstrained mode (see Tamajo et al. 2011). For u Her we ran STARFIT in unconstrained mode with the light ratio fixed to that from the light curve model and the $\log g$ values of the stars fixed. Since the intrinsically

Table 6.2: The absolute dimensions and related quantities determined for u Her. V_{synch} is the calculated synchronous rotational velocity.

Parameter	Unit	Star A	Star B
Semimajor axis	R_{\odot}	14.95 ± 0.17	
Mass	M_{\odot}	7.88 ± 0.26	2.79 ± 0.12
Radius	R_{\odot}	4.93 ± 0.15	4.26 ± 0.06
$\log g$	cm s^{-2}	3.948 ± 0.024	3.625 ± 0.013
T_{eff}	K	$21\,600 \pm 220$	$12\,600 \pm 550$
$\log L$	L_{\odot}	3.68 ± 0.03	2.63 ± 0.08
$V_{\text{eq}} \sin i$	km s^{-1}	124.2 ± 1.8	107.0 ± 2.0
V_{synch}	km s^{-1}	121.7 ± 3.5	105.0 ± 1.5

broad Balmer lines are almost unaffected by the rotational kernel, the $v \sin i$ values for both components were first derived by iteratively fitting helium and metal lines. The T_{eff} s were then determined from the optimal fitting of the $H\gamma$ and $H\beta$ lines. The results for T_{eff} and $v \sin i$ for both components are given in Table 6.2. The quality of the fits is illustrated in Fig. 6.3. The spectroscopically-determined T_{eff} for the secondary component is in perfect agreement with the results from the light curve analysis (c.f. Table 6.1).

6.5.2 Abundances

Theoretical spectra for the atmospheric parameters of the primary and varying microturbulence velocities (v_{turb}) and elemental abundances were calculated in a ‘hybrid’ approach (Nieva & Przybilla 2007, Przybilla et al. 2010), which combines local thermodynamic equilibrium (LTE) atmospheres and non-LTE line-formation calculations. We computed model atmospheres with the ATLAS9 code, which assumes plane-parallel geometry, chemical homogeneity, and hydrostatic, radiative and local thermodynamic equilibrium. Line blanketing was realised by means of opacity distribution functions (ODFs). Solar abundances were adopted in all computations. Non-LTE level populations and model spectra were obtained with the DETAIL and SURFACE codes (Giddings 1981, Butler & Giddings 1985). Non-LTE level populations and synthetic spectra of H, He, C, N, O, Mg, Si and Al were computed using the most recent model atoms (see Table 3 in Nieva & Przybilla 2012). The v_{turb} was determined from the condition of null-correlation between O abundance and equivalent width. Oxygen is used for this purpose since the O lines are the most numerous in spectra for T_{eff} s similar to that of the primary component. Only the lines selected by Simón-Díaz (2010) were used. The v_{turb} determined, $2 \pm 1 \text{ km s}^{-1}$, is in the range of typical values for early-B type stars on the main sequence (c.f. Simón-Díaz 2010, Nieva 2011, Nieva & Simón-Díaz 2011, Nieva & Przybilla 2012). Abundances are estimated by line profile fitting and are listed for all transitions calculated and for lines which are not severely blended. They are given in Table 6.3 for He I and Table 6.4 for all other ions. The mean values of abundances and their uncertainties for all elements studied in the disentangled spectrum of the primary component are given in Table 6.5. The uncertainties in the abundances

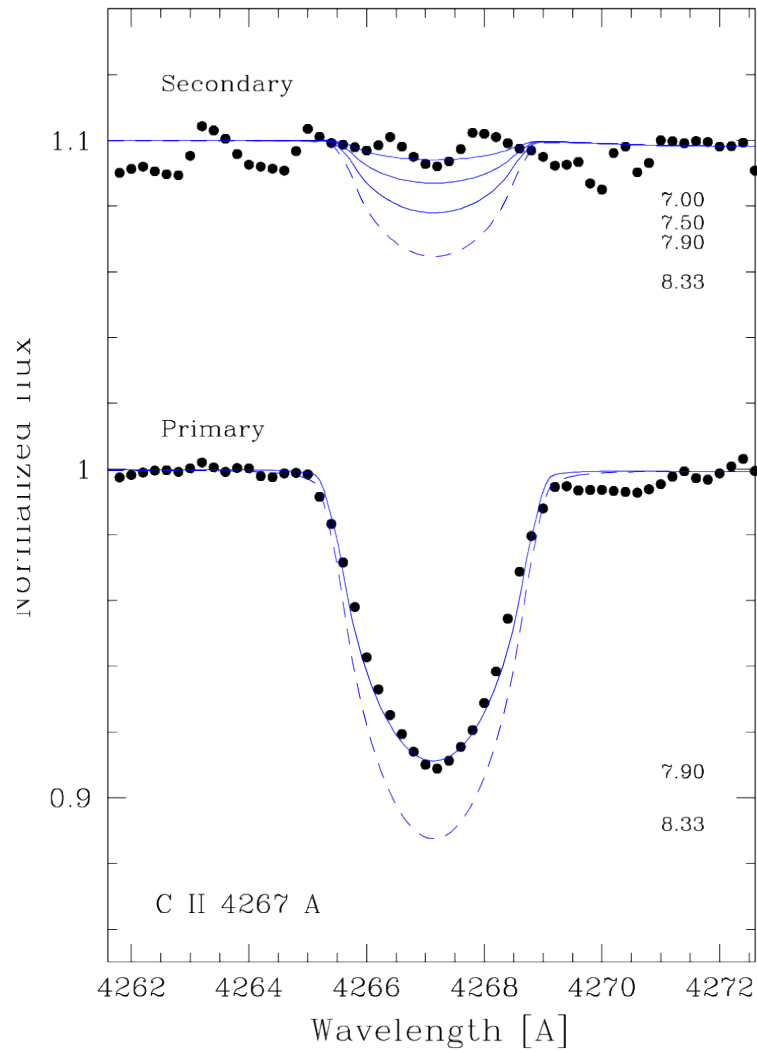


Figure 6.6: Renormalised line profiles of C II 4267 Å for the components of u Her. The secondary spectrum is shifted by +0.1 for clarity. Theoretical spectra calculated for different abundances (indicated in the labels) are shown for comparison. Dashed lines represent the ‘present-day cosmic abundance’ of carbon derived by Nieva & Przybilla (2012). Whilst the carbon abundance is depleted in the primary, it is almost an order of magnitude less in the atmosphere of the secondary component. See Sect. 6.5.2 for details.

Table 6.3: Photospheric helium abundance for the primary component of u Her as derived from different He I spectral lines. The abundances are given as the fractional number of helium atoms to the total number of atoms in the stellar atmosphere ($N(\text{H}) + N(\text{He})$).

Line	$N(\text{He})$	Line	$N(\text{He})$
4387.9	0.087 ± 0.008	5015.7	0.075 ± 0.006
4437.6	0.101 ± 0.010	5047.7	0.091 ± 0.007
4471.5	0.088 ± 0.007	5876.7	0.095 ± 0.002
4713.2	0.078 ± 0.006	6678.1	0.086 ± 0.007
4921.9	0.104 ± 0.005		

are calculated from the scatter in the estimated abundances for different lines, and for 1σ deviations in the T_{eff} and v_{turb} . However, the prevailing uncertainty in abundances comes from the scatter between different lines.

Cugier (1989) determined the carbon abundances in the mass-gaining components of six Algol-type systems, including u Her. He used UV spectra taken with the IUE, and measured the total equivalent widths of the C II multiplets at 1334.5–1335.7 Å and 1323.8–1324.0 Å. He constrained the components' T_{eff} s from the UV flux distribution and van der Veen's (1983) photometric solution, finding $T_{\text{eff},1} = 22\,200 \pm 1500$ K and $T_{\text{eff},2} = 13\,300 \pm 1000$ K. After correction for non-LTE effects he found $\log \epsilon(\text{C}) = 8.62 \pm 0.30$, and concluded that the primary of u Her shows no indication of a change in the carbon abundance, in contrast to other Algols in his sample.

Tomkin et al. (1993) reported high-resolution CCD spectra of the C II 4267 Å line in the same Algol systems that were studied by Cugier (1989) and Cugier & Hardorp (1988). They estimated carbon abundances in the Algol primaries differentially with respect to single B-type stars. They derived the T_{eff} s from Strömgren photometry using the calibration by Napiwotski et al. (1993), finding $T_{1,\text{eff}} = 20\,000$ K. Tomkin et al. obtained a carbon abundance of $[\text{C}/\text{H}] = -0.34$ with respect to the average abundance of the standard stars, $\log \epsilon(\text{C}) = 8.28$.

The carbon abundance determined in this work, $\log \epsilon(\text{C}) = 7.92 \pm 0.02$, is based on the measurements of five lines, and is in almost perfect agreement with the value derived by Tomkin et al. (1993) from a single carbon line. A considerable difference in the adopted T_{eff} s between Tomkin et al. and our values has little influence probably because the temperature dependence of the carbon line strengths is weak in the region from 19 000 to 24 000 K, where C II lines reach their maximum strength. A comparison between the renormalised disentangled spectrum of the primary component and a grid of the theoretical spectra for several C II lines in the 5130–5154 Å region is shown in Fig. 6.4 (upper panel).

The nitrogen abundance is based on measurements of 17 lines, and is firmly determined to be 0.20 ± 0.06 dex above the solar value. In turn, this gives the $[\text{N}/\text{C}]$ abundance ratio 0.05 ± 0.03 dex, considerably different to the 'standard' cosmic (-0.54 ± 0.06 ; Nieva & Przybilla 2012) or solar (-0.61 ± 0.08 ; Asplund et al. 2009) values. Changes in the N/C abundance ratio in the course of mass transfer preserve the imprint of the components' evolutionary history.

Table 6.4: Estimated photospheric abundances for different ions in the atmosphere of the primary component of u Her. Abundances are expressed relative to the abundance of hydrogen, $\log \epsilon(\text{H}) = 12.0$.

Line	$\log \epsilon(\text{X})$	Line	$\log \epsilon(\text{X})$	Line	$\log \epsilon(\text{X})$
C II		O II		Mg II	
4267.00	7.90	4185.46	8.55	4481.13	7.50
5132.95	7.95	4189.79	8.70	5264.22	7.40
5137.26	7.97	4414.88	8.55	5401.54	7.50
5143.40	7.95	4416.97	8.62	Si II	
5151.08	7.85	4590.97	8.70	4128.05	7.55
N II		4596.20	8.68	4130.88	7.40
4227.75	8.00	4609.42	8.50	Si III	
4236.91	7.98	4661.63	8.62	4552.62	7.48
4241.80	7.95	4673.75	8.65	4567.82	7.37
4447.03	8.00	4676.23	8.65	4574.76	7.55
4507.56	8.00	4677.07	8.70	4716.65	7.70
4607.15	8.05	4698.48	8.60	4819.72	7.50
4613.86	8.00	4699.21	8.68	4828.96	7.35
4643.09	7.90	4703.18	8.48	Al III	
4803.27	8.05	4705.35	8.55	4149.92	6.30
4987.38	8.00	5206.64	8.50	4479.97	6.40
4994.36	8.02			4512.54	6.20
5001.47	7.95			4528.94	6.40
5007.31	7.83				
5010.62	7.90				
5045.09	7.93				
5495.65	8.03				
5666.63	7.85				

Table 6.5: Photospheric abundances derived for the primary component of u Her. Abundances are expressed relative to the abundance of hydrogen, $\log \epsilon(\text{H}) = 12.0$. The third column gives the number of lines used. Present-day cosmic abundances from Galactic OB stars (Nieva & Przybilla 2012) are given in the fourth column, and the fifth column lists the solar abundances from Asplund et al. (2009).

El.	$\log \epsilon(\text{X})$	N	$[\text{X}/\text{H}]$	OB stars	Sun
He	10.99 ± 0.05	6	0.02 ± 0.05	10.99 ± 0.01	10.97 ± 0.01
C	7.92 ± 0.02	5	-0.47 ± 0.05	8.33 ± 0.04	8.39 ± 0.05
N	7.97 ± 0.02	17	0.20 ± 0.06	7.79 ± 0.04	7.78 ± 0.06
O	8.61 ± 0.02	16	-0.05 ± 0.05	8.76 ± 0.05	8.66 ± 0.05
Mg	7.47 ± 0.03	3	-0.06 ± 0.09	7.56 ± 0.05	7.53 ± 0.09
Si	7.49 ± 0.04	8	-0.02 ± 0.06	7.50 ± 0.05	7.51 ± 0.04
Al	6.32 ± 0.05	4	-0.05 ± 0.06		6.37 ± 0.04

These findings are discussed in the next section, in the context of the chemical evolution in mass transfer binary systems, and provide a strong argument for case A evolution for the u Her binary system. In Fig. 6.4 (middle panel) the comparison of the three N II lines in the 4225–4245 Å spectral region to a grid of theoretical spectra are shown. Fig. 6.4 (bottom panel) shows a portion of the spectrum containing O II lines.

Helium is a final product of CNO nucleosynthesis and its abundance steadily increases during the components’ evolution. The helium abundance derived for the primary component is in perfect agreement with the value found by Nieva & Przybilla (2012) for OB stars, albeit that the uncertainty in our determination is quite large. The quality of the fits for selected He I lines are shown in Fig. 6.5. The model calculations show an increase in the helium abundance by mass fraction after the phase of mass transfer by a factor of approximately 1.25, which settled again to almost the initial value after thermohaline mixing. The remaining helium enhancement of only 2% could not be detected in our measurements because it is below the level of the uncertainties.

The three metals magnesium, silicon and aluminium have a marginally subsolar abundance, giving on average $[M/H] = -0.04 \pm 0.03$. In our subsequent modelling we therefore assumed a solar composition.

Despite the importance we did not attempt a detailed abundance analysis for the secondary star because its renormalised disentangled spectrum suffers from low S/N. In combination with a high projected rotational velocity, $v \sin i \sim 100 \text{ km s}^{-1}$, this makes the results unreliable. However, we notice a complete absence of the C II 4267 Å line, which should be visible given the T_{eff} of this star. This is illustrated in Fig. 6 in which C II 4267 Å lines for both components are shown. The optimal fit for the primary’s line gives the abundance $\log \epsilon(C) = 7.90$ (c.f. Table 5). It is clear that the primary’s carbon abundance does not hold for the secondary. A rough estimate yields a carbon abundance for the secondary of $\log \epsilon(C) \leq 7.5$, which is more than an order of magnitude lower than the ‘present-day cosmic abundance’ of carbon (Nieva & Przybilla 2012), also indicated in Fig. 6. The calculations to be presented in Sect. 6 give a depletion of carbon by a factor of ~ 7.5 after mass transfer phase has been settled, hence the expected carbon abundance in the atmosphere of the secondary would be $\log \epsilon(C) \sim 7.4$. Non-detection of the secondary’s C II 4267 Å line therefore corroborates the predictions of the theoretical models. However, additional spectra of u Her are needed to enhance the S/N of disentangled spectrum of the secondary star to enable a more definitive conclusion.

6.6 Evolutionary analyses

As discussed above, u Her belongs to a special group of hot Algols, which differ from ordinary systems by having a larger total mass and mass ratio. Eighty years of accumulated photometric data show no evidence for an orbital period change, which suggests that u Her is in a very advanced episode of slow mass transfer (SMT). But this finding is puzzling given its short orbital period, as one would expect a wider orbit at the end of the mass transfer phase. In any

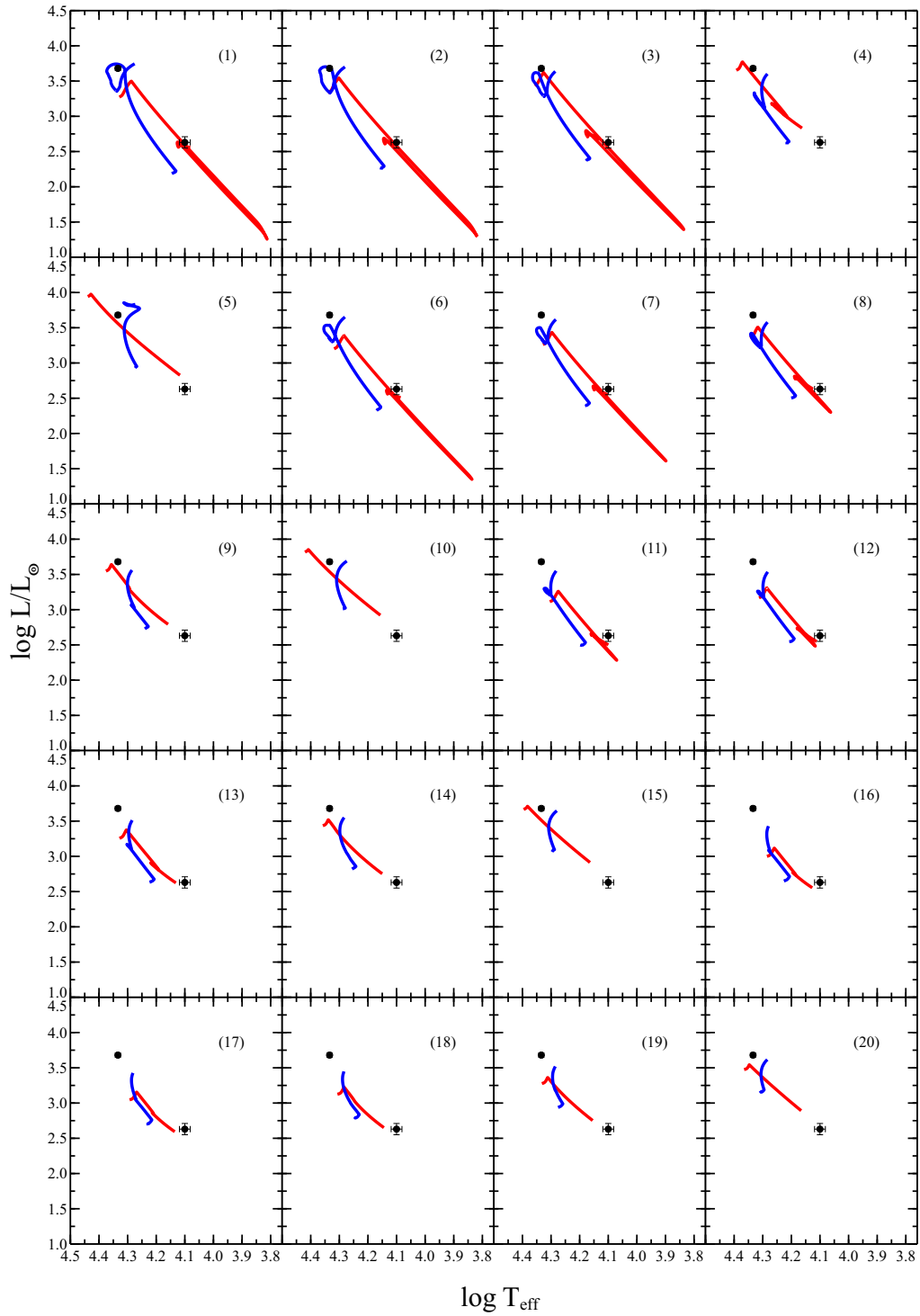


Figure 6.7: The grid of binary evolution tracks on the HR diagram. For given ID from Table 6, we show the evolution of the mass donor (red) and mass gainer (blue), as well as u Her’s observed $\log L/L_{\odot} - \log(T_{\text{eff}}/K)$. Each set of tracks was terminated when the mass gainer fills its Roche lobe at the end of SMT.

binary, whenever mass transfer occurs from the higher mass to the lower mass companion, it is expected that the orbital period decreases until mass ratio reversal. So, tracing back the mass exchange clearly shows that this system may be in a contact configuration during the rapid mass transfer (RMT) phase.

It has been considered that u Her is a product of case A mass transfer (Webbink 1976). The first detailed binary evolution models have been done by Nelson & Eggleton (2001). Based on a grid of 5500 binary tracks with various values of initial primary mass, mass ratio and period, they found that the best fitting initial model to produce a system like u Her has an initial donor-star mass of $M_d^i \sim 6.31 M_\odot$, a mass ratio of $q^i \sim 1.41$ and an orbital period of $P^i \sim 1.32$ d. But they restricted their calculations to a conservative approach and avoided all contact encounters during mass transfer. Their result for u Her can therefore be taken as a maximum initial mass and period pair which cannot get into contact during the RMT phase.

de Mink et al. (2007) extended this study with 20 000 detailed calculations of binary evolutionary tracks using a modified code based on that of Nelson & Eggleton (2001). They modified the Nelson & Eggleton code so that stellar structure equations of both stars are solved simultaneously, which is needed for accurately modelling mass transfer phases. Moreover, they accounted for non-conservative mass loss and short contact phases during RMT, and concentrated on binaries in the Small Magellanic Cloud. de Mink et al. (2007) suggested a new subtype of Algol systems (AR (rapid contact) \rightarrow AN (no contact)) which shows a short-lived contact phase during the thermal response of the mass gainer to the RMT. After this the mass gainer restores its thermal equilibrium and shrinks, then mass transfer proceeds. To evaluate non-conservative evolution they introduced a mass transfer efficiency parameter (β) which is a measure of how much matter is lost relative to that transferred. For the angular momentum evolution, they assumed that all the matter is lost via bi-polar emission from the mass-accreting star hence carries this star's specific angular momentum. One of the hot Algols in their sample (OGLE 09 064498) has a configuration very close to that of u Her: $M_p \sim 8.4 \pm 0.7 M_\odot$, $q \sim 0.323$ and $P \sim 2.64$ d. The best-fitting initial model that they found had $M_d^i \sim 7.10 M_\odot$, $q^i \sim 1.68$ and $P^i \sim 1.34$ d.

Instead of making a large grid of binary tracks which is more suited for a large sample of systems, we specifically prepared initial models for u Her for different initial mass ratios and mass loss rates. Since the uncertainty on angular momentum loss has a big influence on our understanding of binary evolution, there is little value in using a very fine grid in parameter space. We then made some simplifications to reduce the number of initial models to reach plausible results. After determining the initial parameters, we searched for the best fitting models produced by the binary evolution code in this grid.

We first considered four main sets of initial mass ratios q^i : 1.25, 1.50, 1.75 and 2.00. These are typical values to produce Algol-like systems at the end of mass transfer. We did not go beyond $q^i > 2.0$ because mass-gaining stars in these systems are unlikely to regain thermal equilibrium during RMT. To prepare a subset of initial models to take into account non-conservative mass transfer, we adopted the approach of de Mink et al. (2007). The mass transfer

efficiency parameter β is defined as,

$$\beta = 1 - \left| \frac{\dot{M}_g}{\dot{M}_d} \right| \quad 0 \leq \beta \leq 1 \quad (6.1)$$

where g denotes the mass gainer and d the mass donor. From Eq. 6.1, one can easily see that $\beta = 0$ corresponds to conservative evolution. To evaluate angular momentum loss, we used the Hurley et al. (2002) approximation which assumes that mass loss takes the specific angular momentum of the mass-losing star. This is likely true for case A evolution due to the lack of an accretion disc producing bipolar mass loss. Using this approximation and taking logarithmic differentiation of the angular momentum equation for a two-mass system

$$J^2 = \left(G \frac{M_d^2 M_g^2}{M_d + M_g} \right) 4\pi^2 A \quad (6.2)$$

where A is a separation of binary, one can easily derive a relation for the orbital period evolution with the help of Kepler's second law:

$$\frac{P^f}{P^i} = \left(\frac{M_d^i + M_g^i}{M_d^f + M_g^f} \right)^{1/2} \left(\frac{M_g^i}{M_g^i + (1 - \beta)(M_d^i - M_d^f)} \right)^3 \left(\frac{M_g^i + M_d^i}{M_g^i + (1 - \beta)M_d^i + \beta M_d^f} \right)^{-3/2} \left(\frac{M_d^i}{M_d^f} \right)^{3(1-\beta)} \quad (6.3)$$

where superscripts i and f stand for initial and final parameters. The evolution of the total mass of system is adapted from Giuricin & Mardirossian (1981);

$$\frac{M_t^i}{M_t^f} = \frac{(1 + q^i) [1 + q^f(1 - \beta)]}{(1 + q^f) [1 + q^i(1 - \beta)]} \quad (6.4)$$

Using a range of $\beta = [0.0, 0.10, 0.25, 0.50, 0.75]$, i.e. from conservative to highly non-conservative, we created 20 different initial models as candidate progenitors of u Her ($M_g^f \sim 7.9 \pm 0.26$, $q^f \sim 0.35 \pm 0.02$ and $P^f = 2.05$ d). But since Eqs. 6.3 and 6.4 do not consider the properties of the stellar structure under the effect of mass transfer, one has to run detailed evolution codes to compare all of the observed properties of each companion as well as the orbit.

To calculate detailed binary evolution tracks, we used the Cambridge version of the STARS² code which was originally developed by Eggleton (1971, 1972). The most recent updates allow calculation of the evolution of each component simultaneously, the prescription of mass transfer and various physical improvements, and are explained in Stancliffe & Eldridge (2009). Since both observed and candidate initial masses of the components are in the intermediate-mass regime, we fixed the overshooting parameter at $\delta_{os} = 0.12$. We also assumed a solar

²Freely available at <http://www.ast.cam.ac.uk/~stars/>

composition in all of our components at the ZAMS. Each binary evolution track was terminated whenever the mass gainer filled its Roche lobe at the end of SMT, i.e. reverse mass transfer.

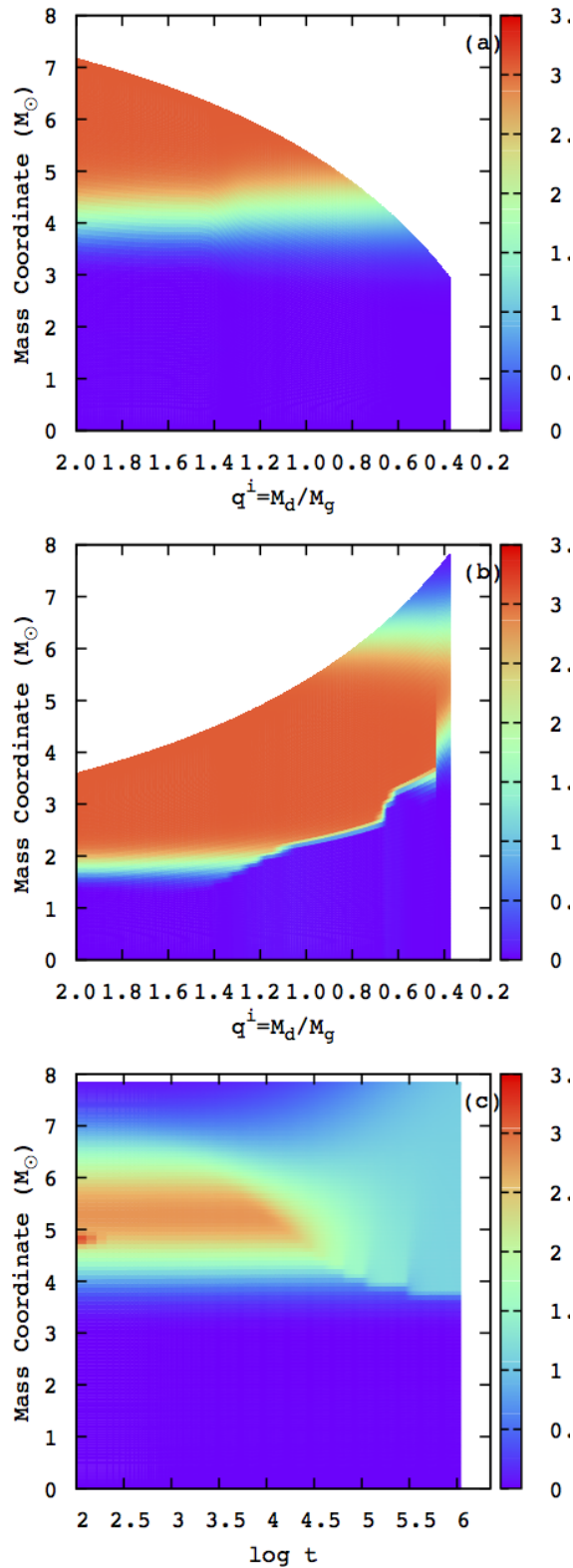


Figure 6.8: The internal C/N ratio changes at mass coordinates for the mass donor (panel 1) and the mass gainer (panel 2) during the mass ratio change as an indicator of rapid mass transfer (RMT), derived from the evolution tracks of the best fitting model – ID(1). The effect of thermohaline convection on the internal profile of mass gainer after slow mass transfer (SMT), $t = 0$ and $q^i < 0.4$ is shown in panel 3.

Table 6.6: The list of initial and final parameters for our binary evolution grid. The first eight columns are input parameters of STARS evolution code runs. The remainder are the best fitting model results for representing the current state of u Her. Run ID(1) is chosen to be the best fitting progenitor system.

ID	q^i	β	M_t^i M_\odot	M_g^i M_\odot	M_d^i M_\odot	P_{lim} d	P^i d	M_d^f M_\odot	M_g^f M_\odot	P^f d	$\log L_d$ L_\odot	$\log T_d$ K	$\log R_d$ R_\odot	$\log L_g$ L_\odot	$\log T_g$ K	$\log R_g$ R_\odot
1	2.00	0.00	10.74	3.58	7.16	0.77	1.35	2.90	7.84	1.93	2.56	4.09	0.63	3.73	4.28	0.83
2	2.00	0.10	11.21	3.74	7.47	0.78	1.29	3.06	7.71	1.77	2.60	4.11	0.62	3.69	4.28	0.80
3	2.00	0.25	12.04	4.01	8.03	0.80	1.20	3.37	7.51	1.59	2.68	4.13	0.60	3.62	4.29	0.76
4	2.00	0.50	14.00	4.67	9.33	0.84	1.06	3.86	7.41	1.54	2.85	4.17	0.61	3.58	4.29	0.74
5	2.00	0.75	17.26	5.75	11.51	0.90	0.91	3.16	7.83	2.34	2.84	4.12	0.70	3.83	4.28	0.88
6	1.75	0.00	10.74	3.91	6.83	0.76	1.19	3.16	7.58	1.65	2.51	4.09	0.60	3.64	4.28	0.77
7	1.75	0.10	11.17	4.06	7.11	0.77	1.15	3.31	7.48	1.55	2.56	4.11	0.59	3.60	4.29	0.75
8	1.75	0.25	11.94	4.34	7.60	0.79	1.10	3.56	7.37	1.48	2.64	4.13	0.59	3.56	4.29	0.73
9	1.75	0.50	13.69	4.98	8.71	0.82	1.00	4.03	7.34	1.45	2.81	4.16	0.60	3.54	4.29	0.72
10	1.75	0.75	16.51	6.01	10.51	0.87	0.90	3.85	7.67	1.89	2.94	4.16	0.67	3.68	4.28	0.81
11	1.50	0.00	10.74	4.30	6.44	0.75	1.07	3.46	7.28	1.42	2.51	4.10	0.57	3.53	4.29	0.72
12	1.50	0.10	11.13	4.45	6.68	0.76	1.05	3.57	7.25	1.39	2.56	4.12	0.57	3.52	4.29	0.71
13	1.50	0.25	11.81	4.72	7.09	0.77	1.01	3.80	7.19	1.35	2.64	4.14	0.57	3.49	4.29	0.70
14	1.50	0.50	13.34	5.33	8.00	0.80	0.96	4.02	7.32	1.44	2.77	4.15	0.60	3.53	4.29	0.72
15	1.50	0.75	15.70	6.28	9.42	0.84	0.91	4.12	7.60	1.71	2.93	4.17	0.65	3.63	4.28	0.77
16	1.25	0.00	10.74	4.77	5.97	0.73	0.98	3.82	6.92	1.22	2.57	4.13	0.54	3.41	4.28	0.66
17	1.25	0.10	11.07	4.92	6.15	0.74	0.97	3.93	6.92	1.22	2.61	4.14	0.55	3.41	4.28	0.66
18	1.25	0.25	11.66	5.18	6.48	0.75	0.96	4.05	7.00	1.25	2.66	4.15	0.56	3.43	4.29	0.67
19	1.25	0.50	12.93	5.74	7.18	0.77	0.95	4.18	7.24	1.36	2.77	4.16	0.59	3.50	4.29	0.70
20	1.25	0.75	14.80	6.58	8.22	0.81	0.95	4.31	7.56	1.58	2.91	4.17	0.64	3.60	4.29	0.75

In Table 6.6, we list the grid of our binary tracks. We show the initial parameters of the systems as well as the best fitting model compared to the observed absolute parameters in Table 6.2. We checked each system's initial period with limiting period, i.e. the smallest period for given binary, via this equation from Nelson & Eggleton (2001):

$$P_{\text{lim}} \approx \frac{0.19M_d^i + 0.47M_d^{i2.33}}{1 + 1.18M_d^{i2}}. \quad (6.5)$$

We also show the binary tracks and observed parameters of the system on the HR diagram in Fig. 6.7. Providing that each system starts with different initial parameters, the thermal responses of each component determine the length of the RMT and SMT phase. Most of the systems in Table 6.6 cannot accrete enough mass to reach the observed masses of the components of u Her before reverse mass transfer. Based on χ^2 minimisation and visual inspection, the best fitting model belongs to a group of conservative and high initial mass ratio systems. This was also the case for OGLE 09 064498 as discussed above. We also noticed a short-term contact phase, as also discussed by de Mink et al. (2007), in high initial mass ratio systems for the case of highly efficient mass transfer $q^i \geq 1.75$ and $\beta \leq 0.25$.

Finding the best initial model parameters allowed us to trace the chemical evolution of both components during mass transfer. In Fig. 6.8a,b we show the change in internal profile of the ratio C/N from the centre to the surface of each component. Due to the very different timescales of the RMT and SMT phases, we plot this change versus the mass ratio instead of time. One can easily recognize the abrupt internal change in the mass gainer's profile which corresponds to the transition from RMT to SMT. From Fig. 6.8a, we find that the mass donor lost its mass up to the depth at which the CNO cycle reduced the C/N ratio from the cosmic (~ 3.2) to the equilibrium (~ 0.1) value. This nucleosynthetically processed material was then accreted on the surface of mass gainer. The accreted material had a higher mean molecular weight than that from the surface of the mass gainer. In such a case, one may expect thermohaline convection to mix this material and alter the surface composition. As shown by Stancliffe & Eldridge (2009), the effect of thermohaline mixing on the surface is negligible during RMT. We therefore ran all of our tracks without thermohaline mixing to find the lower limit of the C/N ratio on the surface. We then applied thermohaline mixing to the model of the mass gainer to trace the change of chemical composition on its surface. As the thermohaline condition is not satisfied, we ignored the mass donor.

In Fig. 6.8c, we show the effect of thermohaline mixing on the whole internal profile of the star. Due to the material originating from different layers of mass donor, the outer layers of the stars have a variable composition profile. We find that the thermohaline mixing alters the surface composition of the stars on relatively short timescale ($\sim 10^5$ yr). Thus we expect the surface C/N ratio of the gainer to be between non-mixed (~ 0.1) to mixed (~ 1), based on the model results. This result is in good agreement with our observed ratio of C/N = 0.89.

We believe that determining the composition of the mass donor would be an important

opportunity to constrain the initial evolutionary parameters. Such a situation would allow us to build a fine grid of binary tracks to compare results with observations as well as our understanding of the processes involved in binary evolution such as mass loss mechanisms and thermohaline mixing. Even though we could not determine the surface composition of the mass donor, the lack of a prominent C II 4267 Å line compared to single stars of the same T_{eff} is a strong indication of decreased carbon abundance on the surface as a result of case A mass transfer. This is because, in a wider orbit, the mass donor may only lose the upper layers without reaching CNO processed regions. So far our evolutionary calculation shows that u Her could start its evolution with $M_d^i \sim 7.16 M_{\odot}$, $q^i \sim 2.00$ and $P^i \sim 1.35$ d.

Chapter 7

Spectroscopically resolving the Algol triple system

7.1 Introduction

In his opening speech to IAU Colloquium 107 (“Algols”), Batten (1989) was tempted to define an Algol system simply as ‘a binary in which the less massive component fills its Roche lobe and the other, which does not, is not degenerate’. The resulting evolutionary paradox can be solved by postulating an episode of mass transfer from what was initially the more massive component to its then less massive, and consequently less evolved, companion (Crawford 1955). This first, rapid, phase of matter exchange between the components eventually leads to an Algol-type system. Numerical calculations of the evolution of stars in binary systems have proved this hypothesis to be very plausible (c.f. Paczyński 1971).

Direct comparison of the observed properties of Algol systems to evolutionary model calculations are sparse, because only a few Algols have reliable measurements of their physical properties (Maxted & Hilditch 1996), and because models are unavailable for the relevant parameters. Model calculations for Algol with both conservative and non-conservative binary evolution have only been calculated by Sarna (1993).

Changes in the chemical composition of the surface layers of stars which have experienced mass transfer are a feature of theoretical predictions. Layers that were once deep inside the star become exposed after mass transfer. This makes it possible to observationally probe CNO nucleosynthesis processes in stellar cores, and the efficiency of different mixing processes in stellar interiors. In that sense CNO abundances can serve as a sensitive probe of stellar structure and evolution.

Carbon depletions have been detected in Algol and Algol-type systems (Parthasarathy, Lambert & Tomkin 1979, 1983; Cugier & Hardorp 1988; Cugier 1989, Tomkin et al. 1993, Ibañoğlu et al. 2012). However, comparisons to theoretical models were rather scarce since detailed evolutionary calculations were done for only a few Algol-type systems, and were limited to tracing carbon evolution (De Greve & Cugier 1989, Sarna 1992, 1993, De Greve 1993). From the

observational side, Algol systems can be rather difficult. The secondary stars are Roche-lobe filling subgiants, which are usually intrinsically faint but still bright enough to contaminate the spectrum of the primary stars. Many contain third components, as in Algol itself, which further complicates spectroscopic analysis. Therefore, we initiated a new observational project of échelle high-resolution spectroscopy of Algols to which we could apply the powerful technique of spectral disentangling (hereafter SPD) for the separation of the individual spectra of the component stars. This puts spectroscopic analysis on firmer ground, and allows study of the entire optical spectra of both or all components. For proper comparison with the theoretical evolutionary models we extended calculations to follow-up other diagnostic species, first of all nitrogen abundance which is very sensitive to CNO nucleosynthesis processes. Theoretical models of binary star evolution have also been extended to non-conservative cases. We presented our methodology in detail in a recent study of the hot Algol u Her (Kolbas et al. 2014). Only a systematic study of a large sample of mass transferring binaries of Algol type can reveal all the different evolutionary paths which these complex binary systems encounter.

The chemical composition was determined from a whole optical spectrum for only a few Algol-type binaries. Beside u Her (Kolbas et al. 2014), abundance patterns have been derived for RZ Cas (Narusawa et al. 2006, Tkachenko et al. 2009), TW Dra (Tkachenko et al. 2010), TX UMa (Glazunova et al. 2011), and AS Eri (Narusawa 2013). All these Algols except u Her have an oscillating primary component.

In this work we firstly summarise the rich observational history of Algol, and highlight some recent observational results. In Sect. 7.3 we present new échelle spectra of Algol. Sect. 7.4 covers the SPD of the spectra and the determination of new orbital elements for both inner and outer orbits. The analysis of the disentangled spectra for all three components is presented in Sect. 7.5, including detailed calculations of abundances for Algol A and metallicity for Algol C. The results are discussed in the context of mass transfer between Algol A and B in Sect. 7.6.

7.2 Algol in a nutshell

Algol (β Persei, HD 19356) is a hierarchical triple star system (Frieboes-Conde et al. 1970, Söderhjelm 1980). It is extremely bright ($V = 2.12$ mag) and there is a long observational history of its periodic variability. There is evidence that Algol's periodicity was recorded by the ancient Egyptians three millennia ago, in the Cairo Calendar (Jetsu et al. 2013). The first well-documented discovery of the 2.867 day periodicity and an explanation in terms of stellar eclipses is due to naked-eye observations by Goodricke (1783). Thanks to its brightness, Algol also has a long history of observations with many techniques and at many wavelengths. An outstanding and exhaustive account of these studies was given by Wecht (2006).

The inner pair consists of a late-B type star in orbit with an early-K type subgiant which fills its Roche lobe. This close system exhibits partial eclipses, and is the prototype of the Algol class of eclipsing binaries. A tertiary component occupies a 680 d orbit around the inner pair;

it has been variously classified as a late-A type, an early-F type star, and an Am star. This description of Algol emerged from decades of primarily spectroscopic and photometric studies (c.f. Friebos-Conde et al. 1970, Hill et al. 1971, Söderhjelm 1980, Richards et al. 1988). The main difficulty of these early studies was the intrinsic faintness of the cool subgiant, which is exacerbated by dilution with the light of component C. Algol C is brighter than Algol B, but its contribution was very difficult to quantify (Richards et al. 1988). A real breakthrough came with its eventual spectroscopic detection (Glusheva & Esipov 1967) in the infrared, and then radial velocity (RV) measurements which eventually led to the determination of the dynamical masses for the components (Tomkin & Lambert 1978).

Other observational techniques were helpful in further constraining the orbital and physical characteristics of Algol. Rudy & Kemp (1978) found phase-locked polarisation and independently determined the inclination of the eclipsing binary. Subsequently Kemp et al. (1983) discovered eclipse polarisation, or the Chandrasekhar effect, further evaluated by Wilson & Liou (1993). The problem of the determination of the mutual orientations of the orbits in the Algol system has remained open (Kemp et al. 1981).

Since the successful detection of Algol C with speckle interferometry (Labeyrie et al. 1974), Algol has often been a target for interferometric measurements, which eventually settled the issue of the true orientation of both orbits. Csizmadia et al. (2009) spatially resolved the inner pair with long baseline interferometry in combination with very long baseline interferometry (VLBI) radio observations. They found the inner orbit to be prograde, in disagreement with the retrograde movement found by Lestrade et al. (1993) from radio observations. This long-term controversy was solved by Zavala et al. (2010), who simultaneously resolved all three stellar components in the optical achieving the then highest precision in angular measurements. The outer orbit was shown to be prograde and the inner orbit retrograde. Subsequently VLBA radio (Peterson et al. 2010, 2011) and CHARA *H*-band measurements (Baron et al. 2012) confirmed these orientations for both orbits. The most recent highlight of the interferometric studies is an unambiguous spatial resolution of the three stars in the Algol system with angular resolution <0.5 mas (Baron et al. 2012). This made possible the determination of the orbital and physical characteristics of the components (angular sizes and mass ratios) independently from previous studies. Baron et al. (2012) also determined the mutual inclination of the orbits to be much closer to perpendicularity than previously established. The distortion of the Roche-lobe-filling component B is clearly seen in the reconstructed image.

Still another highlight of the modern astrophysical research of Algol is the first three-dimensional (3D) reconstruction of this system (Richards et al. 2012). These 3D tomograms have revealed evidence of the mass transfer process not previously detected as loop prominences and coronal mass ejections. Early predictions of the superhump phenomenon in Algol, i.e. the gas between the stars in close pair being threaded with a magnetic field even though the hot mass-gaining star is not known to have a magnetic field (Retter et al. 2005) has been supported by this new technique. Algol B is a late-type magnetically active subgiant found to

be a strong radio and X-ray source (Wade & Hjellming 1972, White et al. 1986, Stern et al. 1992, 1995), and dominates in these parts of the Algol spectrum. In particular, X-ray studies made possible an abundance determination in the corona of Algol B (Drake 2003) as well both the X-ray-bright star Algol B and the X-ray-faint star Algol A (Yang et al. 2011).

7.3 High-resolution spectroscopy

Our observational programme of high-resolution and high signal-to-noise (S/N) spectroscopy of Algol was initiated with two observing runs in 2006 and 2007 at the 2.5-m Nordic Optical Telescope (NOT) at La Palma, Spain. We obtained 85 spectra of Algol using the Fibre-fed Echelle Spectrograph (FIES; Telting et al. 2014). FIES is housed in a separate climate-controlled building and has a high thermal and mechanical stability. The wavelength scale was established from thorium-argon exposures taken regularly throughout the observing nights. We used fibre 4 in bundle B, giving complete spectral coverage in the interval 3640–7360 Å at a reciprocal dispersion ranging from 0.023 Å px⁻¹ in the blue to 0.045 Å px⁻¹ in the red. The resolution of the instrument is roughly 3.5 px, giving a resolving power of 48 000. An exposure time of 15 s was used for all spectra, resulting in continuum S/N ratios in the region of 200–500 in the B and V bands.

In order to cover the long-period outer orbit of Algol, spectroscopic observations were taken from 2009 to 2010 at the Bohyunsan Optical Astronomy Observatory (BOAO), South Korea. A set of 36 spectra were secured with Bohyunsan Optical Échelle Spectrograph (BOES) mounted on the 1.8-m telescope (Kim et al. 2007). BOES has multiple spectral resolving powers up to 80 000, covering the large wavelength range 3600 to 10 200 Å. A thorium-argon lamp was used for wavelength calibration and S/N ratios of 300–550 were achieved.

The spectra were bias-subtracted, flat-fielded and extracted with the IRAF échelle package routines. Normalisation and merging of the orders was performed with great care, using custom programs, to ensure that these steps did not cause any systematic errors in the resulting spectra.

7.4 Orbits and masses through spectral disentangling

The method of SPD enables determination of the orbital elements of binary and multiple systems, along with the simultaneous separation of the individual spectra of the components, in a self-consistent way (Simon & Sturm 1994). In that sense it is a generalisation of the Doppler tomography method of Bagnuolo & Gies (1991) which was the first successful reconstruction of individual spectra for binary stars but which relies on predetermined RVs of the components. In SPD only a time series of observed spectra are needed, with roughly uniform coverage of the RV motion of the stars (c.f. Hensberge et al. 2008). Optimisation for the RVs is bypassed in favour of directly fitting for the orbital elements, as first implemented by Simon & Sturm

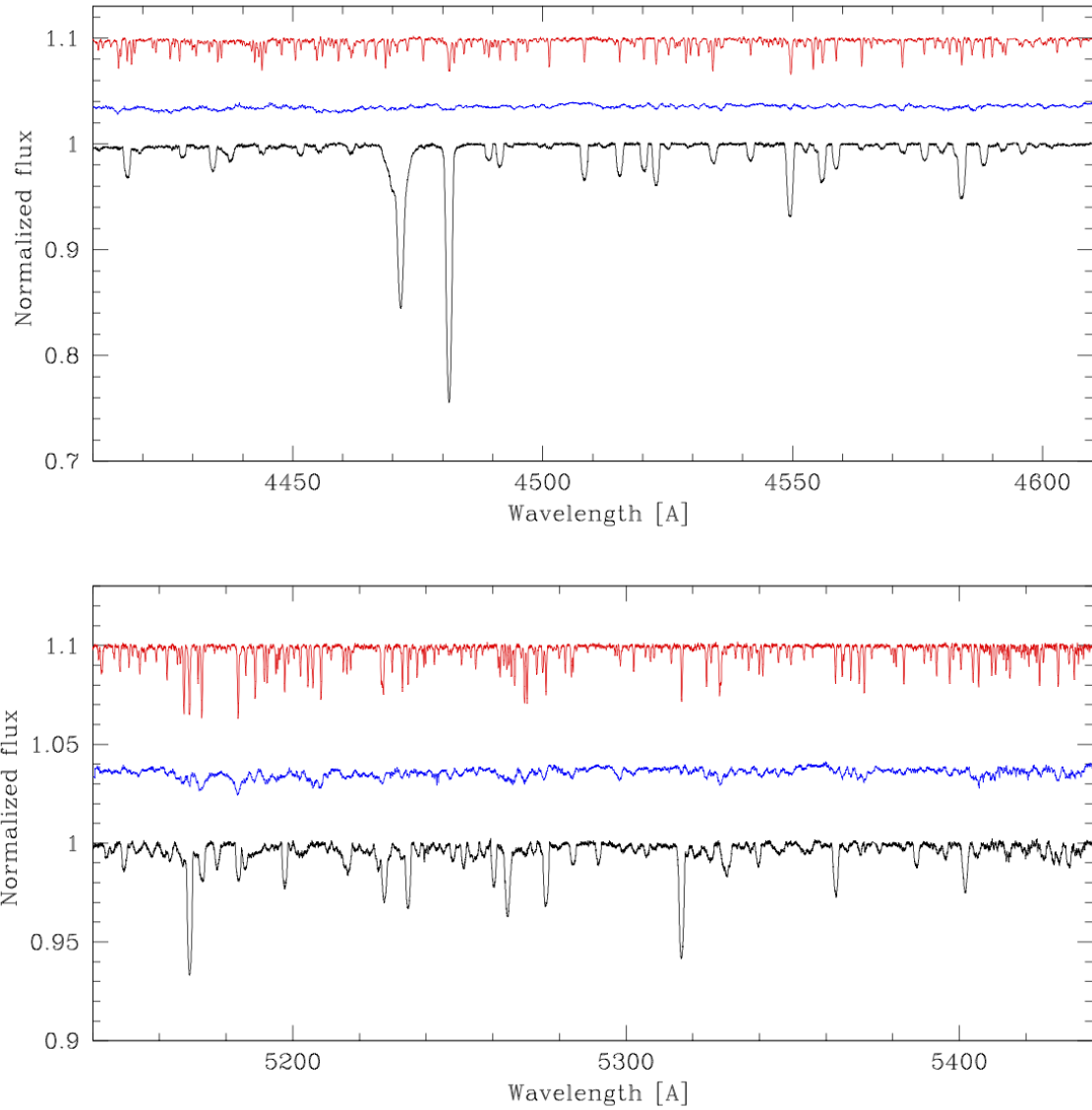


Figure 7.1: Two portions of disentangled spectra for the three components of the Algol system. In each panel from top to bottom are shown Algol C, Algol B, and Algol A. The plots are not on the same scale, and disentangled spectra for Algol B and C are shifted up by 0.04 and 0.10 of the continuum flux, respectively, for clarity.

(1994).

With no need for input template spectra, SPD does not suffer from the bias due to template mismatch which affects cross-correlation methods (c.f. Hensberge & Pavlovski 2007, and references therein). However, no comprehensive study of the error propagation in SPD and comparison to cross-correlation has been undertaken yet. Some initial studies have indicated the method is ‘well-behaved’ (Hynes & Maxted 1998, Ilijić et al. 2001, Hensberge & Pavlovski 2007, Southworth & Clausen 2007).

The SPD of Algol is challenging for the following reasons: (i) the system is triple; (ii) the secondary component is barely visible in the optical spectra; (iii) the period of the outer orbit is long (680 d); (iv) eclipse spectra could not be used due to significant distortion of the line profiles. Spectra of several multiple systems have previously been successfully separated using different variants of the SPD method (c.f. Frémat et al. 2005, Gonzáles et al. 2006, Lee et al. 2008, Tamajo et al. 2012). Faint components with a fractional light contribution of only $\sim 5\%$ have been detected using SPD (e.g. Pavlovski et al. 2009, Lehmann et al. 2013, Tkachenko et al. 2014, Borkovits et al. 2014); even down to $\sim 2.5\%$ in the V spectral region (Torres et al. 2014), and $1.5\text{--}2\%$ (Holmgren et al. 1999, Mayer et al. 2013). As was shown in our preliminary reports on SPD of Algol (Pavlovski et al. 2010, Kolbas et al. 2012) we are pushing the limit of the method because of the extreme faintness of Algol B (see Sect. 7.5.1).

The code `FDBINARY` (Ilijić et al. 2004) was used to perform SPD. `FDBINARY` implements disentangling in the Fourier domain (Hadrava 1995), an important time-saving aspect in SPD of a large collection of high-resolution spectra. It also allows solving for two orbits and three individual spectra, as is required for Algol. The code uses Fast Fourier Transforms, which allows flexibility in preparing input spectra for SPD whilst preserving the original spectral resolution. Five spectral segments were selected, taking care that each one contains enough spectral lines of Algol B to allow its velocity semiamplitude to be determined with certainty. For the blue spectral region this is challenging since the fractional light contribution is less than 1% (see Sect. 7.5.1 and Fig. 7.1). The following spectral segments were used for SPD: 4176.9–4277.0, 4400.2–4614.7, 4929.1–5118.9, 5140.6–5305.1 and 5311.0–5520.0 Å. Only spectra taken outside eclipse were used, which means a total of 112 input spectra. To limit the computational demand we also stacked spectra taken in close succession, resulting in a total of 49 input spectra. The FIES and BOES datasets were also analysed first separately with the outer orbit fixed according to recent interferometric results (Czismadia et al. 2009, Zavala et al. 2010, Baron et al. 2012). The solution for the inner orbit was then used as an initial set of the orbital elements for solving both orbits simultaneously using the 49 spectra.

Hill et al. (1971) found that the inner orbit is slightly eccentric, $e_{A-B} = 0.015 \pm 0.008$. In our SPD calculations it was evident that the eccentricity of the inner orbit always converges to $e_{A-B} = 0.0$ with a high confidence. Therefore, in the final set of the calculations, the eccentricity of the inner orbit was fixed to zero.

The distribution of the observations for the outer orbit is not sufficient to determine all pa-

Table 7.1: The final solution for the orbital elements of the inner and outer orbit in the Algol triple system as obtained by SPD. The periods are taken from Baron et al. (2012), as well as the eccentricity of the outer orbit. Trial calculations for the inner orbit has shown it is circular, and in the final calculations e_{A-B} and ω_{A-B} were set to 0.

Quantity	Notation	Unit	Value	Error
INNER ORBIT				
Period	P_{A-B}	d	2.871362	fixed
Eccentricity	e_{A-B}		0.	fixed
Periastron longitude	ω_{A-B}	deg	90.	fixed
RV semiamplitude	K_A	km s ⁻¹	44.1	0.2
RV semiamplitude	K_B	km s ⁻¹	194.2	1.2
Mass ratio	q_{A-B}		0.227	0.005
OUTER ORBIT				
Period	P_{AB-C}	d	680.168	fixed
Time of periastron	$T_{AB-C,0}$	d	2454433.2	1.1
Eccentricity	e_{AB-C}		0.227	fixed
Periastron longitude	ω_{AB-C}	deg	138.1	0.6
RV semiamplitude	K_{AB}	km s ⁻¹	11.9	0.4
RV semiamplitude	K_C	km s ⁻¹	32.9	0.8
Mass ratio	q_{AB-C}		0.364	0.009

rameters simultaneously, so we decided to fix the eccentricity of this orbit. Recent independent interferometric studies give a very consistent result on its value of $e_{AB-C} = 0.227 \pm 0.002$ (Baron et al. 2012). Since the SIMPLEX algorithm is used for the minimisation in FDBINARY a large number of the calculations should be performed to avoid being trapped in some of many local minima. We have opted for 50 runs with 1000 iterations each. Fixing e_{AB-C} made the convergence stable and consistent. Our final solution for the two orbits is given in Table 7.1. It represents the mean values from the solutions of SPD in the five selected spectral segments specified early in this Section. The errors quoted in Table 1 are standard deviations of the mean calculated from the solutions obtained for the five segments. More sophisticated error calculations for SPD, such as the jackknife method (Pavlovski et al. 2011, 2014), were beyond our computational capabilities.

The results presented in Table 7.1 deserve some comments in the context of the previous results. First, we did not confirm the eccentricity for the inner orbit (e_{A-B}) which was reported in some previous studies, but rejected in others. In an extensive spectroscopic study Hill et al. (1971) examined a series of medium-resolution photographic spectra obtained at the Dominion Astrophysical Observatory. They found $e_{A-B} = 0.015 \pm 0.008$ but suffered from non-detection of the secondary's spectrum. It is not clear if and how this might affect the determination of RVs for the primary. Also, it should be noted that Hill et al. (1971) attributed a 32 year periodicity to apsidal motion in the inner orbit. Orbital eccentricity of the eclipsing pair in the inner orbit has not been indicated in the photometry of Algol (Wilson et al. 1972, Guinan et al. 1976, Söderhjelm 1980, Kim 1989).

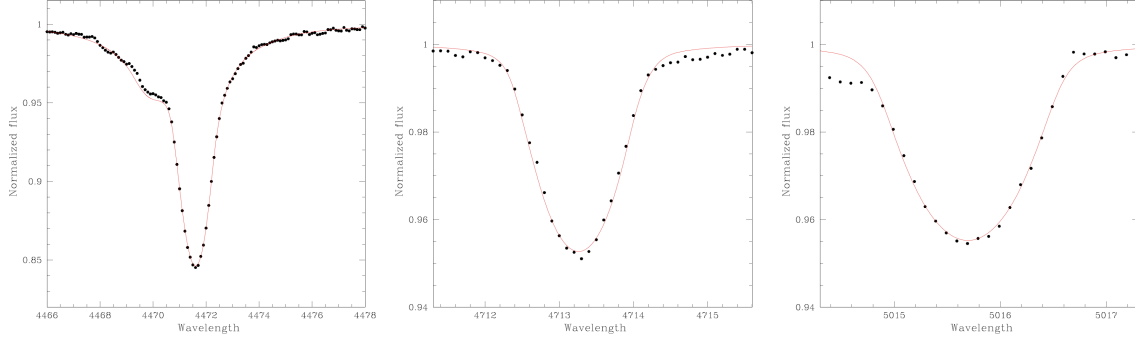


Figure 7.2: Determination of the fractional light contribution for Algol A from optimal fits of He I lines in its disentangled spectrum. Synthetic NLTE He I line profiles were calculated for $T_{\text{eff}} = 12\,550\text{ K}$, $\log g = 4.05$ and $v \sin i = 50.5\text{ km s}^{-1}$.

The velocity semi-amplitude for Algol A found by Hill et al. (1971), $K_A = 44.0 \pm 0.4\text{ km s}^{-1}$, agrees within the uncertainties with the value derived in our work, $44.1 \pm 0.2\text{ km s}^{-1}$. Also, it is encouraging that their velocity semi-amplitudes of the outer orbit, $K_{AB} = 12.0 \pm 0.4\text{ km s}^{-1}$ and $K_C = 31.6 \pm 1.2\text{ km s}^{-1}$, are in agreement with our values, $K_{AB} = 11.9 \pm 0.4\text{ km s}^{-1}$ and $K_C = 32.9 \pm 0.8\text{ km s}^{-1}$. Hill et al. (1971) were also able to determine the eccentricity of the outer orbit, $e_{AB-C} = 0.23 \pm 0.04$, which was corroborated and improved by interferometric measurements (Zavala et al. 2010, Baron et al. 2012).

Two portions of disentangled spectra of the three components are presented in Fig. 7.1. The secondary spectrum is clearly isolated in the whole optical range, albeit contributing barely 1% around 4500 \AA and somewhat less than 2% around 5500 \AA (Sect. 5.1). The RV semi-amplitude for Algol B, K_B , has two almost equally deep local minima around 194 and 211 km s^{-1} . It is difficult to trace the reason for this ambiguity but, besides the small light contribution, the reasons might include imperfect phase distribution of the observations for the inner orbit, gaps in the phase distribution for the outer orbit, and possible systematics due to the use of two spectrographs and varying observing conditions. The χ^2 for the lower solution is slightly better, so we adopted this as our final solution, $K_B = 194.2 \pm 1.2\text{ km s}^{-1}$. This value agrees with the only previous measurement, $K_B = 201 \pm 6\text{ km s}^{-1}$ (Tomkin & Lambert 1978).

Tomkin & Lambert (1978) calculated the spectroscopic mass ratio using the K_A determined by Hill et al. (1971) and their own K_B measurement, finding $q_{A-B} = 0.219 \pm 0.007$. This mass ratio was subsequently used in many studies on Algol, as it was the first mass ratio found from dynamical effects. Our value is slightly higher, $q_{A-B} = 0.227 \pm 0.002$. Since the mass ratio could be estimated in the light curve analysis if the eclipsing binary is semi-detached, there were some attempts to derive it this way. Kim (1989) used the ‘ q -search method’ to obtain exactly to the same value from BV light curves, $q_{\text{phot}} = 0.227 \pm 0.002$. Determination of the astrometric orbit from the interferometric measurements also could yield the mass ratio. Baron et al. (2012) solved the orbital elements for both orbits and the mass ratio of the inner orbit from the relative positions of the components derived from the visibility functions. In addition,

they derived the mass ratio of outer orbit independently from parallax assumptions. They found $q_{A-B} = M_B/M_A = 0.219 \pm 0.017$ and $q_{AB-C} = M_C/(M_A + M_B) = 0.456 \pm 0.022$. This q_{A-B} agrees with our value to within its relatively large uncertainties.

The mass ratio for the outer orbit derived from these different techniques is highly discrepant and needs clarification. However, it is encouraging that spectroscopic analyses are consistent, as Hill et al. (1971) found $q_{AB-C} = 0.380 \pm 0.051$, compared to our value of $q_{AB-C} = 0.362 \pm 0.042$.

7.5 Atmospheric diagnostics

7.5.1 Renormalisation of disentangled spectra

In the course of the primary eclipse, the line profiles of the primary component in Algol are distorted due to the Rossiter-McLaughlin effect (Rossiter 1924, McLaughlin 1924). It is the principal assumption of spectral disentangling that spectral line profiles are not intrinsically variable. Therefore, eclipse spectra cannot be used, and the zeroth mode in the Fourier expansion is undetermined. As a consequence, this means that spectra can be only separated (they are still in the common continuum of the system), and renormalisation to their individual continua can be performed only with an external information on the individual components' fractional contribution to the total light of the system.

An obvious way is to use the light ratio between the components from the light curve solution for eclipsing binaries (c.f. Hensberge et al. 2000). However, the light curve solution of Algol is rather uncertain because the eclipses are partial and there is 'third light' from component C. On top of these obstacles, it is extremely difficult to acquire photometry of Algol due to its brightness and lack of suitable comparison stars within 10° .

It is therefore not surprising that only a few complete light curves for Algol have been published. The most recent photometry (Kim 1989) was a series of photoelectric measurements in the B and V filters, obtained from 1982 to 1984 at Yonsei Observatory, Korea. The other light curves of Algol from the era of photoelectric photometry are those of Guinan et al. (1989) and Wilson et al. (1972). In addition, Stebbins secured an incomplete light curve in multiple passbands from 1949 to 1951 (Stebbins & Gordon 1975), Al-Naimy et al. (1985) obtained unpublished observations in 1981, and light curves in the ultraviolet (Eaton 1975), and near-infrared (Chen & Reuning 1966) exist.

Published light curve analyses have not yet given an unique solution for Algol, primarily because of its complexity. Solutions of partially eclipsing binary stars inevitably suffer from degeneracy, which should be lifted using additional information (Garcia et al. 2014, Southworth et al. 2007). This is illustrated in Table 7.2 in which fractional light contributions (light dilution factors) are listed from selected works. Wilson et al. (1972) used an estimate of the third light contribution derived spectroscopically by Fletcher (1964). The same approach was

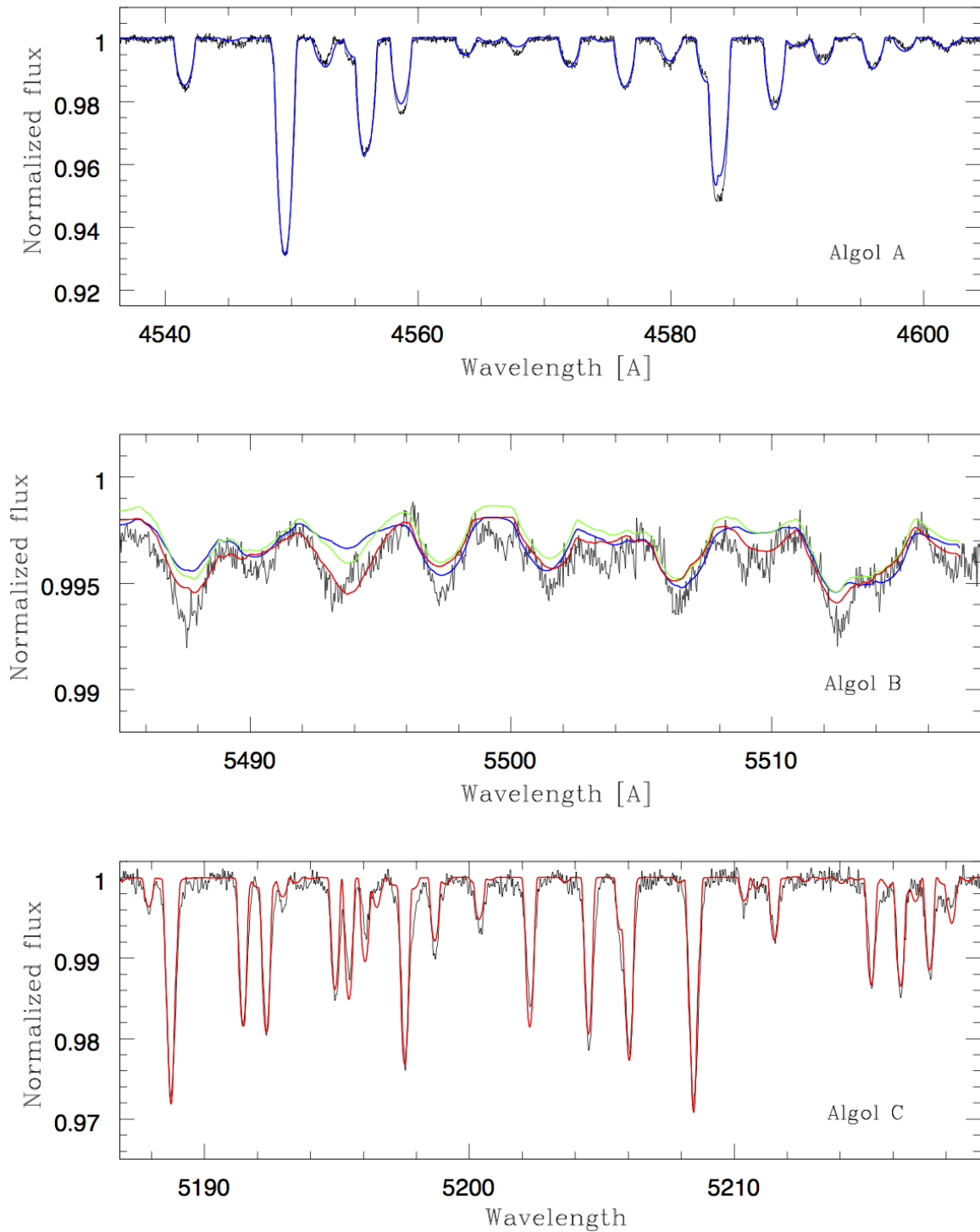


Figure 7.3: Optimal fits of the disentangled spectra of the components in Algol. From top to bottom are shown Algol A, Algol B, and Algol C, respectively. These short portions of the components' disentangled spectra show the quality of the optimal fitting for the atmospheric parameters listed in Table 5, except for Algol B (middle panel) for which best fits for three T_{eff} s are shown (red line 5000 K, green line 4500 K, blue line 4000 K).

Table 7.2: Summary of the fractional light contribution of the components of Algol to the total light of the system determined by different techniques. ‘Photometry’ indicates light curve analysis. Only B and V photometry are listed as this is the wavelength region covered by our spectra. References: (1) Wilson et al. (1972); (2) Demircan (1978); (3) Richards et al. (1988); (4) Kim (1989); (5) Zavala et al. (2010); (6) This work.

Method	B			V			Source
Photometry	0.940	0.010	0.050	0.893	0.029	0.078	(1)
Photometry	0.909	0.041	0.050	0.857	0.065	0.078	(2)
Photometry	0.929	0.012	0.059	0.894	0.035	0.071	(3)
Photometry	0.854	0.040	0.106	0.814	0.067	0.119	(4)
Interferometry				0.863	0.063	0.065	(5)
Spectroscopy	0.943	0.008	0.049	0.915	0.018	0.067	(6)

followed by Demircan (1978) who analysed the photometry published in Wilson et al. (1972). Since at that time the secondary component was not yet detected in Algol’s spectra, the mass ratio between the components of the inner eclipsing pair had to be assumed from other considerations. But it is evident from the solutions derived in Richards et al. (1988) and Kim (1989) that the dynamical mass ratio measured by Tomkin & Lambert (1978) did not help to provide a consistent description of the Algol system. Richards et al. (1988) calculated a grid of models with different assumptions for the radiative properties of the third star, whilst Kim (1989) attempted to derive its contribution directly from his BV light curves. In this context we also list estimates of the light ratios measured in the interferometric observations by Zavala et al. (2010). Their estimates suffered from large uncertainties, and the fractional light contribution of $\sim 6\%$ for Algol B is certainly too large.

Facing all these uncertainties in the determination of the fractional light contributions of the components, we rely on the extraction of these quantities from the disentangled spectra themselves. The information on the light dilution factor is contained in the spectral line depths in the disentangled (separated) spectra of an individual component. But caution is needed at this point since other effects could change the line depth in stellar spectrum and mimic light dilution effects in binary or multiple systems. First of all, this might be metallicity or chemical peculiarity of the component(s). Algol C is often characterised as an Am star, starting with the spectroscopic examination by Fletcher (1964).

In the optical spectra of Algol the most prominent lines are H I and He I originating in the photosphere of the primary component (c.f. Struve & Sahade 1957). Since He I lines are present in the primary’s spectrum only, we used them for the determination of its effective temperature, $T_{\text{eff,A}}$, and fractional light contribution, lf_A . We used the program STARFIT (Kolbas et al. 2014) which compares disentangled component spectra to a grid of calculated theoretical spectra. STARFIT can handle the following parameters: effective temperature T_{eff} , surface gravity $\log g$, fractional light contribution lf , projected rotational velocity $v \sin i$, relative velocity shift between disentangled spectrum and rest-frame laboratory wavelengths, v_0 , and continuum

corrections, *cc*. Optimisation is performed by a genetic algorithm (Charbonneau 1995), and can be done in constrained mode with disentangled spectra of the components for which the sum of the fractional light contributions should be ≤ 1 (Tamajo et al. 2011). Grids of theoretical spectra are calculated in LTE with the program UCLSYN (Smith 1992, Smalley et al. 2001)

$T_{\text{eff,A}}$ is constrained to be in the range 12 000 to 13 000 K (Richards et al. 1988, Kim 1989). Our disentangled spectra contain three He I lines suitable for the optimisation, at 4471, 4713 and 5015 Å. Unfortunately, the He I lines at 4388, 4920, 5047, and 5788 Å are either on the wings of Balmer lines, or are contaminated by metal or telluric lines, so are not suitable. To facilitate optimisation we first determined $v \sin i$ by optimal fitting of unblended metal lines in the primary's disentangled spectrum ($v \sin i$ or FWHM does not depend on the light dilution). In hot stars, a degeneracy exists between T_{eff} and $\log g$ for H I and He I lines, so we fixed $\log g$ in our calculations to $\log g_{\text{A}} = 4.05$ (Richards et al. 1988). Also, it should be noted that model atmospheres are calculated assuming the 'standard' (solar) helium abundance with the fraction of helium atoms $N_{\text{He}}/(N_{\text{H}} + N_{\text{He}}) = 0.089$.

We found that the three He I line profiles are not well and consistently reproduced in the LTE (local thermodynamic equilibrium) approximation. Thus we decided to calculate He I line profiles in non-LTE. Our grid of theoretical spectra (Kolbas et al. 2014) was extended down to $T_{\text{eff}} = 12\,000$ K. This is below the usual borderline used for NLTE spectrum synthesis of $T_{\text{eff}} = 15\,000$ K. Almost perfect fits were achieved with He I line profiles in NLTE (Fig. 7.2, solid lines). Optimisation was performed separately for each line to find the wavelength-dependent fractional light contribution, ldf . An excellent convergence was found for almost same effective temperature, $T_{\text{eff,A}} = 12\,600 \pm 90$ K, and $lf(4471 + 4713) = 0.943 \pm 0.002$, and $lf(5015) = 0.915 \pm 0.002$. Uncertainties in T_{eff} and lf were calculated with a Markov chain Monte Carlo technique (Ivezić et al. 2014). The T_{eff} for Algol A will be further improved in a detailed analysis of its renormalised spectrum in Sect. 7.5.2.

As described in Sect. 7.4, SPD enabled us to reconstruct almost the entire optical spectrum of Algol B, the first time this has been achieved (Figs. 7.1 and 7.3). A first attempt to match it to theoretical spectra with $T_{\text{eff,B}} \sim 4500$ K indicated a low fractional light contribution, evidently less than the light curve solutions have given (Table 7.2). Again, the program STARFIT was used with only surface gravity as a fixed parameter, $\log g_{\text{B}} = 3.11$ (Richards et al. 1988). The projected rotational velocity converged to $v_{\text{B}} \sin i_{\text{B}} = 62 \pm 2 \text{ km s}^{-1}$, in perfect accordance with the expected synchronous rotational velocity for this star ($v_{\text{synch}} = 61.8 \pm 0.5 \text{ km s}^{-1}$). The optimal fractional light contributions of Algol B are: $ldf(4500) = 0.008 \pm 0.001$ and $ldf(5500) = 0.018 \pm 0.001$, with $T_{\text{eff,B}} = 4900 \pm 300$ K. This is the most unexpected result of our study compared to previous results but quite secure since the spectral lines for the late G or early K subgiant are intrinsically deep, and, for the expected $v \sin i$, the light dilution is certainly no more than 2% in V and less than 1% in B .

7.5.2 Effective temperatures for the components

Detailed spectral analysis is possible for Algol A and Algol C, making it possible to fine-tune their T_{eff} measurements. The values determined in Sect. 7.5.1 served as initial points. Spectral analysis of the entire disentangled spectral range (4400–5800 Å) was performed, using UCLSYN. The equivalent widths (EWs) were measured for suitable lines in the renormalised disentangled spectra. Model atmospheres were calculated in LTE with the program ATLAS9 (Kurucz 1979), and abundances calculated for the measured EWs. Since Fe lines are the most numerous in the spectra of both stars, they served for the determination of T_{eff} and microturbulent velocity, ξ_t . The spectrum of Algol A contains many Fe II lines, but those of Fe I are few and weak. That of Algol C contains many Fe I lines but also a substantial number of Fe II lines, which means fine-tuning of $T_{\text{eff,C}}$ is possible using the Fe ionisation balance.

We determined T_{eff} and ξ_t in a few iteration steps. $T_{\text{eff,A}}$ was tuned so there was no correlation between Fe II abundance and the excitation potential, EP, whilst the microturbulence, $\xi_{t,A}$ was found by requiring the Fe II abundance to be independent of EW. We found $T_{\text{eff,A}} = 12\,550 \pm 120$ K and $\xi_{t,A} = 0.4 \pm 0.2$ km s⁻¹. The uncertainties were calculated from the uncertainties in the determination of the slopes of $\log \epsilon(\text{Fe II})$ versus EP for T_{eff} and $\log \epsilon(\text{Fe II})$ versus EW for ξ_t .

The atmospheric parameters for Algol C were determined in the same manner. Moreover, the Fe ionisation balance could be used in fine-tuning $T_{\text{eff,C}}$. Our final results are $T_{\text{eff,C}} = 7\,540 \pm 80$ K, and $\xi_{t,C} = 1.64 \pm 0.08$ km s⁻¹. The uncertainties were derived in the same way as for Algol A, except that Fe I was used. The ionisation balance of Fe is well satisfied with the difference in abundance derived from Fe I and Fe II lines of only $\Delta \log \epsilon(\text{Fe}) = 0.05 \pm 0.11$.

Since we have renormalised the disentangled spectra of the components with the light dilution factors determined from these spectra themselves, the wavelength dependence of the Fe abundance could be an important check of the correctness of the procedure. Fe II and Fe I lines are well distributed in the optical spectra of Algol A and Algol C, respectively. This test is more sensitive for Algol C as the multiplication factor needed to normalise its spectrum to unit continuum is much higher than in the case of Algol A, ~ 16.5 versus ~ 1.1 . As is illustrated in Fig. 7.4 no wavelength dependence of iron abundance is present for either of the components. This provides encouraging support for the reliability of our estimates for the luminosity contribution of the components to the total light of the system. The ξ_t for Algol A is also in agreement with that generally found for late B-type stars (Fossati et al. 2009), which is usually considerably less than 1 km s⁻¹.

7.5.3 The elemental composition and metallicity

The number of spectral lines available for the determination of the photospheric composition of Algol A are rather limited. This does have the advantage that line blending and smearing do not prevent detailed analysis despite the relatively high $v \sin i$ of 50 km s⁻¹. Beside the strong

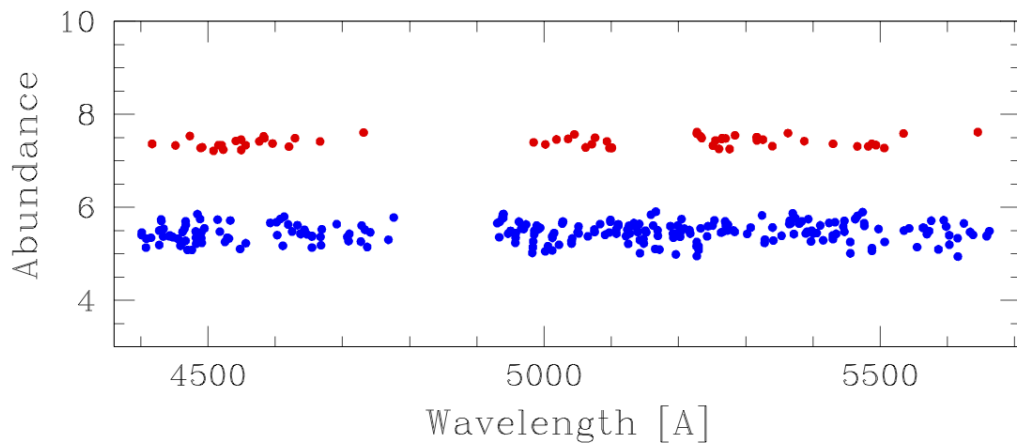


Figure 7.4: Dependence of iron abundance on wavelength for Algol A (filled red circles) and Algol C (filled blue circles). In the case of Algol A, the abundances of Fe II are shown. For Algol C, Fe I abundances are shown. The scatter is large for Algol C because the S/N of the renormalised disentangled spectrum of this component is much less than that for Algol A due to the differing fractional contributions to the total light of the system.

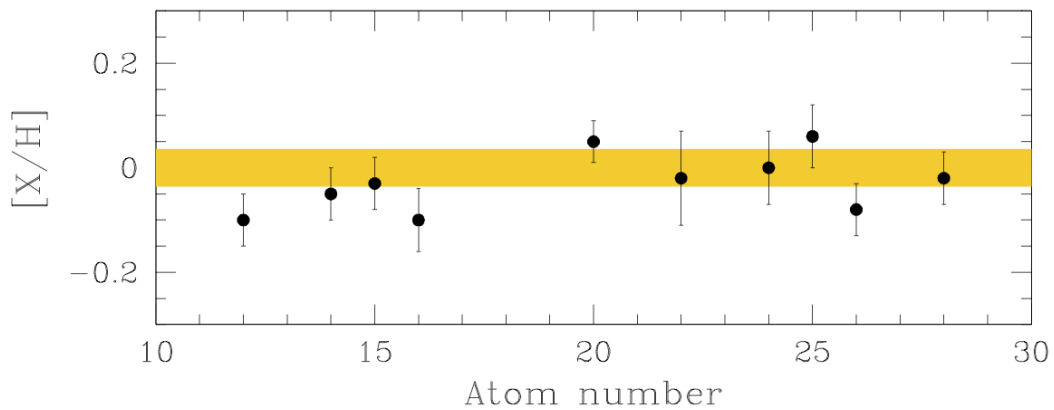


Figure 7.5: Abundance pattern measured for the photospheric composition of Algol A (symbols) compared to the standard solar composition (grey shading) which represents the 1σ uncertainty in the solar composition determined by Asplund et al. (2009).

Table 7.3: Photospheric abundances derived for Algol A. Abundances are expressed relative to the abundance of hydrogen (column 2), $\log \epsilon(H) = 12.0$. The third column gives the number of lines used, and abundances relative to the Sun are given in the fourth column.

El.	$\log \epsilon(X)$	N	[X/H]
C	8.64 ± 0.02	3	0.21 ± 0.05
N	7.92 ± 0.04	4	0.09 ± 0.06
O	8.93 ± 0.02	11	0.24 ± 0.05
Mg	7.49 ± 0.03	7	-0.10 ± 0.05
Si	7.46 ± 0.04	14	-0.05 ± 0.05
P	5.38 ± 0.05	3	-0.03 ± 0.05
S	7.02 ± 0.02	21	-0.10 ± 0.06
Ca	6.37 ± 0.02	3	0.05 ± 0.04
Ti	4.91 ± 0.03	11	-0.02 ± 0.09
Cr	5.62 ± 0.04	9	0.00 ± 0.07
Mn	5.48 ± 0.05	5	0.06 ± 0.06
Fe	7.39 ± 0.02	70	-0.08 ± 0.05
Ni	6.18 ± 0.02	17	-0.02 ± 0.05

Table 7.4: Photospheric abundances derived for Algol C. Explanations are the same as for Table 7.3.

El.	$\log \epsilon(X)$	N	[X/H]
C	8.53 ± 0.04	21	0.10 ± 0.06
O	8.72 ± 0.06	6	0.03 ± 0.08
Na	6.31 ± 0.08	7	0.10 ± 0.09
Mg	7.50 ± 0.09	7	-0.09 ± 0.10
Si	7.58 ± 0.06	23	0.07 ± 0.07
S	7.16 ± 0.04	10	0.04 ± 0.05
Ca	6.37 ± 0.09	21	0.02 ± 0.09
Sc	3.03 ± 0.07	12	-0.13 ± 0.08
Ti	5.01 ± 0.07	106	0.08 ± 0.08
V	4.10 ± 0.10	17	0.21 ± 0.13
Cr	5.69 ± 0.07	97	0.07 ± 0.08
Mn	5.33 ± 0.08	23	-0.09 ± 0.09
Fe	7.45 ± 0.08	296	-0.02 ± 0.09
Co	5.03 ± 0.07	21	0.10 ± 0.09
Ni	6.25 ± 0.07	161	0.05 ± 0.08
Cu	4.19 ± 0.13	3	0.01 ± 0.14
Y	2.32 ± 0.06	14	0.11 ± 0.08
Zr	2.59 ± 0.06	11	0.09 ± 0.07
Ba	2.38 ± 0.34	3	0.29 ± 0.18
La	1.35 ± 0.07	6	0.23 ± 0.08
Ce	1.69 ± 0.06	16	0.11 ± 0.07
Nd	1.57 ± 0.08	8	0.15 ± 0.09

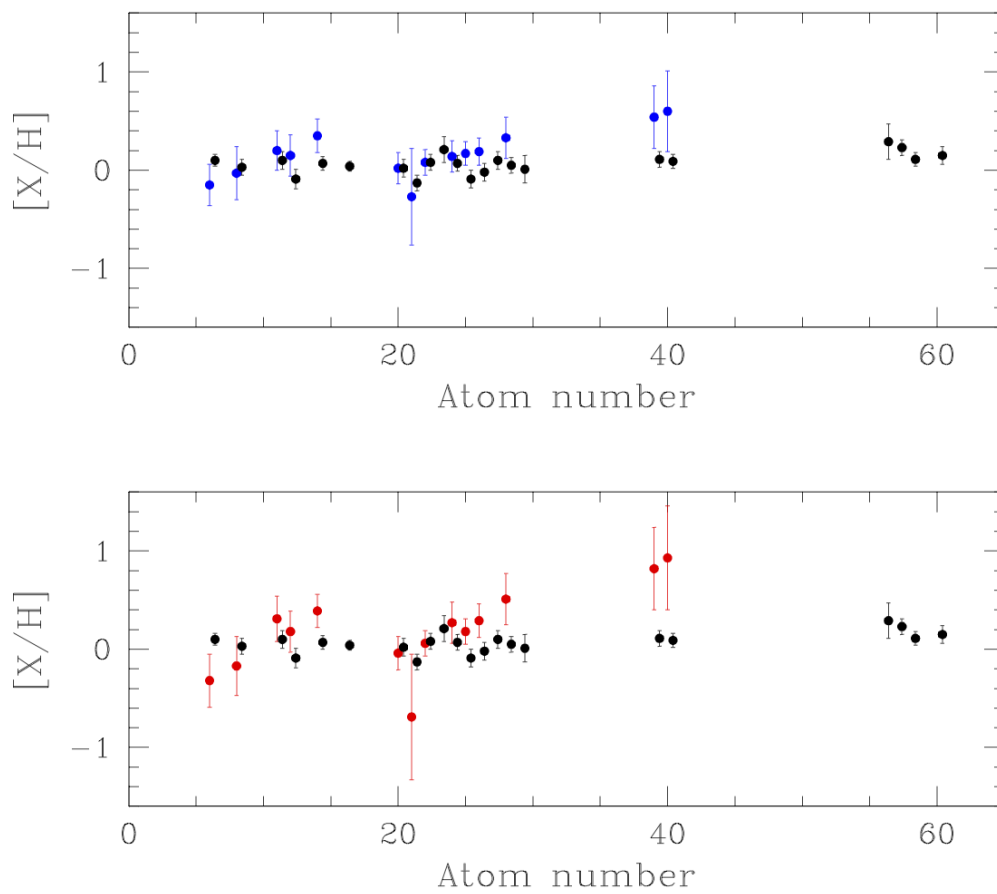


Figure 7.6: Abundance pattern measured for the photospheric composition of Algol C (black dots) compared to the average abundance pattern of ‘normal’ A-type stars (upper panel, blue dots) and Am stars (lower panel, red dots), following Gebran et al. (2010).

hydrogen (not disentangled) and helium lines, the most prominent are lines of Fe II. For the T_{eff} of Algol A, spectral lines of the CNO elements are rather weak: the EWs of C lines are all <4.5 mÅ except for the C II 4267 Å line, <3 mÅ for N, and <15 mÅ for O. Therefore, abundance estimates for these elements should be considered with caution, except for C II 4267 Å whose EW of 44.8 mÅ gives a carbon abundance of $\log \epsilon(\text{C}) = 8.27 \pm 0.06$. This is 0.16 ± 0.08 dex less than solar (Asplund et al. 2009). Carbon deficiency is also indicated from the comparison of the EW for the C II 4267 Å line to EWs of standards from Tomkin et al. (1993) and İbanoğlu et al. (2012).

The mean photospheric metal abundance of Algol A has been calculated for all elements listed in Table 7.3 except CNO. Abundances of these elements were not used because of possible changes due to mass transfer, and the small EWs of the lines on which they are based. The remaining 10 elements give an average abundance of $[\text{M}/\text{H}]_{\text{A}} = -0.03 \pm 0.08$. This is less than 1σ away from the $[\text{Fe}/\text{H}]_{\text{A}} = -0.08 \pm 0.05$ value derived from the most numerous lines. We calculated the bulk metallicity using the approximate equation, $Z = Z_{\odot} 10^{-[\text{M}/\text{H}]}$, finding it to be solar to within its uncertainty: $Z_{\text{A}} = 0.014 \pm 0.002$ (using the present day solar metallicity $Z_{\odot} = 0.0134$ from Asplund et al. 2009). The measured elemental abundances in the photosphere of Algol A are displayed in Fig. 7.5 relative to standard solar values (Asplund et al. 2009).

The rich and relatively unbroadened ($v_{\text{C}} \sin i_{\text{C}} \sim 12 \text{ km s}^{-1}$) line spectrum of Algol C made possible the determination of photospheric elemental abundances for 20 elements. Seven appear in two ionisation stages (neutral and singly-ionised). In the spectral range studied (4500–5700 Å) the most numerous lines are of Fe I, Ni I, Cr I and Ti II. The measured abundances are listed in Table 7.4, along with the number of spectral lines used, and abundances relative to standard solar (Asplund et al. 2009). The slightly larger uncertainties compared to Algol A, despite having more lines available, are due to the smaller S/N of the renormalised disentangled spectrum after multiplication by ~ 16 to put the continuum level to unity. In Fig. 7.6 we compare the photospheric composition of Algol C with the abundance pattern derived in Gebran et al. (2010) for a sample of 'normal' A-type stars (upper panel) and Am stars (lower panel). The abundances in Algol C do not show the principal characteristics of the Am phenomenon, i.e. strong Sc underabundance, often a Ca underabundance, and a moderate to strong overabundance of iron-group elements. The mean metallicity for Algol C is consistent with solar, at $[\text{M}/\text{H}]_{\text{C}} = 0.04 \pm 0.09$. The corresponding bulk metallicity is $Z_{\text{C}} = 0.012 \pm 0.002$.

The photospheric elemental compositions of Algol A and Algol C are the same to within the 1σ uncertainties, with a formal difference of $\Delta[\text{M}/\text{H}] = [\text{M}/\text{H}]_{\text{A}} - [\text{M}/\text{H}]_{\text{B}} = -0.07 \pm 0.12$. Both correspond to the standard solar composition (Asplund et al. 2009).

Table 7.5: Astrophysical quantities for the components of Algol triple system derived in this work (masses, T_{eff} , $v \sin i$ values, or calculated in conjunction with previous studies (radii, $\log g$ values, synchronous velocities). The radius for Algol C is from the interferometric study by Baron et al. (2012). All other quantities are determined or calculated in this work.

Quantity	Notation	Unit	Algol A	Algol B	Algol C
Mass	M	M_{\odot}	3.39 ± 0.06	0.770 ± 0.009	1.58 ± 0.09
Radius	R	R_{\odot}	2.87 ± 0.04	3.43 ± 0.01	1.7 ± 0.3
Surface gravity	$\log g$	[cgs]	4.05 ± 0.01	3.254 ± 0.006	4.18 ± 0.16
Effective temperature	T_{eff}	K	$12\,550 \pm 120$	4900 ± 300	7550 ± 250
Projected rotational velocity	$v \sin i$	km s^{-1}	50.5 ± 0.8	62 ± 2	12.4 ± 0.6
Synchronous velocity	v_{synch}	km s^{-1}	51.2 ± 0.5	64 ± 1	14.1 ± 2.5
Microturbulence velocity	ξ_t	km s^{-1}	0.4 ± 0.2		1.68 ± 0.06
Mean metal abundance	[M/H]		-0.03 ± 0.08		0.04 ± 0.09
Bulk metallicity	Z		0.014 ± 0.002		0.012 ± 0.002

7.6 Discussion

7.6.1 Fundamental properties of the components of Algol

With RV semi-amplitudes determined for all the components of the Algol system, we are able to derive their dynamical masses. The orbital inclinations are taken from Richards et al. (1988) for the inner orbit, $i_{A-B} = 81.4 \pm 0.2$, and from Baron et al. (2012) for the outer orbit, $i_{AB-C} = 83.66 \pm 0.03$. In the latter study i_{A-B} was also derived, and was in agreement with Richards et al. (1988) but with lower accuracy. The inclinations are well constrained from several different studies and techniques. We also used the orbital periods from Baron et al. (2012): $P_{A-B} = 2.867328 \pm 0.00005$ d and $P_{AB-C} = 680.168 \pm 0.54$ d. We find the masses $M_A = 3.39 \pm 0.06 M_{\odot}$, $M_B = 0.770 \pm 0.009 M_{\odot}$ and $M_C = 1.58 \pm 0.09 M_{\odot}$. Moreover, from the outer orbit we get sum of the masses for Algol A and Algol B, $M_{AB} = (M_A + M_B)_{\text{outer}} = 4.38 \pm 0.27 M_{\odot}$, which is in accordance with the sum of the individual masses of Algol A and Algol B from the inner orbit, $(M_A + M_B)_{\text{inner}} = 4.16 \pm 0.06 M_{\odot}$. Table 7.5 contains the physical properties of all three stars in the Algol system derived in the current work.

The component masses we find are about 8% smaller than the most commonly quoted values (Richards et al. 1988). This corroborates the findings of Baron et al. (2012), although these authors found masses about 15% smaller than those from Richards et al. (1988). Besides improving the mass values we were able to improve the measurement precision to 1.8% for Algol A and 1.2% for Algol B. That for Algol C is less improved, at 5%.

Published determinations of the radii of the stars suffer from degeneracy due to the third light and partial eclipses (see Sect. 7.5.1). Richards et al. (1988) found $R_A = 2.90 \pm 0.04 R_{\odot}$, $R_B = 3.5 \pm 0.1 R_{\odot}$ and $R_C = 1.7$ (no error given). Baron et al. (2012) achieved better than 0.5 mas spatial resolution in the H -band with the CHARA interferometer, and unambiguously resolved

the three stars. They found angular diameters of $\phi_A = 0.88 \pm 0.05$ mas, $\phi_B = 1.12 \pm 0.07$ mas and $\phi_C = 0.56 \pm 0.10$ mas. With the parallax of Algol determined by Zavala et al. (2010), $\pi = 34.7 \pm 0.6$ mas, they found linear radii of $R_A = 2.73 \pm 0.20 R_\odot$, $R_B = 3.48 \pm 0.28 R_\odot$ and $R_C = 1.73 \pm 0.33 R_\odot$. The interferometric measurements clearly suffer from large uncertainty, but are in agreement.

The dimensions of the Roche-lobe filling component B are constrained by the mass ratio. This is another possibility to determine its linear radius and synchronous rotational velocity. With our mass ratio for the semidetached pair, $q_{A-B} = 0.227 \pm 0.005$ we have a relative radius of Algol B, $r_B = 0.251 \pm 0.002$ (radius at the sides of the secondary star perpendicular to the line connecting the centres of the two stars). The semi-major axis of the inner orbit is $a_{A-B} = 13.65 \pm 0.07 R_\odot$. The linear radius is $R_B = r_B a_{A-B} = 3.43 \pm 0.01 R_\odot$. This is consistent with the Baron et al. (2012) value. The synchronous rotational velocity for this R_B is $v_{\text{synch},B} = 60.2 \pm 0.2 \text{ km s}^{-1}$. We measured $v_B \sin i_B = 62 \pm 2 \text{ km s}^{-1}$ from the spectral line broadening, which also supports our estimate of the radius of Algol B.

If we use the condition of synchronous rotation for Algol A, which does not have to be fulfilled, then for the measured $v_A \sin i_A = 50.5 \pm 0.8 \text{ km s}^{-1}$ we get $R_A = 2.87 \pm 0.04 R_\odot$. If Algol A has been spun up by mass transfer (c.f. Packet 1981, Dechamps et al. 2013) then this would be an upper limit for its radius. An improvement in direct interferometric measurements of its angular diameter, and/or revising the light curve analysis with new constraints from the spectroscopy presented in this work, might allow the radius of this component to be measured to high precision.

7.6.2 Chemical composition and evolution of the components

Predictions of carbon depletion in the atmospheres of mass-transferring systems prompted several observational studies. Carbon underabundances relative to solar were found by Cugier & Hardorp (1988) in an analysis of far-ultraviolet spectra secured from the IUE satellite. The carbon abundance they reported for Algol A, relative to the modern standard solar value, is $[C/H] = -0.32 \pm 0.20$ dex. Tomkin et al. (1993) studied a sample of Algol-type binaries, including Algol itself, and confirmed carbon deficiencies in the whole sample. For Algol A they found $[C/H] = -0.22 \pm 0.15$ dex using high-resolution observations of the C II 4267 Å line. The reported value is relative to the average abundance, $\log \epsilon(C) = 8.28 \pm 0.21$, they determined for the standards. Our result reported in Sect. 7.5.3, $[C/H]_A = -0.16 \pm 0.08$, confirms a small carbon depletion for Algol A, both in terms of the abundance determined from the strongest carbon line in its spectrum (C II 4267 Å) and the deviation of its EW from a calibration derived from standard late-B type stars. Nitrogen lines show a slight overabundance with $\log \epsilon(N) = 7.97 \pm 0.02$, but with the caution that the N II lines used are very weak (EW = 1.0–2.7 mÅ). Referring to the standard solar nitrogen abundance (Asplund et al. 2009), the abundance deviation for Algol A is $[N/H]_A = 0.14 \pm 0.05$.

The ratio between C and N abundances is a sensitive indicator of CNO nucleosynthesis and the efficiency of mass-transfer and mixing processes in stellar interiors. For Algol A we get $(C/N)_A = 2.0 \pm 0.3$ which, compared to the solar value, $(C/N)_\odot = 4.0 \pm 0.7$, indicates that a change in the C/N ratio in Algol A has been detected. CNO-processed layers from Algol B, formerly the more massive of the two inner components, are evidently now exposed on the surface of Algol A, the mass-gaining and currently more massive star. In our previous study on the hot Algol-type binary system u Her (Kolbas et al. 2014) we determined $C/N = 0.89$ for the mass-gaining component. u Her contains components with masses of 7.8 and $2.8 M_\odot$, substantially larger than the masses of the inner pair in Algol. As predicted by detailed chemical evolution models, Kolbas et al. (2014) found stronger carbon depletion in the mass-losing component than in the mass-gaining companion. The progenitor mass of what is now the less massive component in u Her was estimated from evolutionary model calculations to be $M_{\text{donor}} \sim 7.2 M_\odot$, whilst an estimate for the initial mass of Algol B is $M_{B,\text{init}} = 2.7 M_\odot$ (Sarna 1993).

Whilst we succeeded in separating and reconstructing the spectrum of Algol B, a detailed analysis would be premature. The disentangled spectrum still suffers from a low S/N, and the spectral lines are smeared due to its high rotational velocity. But this object dominates X-ray spectra of the Algol system. Drake (2003) used *Chandra* Low Energy Transmission Spectrograph observations to determine the abundances of C and N in corona of Algol B. The analysis was performed relative to the ‘standard’ star, HR 1099. These two stars have shown many similarities in their X-ray spectra, except for the strengths of C and N lines. N enhancement by a factor of 3 compared to the standard star is found, whilst no C lines are detected in the Algol B spectrum, indicating a C depletion relative to ‘standard’ by a factor of 10 or more. Moreover, Drake (2003) found a standard (solar) Fe abundance for Algol B, in agreement with our findings for Algol A and Algol B.

Chapter 8

Discussion and conclusions

Close binary stars of Algol type consist of a main sequence star accompanied with a cool sub-giant or giant, where former is now a more massive component. Apparently, this violates principles of the stellar evolution, and episodic mass transfer between the components has been postulated to explain this evolutionary paradox. In this short-lived process the initially more massive component has been converted into a low-mass giant, and layers which were originally deep within the star and have been altered by thermonuclear fusion during the stars's main sequence evolution are now exposed. The surface chemical composition of both stars are precious diagnostic of the nucleosynthesis processes that occur deep within stars. Theoretical evolutionary models predict changes in abundances of the elements involved in CNO nucleosynthesis.

The intention of this work was to perform detailed analysis of the two mass-transfer binary stellar systems. In order to achieve that new tools for spectra reduction and analysis of disentangled spectra are introduced and applied. Using them we can determine both system orbital parameters, parameters of all the components and their photospheric elemental abundances. Only with high precision in determined quantities makes possible analysis of both CNO element evolution by determining changes in the CNO and metal abundances, and even tracing system's evolution. In order to achieve that, we needed to obtain a time series of high resolution, high S/N ratio spectra of stellar systems of interest in order to perform spectral disentangling, a method of separating components' spectra from the composite ones. Due to co-addition, resulting S/N of separated spectra are even higher. With those high S/N spectra, which now contain spectral features of a single component without contribution from other stars, we performed a detailed stellar photosphere analysis and confident abundance determination that is otherwise not possible with sufficient accuracy. Using spectral disentangling, apart from components' spectra, a set of orbital elements is also optimised. Since the method does not need input template spectra, it does not suffer from different mismatches or bias as cross-correlation technique for measurement of binary star's radial velocities. High stability of fibre-fed spectrograph ensures wavelength stability of all the obtained spectra.

All these steps are necessary in order to produce reliable spectra. Renormalisation of disentangled spectra should be performed with care not to produce artefacts in the stage of as-

trophysical parameter determination and while measuring elemental abundances. Sufficient phase coverage and time series of long-period objects is also difficult to obtain. Also, due to mass accretion and orbit synchronisation, Algols can have high rotational velocities which blend spectral lines making abundances determination difficult. For giant components, which are usually G or K spectral types, low light contribution, high rotational velocity and blended lines introduce further difficulties to analysis.

Due to all the mentioned problems, it is clear that need extra careful reduction procedure is necessary in order to obtain real stellar spectra with no or at least as little as possible bias to be analysed. For analysis many programs were developed from scratch in order to have full control and understanding of their inner procedures to have complete control and understanding of involving procedures. They are along with reliable spectra a necessary counterpart in order to determined stellar parameters and abundances with great confidence.

8.1 Development of new tools

For the purpose of this dissertation, computer codes were developed to facilitate analysis and quantify error calculations. Quality of reduced spectra is of a paramount importance of all subsequent measurements. Therefore, spectra should be carefully reduced with great care in order to exclude all biases and unphysical influences that may remain in badly reduced spectra. The same applies both for high S/N spectra where we have an opportunity to make very precise measurements and lower S/N where careful reduction can be the difference between real and false discoveries. It became apparent that procedure of reduction can depend both on spectrograph used, and spectral type of the star observed, resulting in many approaches for data reduction. Unfortunately, there is no unique recipe that can be followed. Many spectra are poorly reduced using pipelines, resulting in unreliable data and highly biased results. Additionally, normalisation of pipeline spectra can be very questionable, sufficient for cross-correlation velocity measurements, but inadequate for the spectral disentangling. Therefore, we believe that we've developed procedures for optimal and unbiased spectra reduction necessary for reliable and precise subsequent data analysis. This manual reduction procedure can be a lengthy process, depending on the spectrograph and spectral type, but the quality of final results outweigh the invested time for reduction.

- MULTIPLEGLA software for spectra normalisation was developed in JAVA. As there are no adequate routines for the purpose of spectra manipulation needed for the process of échelle orders normalisation, drawing components were developed from scratch. Resulting processed files are a set of normalised spectral orders ready for joining.
- SPECTRAJOINER is also completely custom software developed for optimal joining of merged orders produced by the code MULTIPLEGLA

- The code `PARALLEL` makes possible simultaneous spectroscopic and interferometric orbital solution with some complementary variables acting as mutual constraints and cross-checks.
- If light curves are available, `WDGEN` code uses genetic algorithm and Wilson-Devinney code to find optimal light curve solution.
- `STARFIT` code was developed to find optimal stellar atmosphere parameters. Using disentangled composite spectra, we can simultaneously determine effective temperature, surface gravitational acceleration, light dilution factor and rotational velocity of both components by optimal fitting various available model spectra to the measured ones using the `STARFIT` code. To compensate for systematic velocity shifts and shifts in the continuum, two additional factors are optimised. Finally, light dilution factors can be determined both in unconstrained mode, and constrained mode where their sum must be either 1.0 for binary system or a constant less than one for multiple system. Also, a great check for the quality of optimisation and input spectra is the resulting sum of near 1.0 in unconstrained mode. For excluding parts of spectra with blemishes or spectral features not available in model spectra, parts of fitted spectra can be omitted by editing one of the configuration files. Listed below are only the most important codes developed.
- Genetic disentangling code performs disentangling using genetic algorithm. It makes possible spectra separation overcoming all the intrinsic limits of SVD and Fourier disentangling procedures, especially in used spectral ranges, but at the expense of run time.
- `MCMCBINARY` is a program implementing Monte Carlo Markow Chain (MCMC) error estimates to the `STARFIT` results which do not contain error estimates.
- `FDBOOTSTRAP` code produces error estimates for the orbital parameters optimised by spectral disentangling.

8.2 Abundance pattern for mass-transfer systems

Hot Algol-type system *u Her*, a mass transfer system which components are both more massive and hotter than classical algols was first analysed. As CNO energy production is more pronounced in massive stars, measurable C and N abundance changes are expected. We have secured 43 high resolution échelle spectra from FOCES spectrograph mounted on a 2.2m telescope at CAHA.

After careful reduction, spectral disentangling was performed resulting in two component spectra. As a result of coaddition, already high S/N ratio of resulting spectra was even increased. Spectral disentangling gave us precise orbital semi-amplitudes and reliable mass ratio q . Derived mass ratio was an input parameter for photometric solution as `WD` code is sensitive to the

mass ratio. Photometric data in H_p -band from Hipparcos satellite was also analysed obtaining orbital and component parameters. Light dilution factor were also determined.

Both primary and secondary spectra were simultaneously analysed using STARFIT code in a constrained mode. Surface gravitational acceleration was kept fixed for values obtained from light-curve solution, lifting the degeneracy between T_{eff} and $\log g$ as well as light dilution factor. Projected rotational velocity was measured on metallic lines. From the determined values, we conclude that the system is in a synchronised orbit. Effective temperature was determined by optimisation performed on H_β and H_γ Balmer lines in the stars' disentangled and renormalised spectra. Microturbulent velocity of the primary component was determined from O lines analysis and is found to be consistent with typical early B spectral type stars on the main sequence.

A detailed elemental abundance analysis was performed for the primary component only due to an inadequate S/N ratio of the secondary component spectrum. Abundance analysis was done on a number of spectral lines in high S/N separated component spectrum with no contamination from other component's spectral features. Measured C and N abundances confirmed expected C underabundance of $[C/H] = -0.47 \pm 0.05$ dex and N overabundance of $[N/H] = 0.20 \pm 0.06$ dex, compared to standard cosmic abundance pattern. The uncertainty in derived He abundance does not allow a firm conclusion for its predicted enhancement. Inspecting secondary component's spectrum at position where a strong 4267 Å C line should be present, we detected no measurable line limiting the C abundance to $\log \epsilon(C) \leq 7.5$ dex, also in good agreement with expected theoretical value of 7.4 dex.

Finally, we performed a series of runs using STARS evolutionary code to determine possible initial conditions of u Her. For mass transfer, cases from fully conservative to highly non-conservative were taken into account, and also starting mass ratios ranging from $q^i = 1.25 - 2.0$, the latter being the upper limit considered as higher mass ratio system primaries can not remain in thermal equilibrium during rapid mass transfer phase. The criterium for best solution was matching the current component position in $\log L - \log T_{\text{eff}}$ diagram and matching current component masses and orbital period. Best fitting solution based both on visual inspection of results and finding minimal χ^2 a best solution is found for a highly conservative mass transfer scenario with $q^i = 2.0$. The solutions show that thermohaline mixing changes the C/N ratio on a relatively short time scale. The measured C/N abundance ratio corroborates this picture and indicates a strong mixing of the stellar material. As u Her is composed of two stars with mass high rate of CNO nucleosynthesis, the result is expected.

Algol is an hierarchical triple system consisting of the inner pair, Algol A and B which has undergone a mass transfer phase. The third component, Algol C, is in the outer orbit and has no influence on the mass transfer processes in the close inner pair. Theoretical evolutionary models (Sarna 1992) predict changes in C abundances. In order to confirm those expectations, a time series of high resolution and high S/N spectra were obtained from fibre-fed FIES and BOES échelle spectrographs, which were carefully reduced using manual process and devel-

oped dedicated programs. Due to lengthy SPD process for the available high-resolution spectra, successive same phase spectra were binned in order to reduce their number. Only with even increased S/N due to SPD and large wavelength range renormalised component spectra can we determine confident orbital and component properties and elemental abundances (for Algol A and C). Only with those preparations we can separate all three components, even Algol B which contributes 1-1.5% to the total light of the system, depending on the wavelength range.

Stellar atmosphere parameters were first determined by optimal fitting of disentangled component spectra using STARFIT code. With fixed $\log g_C$ from Richards et al. (1988) solution. Rotational velocity was optimised using unblended metal lines. Initial T_{eff} s were determined. Additional tuning was performed from null-correlation between T_{eff} and EW of Fe I lines for both Algol A and C. Algol C temperature was further tuned by the requirement of ionisation balance between atom Fe I and singly-ionised Fe II. As a further check of the procedure, the difference in measured abundances of two ionisation stages was determined to be very consistent with difference of $\Delta \log \epsilon(\text{Fe}) = 0.05 \pm 0.11$. As light dilution factors were also determined from disentangled spectra using STARFIT, an additional check on determined values was the non-correlation of determined Fe abundance of wavelength of the measured line. As the multiplication factor for renormalising Algol C is much higher, ~ 16.5 , the success of the test on that component is even more critical.

The most interesting task was determination of the elemental abundance of A component, especially CNO elements. For the tertiary component discriminating between the proposed Am and A spectral was of special interest. Spectrum of Algol B, although disentangled was not of sufficient quality for detailed abundance analysis, with further complication due to its relatively high rotational velocity making a spectrum already high in number of spectral features highly blended. Fortunately high rotational velocity of Algol A was not a problem due to its relative scarceness in spectral lines so the line blending is not severe. Although the many interesting spectral lines of C, N and O in the Algol A have relatively low EWs, a high S/N of ~ 1000 and uncontamination of disentangled spectra with other components contribution makes reliable abundance determination possible. Carbon deficiency of $[\text{C}/\text{H}] = -0.16 \pm 0.08$ dex was determined compared to recent standard solar carbon abundance values from Asplund et al. (2009). An excellent indicator of CNO nucleosynthesis is the ratio between C and N abundance. Determined value for Algol A is $(\text{C}/\text{N})_A = 2.0 \pm 0.3$.

The main CNO process marker is C/N abundance ratio which was determined for the two mass transfer systems. For Algol, the determined value is $(\text{C}/\text{N})_A = 2.0 \pm 0.3$ and for higher mass u Her $(\text{C}/\text{N})_A = 0.89 \pm 0.2$. Both values are well below the current expected solar ratio value of $(\text{C}/\text{N})_{\odot} = 4.0 \pm 0.7$. The maximum expected theoretical values for CNO processed C/N ratios range from 0.1 before Thermohaline mixing to 1.0 after the mixing has occurred. As the u Her is a high mass, so called 'hot Algol' system with efficient CNO cycle, a larger C/N ratio change is expected that in the case of lower mass Algol, as is determined. Tracing

evolutionary paths of u Her, best found initial donor-star mass was $7.16 M_{\odot}$ resulting in efficient CNO cycles. As evolutionary paths for Algol were not determined and we rely on previous evolutionary calculations (Sarna 1992) which should be revised with this improved data. We can only limit the minimal initial mass of mass-donor to one half of the total Algol A-B inner mass of $M_A + M_B = 4.16 M_{\odot}$ or $M_{\text{donor}}^i \geq 2.08 M_{\odot}$, near the lower mass limit for expected CNO abundance changes to be measurable.

8.3 Future plans

Despite of all the results from this work, there are plans to expand developed tools and revisit observed stellar systems to further improve current results and perform additional analyses.

As genetic forward disentangling code is still in early stages of development, it is my intention to further develop it. Only two components can be separated for now and in the future, the code should be able to include multiple star systems.

PARALLEL code for constrained spectral disentangling and astrometry solution currently links some common parameters serving as constraint. However, an additional possible constraint is by matching semimajor axes from astrometric solution and SPD, which are currently independent. That would further constrain the derived orbital parameters and make them even more reliable.

STARFIT now optimises only two stellar components and it is my intention to implement simultaneous optimisation for an arbitrary number of components. Further, the current models included in the code are calculated for a single metallicity. If that grid of models was expanded with ones calculated for a range of metallicities, one should be able to include metallicity into the optimisable parameters.

By obtaining even more spectra of the system, the S/N can be improved making possible the detailed abundance analysis of the secondary component, further proving expected CNO abundance patterns.

Securing even more spectra of Algol, we could further improve the orbital solution for the large 680 d orbit. It may even be possible to obtain enough S/N ratio for the secondary component, making possible even better stellar atmosphere parameters determination and possibly a preliminary abundance analysis.

I hope to include more stellar systems in the detailed elemental abundance analysis. I wish to cover a complete range of stellar masses, from stars that have just enough mass to have significant energy production from CNO cycle to high mass systems with efficient CNO en-

ergy production, in order to confirm our understanding of evolutionary changes in elemental abundances and components evolutionary paths.

Poglavlje 9

Prošireni sažetak

Zvijede su glavni građevni elementi galaksije i generatori njihove evolucije. Razumijevanje njihove strukture bilo je velik uspjeh astrofizike 20. stoljeća. Ipak, teorija zvjezdane evolucije još uvijek nije riješena. Otvoren je broj pitanja koja čekaju odgovor.

Kako bismo razumjeli zvjezdanu strukturu, nuklearne izvore energije i evoluciju, potrebna su nam precizna opažanja različitim metodama. Samo tako možemo usporediti rezultate teorijskih predviđanja sa opažanjima te ih potvrditi i upotpuniti. Dvojni su zvjezdani sustavi neprocjeniv izvor fundamentalnih zvjezdanih svojstava (mase i radiusi) određeni sa visokom preciznošću. Stoga nam oni služe kao testovi za evolucijske modele. Obje komponente moraju biti spektroskopski opažene kako bi se direktno izmjerili parametri. Za korisnu usporedbu s modelima trebamo dodatno informacije o efektivnoj temperaturi i metalicitetu. Tada možemo provesti detaljnu analizu kemijske zastupljenosti u zvjezdanoj fotosferi.

9.1 Motivacija i ciljevi

Motivacija ovog rada je određivanje zastupljenosti CNO i drugih elemenata kako bismo dobili uvid u zvjezdanu unutrašnjost za CNO ciklusa nukleosinteze. CNO promijenjenu zastupljenost možemo direktno opažati samo u dvojnim sustavima koji su prošli fazu prijenosa tvari u jednoj fazi svoje evolucije. Preciznim mjerenjem zastupljenosti, možemo odrediti tijek prijenosa tvari, kao i prošlost razvoja sustava (početne parametre). Također, (ne)opažanjem promjena u CNO zastupljenosti možemo odrediti uvjete odnosno evolucijsku fazu u kojoj je došlo do prijenosa tvari. Mjerena zastupljenost određena na zvijezdi primaocu se polako vraća prema početnoj zastupljenosti zbog termohalinskog miješanja. Miješanje na površini zvijezde davaoca se zbiva zbog pojave konvektivnog sloja na površini zvijezde. Za potrebe ovog rada za analizu su izabrana dva sustava sa prijenosom tvari, u Her i β Per. Spektri visoke rezolucije i odnosa signal/šum su snimljeni kako bismo procesom spektralnog raspletljavanja razdvojili kompozitne spektre u spektre zasebnih komponenata. Na razdvojenim spektrima možemo vršiti detaljnu analizu uvjeta zvjezdanih fotosfera kako i mjeriti zastupljenost elemenata.

9.2 Dvostruki i višestruki zvjezdani sustavi

Do nedavno se pretpostavljalo da je većina zvijezda samistalna, bez pratilaca a kamoli planeta. Sada znamo da većina zvijezda ima jednog ili više pratilaca, od kojih su neki direktno opazivi, a neki neopazivi. Ove potonje možemo detektirati spektroskopski (mjeranjem Dopplerovog pomaka spektralnih linija u vremenskom nizu spektara), fotometrije (praćenjem promjene sjaja) te astrometrijski (praćenjem promjene položaja zvijezde). Zvijezde u dvojnog sustavu prolaze kroz evoluciju slično kao samostalne zvijezde, ali njihovi pratioci mogu imati utjecaj i na evoluciju i na rezultate pojedinih faza razvoja. Dvojne su zvijezde međusobno gravitacijski vezane te obje kruže oko zajedničkog centra mase. Također su vezane u zajedničkom gravitacijskom potencijalu koji je kompleksnijeg oblika nego za samostalne zvijezde. U ovom slučaju u blizini sustava ekvipotencijalne plohe čine zatvorene krivulje oblika broja osam te postaju sferične tek na većim udaljenostima od sustava. Ekvipotencijalna ploha na kojoj tvar prestaje biti vezana za matičnu zvijezdu zove se kritična Rocheova ploha (Slika 2.1).

9.2.1 Zašto su dvojne zvijezde važne

Dvojne su zvijezde važne zbog mogućnosti preciznog određivanja fundamentalnih zvjezdanih parametara, osobito u usporedbi s onima za samostalne zvijezde. To nam daje mogućnost ka precizno usporedimo mjerene parametre sa rezultatima modela te ih potvrdimo ili upotpunimo. Gravitacijska interakcija između dvije zvijezde nam omogućava da odredimo njihove mase. U općenotom slučaju možemo odrediti samo omjer mase, a u povoljnijim slučajevima i individualne mase komponenata. Iz spektroskopskih mjerenja možemo odrediti i projekciju brzina, kao i orbitalnu udaljenost te masu. Analizom spektralnih linija možemo dobiti daljnji uvid u zvjezdanu rotaciju, temperaturu i površinsko gravitacijsko ubrzanje, kao i doprinos svjetla pojedine komponente ukupnom svjetlu sustava. Nadalje, zbog mogućih interakcija između komponenata, oblik zvijezde može odstupati od kružnog što uzrokuje promjenu vidljivih svojstava i promjenu u evoluciji. Stoga, još nije sigurno da li evolucijski modeli samostalnih zvijezda u potpunosti opisuju i evoluciju zvijezda u višestrukim zvjezdanim sustavima.

9.3 Orbitalni elementi

Termin orbitalni elementi potječe još iz doba proučavanja gibanja planeta, ali se može direktno primijeniti na orbite zbijezda. Da bismo je definirali, trebamo 7 parametara.

- P - period dvojnog sustava
- i - kut inklinacije ravnine orbite
- Ω - kut položaja linije čvorova

- ω - argument periastrona, definira orijentaciju najduže osi eliptične orbite u orbitalnoj
- a - velika poluos orbite
- e - ekscentricitet
- T - vrijeme prolaska kroz periastron, točku najbližu centru orbite

Grafički prikaz navedenih elemenata dan je na slici 2.2 Period P je povezan sa velikom poluos orbite općenitim oblikom Keplerove jednadžbe

$$\frac{a^3}{P^2} \propto M_1 + M_2 \quad (9.1)$$

gdje su M_1 i M_2 mase dvije zvijezde. Kompletan dinamički opis sustava zahtjeva poznavanje perioda, koji se smatra dodatnim orbitalnim elementom. Parametri P , i , ω , e i T mogu biti određeni promatranjem dvostrukog sustava. Ukoliko nisu dostupna mjerenja radijalnih brzina, nije moguće razlučiti točan iznos Ω do na neodređenost od 180° . Velika poluos može biti određena samo u relativnom iznosu ukoliko ne znamo udaljenost do sustava, kada možemo odrediti i apsolutnu vrijednost. Ukoliko postoje mjerenja radijalnih brzina te su mase komponenta pretpostavljene iz spektralnog tipa (računajući na veliku nepouzdanost tako određenih masa), velika poluos može biti ugrubo određena iz 3. Keplerovog zakona. Ova metoda se naziva dinamička paralaksa. e i ω mogu biti određeni iz oblika krivulje brzina. Uz to, moguće je odrediti i još dva parametra:

- V_o - radijalna brzina centra mase sustava
- K_1 - poluamplituda radijalne brzine primarne komponente
- K_2 - poluamplituda radijalne brzine sekundarne komponente

Brzine su izražene u jedinicama km/s, a period u danima. U tim jedinicama, vrijednosti K su vezane uz orbitalne elemente kao

$$a_{1,2} \sin i = 13751(1 - e^2)^{1/2} K_{1,2} P \text{ [km]} \quad (9.2)$$

$$M_{1,2} \sin i = 1.0385 \cdot 10^{-7} (1 - e^2)^{3/2} (K_1 + K_2)^2 K_{2,1} P \text{ [M}_\odot\text{]} \quad (9.3)$$

uz vezu

$$a = a_1 + a_2 \mathbf{i} \quad (9.4)$$

$$a_2/a_1 = K_2/K_1 = M_1/M_2 \quad (9.5)$$

$K_1 + K_2$ je stoga mjera projekcije velike poluosi u ravninu koja sadrži doglednicu. Ukoliko je dostupan samo jedan spektra, može se odrediti samo vrijednost $a_1 \sin i$ te je jedina informacija o masi tzv. funkcija mase

Ukoliko je sekundarna komponenta manje mase od primarne, može se pokazati da su minimalne vrijednosti za $M_{1,2} \sin^3 i$ određene kao $4f(m)$.

U slučaju pomrčinske dvojne zvijezde, period se može jednostavno odrediti, kao i kut i obzirom da utječe na oblik i dubinu krivulje sjaja. Ukoliko se mogu opaziti obje pomrčine, može se odrediti veličina $e \cos \omega$ iz razmaka među njima, izražena u jedinicama dijela perioda. Iz krivulje sjaja ne može se dobiti nikakva informacija o poluosi. Oblik i trajanje pomrčina u krivulji sjaja ovisi o dimenzijama komponenata R_i , izraženima u jedinicama dijela razmaka. Ukoliko je sustav također promatran i spektroskopski, dimenzije mogu biti izračunate u apsolutnoj vrijednosti.

9.4 Poluodvojene dvojne zvijezde

Ukoliko u dvostrukom zvjezdanom sustavu jedna komponenta ispuni svoju kritičnu Rocheovu plohu, to znači da je sustav prošao barem kroz jednu fazu prijenosa tvari između dvije komponente, gubitak tvari iz sustava ili oboje. Stoga, bilo bi pogrešno direkto uspoređivati podatke i masama i dimenzijama zvijezda u dvostrukom sustavu sa rezultatima modela za samostalne zvijezde. Evolucijski kodovi moraju biti modificirani kako bi uzeli u obzir postojanje najvećeg mogućeg volumena kojega zvijezda može imati u dvostrukom zvjezdanom sustavu te omogućiti promjene u orbitalnom periodu i dimenzijama kao posljedicu procesa prijenosa tvari.

Klasični Algoloidi su poznati po tome što imaju primarnu komponentu srednje mase koja se nalazi na glavnom nizu te se nalazi unutar svoje dostupne Rocheove plohe te sekundarnu komponentu koja ispunjava kritičnu Rocheovu plohu sa tipičnim omjerom mase od $q \sim 3$. Sekundarna je obično u fazi pod-divova te je naizgled kasnije evolucijske faze od svojeg masivnijeg pratioca, što je paradoksalna situacija sa standardnog evolucijskog gledišta. Paradoks je objašnjen u šezdesetim godinama na temelju prijedloga objašnjenja Crawford (1995) koji je predložio da je prepunjenje Rocheovog volumena kao važan mehanizam u evoluciji dvojnih sustava koji vodi obrnutu omjera masa, tako da je inicijalno masivnija komponenta postala sekundarna, dok je inicijalno manje masivna postala primarna komponenta. Prvi modeli prijenosa tvari uključivali su samo konzervativan prijenos, da bi se smanjio parametarski prostor modela. Kako je postalo evidentno da je konzervativan slučaj preoptimističan i prejednostavan model (Popper 1973, Refsdale et al. 1974) postalo je nužno postulirati ne-konzervativan prijenos tvari i zakretnog momenta. Mnoge mreže modela uključuju slučajeve A, B i C prijenosa tvari (poglavlje 2.5) te promijenjiv iznos izgubljene tvari i zakretnog momenta. Konkretno za sustave slične Algolu, De Greve (1989, 1993), De Greve i de Loore (1992) te de Loore i De Greve (1992) su uzeli u obzir velik raspon evolucijskih modela, dok je Sarna (1993) u detalje proučavao evoluciju samog Algola. Ukupan je zaključak da konzervativna evolucija ne može objasniti

svojstva Algoloida te da je nekonzervativan prijenos nužan za rane faze B. U nastojanju da da bolje kvantitativne podatke za usporedbu s modelima, Maxted (1994) te Maxted i Hilditch (1996) sakupljaju podatke za 9 Algoloidnih sustava za koje su parametri bili određeni konzistentno i pouzdano iz rješenja svjetlosnih krivulja i radijalnih brzina dvije komponente, uključivši i ne-keplerske korekcije. Trenutne primarne komponente su zvijezde na glavnom nizu, dok su sekundarne sve prevelike i presjajne za odgovarajuću zvijezdu dane mase na glavnom nizu, za faktor od 10 puta ili više. Na temelju usporedbe mjerenih podataka i modela, čini se da je gubitak zakretnog momenta nužan pri proračunima. U granicama točnosti mjerenja za Algolovske sekundarne komponente, određene zastupljenosti ugljika mogu služiti kao jako ograničenje na evolucijski model, pod pretpostavkom da su podaci dovoljno točni. Po postojećim mjerenjima, Sarna i De Greve su pokazali da slaganje između mjerene podzastupljenosti ugljika i teorijskih modela kao dobra indikacija, ali ne i konačna vrijednost.

9.5 Échelle spektrografi

Échelle spektrografi su posebna verzija spektrografa sa difrakcijskom rešetkom koji dobiveni spektar razdvajaju u spektar koji se sastoji od više segmenata koji pokrivaju kompletan raspon valnih duljina, ali sa visokom rezolucijom. Kao i spektrograf sa difrakcijskom rešetkom, opisan je jednadžbom

$$m\lambda = d(\sin\alpha \pm \sin\beta) \quad (9.6)$$

pri čemu je m red disperzije, d udaljenost zareza, kut α upadni kut u odnosu na normalu, a kut β kut raspšenja te λ valna duljina (slika 4.1).

Jedno od najvažnijih svojstava svakog spektrografa je njegova rezolucija, definirana jednadžbom

$$R_o = \frac{\Delta\lambda}{\lambda} = \frac{mW}{d} = mN \quad (9.7)$$

R_o je rezolucija, $\Delta\lambda$ najmanja razlučiva razlika u valnim duljimama, W dimenzija rešetke te N broj disperzivnih elemenata.

Échelle spektrograf se zasniva na rešetci kao disperzivnom elementu, međutim upadno svjetlo se raspršuje na manjoj površini rešetke (onoj pod visokim kutem u odnosu na normalu rešetke). Rezultat je taj da su reflektirani redovi bliže te se znatno preklapaju. Zbog toga bi u normalnom korištenju bili praktički neupotrebljivi. Kako se u échelle spektrografu koristi dodatni disperzivni element koji raspršuje spektar u smjeru okomitom na smjer prve disperzije, redovi više nisu stopljeni. Ovaj se postav može vidjeti na slici 4.1, gdje se i upadna i reflektirana zraka nalaze sa iste strane u odnosu na normalu rešetke. U ovom je modu rada rezolucija definirana kao

$$R_0 = \frac{2W \sin \delta}{\lambda} \quad (9.8)$$

gdje je δ kut kao prikazan na slici 4.1. Spektralni redovi u ovom postavu sa visokim redom disperzije se preklapaju, tako da možemo dodatno definirati i veličinu koju nazivamo slobodno spektralni raspon, raspon valnih duljina koje nisu prekrivene susjednim redom, pomoću relacije

$$m\lambda' = (m + 1)\lambda \quad (9.9)$$

gdje je λ' valna duljina sredine reda m , a λ reda $m + 1$. Centralna valna duljina $i + 1$ -og reda (također zvana valna duljina blejza) može se izračunati relacijom

$$\lambda_i = \frac{2d \sin \delta \cos \theta}{m} \quad (9.10)$$

gdje su δ i θ definirani kao na slici 4.1. Stoga je slobodni spektralni raspon $\Delta\lambda$ reda m

$$\Delta\lambda = \lambda' - \lambda = \frac{\lambda}{m} \quad (9.11)$$

te je prikazan na slici 4.2. Očito je da se mijenja monotono od reda do reda.

Konačno, intenzitet svakog reda se mijenja. Jednadžba rešetke opisuje u kojem smjeru je svjetlo reflektirano, ali ne i njegovu količinu. Količina je određena relacijom 9.12

$$I(\alpha, \beta) = \left(\frac{\sin \left(N \frac{\pi d}{\lambda} (\sin \beta + \sin \alpha) \right)}{N \sin \left(\frac{\pi d}{\lambda} (\sin \beta + \sin \alpha) \right)} \right)^2 \cdot \left(\frac{\sin \left(\frac{\pi b}{\lambda} (\sin \beta + \sin \alpha) \right)}{\frac{\pi b}{\lambda} (\sin \beta + \sin \alpha)} \right)^2 \quad (9.12)$$

gdje je b dimenzija zareza. Blaze funkcija ima maksimum pri uvjetu $\alpha = \beta$, odnosno u totalnoj refleksiji, što nije iskoristivo. Da bi se koristila kao disperzivni element, rešetka mora imati vrh blazea u nekom korisnom višem difrakcijskom redu, što se može postići zakretanjem zareza dok se ne postigne uvijek spekularne refleksije.

Kao što je spomeunuto, susjedni reflektirani redovi se dodatno raspršavaju elementom dodatne disperzije koji razdvaja do tada preklapajuće redove. Pošto za to nije potrebna visoka disperzija, za tu svrhu se obično koristi prizma. Rezultantni spektra je prikazan na slici 4.3. Kompletan postav spektrografa je prikazan na slici 4.4.

Sam spektrograf mora biti vrlo stabilan, otporan na fizičke deformacije uzrokovane i pokretanje i vanjskim uvjetima. Stoga mora biti maksimalno izoliran. Da bi se to postiglo, uobičajeno je da se ne montira na teleskop već se nalazi u obližnjoj zgradi koja je zaštićena i od pokreta i atmosferskih uvjeta. Također, drži se u stalnim atmosferskim uvjetima te fiksnoj temperaturi i vlazi kako ne bi bilo utjecaja termičkih distorzija na uređaj i optički put. Zbog pojave termalnog šuma, CCD kamera se drži na niskoj temperaturi, u kriostatu. Kako je spektrograf dislociran od teleskopa, signal sa teleskopa se dovodi pomoću optičkog vlakna.

9.5.1 Korišteni échelle spektrografi

Spektri u ovoj disertaciji su snimljeni na tri različita uređaja - FIES na Nordic Optical Telescope (NOT, La Palma), BOES na Bohyunsan Optical Astronomy Observatory (BOAO, J. Koreja) te FOCES, Centro Astronomico Hispano-alemagne (CAHA, Španjolska).

FIES

FIES je échelle spectrograf na 2.5m teleskopu maksimalne spektralne razlučivosti $R = 67000$. Pokriva valne duljine od 3700 do 7300 Å, bez praznina u svim redovima. Lociran je u zasebnoj, dobro izoliranoj zgradi do teleskopa. Koristi Thorij-Argon (ThAr) žarulju kao izvor za kalibraciju valnih duljina. Od svih korištenih spektrografa, FIES se pokazao kao najkvalitetniji, sa odlično definiranim blejzovima što je nužan uvjet za kvalitetnu redukciju spektara. Također, dostupan je detaljan ThAr atlas valnih duljina za provedbu kalibracije.

BOES

BOES je montiran na 2m teleskopu na Bohyunsan Optical Astronomy Observatory u Južnoj Koreji.

FOCES

FOCES je bio instaliran na 2.2m teleskopu na CAHA opservatoriju. Maksimalna mu je spektralna rezolucija bila $R = 65000$, što je više nego zadovoljavajuće, međutim imao je ograničenje odnosa signal-šum na maksimalno 250, što je utjecalo na konačnu kvalitetu spektara. Raspon valnih duljina koji je pokrivao je od 3800 do 7500 Å u 70 spektralnih redova koji se svi preklapaju. Kako je održavanje prekinuto, počele su se javljati greške, osobito na CCD kameri, što je evidentno na snimljenim slikama te drastično utječe na redukcije. Greške su i defekti na linijama mreže CCD kamere i defekt u osjetljivosti cijele jedne strane kamere, što rezultira neiskoristivošću cijelog desnog krila svakog reda. Preostali dio spektra je bio zadovoljavajuće kvalitete, međutim u korištenju reduciranih spektara je valjalo paziti na moguće utjecaje navedenih defekata.

9.6 Genetički algoritmi

Genetički algoritmi (GA) postaju sve popularnija metoda optimizacije. Ubrzavanjem centralnih procesora (CPU) omogućuju pronalaženje rješenja kompleksnih problema u sve kraćem i kraćem vremenu. U asrofiziku ih je uveo Charbonneau (Charbonneau 1995) kodom PIKAIA, koji se dalje koristi kao temelj za implementaciju svih modernijih izvedbi.

Osnovna je ideja genetičkog algoritma oponašanje prirodne selekcije kako bi se pronašla i očuvala najbolja rješenja (preživljavanje najboljih) za neki problem. Genetički algoritmi opon-

ašaju taj prirodni proces u proceduralnoj implementaciji koja se može implementirati u obliku računalnog koda. Naravno, GA ima mnoge prednosti u odnosu na druge metode optimizacije, kao i mane. Glavna je prednost mogućnost pretraživanje kompletnog danog parametarskog prostora, primjerice za globalnim minimumom ili maksimumom, bez da rješenje u procesu permanentno završi u nekom od lokalnih ekstrema, kao što je slučaj u metodama koje se zasnivaju na gradijentnom načinu optimizacije. Upravo zbog te mogućnosti odmaka od lokalnih ekstrema, položaj početne točke traženja rješenja u parametarskom prostoru nije od kritičnog značenja, kao u drugim metodama. S druge strane, najveća je mana algoritma njegova zahtjevnost na računalno vrijeme. Srećom, danas su dostupna računala za više procesora i jezgara što donekle umanjuje taj nedostatak. Također, otegotna je okolnost što GA zbog svoje prirode ne garantira da će pronaći optimalno rješenje. Iako malo vjerojatan, valja imati na umu i ovaj mogući ishod.

Osnovna ideja implementacije GA je vrlo jednostavna. Obzirom da je motiviran prirodnom selekcijom, terminologija korištena pri opisu prirodnog odabira se koristi i za računalnu verziju algoritma. Glavni objekt u GA je jedinka, u našem slučaju jedno od beskonačno mogućih rješenja problema. Jedinka se sastoji od gena, svojstava koja opisuju zadani parametarski prostor. Skup jedinki čini generaciju u kojoj je svaka od njih testina da se vidi kako zadovoljava rješenje problema. Testiranjem adekvatnosti joj se pridjeljuje numerički iznos adekvatnosti, time viši što jedinka bolje rješavan problem. Jedinke iz pojedine generacije se kombiniraju (reprodukcija) da bi se stvorila nova generacija jedinki koja se također testira i dalje reproducira. Ova je ideja u teoriji vrlo jednostavna, ali je njezina računalna implementacija komplicirana. Kompleksnost se manifestira u odabiru načina kao će se prikazati geni te u nužnosti odabira metode testiranja svake od jedinki kako bi joj se pridijelila objektivna numerička vrijednost sposobnosti rješavanja problema. Zoran primjer jednog mogućeg problema koji valja riješiti je prikazan na slici 5.9. Na slici je iscrtana funkcija

$$(x, y) = [x(1 - x)y(1 - y)\sin(n\pi x)\sin(n\pi y)]^2, \quad n = 7 \quad (9.13)$$

kao dobar primjer. Ispod 3D prikaza je 2D prikaz intenziteta zbog boljeg zora. Očito je da postoji samo jedan, dobro definiran globalni maksimum, ali također da postoji mnoštvo sličnih lokalnih maksimuma koji bi napravili znatne probleme drugim metodama. Međutim, uz dovoljno generacija (računalnog vremena), algoritam jednostavni izlazi s njima na kraj.

Osnovna je ideja GA vremenska evolucija jedinki. Pod jedinkom se smatra potpun skup informacija koji, više ili manje uspješno rješava dani problem. Definirana je svojim parametrima - genima. Primjerice, da bi se riješio problem pronalaženja globalnog maksimuma sa slike 5.9, pomoću gena nužno je držati informaciju o x i y položaju unutar parametarskog prostora. Stoga, svaka jedinka ima dva gena, od kojih svaki opisuje položaj na jednoj od koordinatnih osi. Zbog jednostavnosti implementacije, jedinke imaju numeričku vrijednost od 0.0 do 0.9. Taj se normalizirani raspon onda može proširiti na bilo koji željeni raspon parametara u parametarskom

prostoru. Prvi problem u implementaciji je kako računalno prikazati gene. Pokazalo se da je za tu svrhu najbolje koristiti računalno polje znakova ili stringove, ovisno o računalnom jeziku u kojem se vrši implementacija. Iako se to čini kontraintuitivno i pomalo nespretno, pokazuje se da je to vrlo praktično za daljnju implementaciju. Također, važno je donijeti odluku o potrebnoj numeričkoj preciznosti pri prikazu gena. Slijedeći problem je ocjena adekvatnosti. U danom primjeru, jednostavno je uvrstiti vrijednosti gena u danu relaciju i izračunati rezultat, međutim u realnim primjerima najčešće ne znamo funkcionalnu ovisnost problema koji želimo riješiti te je moramo nekako definirati. Stoga, često ne znamo apsolutni iznos adekvatnosti već samo možemo uspoređivati relativne adekvatnosti pojedinih jedinki, bili unutar generacije ili između njih.

Kao stvarni primjer implementacije, prvo valja odabrati broj jedinki u (početnoj) generaciji. Uzmimo ih, na primjer, 100. Svako od 100 jedinki damo za inicialne vrijednosti gena generirani nasumičan broj, po jedan za svaku dimenziju problema. Također biramo i preciznost, na primjer 6 decimalnih mjesta. Tako npr. jedna od jedinki može imati gene

$$x = 0.234354$$

$$y = 0.594839$$

Zatim valja izračunati adekvatnost svake od 100 jedinki sa tako generiranim genima. Time smo završili sa inicijalnom populacijom. Slijedeći je korak reprodukcija - kombiniranje jedinki iz trenutne generacije u novu. Biramo 50 parova jedinki. Izbor nije nasumičan, već bolja jedinka ima veću vjerojatnost da će biti izabrana za reprodukciju. Algoritama za izbor ima više, a najkorišteniji su algoritmi nizanja i ruletnog izbora.

Nizanje je jednostavno sortiranje jedinki prema njihovoj adekvatnosti. Tada, svaka jedinka dobiva vjerojatnost izbora kao $1/i$ gdje je i njezin redni broj u sortiranju. Stoga, najbolja jedinka ima vjerojatnost izbora (ne-jediničnu!) od 1, slijedeće $1/2$, $1/3$ itd. Ukupna vjerojatnost izbora je zbroj svih vjerojatnosti. Tada se bira nasumičan broj od 0 do ukupne zbrojene vjerojatnosti te se gleda u zbroju kojoj jedinki pripada taj izabrani broj. Naravno, prva jedinka ima najveću vjerojatnost izbora.

Ruletni izbor je alternativan način pridavanja vjerojatnosti izbora za reprodukciju, u kojem se koristi jedinkina numerička vrijednost adekvatnosti. Pri tome može postojati znatna razlika u iznosima pa najbolja jedinka može imati adekvatnost 50.0, a neka u sredini populacije samo 0.15. Ostatak procedure se ponavlja kao i ranije, samo što bolje jedinke imaju znatno veću vjerojatnost da budu izabrane.

Izbor izbornog algoritma varira od primjene do primjene te se zasniva na korisnikovom odnosno programerovom iskustvu sa GA te razumijevanju problema koji se želi riješiti. Ukoliko adekvatnost nekoliko najboljih jedinki drastično zasjenjuje ostatak populacije, tada ruletni izbor brzo može završiti u degeneraciji populacije - iscjepenje genetskog raspona nakon samo

nekoliko generacija. S druge strane, izbor nizanem može favorizirati i jedinke s manjom adekvatnošću te njihovim opetovanim držanjem u populaciji drastično usporiti konvergenciju ka rješenju i produžiti trajanje optimizacije. Kako GA može zahtjevati rad i po nekoliko dana, i duže, evidentno je da je optimalan izbor parametara nužan.

Pogodno izabравši način izbora, možemo prosljediti sa reprodukcijom. Osnovna je ideja stvoriti novu generaciju od 100 jedink. Za tu svrhu biramo 50 parova jedinki iz prošle generacije, pri čemu pazimo da su obje jedinke-roditelja različite. Izabравši roditelje, izabiramo novi nasumični broj od 0 do 1. Ukoliko je broj manji ili jednak nekoj izabranoj vrijednosti, recimo 0.3, jedinke samo prekopiramo u novu generaciju. U suprotnom, vršimo preklapanje gena. Za tu proceduru biramo nasumičan broj od 0 do izabrane preciznosti prikaza gena. Dobijemo li npr. broj 3, svaki od gena ćemo prekinuti na tom mjestu i napraviti zamjenu segmenata između roditelja. Na primjeru za x -gen roditelja 1 i 2 zamjena izgleda (zanemarivanjem početne vrijednosti 0.):

$$x_1 = 0.234354$$

$$x_2 = 0.670383$$

postane

$$x_1 = 234354$$

$$x_2 = 670383$$

prekinuto nakon 3. znamenke

$$x_1 = 234|354$$

$$x_2 = 670|383$$

(9.14)

Nakon toga, stvaramo dvije nove jedinke, djece, u novoj generaciji preklapanjem gena roditelja na toj nasumično izabranoj lokaciji, uz dodavanje početne vrijednosti 0.

$$x_1 = 0.234383$$

$$x_2 = 0.670354$$

(9.15)

Ovisno o položaju točke cijepanja, novo stvoreni geni uzrokuju veći ili manji pomak u parametarskom prostoru. Konačno, uvodimo i mutaciju kao mogućnost promjene genetske baze. Ponovno za svaku znamenku u reprezentaciji gena biramo nasumičan broj od 0 do 1 te ako je manji od neke predefinirane vrijednosti, npr. 0.02, mutiramo gen. Mutacija se vrši tako da se generira novi nasumičan broj od 0 do 9 te se postojeće znamenka u genu mijenja novostvorenom, primjerice za prvu znamenku:

$$x_2 = 0.670354 \Rightarrow x_2 = 0.270354$$

Obzirom da položaj mutacije, značajno smo promijenili položaj jedinke u parametarskom prostoru. Ponavljajući ovaj cjelokupni postupak 50 puta, stvaramo novih 100 jedinki od kojih njih 70 ima preklapljene gene na nekoj nasumičnoj poziciji te su moguće i dodatno mutirani. Zapravo, stvaramo samo 98 novih jedinki ukoliko se odlučimo za pravilo elitizma, što znači da se dvije najbolje jedinke automatski preslikavaju u novu generaciju, osiguravajući da nikada ne izgubimo najbolje rješenje. Elitizam može znatno ubrzati proces konvergencije, a u mnogim kompleksnim slučajevima može biti prevaga između pronalaženja i nepronalaženja rješenja uopće.

Za kompleksnije primjene GA, gde simultano prilagođavamo mnogo parametara, od 5 pa do više stotina ili tisuća kao u primijeni na genetičko raspetljavanje spektara, moramo uvesti dodatne mehanizme optimizacije parametara algoritma i njihova izbora. Primjerice, pri zahtjevnom i dugotrajnom testiranju adekvatnosti, koristimo manji broj jedinki u generaciji uz povećavanje vjerojatnosti mutacije. Izabrana preciznost u prikazu gena ne utječe znatno na brzinu provedbe algoritma, stoga se koristi uobičajena preciznost od 6 do 10 znamenaka. U slučajevima gdje mali broj jedinki ima veliku ukupnu vjerojatnost reprodukcije, često kod ruletnog izbora ili malog broja jedinki u generaciji, biramo odgovarajuću metodu izbora. U slučaju da nam se genetski izbor suzi na mali broj gena odnosno da mnoge jedinke imaju iste ili slične gene, možemo izabrati da svaki odabrani broj generacija drastično povećamo vjerojatnost mutacije, sa na primjer 0.3 na 30% kako bismo unijeli novu numeriku. Alternativni pristup je da se također u uvjetima kada dolazi do generacije u odabranoj generaciji izbriše najslabijih 30% jedinki te ih se zamijeni potpuno novo generiranim jedinkama, kao pri kreiranju inicijalne populacije i time omogućimo efikasnije pretraživanje parametarskog prostora. Mogućnosti su brojne te su ograničene samo inventivnošću osobe koja implementira algoritam te njegovim iskustvom sa GA i različitim načinima primjene. Nažalost, najkompleksnije primijene algoritma za optimalno korištenje zahtjevaju mnogo iskustva i s programerske i korisničke strane.

Sa novom generacijom računala, relativno je jednostavno ubrzati izvođenje GA korištenjem višejezgrenih ili višeprocesorskih računala koja su dostupna, ili čak grozdova računala. Postoje dijelovi algoritma koji se izvršavaju na svakoj od jedinki zasebno te ne ovise o vanjskim parametrima te su idealan kandidat za paralelizaciju računanja. Najbolji primjer toga je računanje adekvatnosti koje se vrši za svaku jedinku zasebno. U implementaciji u programskom jeziku C, često korištenom zbog brzine, koristimo posix višenitno orgramiranje. Stoga na četverojezrenom procesoru možemo simultano računati 4 procjere adekvatnosti, što rezultira realnim ubrzanjem od 3 do 3.5 puta. Također korištenjem različitih optimizacija kompajlera ili drugih kompajlera, poput LLVM, moguće je dodatno ubrzati izvršavanje koda za 30-40%. Konačno, ukoliko potpuno izbacimo sortiranje jedinki te algoritam baziramo na preglednim tablicama također ubrzavamo izvođenje pri velikom broju jedinki. Sve ovo čini razliku u dugotrajnom izvođenju programa koja može dane pretvoriti u tjedne.

Konačno, postoji fundamentalan problem nepoznavanja točnog rješenje, odnosno neznanja dali je program pronašao optimalno rješenje. Usprkos tome, možemo donijeti informiranu odluku o rješenju te procijeniti njegovu kvalitetu. Kao prvo, rješenje mora biti fizikalno prihvatljivo. Kada GA pronade rješenje te se kreće oko njega u sve manjim i manjim inkrementima, možemo reći da postoji jaka indikacija da je to konačno rješenje. Također, ukoliko se nekoliko pokretanja algoritma zaustavi na istom rješenju (u granicama), možemo reći da se radi o rješenju ili da smo drastično pogriješili u definiranju problema i implementaciji. Usprkos svemu tome GA su se opetovano pokazali vrlo brzim i robusnim rješenjem problema optimizacije, mnogo puta u situacijama kada nam intuicija govori da je problem prekompleksan.

9.7 STARFIT

STARFIT je vjerojatno najkorišteniji program napisan za potrebe ove disertacije. Zasniva se na genetičkom algoritmu u svrhu pronalaženja parametara zvjezdane atmosfere - efektivne temperature, logaritma gravitacijskog ubrzanja, projekcije brzine rotacije te drugih poput doprinosa svjetlu u višestrukome sustavu, kao i dva pomoćna, dopplerov pomak te pomak u y-osi zbog kompenzacije pomaka u opaženom spektru. Dakle, ukupno se može prilagođavati šest parametara. Međutim, jedno od važnih svojstava je i simultano prilagođavanje parametara za dvije zvijezde. Svaki od 6 parametara se može prilagođavati za svaku zvijezdu potpuno zasebno ili u ograničenom načinu rada pri čemu ukupan zbroj doprinosa svjetla mora iznositi 1 ili neki izabran konstantni broj (ukoliko postoji treća ili više komponenata zvjezdanog sustava), što predstavlja međusobno ograničenje. Također, u neograničenom načinu rada, zbroj pojedinačnih doprinosa u blizini vrijednosti 1.0 unosi dodatno povjerenje u valjanost pronađenih parametara.

Program se može koristiti za paralelnu optimizaciju potpuno nezavisnih zvijezda, primjerice dvije samostalne zvijezde pri čemu se ubrzava traženje parametara umjesto dva zasebna pokretanja koda. U tom slučaju se koristi potpuno nezavisna mogućnost rada.

Dodatno važno svojstvo je korištenje tzv. flastera. Program optimizira parametre na pre-

Table 9.1: Modeli uključeni u program

Broj	T_{eff}/K	$\log g$	valne duljine /Å	Napomena
0	15000 - 25000	3.0 - 4.5	968 - 33310278	UCLSyn Z_{sol}
1	25000 - 33000	3.6 - 4.5	968 - 33310278	UCLSyn Z_{sol}
2	5000 - 9750	2.0 - 5.0	3900 - 6000	UCLSyn Z_{sol}
3	27500 - 55000	3.0 - 4.75	3001 - 7490	Hubeny Ostars
4	7000 - 15000	2.5 - 5.0	3900 - 6800	UCLSyn Z_{sol}
5	4000 - 16000	2.5 - 5.0	3900 - 5900	UCLSyn Z_{sol}
6	4000 - 16000	2.5 - 5.0	4200 - 4700	UCLSyn Z_{sol}
7	4000 - 16000	2.5 - 5.0	4700 - 5200	UCLSyn Z_{sol}
8	4000 - 16000	2.5 - 5.0	5200 - 5900	UCLSyn Z_{sol}
9	4000 - 16000	2.5 - 5.0	3900 - 4200	UCLSyn Z_{sol}
10	4000 - 16000	2.5 - 5.0	5900 - 7000	UCLSyn Z_{sol}
11	15000 - 30000	3.0 - 4.75	3201 - 9997	Hubeny Bstars LMC
12	27500 - 40000	3.5 - 4.75	3000 - 7498	Hubeny Ostars LMC
13	15000 - 33000	3.6 - 4.5	968 - 33310278	UCLSyn Z_{sol}
14	11000 - 15000	2.5 - 5.0	3900 - 7000	Gray, H and He only

dodabranom rasponu valnih duljina od interesa, ali se unutra tog raspona također mogu nalaziti ili spektralne linije koje nije moguće optimizirati ili pogreške u spektrima te bi bilo dobro izbjeći optimizaciju na tim podsegmentima. Stoga se mogu definirati podsegmenti spektra, izborom početne i krajnje valne duljine, koji se isključuju iz optimizacije. Oni se definiraju u zasebnoj ASCII datoteci u kojoj je prvi redak broj flastera, a nakon toga slijedi toliko redaka sa početnom i krajnjom valnom duljinom za isključivanje. U datotekama sa rezultatima, jedan od plotova će uključivati i isključena područja označena sa drugačijim intenzitetom iz čega je jednostavno vidjeti koji dio spektra je korišten u optimizaciji, ali koji dijelovi su zanemareni.

Spektri se prilagođavaju prema modelima, koji se nalaze uz program. Trenutno je uključeno desetak modela, većinom rezultat UCLSyn proračuna, kao i drugih kodova. Izbor željenog modela vrši se u konfiguracijskoj datoteci za svaku komponentu zasebno. Također, neki od modela su podijeljeni na podmodele sa manjim rasponom valnih duljina zbog bržeg inicijalnog učitavanja. Pri pokretanju programa, učitava se konfiguracijska datoteka u kojoj je definiran željeni model i raspon valnih duljina. Nakon toga se učitavaju modeli u punom rasponu te se učitavaju i spektri koje se želi optimizirati. Iz njih se iščita rezolucija te se konačno model reinterpoliraju u željenom rasponu u rezoluciji ulaznih spektara. Inicijalni modeli postoje za neki raspon efektivnih temperatura i logaritma gravitacijskog ubrzanja te nisu rotacijski prošireni. Trenutno dostupni modeli su navedeni u tablici 9.1.

Iz učitane mreže modela, za svaku jedinku svake komponente, interpolira se model spektra sa željenom efektivnom temperaturom i gravitacijskim ubrzanjem. Rotacijski širenje se primijeni na interpolirani spektar, a nakon toga se skalira na željeni doprinos svjetla. Tada se izračunati spektar uspoređi sa mjerenim te se odredi adekvatnost pojedinog spektra (jedinke) te se generira jedinkin χ^2 .

9.7.1 Procjena pogreške - Monte Carlo Markow Chain (MCMC)

Monte Carlo Markow Chain (MCMC), detaljno opisan u navedenim radovima (Gilks et al. 1996, Tegmark 2004 and Collier Cameron et al. 2007) se sve češće koristi za procjenu pogrešaka pri višeparametarskoj prilagodbi, osobito pri visokoj dimenzionalnosti problema. Ovje će biti korišten za procjenu nepouzdanosti programa StarFit obzirom da genetički algoritmi intrinzično ne računaju nepouzdanost. Koriste se za provjeru valjanosti seta parametara s_i koji rješavanju naš problem, gdje je $i = 1 \dots N$, a N odabrana/korištena dužina lanca. Procedura počinje izborom početne točke lanca sa inicijalnim parametrijam s_1 . Za njega računamo novi, predloženi set parametara, korak $s_* = s_1 + \Delta p$ gdje Δs is a izabrani korak, skok od početne vrijednosti, određen pomoću vjerojatnosti skoka $f(\Delta s)$. s_i je set parametara, na primjeru STARFIT T_{eff} , $\log g$, $v \sin i$ i $l f$. Svaki od parametara se varira da bi se generirao novi predloženi korak kao

$$T_i = T_{i-1} + \sigma_T G(O, 1) f \quad (9.16)$$

$$\log g_i = \log g_{i-1} + \sigma_{\log g} G(O, 1) f \quad (9.17)$$

$$v \sin i_i = v \sin i_{i-1} + \sigma_{v \sin i} G(O, 1) f \quad (9.18)$$

$$l f_i = l f_{i-1} + \sigma_{l f} G(O, 1) f \quad (9.19)$$

gdje je $G(0, 1)$ nasumično Gaussovo odstupanje sa sredinom u nuli i jediničnom standardnom devijacijom. Faktor skale f je promjenjive veličine koraka te σ standardna devijacija. Inicijalne vrijednosti devijacije su procijenjene ili postavljene na neku smislenu vrijednost. Slijedeći je korak evaluacija u novopredloženoj točki p_* . Ovo znači da svaki korak ovisi samo o prethodnom

$$p(\Theta_{i+1} | \{\Theta_i\}) = p(\Theta_{i+1} | \Theta_i) \quad (9.20)$$

gdje je p vjerojatnost, a Θ parameteri. Stoga možemo reći da su sve prošle i buduće vrijednosti u lancu nezavisne odnosno da lanac nema memoriju. Da bi se postiglo ravnotežno rješenje, nužno je i da je vjerojatnost koraka lanca simetrična

$$p(\Theta_{i+1} | \Theta_i) = p(\Theta_i | \Theta_{i+1}) \quad (9.21)$$

Dakle, ako se χ^2 smanji, predloženi korak se prihvaća, a ukoliko se poveća (što znači da se udaljavamo od rješenja), prihvaća se samo sa 20% vjerojatnosti, a u preostalim 80% odbacuje. Ovo omogućava metodi da istražuje parametarski prostor te rezultira u statistici za procjenu pogreške. MCMC koristi veliki broj ovako definiranih koraka da pronade rješenje i procijeni nepouzdanost. Jedno pokretanje algoritma počinje izborom početne točke te konvergencijom lanca prema području parametarskog prostora gdje se nalazi rješenje, tzv. burn-in faza te pretraživanje prostora oko rješenja u kasnijoj fazi. Algoritam se može pokrenuti više puta da bi

se pokazalo da je pronađeno rješenje stvarno te da bi se poboljšala statistika. Iskoristili smo postojeće STARFIT rutine za kreiranje modela spektara i njihovu manipulaciju prema željenim parametrima te dodali MCMC rutinu koja generira predložene korake i provjerava ih. Prihvaćeni koraci se zapisuju za naknadnu procjenu nepouzdanosti, a odbaćeni odbacuju.

9.8 Analiza CNO područja u dvostrukom sustavu Algolova tipa u Her

Kemijski sastav zvjezdanih fotosfera u zvijezda sa prijenosom tvari je dragocjen izvor informacija o procesu nukleosinteze koji se odvija duboko u zvijezdi te zadržava informacije o njezinoj prošlosti. Dvostruki zvjezdani sustav u Her pripada grupi tzv. vrućih algola obzirom da su obje komponente zvijezde spektralnog tipa B. Razdvojili smo individualne spektre svake od komponenata tehnikom spektralnog raspeljavanja primijenjenoj na vremenskoj seriji od 43 kompozitna échelle spektra visoke rezolucije. Pridodavši analizi svjetlosne krivulje Hipparcos satelita, došli smo do fundamentalnih parametara sustava. Primarna je komponenta (primatelj tvari) mase $M_A = 7.88 \pm 0.26 M_\odot$, $R_A = 4.93 \pm 0.15 R_\odot$ i $T_{\text{eff},A} = 21600 \pm 220\text{K}$. Sekundarna komponenta ima masu $M_B = 2.79 \pm 0.12 M_\odot$, $R_B = 4.26 \pm 0.06 R_\odot$ i $T_{\text{eff},B} = 21600 \pm 550\text{K}$. Ne-LTE analiza atmosfere primarne zvijezde otkriva odstupanja zastupljenosti dušika i ugljika od standardne kozmičke zastupljenosti u skladu s teorijskim očekivanjima za CNO nukleosintezu. Pomoću mreže izračunatih evolucijskih modela najbolje poklapanje sa opaženim svojstvima zvijezda u sistemu u Her moguće je pratiti inicijalnih svojstava i tok evolucije ovog dvojnog sustava. Potvrđuje se pretpostavka A tipa prijenosa tvari. Detaljna analiza zastupljenosti daje omjer $C/N = 0.9$, što podupire teorijske izračune i indicira snažno miješanje u ranoj fazi evolucije sekundarne komponente, koja je inicijalno bila masivnija. Sastav sekundarne komponente služi kao daljnje ograničenje na početna svojstva sistema, ali zahtjeva spektre visoke rezolucije i odnosa signal-šum.

9.8.1 Analiza spektara obje komponente

Efektivne temperature

Da bismo generirali model atmosfere pojedine komponente, nužno je prvo znati njihovu efektivnu temperaturu (T_{eff}) te gravitacijsko ubrzanje ($\log g$). Kada se zvijezde nalaze u dvostrukom sustavu gdje se mase i polumjeri mogu vrlo precizno odrediti iz radijalnih brzina i krivulje sjaja, rezultirajući $\log g$ će biti znatno precizniji od onog određenog samo iz spektara. U slučaju u Her, iako dostupna opažanja daju preciznost mase od samo 3-4% te radiusa 2-3%, odredili smo $\log g$ sa pogreškom od samo 0.0013 dex za primarnu te 0.018 dex za sekundarnu komponentu.

Dostupnost tako preciznih vrijednosti rješava problem degeneracije između efektivne temperature i gravitacijskog ubrzanja koji postoji pri njihovu mjerenju iz profila Balmerovih linija.

S druge strane, otegotna je okolnost što se raspetljani spektri moraju renormalizirati za doprinos svjetla u njihov intrinzičan fluks. Čisti SPD daje spektre u tzv. zajedničkom kontinuumu te su pojedini spektru komponenta skalirani sa faktorom proporcionalnim njihovom pojedinačnom doprinosu ukupnom svjetlu sustava. Ukoliko niti jedan od kompozitnih spektara nije snimljen za pomrčine, rezultatni spektri imaju višeznačnost pri renormalizaciji (Pavlovski & Hensberge 2005). Stoga postoji potreba za dodatnim informacijama kako bi se odredio pojedinačni doprinos (Pavlovski & Hensberge 2010, Pavlovski & Southworth 2012). U slučaju u Her koristimo omjer sjaja određen rješenjem krivulje sjaja $l_1/l_2 = 0.300 \pm 0.003$ gdje su l_1 i l_2 pojedinačni doprinosi ukupnom sjaju sustava.

Optimalna prilagodba Balmerove serije linija u renormaliziranim spektrima komponenta vršena je STARFIT kodom. Glavna prednost nad prošlim sličnim kodom GENFIT (Tamajo et al. 2011) je u tome što STARFIT može raditi u ograničenom modu, simultana prilagodba obje komponente sa uvjetom $l_1 + l_2 = 1.0$ ili neograničenom modu. Za u Her STARFIT se koristio u neograničenom modu gdje je omjer svjetla bio ograničen rješenjem svjetlosne krivulje, kao i *logg*. Pošto su intrinzično široke Balmerove linije slabo modificirane promjenom rotacijske brzine *vsini*, vrijednosti za obje komponente određene su na linijama helija i metala. Efektivna je temperatura određena na Balmerovim linijama H_β i H_γ . Rezultati su vidljivi u tablici 6.3, a rezultat prilagodbe na slici 6.3. Spektroskopski određena efektivna temperatura sekundarne komponente je u savršenom slaganju sa rezultatima analize svjetlosne krivulje.

Kemijska zastupljenost

Teorijski spektri za atmosferske parametre primarne zvijezde te varirajuće vrijednosti mikroturbulentne brzine te zastupljenosti elemenata izračunati su hibridnim pristupom (Nieva & Przybilla et al. 2010) kombinacijom LTE atmosfera i non-LTE računom profila linija. Izračunali smo model atmosfere ATLAS9 kodom koji pordazumjeva planparalelnu geometriju, kemijsku homogenost te hidrostatsku, radijativnu i lokalnu termodinamičku ravnotežu. Prekrivanje linija je riješeno pomoću funkcije distribucije neprozirnosti. Solarna zastupljenost je korištena u svim računima. Ne-LTE populacije i spektri su napravljeni pomoću DETAIL i SURFACE koda (Giddings 1981, Butler & Giddings 1985). Non-lte populacije i sintetički spektri H, He, C, N, O, Mg, Si i Al su svi izračunati pomoću najnovijih modela atoma (Nieva & Przybilla 2012). Mikroturbulentna brzina od određena iz uvjeta neovisnosti zastupljenosti kisika o ekvivalentnoj širini. Linije kisika su korištene zbog njihova najvećeg broja u spektru. Korištene su samo linije probrane od Simon-Diaz (2010). Mikroturbulentna brzina je određena kao $v_{\text{turb}} = 2 \pm 1$ km/s te je u očekivanom rasponu za zvijezde ranog B tipa na glavnom nizu. Zastupljenost je procijenjena prilagodbom profila linija koje nemaju primjesa linija drugih elemenata. Srednje vrijednosti zastupljenosti i pogrešaka dane su u tablicama 6.3 i 6.4. Pogreške zastupljenosti su izračunate iz rasapa vrijednosti zastupljenosti linija za 1σ odstupanja T_{eff} i v_{turb} . Glavni doprinos pogrešci je ipak rasap vrijednosti pojedinih linija. Cugier (1989) je odredio zastupljenost ugljiga u 6 primarnih komponenti algolovog tipa, uključujući u Her. Koristio je UV

dio spektra sa IUE satelita te mjerio ekvivalentnu širinu C II multipleta na 1334.5-1335.7 Å i 1323.8-1234.0 Å. Ograničio je vrijednosti temperature iz UV distribucije fluksa i van der Veenovog (1983) fotometrijskog rješenja, $T_{\text{eff},1} = 22000 \pm 1500 K$ i $T_{\text{eff},2} = 13300 \pm 1000 K$. Nakon korekcije za non-LTE efekte odredio je zastupljenost ugljika $\log\epsilon(C) = 8.62 \pm 0.30$ te zaključio da primarna komponenta u Her ne pokazuje promjenu u zastupljenosti ugljika, u suprotnosti sa ostalim Algolima iz uzorka. Tomkin et al. (1993) su koristili visokorezolucijske CCD spektre C II linije na 4267 Å istih sustava koi su bili proučavani od Cugier (1989) i Cugier & Hardop (1988). Procijenili su zastupljenost ugljika diferencijalno u odnosu na samostalne B-zvijezde. Odredili su temperature iz Stroemgrenske fotometrije koristeći kalibraciju Napiwotski (1993) te dobili $T_{\text{eff},1} = 20000 K$. Tomkin et al. dobili su zastupljenost ugljika u odnosu na zastupljenost standardnih zvijezda $\log\epsilon(C) = 8.28$ Zastupljenost ugljika određena u ovom radu, $\log\epsilon(C) = 7.92 \pm 0.02$ zasniva se na mjerenju pet linija te je u gotovo savršenom slaganju sa Tomkin et al. (1993) mjereno na jednoj liniji. Znatna razlika u temperaturi u odnosu na Tomkin et al. i naše vrijednosti ima mali utjecaj, vjerojatno zbog slabe temperaturne ovisnosti linija ugljika u rasponu 19000-24000 K, gdje linije ugljika imaju najveći intenzitet. Usporedba nekoliko linija ugljika u području 5130-5154 Å dana je na slici 6.4 (gornji dio).

Zastupljenost dušika se zasniva na mjerenju 17 linija, te je precizno određena kao 0.20 ± 0.06 dex iznad sunčeve vrijednosti. To daje [N/C] omjer zastupljenosti od 0.05 ± 0.03 dex, znatno iznad "standardne" kozmičke (-0.54 ± 0.06 ; Nieva & Przybilla 2012) ili solarne (-0.61 ± 0.08 ; Asplund et al. 2009) vrijednosti. Promjene u N/C omjeru u tijeku prijenosa tvari čuvaju utjecaj povijesti evolucije sustava. Ovaj rezultat se diskutira u slijedećem dijelu, u kontekstu kemijske evolucije dvojnog sustava sa prijenosom tvari, u prilog tipu A evolucije sustava u Her.

Helij je zadnji produkt CNO nukleosinteze te se njegova zastupljenost kontinuirano povećava tijekom evolucije. Zastupljenost u primarnoj komponenti je u savršenom slaganju s vrijednošću Nieva & Przybilla (2012) za OB zvijezde, iako je nepouzdanost prilično velika. Izračuni modela pokazuju povećanje zastupljenosti helija po udjelu mase nakon prijenosa faze faktora 1.25, koji se nakon toga vraća prema inicijalnoj zastupljenosti zahvaljujući temohalinskom miješanju. Preostalu prezastupljenost helija od 2% nije bilo moguće potvrditi zbog toga što je takva vrijednost unutar pogrešaka.

Tri glavna metala - magnezij, silicij i aluminij imaju granično pod-solarnu zastupljenost sa srednjom vrijednošću $[M/H] = -0.04 \pm 0.03$. U našem daljnjem modeliranju stoga uzimamo solarnu vrijednost.

Usprkos važnosti, nismo vršili analizu zastupljenosti sekundarne komponente zbog toga što je odnos signal-šum u renormaliziranom spektru neadekvatan za preciznu analizu. U kombinaciji sa visokom projekcijom rotacijske brzine $v_{\text{rot}} \sim 100$ km/s, rezultati su nepouzdana. Ipak, primjećuje se potpun nedostatak C II linije na 4267 Å koja bi trebala biti vidljiva na ovoj temperaturi. Evidentno je da zastupljenost ugljika primarne komponente ne odgovara zastupljenosti sekundarne. Gruba je ocjena zastupljenosti u sekundarnoj komponenti $\log\epsilon(C) \leq 7.5$ što je više od reda veličina manje od trenutne kozmičke zastupljenosti. Izračuni iz slijedeće sekcije daju

podzastupljenost ugljika od 7.5 puta nakon faze prijenosa tvari, što bi postavilo zastupljenost u atmosferi od $\log\epsilon(C) \sim 7.5$. Ne-detekcija ugljikova linije 4267 Å stoga podupire teorijska očekivanja modela. Ipak, dodatni spektri su potrebni da bi se poboljšao S/N odnos te da bi se došlo do definitivnog zaključka.

9.8.2 Evolucijski modeli

Kao što je bilo diskutirano u prošlom poglavlju, u Her pripada posebnoj skupini vrućih Algola koji odudaraju od tipičnih primjera zbog svoje veće i ukupne mase i omjera mase. 80 godina skupljanja fotometrijskih mjerenja ne pokazuje pokazatelj promjene perioda što indicira da je sustav u kasnoj fazi sporog prijenosa tvari. Ipak, ovo je otkriće intrigirajuće obzirom na kratak orbitalni period, obzirom da bi se u toj fazi očekivala šira orbita i time duži period. U svakom dvojnem sustavu, prijenos mase ide sa inicijalno masivnije prema manje masivnoj komponenti te se očekuje da se period smanjuje do postizanja recipročnog odnosa masa. Stoga, prateći prijenos tvari pokazuje se da je sistem mogao biti kontaktni za trajanje brzog prijenosa tvari.

Smatralo se da je u Her produkt prijenosa tvari vrste A (Webbink 1976). Prvu detaljnu analizu evolucije napravili su Nelson & Eggleton (2001). Pomoću mreže 5500 evolucijskih krivulja za različite vrijednosti inicijalne mase, omjera masa i perioda, pronašli su model koji najbolje odgovara opaženim rezultatima za slučaj inicijalne mase donora $M_d^i \sim 6.31 M_\odot$, omjera mase $q^i \sim 1.41$ te orbitalnog perioda od $P^i \sim 1.32$ d. Međutim, ograničili su pretragu samo na konzervativne modele te su izbjegli kontaktnu fazu tijekom prijenosa tvari. Stoga njihov rezultat za u Her može biti uzet kao maksimalna inicijalna masa i period za koje ne može doći do kontakta za brze faze.

de Mink et al. (2007) je proširila istraživanje sa novih 20 000 izračuna evolucijskih traka koristeći modificirani kod baziran na Nelson & Eggleton (2001). Modifikacije su bile u tome što su jednačbe strukture bile rješavane simultano, što je nužno za precizno modeliranje faze prijenosa tvari. Štoviše, uzeli su u obzir i nekonzervativni prijenos tvari te kratke kontaktne faze za brze faze prijenosa tvari. de Mink et al. (2007) su predložili novi pod-tip Algoloida (AR (brzi kontakt) \rightarrow AN (bez kontakta)), koji pokazuje postojanje kratke kontaktne faze za termalnog odgovora primatelja za brze faze. Nakon te faze, primatelj se vraća u termalnu ravnotežu i smanjuje radius, nakon čega dolazi do nastavka prijenosa tvari. Da bi se procijenila nekonzervativna evolucija uveli su pojam efikasnosti prijenosa tvari (β) koji je mjera koliko je tvari izgubljeno u odnosu na prenesenu tvar. Za evoluciju angularnog momenta pretpostavili su da je tvar izgubljena bi-polarnom emisijom sa primaoca. Jedan od vrućih Algola iz njihova uzorka (OGLE 09 064498) ima vrlo sličnu konfiguraciju kao u Her: $M_p \sim 8.4 \pm 0.7 M_\odot$, $q \sim 0.323$ te $P \sim 2.64$ d. Najbolji pronađeni model za taj sustav je $M_d^i \sim 7.10 M_\odot$, omjera mase $q^i \sim 1.68$ te $P^i \sim 1.34$ d.

Umjesto stvaranja velike mreže evolucijskih modela što je primjerenije za velik uzorak proučavanih sustava, pripremili smo inicijalne modele za u Her za različite inicijalne omjere

mase te dinamike gubitka tvari. Pošto neodređenost u gubitku zakretnog momenta ima velik utjecaj na razumijevanje evolucije, mala je korist od korištenja vrlo fine mreže. Stoga smo napravili nekoliko pojednostavljenja da bismo smanjili broj inicijalnih modela da bi se dobio odgovarajući rezultat. Nakon određivanja inicijalnih parametara, tražili smo model iz mreže koji najbolje odgovara opaženim vrijednostima.

Prvo smo uzeli u obzir četiri seta inicijalnih omjera mase q^i : 1.25, 1.50, 1.75 i 2.00. To su tipične vrijednosti koje daju sisteme slične Algolu na kraju faze prijenosa tvari. Nismo išli preko omjera 2.0 zbog toga što primaoci u takvim sustavima teško zadržavaju termalnu ravnotežu za brze faze. Da bismo pripremili podset inicijalnih modela i uzeli u obzir nekonzervativan scenarij, preuzeli smo pristup de Mink et al (2007.). Parametar efikasnosti prijenosa tvari definiran kao

$$\beta = 1 - \left| \frac{\dot{M}_g}{\dot{M}_d} \right| \quad 0 \leq \beta \leq 1 \quad (9.22)$$

gdje d predstavlja donora, a g primaoca tvari. Vidljivo je da je $\beta = 0$ konzervativan slučaj evolucije. Da bi se procijenio gubitak zakretnog momenta, koristili smo aproksimaciju Hurley et al. (2002) koja pretpostavlja da gubitak mase preuzima određeni udio zakretnog momenta donora. Ovo je vrlo vjerojatan slučaj za A tip evolucije zbog nepostojanja akrecijskog diska koji rezultira bi-polarnim gubitkom tvari. Uz tu aproksimaciju i logaritamsko diferenciranje zakretnog momenta za sustav sa dvije zvijezde dobije se zakretni moment

$$J^2 = \left(G \frac{M_d^2 M_g^2}{M_d + M_g} \right) 4\pi^2 A \quad (9.23)$$

gdje je A udaljenost među komponentama. Jednostavno je doći do relacije za period koristeći Keplerov drugi zakon

$$\frac{P^f}{P^i} = \left(\frac{M_d^i + M_g^i}{M_d^f + M_g^f} \right)^{1/2} \left(\frac{M_g^i}{M_g^i + (1 - \beta)(M_d^i - M_d^f)} \right)^3 \left(\frac{M_g^i + M_d^i}{M_g^i - (1 - \beta)M_d^i + \beta M_d^f} \right)^{-3/2} \left(\frac{M_d^i}{M_d^f} \right)^{3(1-\beta)} \quad (9.24)$$

gdje su i i f inicijalne i konačne vrijednosti parametara. Izraz za evoluciju ukupne mase sustava je prihvaćen iz Giuricin & Mardirossian (1981)

$$\frac{M_t^i}{M_t^f} = \frac{(1 + q^i)[1 + q^f(1 - \beta)]}{(1 + q^f)[1 + q^i(1 - \beta)]} \quad (9.25)$$

Koristeći raspon $\beta = [0.0, 0.1, 0.25, 0.5, 0.75]$, dakle od konzervativnog do vrlo nekonzervativnog. Pripremili smo 20 različitih inicijalnih modela kao kandidata za početne vrijednosti u Her ($M_p^f \sim 7.9 \pm 0.26 M_\odot$, $q \sim 0.35 \pm 0.02$ te $P = 2.05$ d). Obzirom da jednadžbe 9.24 i 9.25 ne uzimaju u obzir svojstva pri prijenosu tvari, valja izračunati detaljne evolucijske trake kako

bi usporedio sve opažane parametre svake komponente, kao i orbite.

Da bismo izračunali detaljne evolucijske trake, koristili smo Cambridge verziju koda STARS¹ originalno razvijenog od Eggleton (1971, 1972). Najnovija verzija omogućava izračun simultane evolucije svake komponente te mnoga druga poboljšanja, objašnjena u Stancliffe & Eldridge (2009). Pošto su i opažene i inicijalne mase u području zvijezda srednje mase, fiksirali smo parametar prebacivanja $\delta_{os} = 0.12$. Također smo pretpostavili solarnu zastupljenost elemenata na glavnom nizu. Svaka je evolucijska traka prekinuta u trenutku ispunjenja Rocheove plohe primatelja na kraju faze sporog prijenosa.

U tablici 6.6 pokazujemo našu mrežu modela. Pokazujemo inicijalne parametre sistema, kao i najbolje modele opažene parametre dane u tablici 6.2. Provjerili smo da li svi inicijalni periodi odgovaraju ograničavajućem, najmanjem periodu prema relaciji Nelson & Eggleton (2001)

$$P_{lim} \approx \frac{0.13M_d^i + 0.47M_d^{i2.33}}{1 + 1.187M_d^{i2}} \quad (9.26)$$

Također, prikazali smo evolucijske trake i opažene parametre sistema na HR dijagramu na slici 6.7. Pod pretpostavkom da svaki sistem počinje sa drugačijim početnim vrijednostima, termalni odgovor svake komponente uvjetuje trajanje spore i brze faze prijenosa tvari. Većina sistema ne može nakupiti dovoljno tvari da bi reproducirali opažene mase u Her prije obrnuća omjera mase. Bazirano na minimizaciji χ^2 i vizualnoj provjeri, najbolji modeli pripadaju grupi konzervativnog prijenosa tvari sa visokim inicijalnim omjerom mase, kao u slučaju već diskutiranog sustava OGLE 09 064498. Također smo primijetili kratkotrajnu kontaktnu fazu, diskutirano u de Mink et al. (2007), kod sistema sa visokim inicijalnim omjerom mase i efikasnim prijenosom $q_i \geq 1.75$ i $\beta \leq 0.25$.

Pronalaženje najboljih inicijalnih parametara omogućilo nam je da pratimo kemijsku evoluciju obje komponente tijekom prijenosa tvari. Na slici 6.8 pokazujemo promjenu u profilu omjera C/N of središta prema površini svake komponente. Zbog vrlo različitih vremenskih skala brze i spore faze, nacrtali smo promjenu u funkciji omjera mase umjesto vremena. Evidentna je nagla promjena u primateljevom profilu koji odgovara promjeni iz brze u sporu fazu. Davatelj je u tom trenu izgubio tvar te dosegao slojeve u kojima je CNO ciklus smanjio C/N omjer sa kozmičkog (~ 3.2) na ravnotežnu vrijednost (~ 0.1). Ta nukleosintetski procesirana tvar je tada deponirana na površinu primaoca. Ima veću molekulsku masu od tvari ispod. U tom slučaju možemo očekivati termohalinsko miješanje tvari koje rezultira promjenom sastava površinske tvari. Kao što su pokazali Stancliffe & Eldridge (2009), efekt termohalinskog miješanja je zanemariv za brze faze. Stoga smo kreirali sve evolucijske trake bez termohalinskog miješanja kako bismo pronašli donju granicu omjera C/N na površini. Nakon toga smo primijenili termohalinsko miješanje na model primatelja kako bismo pratili njegovu površinsku zastupljenost. Kako termohalinski uvjet nije zadovoljen, zanemarili smo ga na donoru.

Na slici 6.8 također pokazujemo efekt termohalinskog miješanja na cijelom profilu un-

¹Slobodno dostupan na adresi <http://www.ast.cam.ac.uk/~stars>

utrašnjosti zvijezde. Zbog tvori izvorišta u različitim dijelovima donora, vanjski slojevi zvijezde imaju varijabilan profil sastava. Termohalinsko miješanje promijeni površinski sastav u relativno kratkom roku ($\sim 10^5$ god). Stoga očekujemo C/N omjer primatelja između nemišane (~ 0.1) i miješane (~ 1) vrijednosti. Ovaj je rezultat u dobrom slaganju sa opaženim omjerom od $C/N = 0.89$.

Vjerujemo da je određivanje zastupljenosti elemenata u davatelju važna prilika za ograničavanje inicijalnih parametara. Takva bi nam situacija omogućila da kreiramo finu mrežu evolucijskih traka i provjerimo rezultate na opažanjima kao i razumijevanje procesa evolucije dvojnih sustava kao što su mehanizmi gubitka mase i termohalinsko miješanje. Iako nismo mogli odrediti zastupljenost davatelja, nedostatak jake linije ugljika $C\ II\ 4267\ \text{\AA}$ u usporedbi sa samostalnim zvijezdama te temperature je jak pokazatelj smanjene zastupljenosti ugljika na površini kao rezultat A tipa prijenosa. To je zato što u širokoj orbiti, davatelj izgubi samo vanjske slojeve bez da zahvati područja sa CNO promijenjenim sastavim. Za sada, naši proračuni evolucije pokazuju da je sustav u Her mogao početi sa parametrima $M_i^d \sim 7.16 M_\odot$, $q^i \sim 2.00$ i $P^i \sim 1.35$ d.

9.9 Algol

9.9.1 Spektroskopija visoke rezolucije

Opažački program Algola spektroskopima visoke rezolucije je iniciran u dva perioda 2009. i 2010. godine na Nordic Optical telescope na La Palmi. Snumljeno je 85 spektara pomoću FIES spektrografa koji se nalazi odvojen od teleskopa u zasebnoj zgradi zbog anuliranja vibracija i kontrole atmosferskih uvjeta. Kalibracija valnih duljina vršena je standardnim Th-Ar izvorom snimanim redovito tokom opažanja. Razlučivanje uređaja je $R = 48\ 000$. Trajanje ekspozicije od 300 s za svaki od spektara je rezultiralo u odnosu signal-šum od 300-400 u B i V području.

Kako bi pokrili i vanjsku orbitu perioda $P = 680$ d, nastavili smo opažanje sa BOES spektrografom u Sjevernoj Koreji od 2010. do 2013. godine. Za kalibraciju je korištena standardna ThAr lampa.

Spektri su reducirati standardnom procedurom koristeći IRAF échelle paket. Normalizacija i spajanje redova je pažljivo napravljeno softverom kojega sam razvio kako bi se izbjegli svi neželjeni utjecaji na rezultirajući spektar.

9.9.2 Fundamentalne veličine za komponente sustava

Uz određenje semiamplituda orbitalne brzine svih komponenata sustava Algola, moguće odrediti njihove dinamičke mase. Inklinacija orbite preuzeta je iz Richards et al. (1988) te za unutrašnju orbitu iznosi $i_{A-B} = 81.4 \pm 0.2$, a za vanjsku Baron et al. (2012), $i_{AB-C} = 83.66 \pm 0.03$. Inklinacija je sada višestruko potvrđena iz različitih istraživanja i pomoću više tehnika

opažanja. Također korišteni su periodi orbita iz Baron et al. (2012), $P_{A-B} = 2.867328 \pm 0.00005$ d, i $P_{AB-C} = 680.168 \pm 0.54$ d. Određene su mase sve tri komponente - $M_A = 3.39 \pm 0.06 M_\odot$, $M_B = 0.770 \pm 0.009 M_\odot$, i $M_C = 1.58 \pm 0.09 M_\odot$. čtoviše, iz vanjske orbite možemo odrediti zbroj masa unutrašnje dvije komponente kao $M_{AB} = (M_A + M_B)_{\text{outer}} = 4.38 \pm 0.27 M_\odot$ što je vrijednost koja odgovara zbroju individualnih masa dvije komponente određenih iz dinamike $(M_A + M_B)_{\text{inner}} = 4.16 \pm 0.06 M_\odot$ unutar 1σ nepouzdanosti. Pregled određenih vrijednosti dan je u tablici ???. Također su određene efektivne temperature, projekcije brzine rotacije, mikroturbulentna brzina te metalicitet.

Mase određene u ovom radu su revidirane prema nižim vrijednostima od dosadašnjih rezultata (Richards et al. 1988) te su u skladu sa baron et al. (2012). Osim korekcije iznosa masa, preciznost njihova određivanja je također znatno poboljšana, u slučaju Algola A na 2%, a Algola B 1.1%. Kako se masa C komponente određuje iz unutrašnje orbite, nepouzdanost je ostala na nešto viših 5%.

Radiusi komponenata su određeni analizom svjetlosne krivulje u čijem rješenju postoji degeneracija obzirom da pomrčine unutrašnjeg para nisu potpune te zbog prisustva treće komponente. Rezultati Richards et al. (1988) daju slijedeće vrijednosti $R_A = 2.90 \pm 0.04 R_\odot$, $R_B = 3.5 \pm 0.1 R_\odot$ te $R_C = 1.7$, bez navedenih pogrešaka. Baron et al. (2012) je postigao bolju interferometrijsku razlučivost pomoći CHARA interferometra kako bi u potpunosti razlučili sustav. Dobivene su kutne dimenzije $\phi_A = 0.88 \pm 0.05$ mas, $\phi_B = 1.12 \pm 0.07$ mas, and $\phi_C = 0.56 \pm 0.10$ mas. Pomoću određene paralakse (Zavala et al. 2010) od $\pi = 34.7 \pm 0.6$ mas, određene su apsolutne vrijednosti radiusa komponenata kao $R_A = 2.73 \pm 0.20 R_\odot$, $R_B = 3.48 \pm 0.28 R_\odot$ te $R_C = 1.73 \pm 0.33 R_\odot$. Očito je da interferometrijska mjerenja još uvijek nemaju zadovoljavajuću preciznost, ali su u skladu sa rezultatima analize krivulje sjaja. Površinska gravitacijska ubrzanja dana su u tablici ?? te su korištena za određivanje atmosferskih parametara i doprinosa svjetla komponenata. Određena su korištenjem mjerenih linearnih radiusa (Richards et al. 1988) za određene mase komponenata (Tablica ??).

Veličina komponente koja ispunjava Rocheovu plohu je ograničena omjerom masa. To je još jedna mogućnost određivanja njezinog radiusa, uz očekivanu sinhronu rotaciju. Za omjer masa poluodvojenog para $q_{\text{sp}} = 0.227 \pm 0.005$ dobijemo relativni radius Algola B $r_B = 0.251 \pm 0.002$, iz kojeg možemo odrediti i linearni radius $R_B = 3.43 \pm 0.01 R_\odot$.

To je manja vrijednost od Baron et al. (2012) koja je zasnovana na direktnom interferometrijskom mjerenju te modernim mjerenjima paralakse. Međutim, pogreška od 8% daje prostora usklađivanju rezultata. Očekivana sinkrona brzina rotacije je $v_{\text{synch,B}} \sin i = 60.2 \pm 0.2$ km s⁻¹. Spektroskopski mjerena vrijednost je $v \sin i_B = 62 \pm 2$ km s⁻¹ što također podupire izmjereni radius Algola B.

Ukoliko koristimo sinkronizaciju Algola A, koja ne smije biti ispunjena za komponentu koja još prima tvar, tada za mjerenih $v \sin i_A = 50.5 \pm 0.8$ km s⁻¹ dobijemo $R_A = 2.87 \pm 0.04 R_\odot$. Ako je Algolu A ubrzana rotacija deponiranjem tvari (c.f. Packet 1981, Dechamps et al. 2013) ova bi vrijednost predstavljala gornju granicu mogućeg radiusa. Napredak u direktnom inter-

ferometrijskom mjerenju kutne dimenzije ili bolja fotometrijska mjerenja bi mogla potvrditi konačnu vrijednost te dimenzije.

9.9.3 Kemijski sastav i evolucija komponenata

Predviđeno smanjenje u zastupljenosti ugljika u sustavima sa prijenosom tvari su potaknula nekoliko promatračkih radova. Podzastupljenost ugljika u odnosu na sunčevu su potvrdili Cugier i Hardorp (1998) u analizi UV dijela spektra dobivenog sa IUE satelita. Zastupljenost Algola A u usporedbi sa modernim standardnom solarne zastupljenosti (Asplund et. al 2009) su odredili kao $[C/H] = -0.32 \pm 0.20$ dex.

Tomkin et al. (1993) su proučavali uzorak algoloida i potvrdili podzastupljenost ugljika u cijelom uzorku, uključujući i sam Algol. Za Algol A su pronašli $[C/H] = -0.22 \pm 0.15$ koristeći opažanja visoke rezolucije spektralne linije C II 4267 Å iona. Izmjerena je vrijednost relativna u odnosu na srednju zastupljenost od $\log \epsilon_C = 8.28 \pm 0.21$ utvrđenu za standardne zvijezde. Naš rezultat je $[C/H]_A = -0.16 \pm 0.08$ što potvrđuje malu podzastupljenost ugljika i u zastupljenosti mjerenoj na najjačoj ugljikovoj liniji u spektru Algola A, c II 4267 Å i odstupanju njezine ekvivalentne širine od kalibracije dobivene iz standardnih zvijezda kasnog B spektralnog tipa. Dušikove linije pokazuju laganu prezastupljenost sa $\log \epsilon_N = 7.97 \pm 0.02$, ali uz opasku da su korištene samo slabe N II linije sa ekvivalentnim širinama od 1. - 2.7m. U usporedbi sa modernim vrijednostima zastupljenosti ugljika, određena je prezastupljenost Algola A $[N/H]_A = 0.14 \pm 0.05$.

Omjer zastupljenosti ugljika i dušika je indikator CNO nukleosinteze i efikasnosti prijenosa tvari i procesa miješanja u zvjezdanoj unutrašnjosti. Za Algol A dobijemo omjer $(C/N)_A = 2.0 \pm 0.3$ što u usporedbi sa sunčevom vrijednošću od $(C/N)_\odot = 4.0 \pm 0.7$ pokazuje da je promjena u Algolu A detektirana. Očito su CNO procesirani slojevi inicijalno masivnije komponente sada izloženi na površini komponente primatelja tvari. U prošlom instraživanju sustava tipa vrući Algol - u Her, određen je omjer C/N 0.89 za komponentu primatelja (Kolbas et al. 2014). Ovaj sustav ima komponente masa 7.8 i 2.8 M_\odot , znatno više od masa unutrašnjeg sustava Algola. Kao što je predviđeno detaljnom analizom modela, pronađena je velika podzastupljenost ugljika u komponenti koja gubi tvar nego u primaocu

Iako je spektar Algola B separiran, detaljna analiza nije izvršena zbog prevelikog šuma. Spektra ima nizak odnos signal/šum, a linije su također znatno proširene zbog brze rotacije. Ipak, hladni pod-div dominira u rentgenskom području spektra Drake (2003) je koristio *Chandra* spektrograf akko bi analizirao C i N zastupljenost u koroni Algola B. Analiza je bila u odnosu na standardnu zvijezdu HR 1099. Zvijezde su pokazale velike sličnosti u spektrima, osim u jačini C i N linija. Određena je koncentracija dušika 3 puta veća nego u usporednoj zvijezdi, dok u spektru Algola nisu opažene linije ugljika, pokazujući podzastupljenost ugljika u odnosu na očekivanu vrijednost za faktor 10 ili više. Osim toga, Drake je pronašao kozmičku zastupljenost željeza u Algolu B, u skladu sa očekivanjima.

References

- Al-Naimiy, H. M. K., Mutter, A. A. A., Flaith, H. A. 1985, *Ap&SS*, 108, 227
- Allen, C.W., 1973, *Astrophysical Quantities*, 3rd edn, The Athlone Press, London
- Armstrong, J.T., Mozurkewich, D., Peterson, D. M., Hummel, C. A., Gilbreath, G. C., 2005, *AAS*, 207, 1102
- Asplund M., Grevesse N., Sauval A. J., Scott P., 2009, *ARA&A*, 47, 481
- Balachandran, S., Lambert, D. L., Tomkin, J., 1986, *MNRAS*, 219, 479
- Baron, F., Monnier, J. D., Pedretti, E., et al. 2012, 752, 20
- Batten, A. H. 1989, *SSRv*, 50, 1
- Batter, A. G, 1973, *Binary and multiple systems of stars*, Pergamon press, Oxford
- Bagnuolo W. G., Gies D. R., 1991, *ApJ*, 376, 266
- Borkovits, T., Derekas, A., Fuller, J., et al. 2014, *MNRAS*, 443, 3068
- Butler K., Giddings J.R., 1985, in *Newsletter on Analysis of Astronomical Spectra*, No. 9 (University of London)
- Charbonneau, P., 1995, *ApJS*, 101, 309
- Chen, K. Y., Reuning, E. G. 1966, *AJ*, 71, 283
- Collier Cameron, A., Wilson, D. M., Hebb, L. et al, 2004, *MNRAS*, 380, 1230
- Crawford J. A., 1955, *ApJ*, 121, 71
- Csizmadia, Sz., Borkovits, T., Paragi, Zs., et al. 2009, *ApJ*, 705, 436
- Cugier H., 1989, *A&A*, 214, 168
- Cugier H., & Hardrop I., 1988, *A&A*, 202, 101
- De Greve, J. P., 1989, *In Algols*, IAU Coll. No. 107, ed. Batten, A.H., Kluwer, Dordrecht p. 127

De Greve, J.-P. 1993, *A&AS*, 97, 527

De Greve, J. P, Cugier, H., 1989, *A&A*, 211, 356

De Greve, J. P., De Loore, C., 1992, *A&A Suppl.*, 97, 527

De Lore, C., de Greeve, J. P., 1992, *A&A Suppl.*, 94, 453

de Mink S. E., Pols O. R., Hilditch R. W., 2007, *A&A*, 467, 1181

Demircan, O. 1977, *Ap&SS*, 47, 459

Deschamps, R., Siess, L., Davis, P. J., Jorissen, A. 2013, *A&A*, 557, A40

Dervişoğlu, A., Tout, C.A., İbanoğlu, C., 2010, *MNRAS*, 406, 1071

Drake, J. J. 2003, *ApJ*, 594, 496

Eaton, J. A. 1975, *PASP*, 87, 745

Eaton J.A., 1978, *Acta Astronomica*, 28, 601

Eggleton P. P., 1971, *MNRAS*, 151, 351

Eggleton P. P., 1972, *MNRAS*, 156, 361

Efron, B., 1979, *Bootstrap Methods: Another look at the jackknife*, *Ann. Statistics* 7, 1-26

Fletcher, E. S. 1964, *AJ*, 69, 357

Fossati, L., Ryabchikova, T., Bagnulo, S., et al. 2009, *A&A*, 503, 945

Frémat, Y., Lampens, P., Hensberge, H. 2005, *MNRAS*, 356, 545

Frieboes-Conde, H., Herczeg, T., Høg, E. 1970, *A&A*, 4, 78

Garcia, E. V., Stassun, K. G., Pavlovski, K., Hensberge, H., Gómez Maqueo Chew, Y., Claret, A. 2014, *AJ*, 39

Gebran, M., Vick, M., Monier, R., Fossati, L. 2010, *A&A*, 523, A71

Giddings J.R., 1981, PhD Thesis, University of London

Gilks, W. R., Richardson S., Spiegelhalter, D. D., 1996, *Markow Chain Monte Carlo in Practise*, Chapman & Hall, London

Giuricin G., Mardirossian F., 1981, *ApJS*, 46, 1

Glazunova L.V., Mkrtichian D.E., Rostophchin S.I., 2011, *MNRAS*, 415, 2238

Glushneva, I. N., Esipov, V. F. 1967, *Soviet Astronomy*, 11, 828

González, J. F., Hubrig, S., Nesvacil, N., North, P. 2006, *A&A*, 449, 327

Goodricke, J. 1783, *Phylosophical Transactions of the Royal Society*, 73, 474

Gudehus, D., 2001, *AAS*, 33, 850

Guinan, E. F., McCook, G. P., Bachmann, P. J., Bistline, W. G. 1976, *AJ*, 81, 57

Hadrava P., 1995, *A&AS*, 114, 393

Heger, A., Langer, N., 2000, *ApJ*, 544, 1016

Hensberge, H., Pavlovski, K. 2007, *IAU Symposium*, 240, 136

Hensberge, H., Ilijčić, S., Torres, K. B. V. 2008, *A&A*, 482, 1031

Hensberge H., Pavlovski K., Verschueren W., 2000, *A&A*, 358, 553

Hilditch R. W., 1984, *MNRAS*, 211, 943

Hilditch R. W., 2001, *Close Binary Stars*, Cambridge University Press

Hilditch R. W., 2005, *Observatory*, 125, 72

Holland, J. H., 1975, *Adaptation in Natural and Artificial Systems*, Univ. of Michigan press, Cambridge, MIT

Holmgren, D. E., Hadrava, P., Harmanec, P., et al. 1999, *A&A*, 345, 855

Hunter, I., Brott, I., Langer, N., et al., 2009, *A&A*, 496, 841

Hurley J. R., Tout C. A., Pols O. R., 2002, *MNRAS*, 329, 897

Hynes, R. I., Maxted, P. F. L., 1998, *A&A*, 331, 167

Iben, 1965, *ApJ*, 142, 1447

Iben, 1966, *ApJ*, 143, 483

Ilijčić, S., Hensberge, H., Pavlovski, K. 2001, *Lecture Notes in Physics*, 573, 269

Ilijčić, S., Hensberge, H., Pavlovski, K., Freyhammer, L. S., 2004, *ASP Conf Ser* 318, 111

İbanoğlu C., Dervişoğlu A., ÇakırlıÖ., Sipahi E., Yüce K., 2012, *MNRAS*, 419, 1472

Ivezić Ž., Connolly, A.J., VanderPlas, J.T., Grey, A., 2014, *Statistics, Data Mining, and Machine Learning in Astronomy: A Practical Python Guide for the Analysis of Survey Data*, Princeton University Press

Jetsu, L., Porceddu, S., Lyytinen, J., et al. ApJ, 773, 1

Kemp, J. C., Barbour, M. S., McBirney, R. E., Rudy, R. J. 1981, ApJ, 243, 557

Kemp, J. C., Henson, G. D., Barbour, M. S., Kraus, D. J., Collins, G. W., II 1983, APJ, 273, L85

Kim, H.-I. 1989, ApJ, 342, 1061

Kim, K.-M. Han, I., Valyavin, G. G., et al. 2007, PASP, 119, 1052

Kippenhahn, 1980, A&A, 91, 185

Kolbas, V., Dervişoğlu, A., Pavlovski, K., Southworth, J. 2014, MNRAS, 444, 3118

Kolbas, V., Pavlovski, K., Southworth, J., Lee, C.-U., Lee, J. W., Kim, S.-L., Kim, H.-I. 2012, IAU Symp., 282, 303

Kopal, Z., 1955, AnAp, 18, 379

Kovachev B. J., Seggewiss W., 1975, A&AS, 19, 395

Kurucz, R. L. 1979, ApJS, 40, 1

Kusakin, A.V., Mkrtichian, D. E, Gamarova, A. Yu, 2001, IBVS, 5106, 1

Labeyrie, A., Bonneau, D., Stachnik, R. V., Gezari, D. Y. 1974, ApJ, 194, L147

Langer, N., 2012, ARAA, 50, 107

Lee, C.-U., Kim, S.-L., Lee, J. W., et al. 2008, MNRAS, 389, 1630

Lehmann, H., Southworth, J., Tkachenko, A., Pavlovski, K. 2013, A&A, 557, A79

Lestrade, J. F., Phillips, R. B., Hodges, M. W., Preston, R. A. 1993, ApJ, 410, 808

Maeder, A., Przybilla, N., Nieva, M. F. et al, 2014, A&A, 565, 39

Martins, F., Mahy, L., Hillier, D.J., Rauw, G., 2012, A&A, 538, A39

Maxted, P. F. L., 1994, PhD Thesis, University of St. Andrews

Maxted, P. F. L., Hilditch, R. W., 1996, A&A, 311, 567

Mayer, P., Harmanec, P., Pavlovski, K. 2013, A&A, 550, A2

McLaughlin, D. B. 1924, ApJ, 60, 22

Meynet, G., Maeder, A., 2000, A&A, 361, 101

Morel, T., Hubrig, S., Briquet, M., 2008, A&A, 481, 453

Napiwotzki R., Schoenberner D., Wenske V., 1993, A&A, 268, 653

Narusawa, S. 2013, PASJ, 65, 105

Narusawa, S., Ozaki, S., Kambe, E., Sadakane, K. 2006, PASJ, 58, 617

Nelson C. A., Eggleton P. P., 2001, ApJ, 552, 664

Nieva M. F., 2013, A&A, 550, A26

Nieva M. F., Przybilla N., 2007, A&A, 467, 295

Nieva M. F., Przybilla N., 2012, A&A, 539, A143

Nieva M. F., Simón-Díaz S., 2011, A&A, A2

Packet, W. 1981, A&A, 102, 17

Paczyński, B. 1971, ARA&A, 9, 183

Parthasarathy M., Lambert D. L., Tomkin J., 1979, MNRAS, 186, 391

Parthasarathy M., Lambert D. L., Tomkin J., 1983, MNRAS, 203, 1063

Pavlovski K., Hensberge H., 2005, A&A, 439, 232

Pavlovski K., Hensberge H., 2010, ASP Conf. Ser., 435, 207

Pavlovski K., Southworth J., 2009, MNRAS, 394, 1519

Pavlovski K., Southworth J., 2012, Proc. IAU Symp., 282, 359

Pavlovski, K., Southworth, J., Kolbas, V. 2011, ApJ, 734, L29

Pavlovski, K., Southworth, J., Kolbas, V., Smalley, B. 2014, MNRAS, 438, 590

Pavlovski K., Tamajo E., Koubský P., Southworth J., Yang S., Kolbas V., 2009, MNRAS, 400, 791

Peterson, W. M., Mutel, R. L., Güdel, M., Goss, W. M. 2010, Nature, 463, 207

Peterson, W. M., Mutel, R. L., Lestrade, J. F., Güdel, M., Goss, W. M. 2011, ApJ, 737, 104

Pfeiffer M.J., Frank C., Baumüller D., Fuhrmann K., Gehren T., 1998, A&AS, 130, 381

Popper, D. M, 1973, ApJ, 185, 265

Prša A., Zwitter T., 2005, ApJ, 628, 426

Przybilla N., Firnstein M., Nieva M. F., Meynet G., Maeder A., 2010, A&A, 517, A38

Quian, S.B, Boonruksar, S., 2002, New Astron., 7, 435

Refsdal, S., Roth, M. L, Weigert, A., 1974, A&A, 36, 113

Retter, A., Richards, M. T., Wu, K. 2005, ApJ, 621, 417

Richards, M. T., Agafonov, M. I., Sharova, O. I. 2012, ApJ, 760, 8

Richards, M. T., Mochnacki, S. W., Bolton, C. T. 1988, AJ, 96, 326

Rossiter, R. A. 1924, ApJ, 60, 15

Rovithis P., Rovithis-Livaniou H., 1980, Ap&SS, 70, 483

Rudy, R. J., Kemp, J. C. 1978, ApJ, 221, 200

Saad S., Nouh M., 2011, Bulletin of the Astronomical Society of India, 39, 277

Sarna M. J., 1992, MNRAS, 259, 17

Sarna, M. J., 1993, MNRAS, 262, 534

Sarna M. J., De Greve J.-P., 1994, A&A, 281, 433

Sarna M. J., De Greve J.-P., 1996, QJRAS, 37, 11

Simon K. P., Sturm E., 1994, A&A, 281, 286

Simón-Díaz S., 2010, A&A, 510, A22

Smalley, B., Smith K. C., Dworetzky M. M. 2001, UCLSYN Userguide, available at:
<http://www.astro.keele.ac.uk/~ljbs/pubs/uclsyn.pdf>

Smith, K. C. 1992, PhD Thesis, University College of London

Southworth, J., Bruntt, H., Buzasi, D. L. 2007, A&A, 467, 1215

Southworth, J., Clausen, J. V. 2007, A&A, 461, 1077

Söderhjelm S., 1978, A&A, 66, 161

Söderhjelm S., 1980, A&A, 89, 100

Stancliffe R. J., Elridge, J. J., 2009, MNRAS, 396, 1699

Stebbins, J., Gordon, K. C. 1975, Ap&SS, 33, 481

Stern, R. A., Lemen, J. R., Schmitt, J. H. M. M., Pye, J. P. 1995, ApJ, 444, L45

Stern, R. A., Uchida, Y., Tsuneta, S., Nagase, F. 1992, ApJ, 400, 321

Struve, O., Sahade J., 1957, PASP, 69, 265

Tamajo, E., Munari, U., Siviero, A., Tomasella, L., Dallporta, S. 2012, A&A, 539, A139

Tamajo E., Pavlovski K., Southworth J., 2011, A&A, 526, A76

Tassoul, M., Tassoul, J.L., 1984, ApJ, 279, 384

Tegmark, M., Strauss, A., Blanton, M. R., 2004, Phys Rev D, 69, 103501

Telting, J. H., Avila, G., Buchhave, L., et al. 2014, AN, 335, 41

Tkachenko, A., Degroote, P., Aerts, C., et al. 2013, MNRAS, 438, 3093

Tkachenko, A., Lehmann, H., Mkrtichian, D. 2009, A&A, 504,991

Tkatcheno, A., Lehmann, H., Mkrtichian, D., 2010, AJ, 139, 1327

Tody, D. 1986, Proc. SPIE Instrumentation in Astronomy VI, ed. D. L. Crawford, 627, 733

Tomkin, J., Lambert, D. L. 1978, ApJ, 222, L119

Tomkin, J., Lambert D. L., 1981, MNRAS, 241, 777

Tomkin J., Lambert D. L., Lemke M., 1993, MNRAS, 265, 581

Tomkin, J., Tan, H. 1985, PASP, 97, 51

Torres, K. B. V., Lampens, P., Frémat, V., Hensberge, H., 2010, ASPC, 435, 221

Torres, K. B. V., Lampens, P., Frémat, V., Hensberge, H., Lebreton, Y., Škoda, P., 2011, A&A, 525, A50

van der Veen W. E. C. J., 1984, A&AS, 57, 139

Wade, C. M., Hjellming, R. M. 1972, Nature, 235, 270

Webbink R. F., 1976, ApJ, 209, 829

Wecht, K. 2006, PhD Thesis, Lehigh University (arXiv:astro-ph/0611855)

White, N. E., Culhane, J. L., Parmar, A. N., Kellett, B. J., Kahn, S. 1986, ApJ, 301, 262

Wilson, R. E., De Luccia, M. R., Johnston, K., Mango, S. A. 1972, ApJ, 177, 191

Wilson, R. E., Devinney, E. J., 1971, ApJ, 166, 606

Wilson, R. E., Liou, J.-C. 1993, ApJ, 413, 670

Yang, X.-J., Lu, F.-J., Aschenbach, B., Chen, L. 2011, Res. Astron. Astrophys., 11, 457

Yoon, T.S., Honeycutt, K., 1992, IAUS, 151, 355

Zavala, R. T., Hummel, C. A., Boboltz, D. A., et al., 2010, ApJL, 715, L44

Ziolkowski, J., 1976, ApH, 204, 512

Curriculum Vitae

Vladimir Kolbas was born in 1979. in Zagreb. He attended 4 years of Primary school of Veljko Vlahović following by 4 years of Classical primary school of Izidor Kršnjavi. After that he enrolled General high school. He enrolled graduate studies of physics at Physics department of University of Zagreb, graduating with diploma thesis in the field of astrophysics. After that he continued doctoral studies also at Physics department in the field of Atom and molecular physics, module Astrophysics.

Životopis

Vladimir Kolbas rođen je 1979. godine u Zagrebu. Završio je 4 razreda osnovne škole Veljko Vlahović te nakon toga 4 razreda klasične osnovne škole Izidora Kršnjavoga. Nakon toga upisuje Gornjogradsku opću gimnaziju. Diplomski studij upisuje na Prirodoslovno-matematičkom Fakultetu Sveučilišta u Zagrebu na Fizičkom odsjeku gdje stječe titulu diplomiranog inženjera fizike sa diplomskim radom iz polja astrofizike. Nakon toga upisuje doktorski studij također na Fizičkom Odsjeku iz Atomske i molekulske fizike, modul Astrofizika.

List of publications / Objavljeni radovi:

1. Kolbas, V., Dervisoglu, A., Pavlovski, K., Southworth, J., *Tracing CNO exposed layers in the Algol-type binary system u Her*, 2014, MNRAS, 444, 3118
2. Tkachenko, A., Degroote, P., Aerts, C., Pavlovski, K., Southworth, J., Papics, P. I., Moravveji, E., Kolbas, V., Tsymbal, V., Debosscher, J., Clemer, K., *The eccentric massive binary V380 Cyg: Revisited orbital elements and the interpretation of intrinsic variability of the primary component*, 2014, MNRAS, 438, 3093
3. Tkachenko, A., Degroote, P., Aerts, C., Pavlovski, K., Southworth, J., Papics, P. I., Moravveji, E., Lehmann, H., Kolbas, V., Clemer, K., *Modelling of sigma Scorpii, a high-mass binary with a beta Cep variable primary component*, 2014, MNRAS, 442, 616
4. Borkovits, T., Derekas, A., Fuller, J., Szabo, M., Pavlovski, K., Csak, B., Dozsa, A., Kovacs, J., Scabo, R., Hambleton, K. M., Kinemuchi, K., Kolbas, V., Kurtz, D. W., Maloney, F., Prsa, A., Southworth, J., Szatakovics, J., Biro, I. B., Jankovics, I., *HD 183648: a Kepler eclipsing binary with anomalous ellipsoidal variations and a pulsating component*, 2014, MNRAS, accepted
5. Pavlovski, K., Southworth, J., Kolbas, V., Smalley, B., *Absolute dimensions of detached eclipsing binaries - III. The metallic-lined system YZ Cassiopeiae*, 2014, MNRAS, 438, 590

6. Skoko, Ž., Popović, J., Dekanić, K., Kolbas, V., Popović, S., 2012, *XBroad - program for extracting basic microstructure information from XRD pattern in a few clicks*, JAC, 45, 594
7. Pavlovski, K., Southworth, J., Kolbas, V., *Apsidal motion of the eclipsing binary AS Camelopardalis: discrepancy resolved*, 2011, ApJL, 734, L29
8. Pavlovski, K., Tamajo, E., Koubsky, P., Southworth J., Yang, S., Kolbas, V., *Chemical evolution of high-mass stars in close binaries - II. The evolved component of the eclipsing binary V380 Cyg*, 2009, MNRAS, 400, 791

Publications in conference proceedings / Konferencijski radovi:

1. Kolbas, V., Pavlovski, K., *Constrained Disentangling: Complementary spectroscopic and interferometric solution*, EAS, 64, 407
2. Dervisoglu, A., Pavlovski, K., Kolbas, V., Southworth, J., *Tracing CNO Exposed Layers in the Hot Algol-Type Binary System 68 Her*, 2013, EAS, 64, 389
3. Kolbas, V., Pavlovski, K., *Constrained Genetic Disentangling of Close Binary Spectra*, 2012, IAUS, 282 405
4. Kolbas, V., Pavlovski, K., Southworth, J., Lee, C-U., Lee, J.W., Kim, S.-L., Kim, H.-I., *Chemical History of Algol and its Components*, 2012, IAUS, 282, 303
5. Pavlovski, K., Southworth, J., Tamajo, E., Kolbas, V., *Observational approach to the chemical evolution of high-mass binaries*, BSRSL, 80, 714
6. Pavlovski, K., Kolbas, V., Southworth, J., *Echelle Spectroscopy of Algol and the Chemical Composition of its Components*, 2010, ASPC, 435, 275
7. Pavlovski, K., Tamajo, E., Koubsky, P., Southworth, J., Yang, S., Kolbas, V., *Probing the Models: V380 Cygni Revisited*, 2010, ASPC, 435, 191

Attended conferences / konferencije:

- IAU Symposium 282 - From Interacting Binaries to Exoplanets: Essential Modeling Tools, 2011, Tatranska Lomnica, Slovakia
- XIth Hvar Astrophysical Colloquium - The Most Mysterious Binaries: Significance for Astrophysics, 2012, Hvar, Croatia
- Setting a new standard in the analysis of binary stars, 2013, Leuven, Belgium

Summer schools / ljetne škole:

- Summer School Binary stars, 2012, KU Leuven, Belgium